

# **Filament Winding: a Unified Approach**

Sotiris Koussios



# **Filament Winding: a Unified Approach**

## **Proefschrift**

Ter verkrijging van de graad van doctor  
aan de Technische Universiteit Delft,  
op gezag van de Rector Magnificus prof.dr.ir. J.T. Fokkema,  
voorzitter van het College voor Promoties,  
in het openbaar te verdedigen  
op dinsdag 14 december om 15:30 uur

door

Sotiris KOUSSIOS  
ingenieur luchtvaart en ruimtevaart  
geboren te Hilversum

Dit proefschrift is goedgekeurd door de promotoren:

Prof. ir. A. Beukers

Prof. dr. Z. Gürdal

Prof. dr. ir. M.J.L. van Tooren

Samenstelling promotiecommissie:

Rector Magnificus

voorzitter

Prof. ir. A. Beukers

Technische Universiteit Delft, promotor

Prof. dr. Z. Gürdal

Technische Universiteit Delft, promotor

Prof. dr. ir. M.J.L. van Tooren

Technische Universiteit Delft, promotor

Prof. dr. ir. R. Akkerman

Universiteit Twente

Prof. dr. V.V. Vasiliev

Russian State University of Technology

Prof. dr. S.C. Mantell

University of Minnesota

Dr. ir. O.K. Bergsma

Technische Universiteit Delft

Dr. ir. O.K. Bergsma heeft als begeleider in belangrijke mate aan de totstandkoming van het proefschrift bijgedragen.

*Published and distributed by: DUP Science*

DUP Science is an imprint of

Delft University Press

P.O. Box 98

2600 MG Delft

The Netherlands

Telephone: + 31 15 27 85 678

Telefax: + 31 15 27 85 706

E-mail: [info@library.tudelft.nl](mailto:info@library.tudelft.nl)

ISBN 90-407-2551-9

Keywords: Filament Winding, Pressure Vessel Design, Process Optimisation

Copyright © 2004 by S. Koussios

All rights reserved. No part of the material protected by this copyright notice may be reproduced or utilised in any form or by any means, electronic or mechanical, including photocopying, recording or by any information storage and retrieval system, without written permission from the publisher:

Delft University Press

Printed in the Netherlands

*Dedicated to Janna, with truly infinite love*



## Acknowledgement

In the first place I would like to extensively thank the people who contributed to this thesis with their ideas, expertise and, sometimes, critical remarks: Otto Bergsma, Jos van Kan, Fred van Keulen, Dragan Vidovic, Pyrrhos Stathis, Yiannis Patras, Bas Veldman and Teun Weustink.

The work done by several (former) students proved to be of significant importance as a source of ideas and a compensation medium for the lack of time: Kjelt van Rijswijk, Geert Nouwen, Glen Mitchell, Martin Renggli and Adem Kahrman.

From my colleagues, special thanks go to Darko Stavrov for being an excellent office mate, Rogier Nijssen as a nice replacement of Darko, and Rogier Oosterom for listening to my complaints and for supporting me in the difficult times that inevitably occur when doing a Ph.D. In addition, Simon Joncas, Sebastiaan Lindstedt, Bert Weteringe, Valeria Antonelli, Tjarko de Jong and Bas Veldman belong also to the group of fun-increasing parameters. Additional thanks to Lisette and Gemma for their encourage and workload relief.

The guys of the traditional club of every day dinning at the University restaurant deserve here special attention: Pyrrhos Stathis (undoubtedly my best friend), Dmitry Cheresiz, Peter Celinski and Dan Cristu. Our discussions were not scientific at all, but pretty inspiring.

In regard to my living environment, special thanks to Nikos, Elena and Ferdinand for being the best neighbours one can have, including a former neighbour, Andy Debecker.

The initiation and completion of this work would not have been possible without the supervision of Otto Bergsma, Adriaan Beukers, Zafer Gurdal and M.J.L. van Tooren. Consequently, expressing my appreciation here is, except for political reasons (see list of committee members), a justified action.

The support of Henk and Gerry Bosma is definitely worth mentioning. The interest showed, and encouragement provided by my family is noticeable. Among them, special thanks to Alexandros and Dimitris, the best brothers a Sotiris can have.

In this very dedicated last paragraph, where the meaning of words is probably not sufficient enough, I would like to thank my wife Janna, for her love, patience, understanding and encouragement during these difficult, but unforgettable time. Without her, this work would not have been possible at all.



## **In memoriam**

*During the preparation of this manuscript, the former composites group leader and former dean of the faculty, Professor Theo de Jong, died in the early morning of 6 September at the age of 63. His inspiring lectures, scientific achievements and dedication to the group have significantly influenced several generations of engineers. Among his contributions, the greatest heritage he left is the integral way of designing and understanding composite structures, provided to his students with the unique combination of humour, passion, and rigorous mathematical formulations. It is our duty to keep his spirit alive.*

*Theo, thank you*



# Contents

<b>Abstract</b>	<b>xv</b>
<b>Reader's guide</b>	<b>xvii</b>
<b>Nomenclature</b>	<b>xix</b>
<b>Abbreviations</b>	<b>xxxi</b>
<b>1 Introduction</b>	<b>1</b>
1.1 Background	1
1.2 Thesis justification	5
1.3 Framework	11
<i>Part A: Fundamentals</i>	<u>17</u>
<b>2 Curves in space</b>	<b>19</b>
2.1 Fundamental forms	21
2.2 Curvatures	24
2.3 Frenet frames	27
2.4 Curves on shells of revolution	31
<b>3 Thin anisotropic shells of revolution</b>	<b>35</b>
3.1 Governing equations	37
3.2 Influence of the curvatures on the load distribution	41
3.3 Optimal shape determination	44
<b>4 Application: composite pressure vessels</b>	<b>47</b>
4.1 Shape properties	49
4.2 qrs-parameterisation	51
4.3 Design rules & performance	54
<i>Part B: Reinforcing layer architecture</i>	<u>57</u>
<b>5 Geodesic trajectories</b>	<b>59</b>
5.1 Curves of minimum length	61
5.2 Geodesics on shells of revolution	63
5.3 Numerical evaluation	65
5.4 Basic geodesics	70

## Contents

<b>6</b>	<b>Non-geodesic trajectories</b>	<b>73</b>
6.1	Basic geometry	75
6.2	General path equation	78
6.3	Parameterisation & evaluation	82
6.4	Examples	86
<b>7</b>	<b>Friction determination</b>	<b>93</b>
7.1	Mandrel design	95
7.2	Machine control	103
7.3	Experiments	107
7.4	Results & discussion	111
7.5	Concluding remarks	117
<b>8</b>	<b>Winding patterns &amp; fibre stacking</b>	<b>119</b>
8.1	Basic theory	121
8.2	Pattern generating algorithm	128
8.3	Laminate thickness variation	132
8.4	Example	135
<b>9</b>	<b>Pressure vessels revisited (1)</b>	<b>137</b>
9.1	Trajectories of a finite dimensioned roving	139
9.2	Transitional circuits	141
9.3	Maximum strength versus optimal pattern	146
9.4	Influence of the fibre layer geometry on the mechanical properties	150
<i>Part C: Production process</i>		<b>157</b>
<b>10</b>	<b>Basic geometry</b>	<b>159</b>
10.1	Generic machine configuration	161
10.2	Input parameters	165
10.3	Examples	171
<b>11</b>	<b>Kinematic model</b>	<b>179</b>
11.1	Winding equations	181
11.2	Machine configurations	186
11.3	Solution procedure	191
11.4	Results & discussion	196

<b>12 Dynamics of filament winding</b>	<b>207</b>
12.1 Machine limits & control data	209
12.2 Interpolation techniques	212
12.3 Differentiation & filtering	217
12.4 Results & discussion	220
<b>13 Collision control</b>	<b>223</b>
13.1 Feed eye geometry	225
13.2 Machine limits	228
13.3 Numerical bounds determination	230
<b>14 Process optimisation</b>	<b>235</b>
14.1 Problem formulation	237
14.2 Grid construction	241
14.3 Application of dynamic programming	248
14.4 Results & discussion	254
<b>15 Pressure vessels revisited (2)</b>	<b>259</b>
15.1 Winding of quasi-ellipsoidal shells	261
15.2 Results & discussion	268
15.3 Winding a qrs vessel	273
<i>Part D: Design issues</i>	<u>281</u>
<b>16 Articulated pressurisable structures</b>	<b>283</b>
16.1 Geometry	285
16.2 Structural properties	291
16.3 Applications	297
16.4 Strut elements	299
<b>17 Pressure vessels revisited (3)</b>	<b>303</b>
17.1 Extended netting theory	305
17.2 Isotensoid-related shapes	309
17.3 Aerospace applications: Fuselage element	317
<b>18 Conclusions</b>	<b>319</b>
18.1 Extended summary	319
18.2 Contributions overview	322
18.3 Main issues: Integral design & insight	326
18.4 Future directions	328

## **Contents**

<b>Appendix A:</b> Production process simulation on a tumble winder	331
<b>Appendix B:</b> Production process simulation on a lathe winder	337
<b>Samenvatting</b>	343
<b>Curriculum Vitae</b>	345
<b>List of publications</b>	347
<b>Bibliography</b>	349

# Abstract

In this dissertation we have presented an overview and comprehensive treatment of several facets of the filament winding process. With the concepts of differential geometry and the theory of thin anisotropic shells of revolution, a parametric shape generator has been formulated for the design procedure of optimal composite pressure vessels in particular.

The mathematical description of both geodesic and non-geodesic roving trajectories has been presented, including a proposal for a mandrel shape that facilitates the experimental procedure for the determination of the coefficient of friction. In addition, an overview of several (non-) geodesic trajectories is here given. Furthermore, an algorithm for the automatic generation of suitable winding patterns has been outlined, in combination with several pattern optimisation strategies.

An extensive treatment of the kinematics of filament winding is here presented, in combination with several recommendations for a proper derivation of the associated velocities and accelerations to which the moving machine parts and the roving itself are subjected. A simplified collision control module has resulted in the determination of the limits where the feed eye is allowed to move in. Within this space and with the dynamic machine limits, an optimisation problem has been set up, serving the aim of production time minimisation. This has been achieved by application of dynamic programming that minimises a summation of constraint respecting time increments, after the realisation of a grid-reduction with a technique that is based on elementary sparse matrix multiplication. Furthermore, several novel machine configurations have been proposed, which are dedicated to pressure vessels with various aspect ratios, shape morphology and types of applied wound circuits.

With the shell equilibrium equations as a basis, we have derived the class of articulated pressurisable structures, comprising isotensoids that are axially stacked on each other. Moreover, the non-geodesically overwound isotensoid has been introduced, together with a variant being additionally subjected to external radial forces. The same equilibrium equations have generated shapes like the geodesically overwound hyperboloid and optimal toroidal pressure vessels. Furthermore, we have proposed several application fields for these items.

As a leitmotiv throughout the thesis, the derived methodologies and equations have been applied on the class of isotensoid pressure vessels. The results generated by the roving trajectories description modules and pattern generation algorithms are verified by simulation, while the results of the kinematic solver and the optimiser are evaluated by both simulation and implementation on a winding machine. However, mechanical testing of the proposed structures and test-running of the introduced machine configurations must here be left over to the recommendations.

## Keywords

**Filament winding, Pressure vessel design, Production process, Optimisation**



# Reader's guide

## Assumptions

The surfaces subjected to fibre placement in this dissertation can be divided into two categories: rotationally symmetric and arbitrary, continuous surfaces. With an exception of sections 2.1, 2.2 2.3, 5.1, 10.1, 11.1 and 17.3 we exclusively consider here shells of revolution. In addition, when the winding angle of the roving is expressed in terms of only the shell radius, the path under consideration is geodesic. The assumptions are summarised in the table below:

Equations involving matrices, vectors and / or vector components	No geometrical assumptions
Equations involving the angular quantities $\alpha, \beta, \phi$ in undetermined form (without arguments) or as, among others, a function of the coefficient of friction ( $\mu$ )	Rotational symmetry No path assumptions
Equations involving a description of $\alpha$ in terms of the radial parameters (polar opening radius and actual radius)	Rotational symmetry and geodesic tow paths

*Table: Overview of the assumptions supporting the derived equations throughout the thesis*

## Nomenclature

Matrices and vectors are indicated by **bold**, parameters and functions denoted by a single symbol with *Italic*, while Greek symbols are given in their regular appearance. Reference systems and coordinate rotation matrices are respectively denoted as {symbol} and [symbol].

Several symbols have been reused. In the nomenclature list, at the right side of the rule describing the meaning of a symbol, we indicate the chapter number where the validity of the provided explanation begins. The validity holds until the same symbol is redefined according to a higher chapter number. For example:

$d$	[Kg/m <sup>2</sup> ]	Density	4
	[-]	Number of completely formed layers	8,15
	[m <sup>-1</sup> ]	Minimum total curvature	11

means: the symbol  $d$  denotes the density in chapter 4; in chapter 8 it obtains its new definition (number of completely formed layers) and, from chapter 11, it denotes the minimum total curvature. In chapter 15, the symbol denotes again the number of completely formed layers (as additionally corresponding to chapter 8).

In regard to the dimensions, we use here as example the S.I. units. With an exception for [mm], the units involved in every indicated dimension can freely be chosen. The meaning of [-] is “dimensionless”. The notation [ ] stands for undetermined dimensions that depend on the formulation of the associated function(s).

## Numbering

The thesis is divided into four parts. The numbering of the chapters is continuous throughout the thesis. Reference to a particular chapter or section is indicated with Arabic numbers, for example chapter 2 or section 5.4.

The figures, tables and equations are separately numbered in each chapter, with the first number indicating the chapter they belong to. When cited, equations are always indicated by the combination of two Arabic numbers within parentheses ( ), where the first one is referring to the chapter, and the second one to the equation number, for example (3.1). Figures and tables are indicated without parentheses, e.g. 6.9. The first figure, presented in the introductory page of every chapter is not numbered.

## Bibliography

To increase the usability of the reference list for the interested reader, we divided the bibliography list into 13 subjects, indicated by Greek symbols:

$\alpha$	General filament winding & design
$\beta$	Winding patterns
$\gamma$	Roving trajectories
$\delta$	Dissertations on filament winding
$\epsilon$	Shell theory
$\zeta$	Composite pressure vessels: general design
$\eta$	Cylindrical parts of composite pressure vessels / Drive shafts
$\theta$	Filament wound anisogrid lattice structures
$\iota$	Kinematics & dynamics
$\kappa$	Mechanics of (an-) isotropic materials
$\lambda$	Optimisation
$\mu$	General & numerical mathematics / Differential geometry
$\nu$	Fibre tensioners

The complete set of publications included in one category is consequently numbered, and the references are cited in the text by a combination of the Greek symbol referring to the relevant group and an Arabic number, both within brackets [ ], for example [ $\gamma$ 3].

It should be noted that several publications could alternatively be divided into multiple groups. We use here the division as elaborated during the research stage for this thesis. In addition, the bibliography presented here is by no means intended to be a complete one.

## Nomenclature

Matrices & vectors		Chapter
<b>A, a, B, b</b>	Point positions	13
<b>A<sub>1</sub></b>	Matrix for the continuity condition	12
<b>A<sub>2</sub></b>	VanderMonde matrix	12
<b>A<sub>t</sub></b>	Triple grid combination matrix	14
<b>B</b>	Binormal vector	2
<b>B(t)</b>	Total backward transition matrix	14
<b>C</b>	Vector describing a curve	2
<b>C<sub>col</sub></b>	Collision contour	13
<b>C(t)</b>	Connectivity matrix	14
<b>E<sub>t</sub></b>	Minimum transition cost matrix	14
<b>{E}</b>	Reference system	10
<b>e</b>	Reference unity vector at a roving locus-related point on a shell	2
<b>F(t)</b>	Total forward transition matrix	14
<b>G</b>	Roving position vector, related to the body system	10
<b>g<sub>t</sub></b>	Reduced grid vector	14
<b>i</b>	Reference unit vector in the <i>x</i> -direction	10
<b>j</b>	Reference unit vector in the <i>y</i> -direction	10
<b>k</b>	Reference unit vector in the <i>z</i> -direction	10
<b>M</b>	Set of kinematic equations	11
<b>N</b>	Normal vector	2
	Reduced set of kinematic equations	11
	Total combination matrix	14
<b>N<sub>1</sub>, N<sub>2</sub></b>	Nullspaces	12
<b>P<sub>1</sub>, P<sub>2</sub></b>	Pseudoinverses	12
<b>p</b>	Feed eye position	10
<b>q</b>	Intersection point of line segments	13
<b>R</b>	Spool position	10
<b>R(t)</b>	Reduced transition matrix	14
<b>r<sub>i</sub>(k)</b>	Row contained in the transition matrix	14
<b>[R]</b>	Rotation matrix	10

## Matrices & vectors (S- $\lambda_t$ )

<b>S</b>	Vector function describing a surface	2
	Vector containing a combination of <b>G</b> and $\Delta\mathbf{G}$	11
<b>s(t)</b>	Grid selector vector	14
<b>T</b>	Vector tangent to a curve	2
<b>T(t)</b>	Transition matrix	14
<b>U<sub>t</sub></b>	Triple grid combination matrix with time increments	14
<b>u<sub>1</sub></b>	Vector for the Least Squares condition	12
<b>u<sub>2</sub></b>	Vector for the continuity condition	12
<b>V<sub>t</sub></b>	Double grid combination matrix	14
<b>v</b>	Vector containing the polynomial coefficients	12
<b>v<sub>1</sub></b>	Roving position vector, related to the inertia system	11
<b>v<sub>2</sub></b>	Roving orientation vector, related to the inertia system	11
<b><math>\Delta\mathbf{G}</math></b>	Roving orientation vector, related to the body system	10
<b><math>\Delta\mathbf{T}</math></b>	Time increment vector	14
<b><math>\lambda_t</math></b>	Vector containing the allowed feed eye position ranges	14

Scalars (Latin)			Chapter
<i>A</i>	[N]	Axial force	3
	[ ]	Characteristic functions	6
	[rad]	Feed eye roller inclination	11
	[m <sup>2</sup> ]	Floor surface	16
<i>a</i>	[m]	Shell radius	2
	[-]	Dimensionless fibre force	3
	[mm]	Exponent function (with argument <i>b</i> )	7
<i>B</i>	[-]	Friction function	6
	[-]	Dimensionless roving width	8
<i>b</i>	[m]	Shell meridian function	2
	[m]	Roving width	7
<i>C</i>	[rad]	Spindle rotation	7,13
	[-]	Cubic spline	12
	[-]	Shortcut for expressions	17
<i>c</i>	[MPa]	Elasticity-related constant	3
	[m]	Polar opening radius	5
	[-]	Dimensionless total fibre bed cross section / $\pi$	8
	[-]	Shortcut for a function based on <i>q</i> and <i>r</i>	9
	[ ]	Constant	9
	[m]	Polar opening radius	10
<i>D</i>	[-]	Load-bearing contribution of a single layer	9
	[m]	Shortcut for determinant-related functions	11
<i>d</i>	[Kg/m]	Density per unit of length	4
	[-]	Number of completely formed layers	8,15
	[m <sup>-1</sup> ]	Minimum total curvature	11
<i>E</i>	[m <sup>2</sup> ]	Coefficient of the first fundamental form	2,5
	[MPa]	Modulus of elasticity	3
	[-]	Total measurement error	7
	[-]	Dimensionless roving placement eccentricity	8
<i>e</i>	[m]	Coefficient of the second fundamental form	2
	[MPa]	Elasticity-related constant	3
<i>F</i>	[m <sup>2</sup> ]	Coefficient of the first fundamental form	2
	[N]	Force, general notation	3
<i>f</i>	[m]	Coefficient of the second fundamental form	2
	[N/m]	Fibre force per unity of length	3
	[ ]	Function, general notation	5
	[ ]	Selection function for grid points	14
<i>G</i>	[m <sup>2</sup> ]	Coefficient of the first fundamental form	2
<i>g</i>	[m]	Coefficient of the second fundamental form	2
	[m]	Function for a shell defined in spherical coordinates	6

## Scalars ( $H-n$ )

$H$	$[m^{-1}]$	Mean curvature	2
	$[-]$	Dimensionless cylinder length	4
$h$	$[-]$	Verticality condition of $\mathbf{G}$ and $\Delta\mathbf{G}$	11
	$[m]$	Storey height	16
$i$	$[-]$	Circuit number for the friction experiments	7
	$[-]$	$i^{\text{th}}$ collection of $p$ circuits	8
	$[-]$	Counter	14
	$[-]$	Number of isotensoid cells per storey	16
$j$	$[-]$	Indicative number of placed circuit	10
	$[-]$	Counter	14
$K$	$[m^{-2}]$	Gaussian curvature	2
	$[-]$	Measurement deviation	7
	$[m^2]$	Axial load coefficient	17
	$[-]$	Dimensionless normal curvature	17
$k$	$[m^{-1}]$	Curvature	2
	$[-]$	Elasticity ratio of the main material directions	3
	$[-]$	Dimensionless axial force (with subscript $a$ )	3,15
	$[-]$	Counter	5,14
	$[-]$	Aspect ratio of a spheroid	5
	$[-]$	Pattern constant	8,15
	$[-]$	Truncation number for approximations	12
	$[-]$	Ratio of the cross carriage position and the equatorial radius of the mandrel	15
$L$	$[m]$	Curve length	2
	$[m]$	Total roving length, provided by a single circuit	4
	$[-]$	Dimensionless roving length	4,16
	$[ ]$	Lagrange term	12
	$[m]$	Span	16
$l$	$[m]$	Integration parameter	7
$M$	$[-]$	Dimensionless moment, applied on the pole	16
$m$	$[-]$	Storey counter	16
	$[-]$	Maximal available friction	17
$N$	$[MPa]$	Membrane stress in a shell	3
	$[-]$	Required number of rovings (subscript $f$ )	3,9
	$[-]$	Number of intervals for integration	5
$n$	$[-]$	Circuit counter	7
	$[-]$	Number of rovings fitting in a single layer	8
	$[-]$	Number of storeys	16

**Scalars ( $P$ - $x$ )**

$P$	[MPa]	Internal pressure	3,15
	[-]	Dimensionless modified meridian profile function	9
	[ ]	Profile function, combining cubic splines	12
$p$	[-]	Pattern constant	8
	[-]	Number of points used for the roving discretisation	10
	[m]	Feed eye coordinate for the tumble winder	11
	[ ]	Lagrange polynomial	12
$Q$	[rad]	Primary mandrel rotation	10
$q$	[-]	Shape factor	4
$R$	[m]	Radius of curvature	2
	[-]	Ratio of hoop and polar circuits (subscript $hp$ )	4
	[m]	Maximum radius	6
	[rad]	Secondary mandrel rotation	10
$r$	[-]	Dimensionless axial load	4,15
	[m]	Minimum mandrel radius	7
$S$	[-]	Dimensionless mandrel surface	4
	[m <sup>2</sup> ]	Total mandrel surface (subscript <i>total</i> )	4
	[m]	Total roving length	7
	[m]	Element of the <b>S</b> vector	11
	[m <sup>2</sup> ]	Fibre load coefficient	17
$s$	[m]	Length, as used in differentials and integrals	2
	[-]	Dimensionless cylindrical length, related to $Y_{eq}$	4
$T$	[-]	Approximation function for the turn-around angle	5
	[-]	Dimensionless Fibre layer thickness	8
	[-]	Shortcut for function contained in the reduced determinant $N$	11
	[s]	Time	14
$t$	[ ]	Argument, as used in integration	2,16
	[m]	Thickness	3
	[-]	Counter	14
$U$	[m]	Partial determinant, based on <b>G</b> and $\Delta\mathbf{G}$	11
	[-]	Line segments intersection parameter	13
$u$	[m <sup>-1</sup> ]	Maximum total curvature	11
	[-]	Line segments intersection parameter	13
$V$	[-]	Dimensionless mandrel volume	4
	[m <sup>3</sup> ]	Total mandrel volume (subscript <i>total</i> )	4
$X$	[m]	Cross carriage translation (lathe winder)	11
$x$	[m]	$x$ -coordinate	2

**Scalars (Y-#)**

$Y$	[-]	Dimensionless radius	3,15
	[m]	Carriage translation (lathe winder)	11
$y$	[m]	$y$ -coordinate	2
$Z$	[-]	Dimensionless coordinate in the axial direction	3,15
	[m]	Carriage translation (lathe winder)	7
	[m]	Feed eye elevation	11
$z$	[m]	$z$ -coordinate	2
#	[ ]	Argument in functions, general notation	2

<b>Scalars (Greek)</b>		<i>Chapter</i>
$\alpha$	[rad] Winding angle	2
$\beta$	[rad] Meridian slope angle	3
$\Gamma$	[ ] Inverse of the ODE for the angle $\phi$	5
	[-] Christoffel symbols of the second kind	6
	[-] Ratio of storey height and span	16
$\gamma$	[rad] Angle between the $Q$ and $R$ axes of rotation	10
$\Delta$	[-] Dimensionless roving thickness	8
$\Delta a$	[m] Tolerance value	14
$\Delta g$	[m] Grid increment for the feed eye moving space	14
$\Delta K$	[rad] Angular propagation between two adjacent circuits	8
$\Delta Z$	[-] Polar moment amplitude	16
$\Delta Z_0$	[mm] Initial carriage position referencing error	7
$\Delta\varphi$	[rad] Parallel angle, occupied by a single roving width	8
$\delta$	[rad] Angle between the principal shell directions	2
	[-] Exponent function	5
	[mm] Roving thickness	8
$\epsilon$	[ ] Small deviation	6
	[mm] Roving placement eccentricity at the pole	8
$\zeta$	[-] Dimensionless carriage translation	7
	[-] Ratio of the polar and equatorial radius	15
$\eta$	[-] Shortcut for trigonometric combination	11
$\theta$	[rad] Independent parameter	2
	[rad] First spherical coordinate	5
$\Lambda$	[-] Ratio of cell radius and span	16
$\lambda$	[-] Ratio of the maximum and minimum radius	5
	[m] Metric distance between roving placement point and feed eye	10
	[-] Gradient coefficient in friction function	17
$\mu$	[-] Coefficient of friction	6,17
	[-] Aspect ratio	15
$\nu$	[-] Dimensionless effective polar opening radius	8
	[-] Gearing ratio	11

## Scalars (Greek) ( $\Xi$ - $\omega$ )

$\Xi$	[m]	Argument for the spindle rotation determination	11
$\xi$	[-]	Aspect ratio of a cylinder	6
	[-]	Dimensionless position of the outer roving edge	8
	[-]	Relative deflation	16
$\rho$	[m]	Shell radius	3
$\sigma$	[MPa]	Stress, general	3,16
	[MPa]	Ultimate fibre stress in tension	9
	[m]	Distance between spool and feed eye	11
	[MPa]	Floor load (only with subscript $f$ )	16
$\tau$	[m <sup>-1</sup> ]	Torsion	2
	[MPa]	Shear stress	3
	[rad]	Top angle of a cone	5,6
$\Phi$	[rad]	Turn-around angle for an isotensoid	9
$\phi$	[rad]	Independent parameter	2
	[rad]	Angle in the parallel plane of a shell of revolution	4
$\varphi$	[rad]	Angle enclosed by two adjacent normal radii	3
	[rad]	Circumferential angle	16
$\psi$	[ ]	ODE for the angle $\phi$	5
$\Omega$	[rad]	Additional turn-around angle at the poles	8
$\omega$	[rad]	Angle enclosed by two adjacent geodesic radii	6
	[rad]	Sum of the spindle rotation and the parallel angle $\phi$	11

Indices		<i>Chapter</i>
0	Polar opening related	3
	Constant indicator	7
	Inertia system	10
	Corresponding to zero feed eye translation	11
	Upper pole	11
	Lagrange term indicator	12
	Corresponding to a closed isotenoid (toroid)	15
	Minimum radius of a hyperboloid	17
1	First principal material direction	3
	Constant indicator	7
	Reference system after the $Q$ -rotation	10
	Lower pole	11
	Lagrange term indicator	12
2	Second principal material direction	3
	Reference system after the $Q$ and $\gamma$ rotations	10
	Lagrange term indicator	12
3	Body reference system	10
<i>a</i>	Axial	3
	Approximate	11
<i>acc</i>	Acceleration related	14
<b>B</b>	Induced by the roving width	8
<i>b</i>	Begin (first discrete point)	5,14
<i>c</i>	Initial, for the spherical coordinate $\theta$	6
	Cylinder radius (in combination with $\rho$ )	9
	Complete circuit	10,14
	Cumulative	11
<i>cyl</i>	Related to the cylindrical part	15
<i>def</i>	Related to the deformed shape	16
<i>defl</i>	Related to the (partially) deflated shape	16
<i>down</i>	Lower polar opening	10
<i>e</i>	Strain-related	3,15
	End (last discrete point)	5,14
	Corresponding to the feed eye	13
<i>eff</i>	Effective	8
<i>eq</i>	Equatorial	4

## Indices (*f-tr*)

<i>f</i>	Fibre related	3,4
	Floor	16
<i>g</i>	Geodesic	2,15
	Related to solution search intervals	11
<i>gr</i>	Grid	14
<i>h</i>	According to the Heun method	5
	Hoop winding	17
<i>hp</i>	Ratio hoop / polar	4
<i>in</i>	Close to the feed eye supporting structure	13
<i>init</i>	Related to the initial, undeformed shape	16
<i>L</i>	Lower bound	11
<i>l</i>	Related to the roving length	9
	Related to the linear part	12
<i>m</i>	Meridional direction	2,17
	Measured	7
	Where $\lambda$ and $Y_{eq}$ match	9
	Minimum winding angle	10
	Related to the machine reference system	13
	Corresponding to the maximum meridian height	15
<i>max</i>	Maximum	4
<i>min</i>	Minimum	4
<i>n</i>	Normal	2
<i>out</i>	Related to outer feed eye area, (towards support unit)	13
<i>p</i>	Parallel direction	2,17
	Interpolating polynomial	6
	Related to the periodic part	12
<i>R</i>	Upper bound	11
<i>r</i>	Subscript for internal pressure	3
	Maximum value for $z$ , real value	7
	Radial	16
	Where uncompleted isotenoids are merged	17
<i>req</i>	Required	9
<i>s</i>	Solution, up to a certain increment	11
<i>t</i>	Total	2
	Tuned value, for averaging the measurement error	7
	Counter	14
<i>tot</i>	Total rotation (after $Q$ , $\gamma$ and $R$ )	10
<i>tr</i>	Associated with transitional circuits	9

**Indices (up-\*)**

<i>up</i>	Upper polar opening	10
<i>vel</i>	Velocity related	14
<i>xy</i>	Corresponding to vectors in the <i>x</i> and <i>y</i> direction	11
<i>yz</i>	Corresponding to vectors in the <i>y</i> and <i>z</i> direction	11
<i>zx</i>	Corresponding to vectors in the <i>z</i> and <i>x</i> direction	11
$\Delta$	Induced by the roving thickness	8
$\theta$	In the direction of $\theta$	2
$\mu$	Lateral direction	6
$\nu$	Dimensionless, in the normal curvature direction	3
$\phi$	In the direction of $\phi$	2
$\varphi$	Tangential (circumferential)	16
I, II, III, IV	Meridian quadrant numbers	10
+	Leading	8
-	Lagging	8
*	Dimensionless position where the thickness distribution functions $T_0$ and $T_{\text{polar}}$ match	8
	Modified in an iteration loop	9

## Special functions & operations

$C\#$	Minimum integer containing #
$c$	Shortcut for cosine
$d\#$	Differential
$\text{dim}\#$	Dimension(s) of the vector (matrix) argument
$\text{ellF}$	Incomplete elliptic integral of the first kind
$\text{ellE}$	Incomplete elliptic integral of the second kind
$\text{ell}\Pi$	Incomplete elliptic integral of the third kind
$\text{IP}\#$	Maximum integer, contained in #
$\ln$	Natural logarithm
$\text{mod}$	Modulo
$\text{round}\#$	Round # off to closest integer
$s$	Shortcut for sine
$\text{sgn}\#$	Sign of #, gives the values $\{-1,0,1\}$
$\text{sinc}$	Modified sine function (equation (12.19))
$\Delta\#$	Finite difference
	Deviation (only in chapter 9)
$\delta\#$	First variation
$\#'( \# ), \#_{\#}$	First derivative with respect to #
$\#''( \# ), \#_{\#\#}$	Second derivative with respect to #
$\  \# \ $	Vector length
$\#_1 = \#_2$	Set # <sub>1</sub> equal to # <sub>2</sub>
$\#_1 \stackrel{?}{=} \#_2$	Check whether # <sub>1</sub> is equal to # <sub>2</sub>
$\#_1 \rightarrow \#_2$	Transition from # <sub>1</sub> to # <sub>2</sub>
$\propto$	Linearly proportional
$\cdot$	Inner vector product
$\times$	Scalar multiplication or outer vector product
$\otimes$	Non-additive multiplication of equally-dimensioned matrices (equation (14.15))
$\circ$	Non-additive multiplication of unequally-dimensioned matrices (equation (14.21))
$\&$	AND
	<u>Only in chapter 14:</u> Links matrices to each other according to common elements in a specified number of columns contained in each of them, and drops doubled combinations (Equations (14.17) and (14.19)).

## Abbreviations

APS	Articulated pressurisable structures
Aspect ratio	The ratio (maximum height) / (maximum diameter) of a body
BS	Bezier spline
CNC	Computerised Numerical Control
CS	Cubic spline
F	Fourier series
$g$	Gravitational constant
ODE	Ordinary differential equation
PLS	Least squares-based approximating polynomial
RTM	Resin transfer moulding
rpm	Revolutions per minute (rotational speed)



# 1

## Introduction

### 1.1 Background

#### Design of composites

When dealing with composite structures in the most general sense of the word, the most common terms for the justification of their introduction and utilisation are: light, strong, stiff, advanced and, occasionally, optimal. The first question arising is: optimal with respect to what? The immediate answer is usually formulated in terms of maximum this by minimum that, or by keeping this constant while etc. etc. Unfortunately (or not), another important question, simultaneously evolved with the extension of the applications field for composite structures, is a rather simple one: how much does it cost?

More specific, since composites are losing the élan of advanced, exotic aerospace materials and become performers of more down-to-earth tasks, the aspect of cost reduction and competitiveness with existing structures is gaining importance. The required implementation of economical aspects into the design stage is more than a change in objective or activation of additional constraints.

As outlined in numerous textbooks [ $\alpha 6, \alpha 7, \alpha 8, \alpha 9, \alpha 48, \kappa 1, \kappa 8, \kappa 9, \kappa 10$ ], an equivalent description for the design of a composite structure is the creation of a composite material. More specific, the tailoring of the mechanical properties characterising an elementary composite structure usually involves the choice of materials, stacking sequence, individual layer thickness and (occasionally continuously varying) fibre orientations. In fact, this is the creation of the structural material itself. Obviously, an alternative materials selection will probably lead to e.g. modified stacking sequence etc. A typical example of this statement is the creation of pressure vessels where the choice of fibres and matrix materials directly affects the optimal roving orientation [ $\zeta 10, \zeta 14, \zeta 15, \zeta 16, \zeta 34, \zeta 35, \eta 3, \eta 13, \kappa 10$ ]. Hence, materials selection and shape determination have to be performed simultaneously. A popular term to indicate this is “integral design”.

Recalling the last sentence of the second paragraph, additional implementation of the costs will increasingly amplify the interaction involved in integral design. Instead of two parameters (materials, geometry), we end up with three (materials, geometry and production process characteristics). Therefore, the design process of a composite product must simultaneously involve the evaluation of the selected and engineered production processes [ $\alpha 4$ ].

## Introduction

One can think about the influence of the manufacturing quality on the mechanical performance, voids, suitability of a design for a certain production process, selection of that process according to the desired product volume (custom or series) and so on.

In this thesis we will limit ourselves to filament winding. This process can be characterised by a significant controllability for the entire set of composites design related issues: shape determination, fibre placement, kinematics and dynamics of the production process and finally, the performance of the product itself. The enlarged ability for controlling and mathematically describing the involved facets is the ideal platform for the comprehensive examination of the previously mentioned interaction.

### Brief history of filament winding

Originating in the 50's as an advanced technique for manufacturing rocket engine cases [α32,α37,α43,] the filament winding process is particularly characterised by:

- Improved accuracy for the placement of the rovings (compared to hand lay-up, RTM and press forming)
- Realisation of relatively high fibre volume fractions
- Constant product quality

Hence, for the creation of advanced structures, filament winding seems to be a very suitable production process. At the beginning time, the creativity for inventing machine configurations was rather extensive: the lathe winder, the polar winder, the tumble winder and the racetrack winder are typical results of it. Nevertheless, due to the nature of their applications, the associated production costs were of secondary importance. It should be noted that at the very beginning of filament winding, the lathe winder was practically the only configuration in use [α31]. More specific, the layout of these machines usually involved only a mandrel rotation and carriage translation possibility.

The (actually necessary, see chapter 11) introduction of a cross carriage movement has been a significant improvement with regard to the windability of more exotic shapes. However, the shapes subjected to that process were almost exclusively rotationally symmetric. Further improvements occurred as a result of the computer, leading to better product quality through improved fibre placement accuracy and speed control. The latter is of particular importance for wet winding.

As the evolution of computers proceeded, the capabilities of the filament winding process were further increased with the introduction of sophisticated simulation programs [α20]. To name a few, CadFil [α28,α34], CadWind™, FiberGraphix™ and CadPath™ [β1]. Except the simulation of roving paths on the mandrel and the determination of the required machine movements, several of these programs include modules for the calculation and simulation

of elbows and T-pieces. The specific difficulties of manufacturing these items are extensively treated in [ $\delta 1$ ] (elbows) and [ $\delta 2$ ] (T-pieces). In addition, the nowadays-available software packages include FEM modules and, although not completely elaborated, production process optimisers.

Most modern filament winding machines are CNC-controlled [ $\alpha 3$ ], hence they can easily be integrated in a CAD/CAM environment [ $\alpha 1, \alpha 2, \alpha 3, \alpha 14, \alpha 26, \alpha 50, \beta 1, \gamma 18$  and especially  $\alpha 19, \gamma 19$ ]. For a more extensive history description, one can take [ $\alpha 21$ ] into consideration. Furthermore, [ $\alpha 35, \alpha 36, \alpha 37$ ] provide useful information about the winding process, especially concerning materials and process characteristics. In addition, the filament winding process is described in [ $\alpha 25, \alpha 48$ ]. Although not very extensive, these two references provide sufficient information for thoroughly understanding the process.

### Related work

From the 50's up to middle 80's, the well-known book of Rosato [ $\alpha 43$ ] and the proceedings of the filament winding conference in Pasadena, CA, 1961 [ $\alpha 27, \zeta 1, \zeta 5$ ] where nearly the only information resources about the process itself (we do not mention here the extensive number of publications containing structural aspects of filament wound products).

With the introduction of affordable computational resources, several authors like Calius [ $\eta 2, \iota 5$ ], DiVita [ $\gamma 2, \gamma 3, \gamma 14, \gamma 16, \zeta 25, \iota 9, \iota 10, \iota 21$ ], Mazumdar [ $\alpha 25, \iota 23, \iota 24$ ], Middleton [ $\alpha 14, \alpha 28, \alpha 34$ ] and Wells [ $\alpha 50, \gamma 20$ ] generated interesting papers covering both the roving trajectories description, as well as the kinematics of the process. In addition, DiVita covered also the theory of optimal dome design. Summarising, the main part of contributions can be assigned to DiVita, Mazumdar and Middleton.

With the dissertations of Kirberg [ $\delta 1$ ] and Scholliers [ $\delta 2$ ] the basis has been set for the evaluation of non-rotationally symmetric objects covered with geodesic and non-geodesic roving trajectories. The topic of non-geodesic winding is covered by several authors; among DiVita and Wells, the work of Liang [ $\gamma 12, \gamma 13$ ] and Xian-Li [ $\gamma 21$ ] provide an elegant description of these trajectories. The work of Steltenpool [ $\iota 28$ ] tackles this problem on an entirely numerical way.

Contrary to the formulation of the fibre path geometry, the creation of suitable winding patterns did probably not gain the attention it deserves. With an exception for Johansen [ $\beta 1$ ] and Liang [ $\beta 5$ ], one can hardly find any literature covering this topic, despite its elegance and specific challenges (see chapter 8).

In regard to the kinematic models covering the winding process, the papers published by Chan [ $\iota 5$ ], DiVita [ $\iota 9, \iota 10$ ], and Mazumdar [ $\iota 23, \iota 24$ ] and the master theses of Belle [ $\iota 4$ ] and Moree [ $\iota 26$ ] provide some solutions. In addition, some work is related to the design of robotic cells [ $\iota 1, \iota 6, \iota 27$ ]. Most of the authors treat the kinematic problem by an entirely incremental way and determine the required machine movements by means of standard numerical techniques for root finding. Furthermore, Lye [ $\iota 20$ ] is proposing a low-cost

## Introduction

system which however does not significantly differ from the lathe winder. It should be noted that although most winding process-related papers emphasise on the cure model for the impregnated tows, the subject of kinematics can be considered as fully covered. However, a fully analytical solution for the lathe winder kinematics is not sufficiently elaborated, at least up to the level of direct usability for engineers in practice. Most kinematic models included in these publications are incremental, even at the very beginning stage of describing the fibre path geometry (which is in some cases unavoidable).

On the other hand, the number of references covering the design of pressure vessels and their structural analysis is rather extensive, so we mention only a few. Significant contributions to this field have been made by de Jong [ $\zeta$ 14,  $\zeta$ 15] and Vasiliev [ $\zeta$ 34,  $\zeta$ 35]. Hofeditz [ $\zeta$ 11] and Zickel [ $\zeta$ 36] belong to the group of the first authors covering this topic.

## 1.2 Thesis justification

### State of the art

With the purchase costs as practically the only drawback, the filament winding related software packages determine the fibre layer architecture and do provide the required machine movements for surfaces having no re-entrant curvatures. With computational power widely available, there is generally no need to incorporate more sophisticated algorithms than already in use.

The basic principle of these packages is, in the same spirit as panel methods, discretisation of the surface. Here the comparison ends. The roving is modelled as a collection of usually very small line segments over the surface elements that are linked to each other according to the physiology of the placement process. More precisely, for geodesic winding the in-plane lateral force on the line segments representing the roving is zero, while the opposite case occurs for non-geodesic winding. In this case, it is assumed that at the node where two adjacent line segments are connected to each other, the lateral in-plane force is equal to the normal force, multiplied by a presumed coefficient of friction. With this roving path formulation, a suitable winding pattern can be constructed. After the completion of that pattern, the set of line segments is subjected to the kinematic solver and occasionally to an optimiser for minimising the production time (at least, in some applications). It should be noted that the theories supporting the complete process, from design to production, are sufficiently covered in the literature. For rotationally symmetric objects, the body is usually modelled as a consequence of conical rings that are outlined in [α15].

In most cases, the provided software covers the complete range of rotationally symmetric objects both geodesically and non-geodesically overwound, in combination with some special modules for elbows and T-pieces. In general, the evaluation of non-symmetrical shapes, especially when covered by non-geodesic trajectories has gained insufficient attention. Nevertheless, the potential for tackling these problems is already available.

In regard to the available filament winding literature, we point out the fact that still up to now, there is no textbook providing the mathematical description of that process, from the very beginning up to the production process optimisation. Although rather detailed, the attempt made by Rosato [α43] does not really provide the mathematical expressions needed for in-house development and production of filament wound items. The SAMPE book [α37] does not provide sufficient improvements, especially in the field of kinematics and winding pattern determination, subjects that are also not covered in [α37]. However, it should be noted that when placing these comments, the author has the direct applicability of these books as a first criterion in mind. The detected gap is sufficiently filled by the work of Mazumdar and DiVita. By combining this with [β1], one probably has sufficient information for the complete design and manufacturing procedure of a product.

## Introduction

In this thesis however, cure models are not considered. Hence, filament winding is here nothing else than placing a tow on some body.

## Challenges

The discrete character of the nowadays-available methodologies obviously enables the advantages of generality, robustness and (relative) simplicity of the incorporated modules. However, particular drawbacks can be indicated; to design and produce a certain filament wound structure, some trial and error work is usually required. In addition, since the supporting geometrical models are not parametrically described, the creation of a similar product will usually require a complete new design session. Furthermore, unless a fine discretisation is used (which means more expensive calculations), the associated calculations usually suffer from cumulative error generation.

This problem is inherent to numerical mathematics: the result is a collection of data (in straight or interpolated form) occasionally serving as input for the next evaluation. Probably the most important drawback of discrete methods is that when several changes of the initial design are required, the engineer does not get any directions for taking actions. For example, consider the problem of covering a mandrel having two polar openings with non-geodesic trajectories. Depending on the mandrel geometry and the distribution of the available friction, say as a function of the roving length, the roving might not reach the desired locus on the mandrel after completion of one circuit. In addition, the resulting pattern might not be feasible. Any action to correct this will lie on trial and error.

The second, perhaps more important drawback, is the lack of connecting several design process-related issues to the resulting winding pattern, product performance, or the associated production process. A typical example of this is the lack of achieving a suitable winding pattern because the number of rovings dictated by strength calculations does not correspond to the required number for completing an integer number of wound layers. Or, geodesic winding does not lead to any usable pattern. Although this match is quite obvious, it is usually forgotten and only discovered when trying to manufacture the corresponding product. Another example is that with a proper choice of the machine configuration, the production time can dramatically be minimised.

The need for integral design is obviously applying to filament wound structures. At the early stage of the shape determination, particular quantities like curvatures and metrics are already providing clues for the producibility of the designed item. In the case of an entirely numerical approach, these clues are not visible anymore. Moreover, a trend analysis of e.g. the dimension of a product versus the production time is not easily achievable.

A more pedagogical reason for creating this thesis is that just using some filament winding software will probably not easily provide the insight required for applying craftsmanship during the design and evaluation stage (to cite Professor Arbocz with respect to usage of FEM programs: garbage in, garbage out). Less dramatically, in the field of filament winding, the associated

calculations are far more straightforward and can be visualised on a more direct way. After all, filament winding is a rather geometrical issue.

Summarising, the detected gaps are: expensive software, cumulative errors (in a rather small extend), lack of integral design, limited insight. However, it should be noted that the switchover to an entirely numerical approach is inevitable, even in the majority of filament winding cases. It is still a reality that we have to make the choice between a generic numerical approach, and an insight-providing analytical description. In this thesis we chose for the latter, but without rejecting numerical solution techniques, where necessary.

### Tackled issues

As a result of the detected gaps in the design and evaluation procedures for filament winding, we tried in this thesis to introduce several improvements, increase the number of connections between the involved facets (for example: the creation of suitable winding patterns versus the roving dimensions) and add several items for facilitating the involved calculations. In figure 1.1, the complete design and production process is schematically depicted. The black dots indicate the connection nodes for which the author believes a contribution or improvement is established. The empty dots correspond to the original situation. The symbols refer to the elaborated items, as presented in the next paragraphs. The arrows indicate the sequence of undertaken actions (note the iteration loop).

#### a Application of differential geometry

Although occasionally applied by a few authors [ $\gamma$ ], a complete overview of the differential geometry subjects being relevant for the filament winding problem is missing in the composites-related literature. Consequently, in this thesis, we provide briefly the basic definitions and derivations that are helpful for both the shape determination of e.g. a pressure vessel, as well as the creation of the roving trajectories and the establishment of the kinematic solutions.

#### b Parametric design

Despite its dedicated character, parameterisation provides an elegant method for summarising several design categories and their production related properties. As an example, we apply here this principle on the design procedure of pressure vessels; this idea is also implemented by [ $\zeta 2, \zeta 14, \zeta 15, \zeta 19, \zeta 20, \zeta 27, \zeta 34, \zeta 35$ ]. In this thesis, the coupling of the associated design parameters with the basic parameters provided by differential geometry, is highlighted.

## Introduction

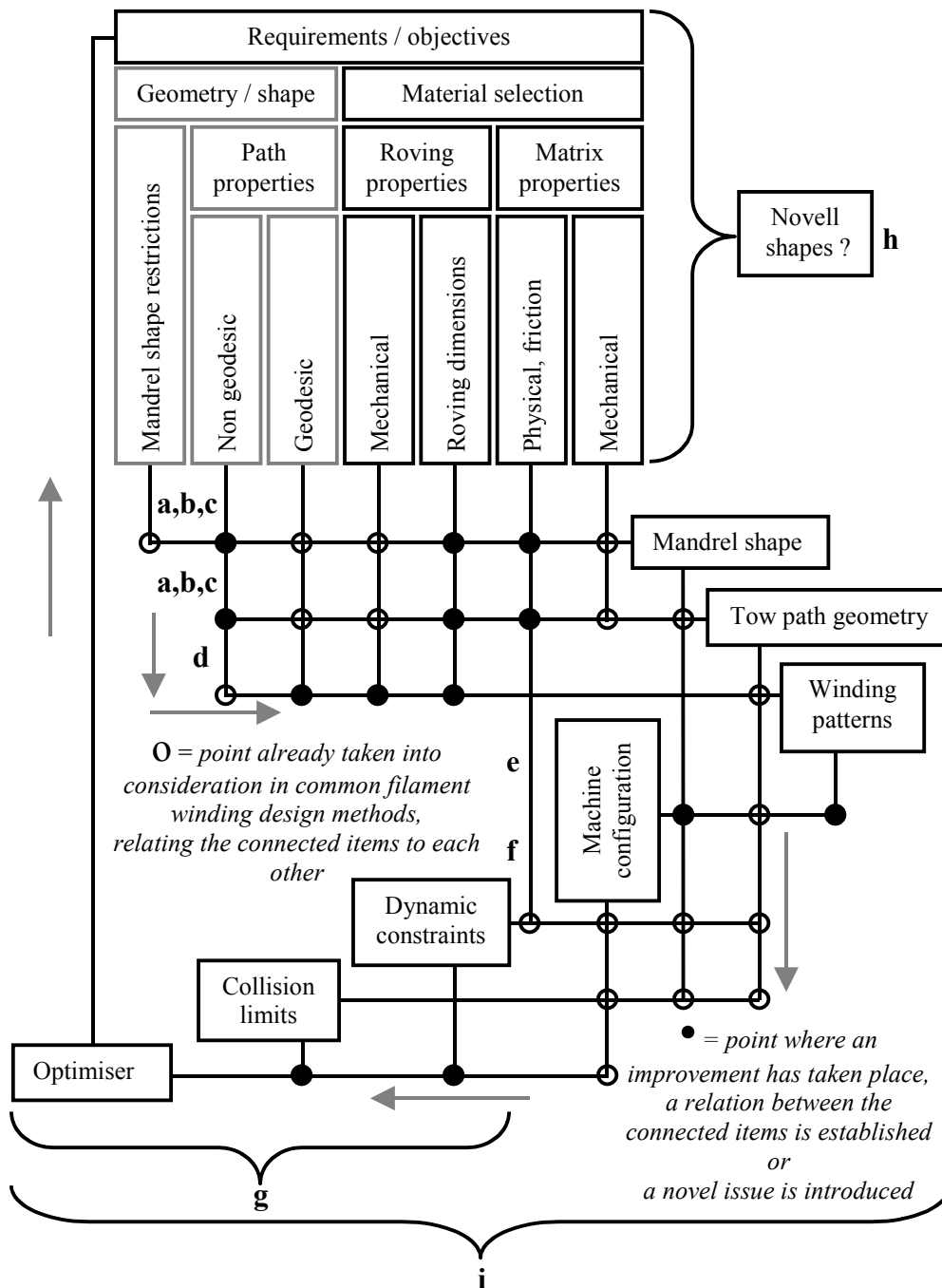


Fig. 1.1: The design and production process for filament wound items

### c Roving trajectories

The majority of the roving trajectory descriptions provided here (both geodesic and non-geodesic) are quasi analytical and do not suffer from significant cumulative error generation. It should be noted that an entirely analytical solution is only possible in few cases. However, with a proper friction distribution along the fibre, such solutions become achievable.

Nevertheless, for non-rotationally symmetric objects, the surface discretisation technique seems to generally be the only solution. Furthermore, we propose here a novel mandrel shape for a more convenient experimental determination of the friction coefficient applying to the interaction between the placed roving and the supporting surface.

### **d Automatic pattern generator**

Most pattern generators are based on the solution of the first order Diophantine equation and try to match the roving path properties with the obtained solution that exclusively contains integers  $[\beta_1, \beta_5]$ . Here the process of suitable pattern determination is reversed. With an initial set of design parameters, an optimal pattern is automatically generated (optimal with respect to the required number of rovings, the aimed number of completed layers, or the minimisation of undesired fibre bundle overlap).

### **e Generic kinematic model**

We tried in this thesis to overcome the problem of the limited availability of comprehensive kinematic models, by introducing a generic kinematic model described in the same rigorous spirit as in dynamics-related textbooks [12,13]. The obtained set of equations leads to a reduced determinant formulation that can easily be tackled by numerical means and is able in some cases (lathe winder) to provide analytical solutions. In addition, we propose here applications of several interpolation and discrete differentiation techniques for the determination of the associated velocities and accelerations, and evaluate them.

### **f Improved machine configurations**

Or, in other words, revisiting some old configurations  $[\alpha_{32}, \alpha_{43}]$  that, in the light of cost reduction, gain particular importance. With the re-introduction of the tumble winder, a significant production time reduction is in several cases achievable. In addition, we propose here some novel configurations from which it is believed that they unify several advantages of single configurations.

### **g Straightforward optimisation & collision control**

As an alternative to stochastic optimisation methods that are additionally used in optimal control problems  $[\lambda_{10}, \lambda_{11}, \lambda_{13}]$ , we propose and evaluate here the idea of applying dynamic programming (or optimal route planning algorithms) as described in [12], using a generic formulation that is based on both dynamic and collision avoidance-dictated constraints. In addition, a simplified technique is here provided for the determination of the allowable space for the machine movements and the reduction of the grid serving as input for the dynamic programming procedure.

## **Introduction**

### **h Novel shapes**

The in this thesis proposed shapes are from a mathematical point of view not novel at all, but they become for filament winding applications rather interesting. We propose here combinations of isotenoid meridians and derive some additional shapes that are the result of simple static equilibrium equations. In addition we introduce, and in some cases we evaluate, several application fields for these novel configurations.

### **i Integral design**

With a unifying basis (differential geometry) as departure point, an attempt has been made throughout the thesis to couple every intermediate result to the initial conditions (e.g. kinematic solution of a rotationally symmetric object on a lathe winder vs. curvature distribution). As a continuously revisited example, the entire design procedure of a pressure vessel has been evaluated and coupled to the initial equilibrium conditions. However, it should be noted that, in the best case, the idea of entirely integral design will only work for a certain well-defined class of objects. Hence, it is believed that a generic parametric integral design model is rather impossible. Nevertheless, the lessons from such an attempt are very fruitful.

### 1.3 Framework

Perhaps more in the spirit of a textbook (the author admires the structure of [μ8]), the thesis is divided into four parts:

- **A:** Fundamentals
- **B:** Reinforcing layer architecture
- **C:** Production process
- **D:** Design issues
- Conclusions

The presented series of subjects has been organised with the same sequence as found in the design procedure of filament wound products in practice (see also figure 1.1). However, we do not attempt in here to provide a practical design guide.

The framework presented here has a certain duality. When reading this thesis according to the traditional sequence (chapter 1, 2, until the conclusions chapter), a suitable title could be "Filament Winding: a Unified Approach". However, at the end of every part (A,B,C,D), we revisit the parametrically described class of isotenoidal pressure vessels, (as defined in chapter 4), figure 1.2. On this class of objects we apply the described theories, contained in each part.

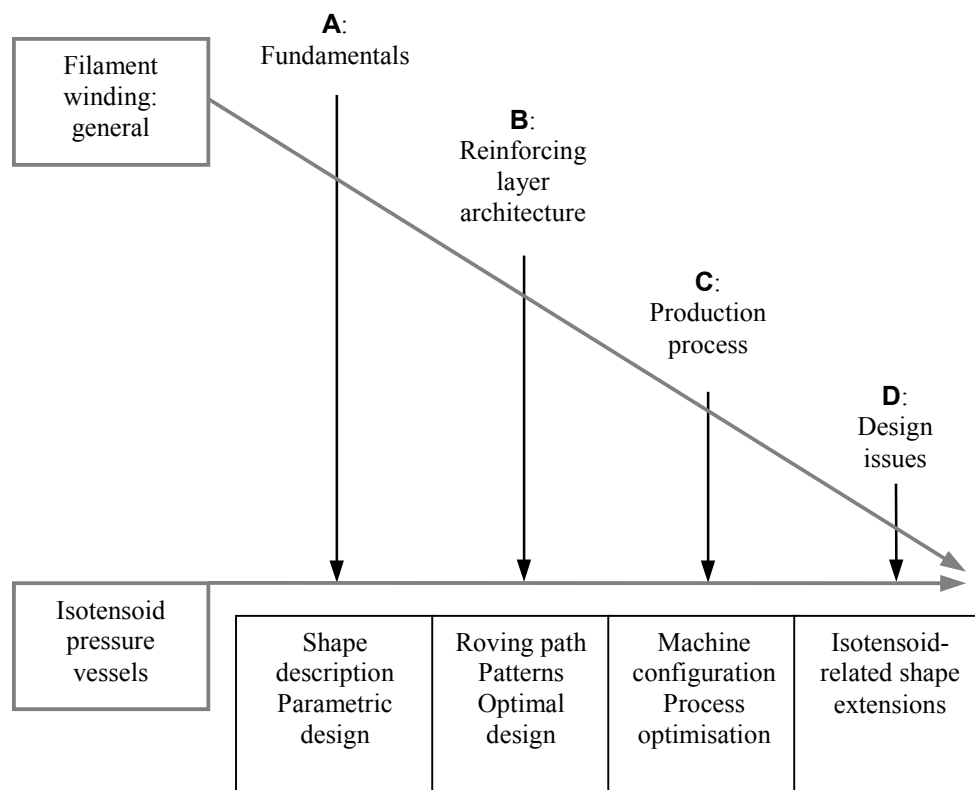


Fig. 1.2: The duality in the framework of this thesis

## **Introduction**

With the creation of a sequence containing only the revisiting chapters (4,9,15,17), the complete design procedure for an optimal pressure vessel is provided (figure 1.2): shape, roving trajectories, pattern creation versus involved roving characteristics and production process evaluation. An item probably not properly fitting in this series is the last revisiting chapter where we propose novel designs. Nevertheless its place in the thesis is dictated by the “classical” sequence. For the reader exclusively interested in pressure vessels we recommend chapters 4, 9, 15 and 17. For a generic filament winding approach without this specific application, one can skip the previously named chapters.

## **Part A: Fundamentals**

The scope of part A is to provide a mathematical basis for the subjects presented in this thesis.

In chapter **2**, the outline of several basic concepts and definitions from differential geometry is provided, in combination with the description of the so-called Frenet frame and the evaluation of some basic concepts applying on shells of revolution.

In the next chapter, **3**, the basic theory for the structural analysis of thin shells is given, where the influence of the curvatures on the resulting optimal roving orientation is highlighted.

In the last chapter of this part, **4**, we present the parameterisation frame for isotensoidal pressure vessels that are subjected to internal pressure and external axial forces, and are occasionally containing a cylindrical part. These vessels will serve as a platform for applying and evaluating the theories and results presented throughout the thesis.

### **Keywords per chapter**

**2: Fundamental forms, Curvatures, Frenet frame**

**3: Membrane theory, Stress analysis, Meridian profile**

**4: Isotensoid, Winding angle, Turn-around angle, Hoop circuits, Polar circuits**

## **Part B: Reinforcing layer architecture**

The main subject of part B is the construction of the reinforcing layer that will finally cover the mandrel. Beginning with an outline of geodesic trajectories in chapter **5**, we propose here an alternative integration scheme and provide an overview of several known solutions.

In chapter **6**, the theory of non-geodesic fibre trajectories is extensively analysed and followed by some path evaluations on shells of revolution. In addition, the idea is here proposed to transform the associated differential equation for the winding angle development into an analytically solvable one by a proper choice of the friction distribution function.

The measurement techniques for the determination of the coefficient of friction are outlined in chapter 7 where we introduce a novel mandrel shape that shows the ability to significantly facilitate the measuring procedure. In addition, in regard to the quantification of the available coefficient of friction, several results and rules of thumb are here presented.

The fully automatic creation of suitable winding patterns is presented in chapter 8, followed by optimisation in terms of optionally minimising the required number of rovings, achieving the desired number of layers, or minimising the roving overlap.

The results and methodologies created in these chapters are integrated in chapter 9 where we present the theory for creating transitional circuits (hoop→polar→hoop) on cylindrical pressure vessels, and a trade off between the number of particular rovings dictated by the strength calculations and pattern-related demands, respectively. The result of this trade-off is a methodology for creating optimal vessels where the strength-dictated and pattern-dictated numbers immediately match (at least, as close as possible). The control parameter set for this procedure consists of the mechanical and geometrical properties of the roving while exclusively following geodesic trajectories. Furthermore, we highlight the influence of fibre bed stacking at the polar areas of the vessels by means of firstly constructing a proper description of the resulting effective meridian profile and secondly by performing a simplified analysis of the mechanical performance reduction. This is the first revisiting procedure of the central example throughout the thesis: the generic pressure vessel.

### Keywords per chapter

- 5: (Non-) Geodesic, Euler-Lagrange equation, Error analysis
- 6: Christoffel symbols, Curvatures, Friction distribution
- 7: Coefficient of friction, Error analysis, Linearity
- 8: Turn-around angle, Diophantine, Laminate thickness
- 9: Transitional circuits, Optimal design, Strength reduction

### Part C: Production process

A comprehensive treatment of the kinematic equations is here outlined. Beginning in chapter 10 with the description of a generic geometric model and the derivation of the input parameters for the corresponding solutions, we present some typical results reflecting on shells of revolutions and we discuss their properties.

The transformation of the kinematic equations into a more convenient form, followed by their solution procedure, is presented in chapter 11. In addition, we derive here the complete set of analytical solutions for the lathe winder and provide several results for the winding process of shells of revolution on a generic machine configuration. With the description of every single machine movement as a function of the locus indicator belonging to the placed roving

## **Introduction**

and with the length quantification of the free-hanging fibre, the basis is here created for the production process optimisation procedure.

The dynamic aspects of filament winding are elaborated in chapter **12**, where we propose the application of several interpolation and numerical differentiation techniques for a proper representation of the resulting velocities and accelerations.

An additional constraint for the winding process can be found in the determination of the allowable moving space for the feed eye, chapter **13**. This space is bounded by the machine limits and is additionally dictated by avoidance of collision between the feed eye structure and the mandrel. In this chapter, we provide some easily accessible techniques for determining the moving space boundaries for the feed eye. The obtained results are formulated in terms of a collection of feasible ranges for the length of the free-hanging fibre.

With the description of the collision boundaries, the dynamic machine limits (both velocities and accelerations for every participating movement) and the analytical kinematic solution for the lathe winder, we formulate in chapter **14** the production optimisation problem. Within the dynamic and collision constraints, the objective is to minimise the production time. Before proceeding to the optimisation problem, a rigorous reduction of the input grid for the control variables is here achieved. The optimisation problem is evaluated by calculating for every incremental machine movement the minimum time needed to respect the dynamic constraints, within the available space for the movements of the feed eye. Next, the summation of these increments is minimised by a proper selection of the control variable value for every incremental step by means of dynamic programming techniques.

In a more general fashion, we revisit again in chapter **15** the generic pressure vessel and provide several results for shapes of gradually varying aspect ratios. From the performed evaluations, in regard to the selection of a proper machine configuration and its adjustments, several rules of thumb are given. Furthermore, we propose some additional machine configurations for enhancing a further production time reduction.

### **Keywords per chapter**

- 10: **Machine configuration, Input parameters, Curvature, Torsion**
- 11: **Kinematic equations, Spindle rotations, Feed eye translations, Roving speed**
- 12: **Lagrange, Splines, Fourier, Least squares, Finite differences, Multipoint approximation, Lanczos convergence factors**
- 13: **Feed eye, Machine limits, Collision bounds**
- 14: **Grid, Finite differences, Transition matrix, Transition costs, Dynamic programming**
- 15: **isotenoid, Spheroid, Aspect ratio, Feed eye amplitude**

### Part D: Design issues

Inspired by the simplicity and elegance of the equilibrium equations for shells of revolution, we describe in chapter **16** a novel configuration that includes isotensoids as basic shells, axially stacked on each other. In addition, particular issues are provided, containing a brief structural analyses and evaluations of several applications. Perhaps the most interesting facet of the configurations considered here, is their ability to displace significant axial loads (lifting applications) while remaining sufficiently stable.

With the same equilibrium equations as point of departure, chapter **17** contains a brief analysis of non-geodesically overwound pressure vessels, application of radial loads to geodesically wound isotensoids, and some novel configuration proposals as an alternative for cylindrical pressure vessels. In addition, we introduce here the class of hyperbolic shells of revolution. Furthermore, we propose another novel configuration combining isotensoids with toroids. The last issue presented in this chapter reflects on a concept for curvature-based surface discretisation providing  $C^2$  continuity, followed by a brief discussion of the application of thin membranes with optimal roving orientation as pressure-resisting elements in aircraft fuselages.

#### Keywords per chapter

- 16: **Articulated Pressurisable Structures (APS), Coefficient of friction, Roving twist, Stability**
- 17: **Non-geodesic trajectories, Radial forces, Toroid, Hyperboloid, Combivessel, Membrane element**

#### Conclusions

The conclusions chapter is divided into four sections. After providing a brief recapitulation of the topics contained in this dissertation, a contributions overview is provided in section 9.2. The subsequent section is discussing the main issues of this thesis: applying integral design and providing insight to the complete process of design and production of filament wound structures. Finally, some recommendations are formulated in section 9.4.

## **Introduction**

# A

## Fundamentals

*The scope of part A is to provide a mathematical basis for the subjects presented in this thesis: differential geometry, theory of thin anisotropic shells of revolution, and the theory of optimal filamentary vessels in a parameterised form.*

*In chapter 2, the outline of several basic concepts and definitions from differential geometry is provided, in combination with the description of the Frenet frame and the evaluation of some basic equations applying on shells of revolution.*

*In the next chapter, 3, the basic theory for the structural analysis of thin shells is given, where the influence of the curvatures on the resulting optimal roving orientation is highlighted.*

*In the last chapter of this part, 4, we present the parameterisation frame for isotenoidal pressure vessels that are subjected to internal pressure and external axial forces, and are occasionally containing a cylindrical part. These vessels will serve as a platform for applying and evaluating the theories and results provided throughout the thesis.*

### **Keywords per chapter**

- 2: Fundamental forms, Curvatures, Frenet frame**
- 3: Membrane theory, Stress analysis, Meridian profile**
- 4: Isotenoid, Winding angle, Turn-around angle, Hoop circuits, Polar circuits**

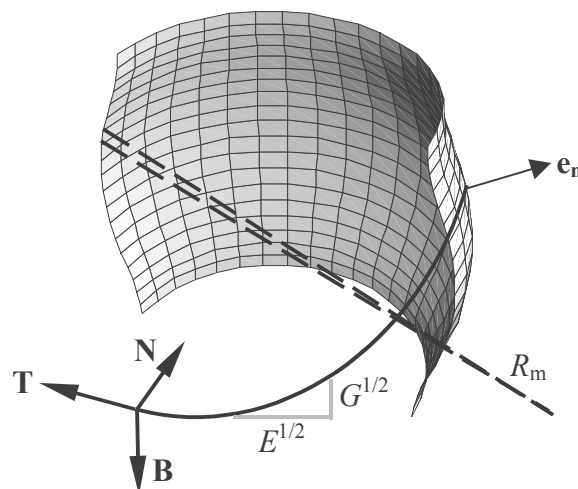
## **Part A: Fundamentals**

## 2

## Curves in space

*The differential geometry of curves and surfaces is a powerful tool for designing, analysing and implementing several filament winding-related parameters. Except for the description of fibre trajectories and their related vector quantities, the available tools can additionally be useful for the solution of the kinematic equations and the parametric design and optimisation of particular filament-wound structures. One of the main advantages provided by differential geometry is the coordinate-independent formulation of e.g. metrics and curvatures.*

*The subjects covered here can be found in several textbooks. However, since the theory presented here is extensively used throughout this thesis, we present here a summary of the most important topics, tailored for filament winding applications. After a short presentation of the fundamental forms (which provide some basic metrics) we proceed to the outline of several curvatures (seven in total). Due to their diversity, it is important for the reader to realise their idiosyncrasies and differences. To enhance this recognition, we present a summarising table at the end of section 2.2. Section 2.3 outlines the Frenet frame, which provide the key for determining some important path properties. In the last section, the differential geometry of curves on generic shells of revolution is summarised; due to rotational symmetry, the resulting expressions become relatively simple.*



**Impression of some metrics, curvatures, vectors and reference frames on a three-dimensional surface with a continuous curve, partially placed on it**

## **Part A: Fundamentals**

## 2.1 Fundamental forms

We consider here an arbitrary, continuous curve on a regular, three-dimensional surface. The surface under consideration is continuous, and the orientation of its normal vector is unambiguous for every point on that surface. Furthermore, we assume that the surface can be described as a vector function of two independent real parameters, say,  $\theta$  and  $\phi$ :

$$\mathbf{S}(\theta, \phi) = \{x(\theta, \phi), y(\theta, \phi), z(\theta, \phi)\} \quad \text{with } \theta, \phi \in \mathfrak{R} \quad (2.1)$$

The arc length of a curve placed on this surface is given by [μ6,μ9,μ15]:

$$L = \int \sqrt{(dx)^2 + (dy)^2 + (dz)^2} \quad (2.2)$$

For simplicity, we replace  $x, y, z$  with the general symbol  $\#$ . Every participating differential can then be expressed as follows:

$$d\#^2 = \left(\frac{\partial\#}{\partial\theta}\right)^2 (d\theta)^2 + 2\frac{\partial\#}{\partial\theta}\frac{\partial\#}{\partial\phi} d\theta d\phi + \left(\frac{\partial\#}{\partial\phi}\right)^2 (d\phi)^2 \quad (2.3)$$

Substitution of (2.3) into (2.2) followed by rearrangement results in:

$$L = \int \left( \sqrt{G + 2F \frac{d\phi}{d\theta} + E \left(\frac{d\phi}{d\theta}\right)^2} \right) d\theta = \int \left( \sqrt{G \left(\frac{d\theta}{d\phi}\right)^2 + 2F \frac{d\theta}{d\phi} + E} \right) d\phi \quad (2.4)$$

where:

$$\begin{aligned} G &= \left(\frac{\partial x}{\partial \theta}\right)^2 + \left(\frac{\partial y}{\partial \theta}\right)^2 + \left(\frac{\partial z}{\partial \theta}\right)^2 = \mathbf{S}_\theta \cdot \mathbf{S}_\theta \\ F &= \frac{\partial x}{\partial \theta} \frac{\partial x}{\partial \phi} + \frac{\partial y}{\partial \theta} \frac{\partial y}{\partial \phi} + \frac{\partial z}{\partial \theta} \frac{\partial z}{\partial \phi} = \mathbf{S}_\theta \cdot \mathbf{S}_\phi \\ E &= \left(\frac{\partial x}{\partial \phi}\right)^2 + \left(\frac{\partial y}{\partial \phi}\right)^2 + \left(\frac{\partial z}{\partial \phi}\right)^2 = \mathbf{S}_\phi \cdot \mathbf{S}_\phi \end{aligned} \quad (2.5)$$

The expressions indicated by  $G, F$  and  $E$  are referred to as “coefficients of the first fundamental form”. In addition, equation (2.2) is usually indicated as “Riemannian metric”. To illustrate their physical meaning, the expression  $G$  represents the metric along the meridian of a shell of revolution, whereas  $E$  is providing the metric along the parallel direction of that shell, as indicated in figure 2.1:

## Part A: Fundamentals

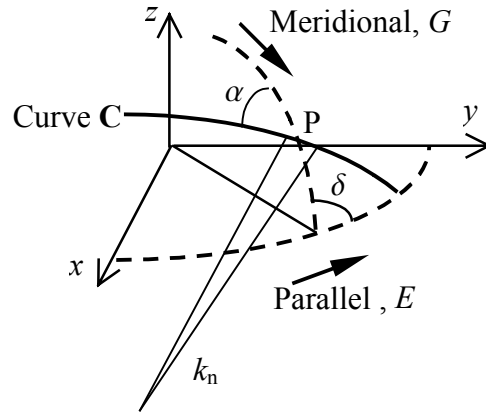


Fig. 2.1: Schematic representation of the two main directions for surfaces of revolution

An infinitesimally small part of a curve that is placed on the surface is now considered. The length in the meridional direction and parallel direction is respectively given by:

$$ds_{meridional} = \sqrt{G}d\theta, \quad ds_{parallel} = \sqrt{E}d\phi \quad (2.6)$$

The third coefficient,  $F$ , is the inner product of the derivatives of  $\mathbf{S}$  with respect to the main directions (equation (2.5)). The angle  $\delta$  between the main directions is then given by (fig. 2.1) [μ12]:

$$\cos \delta = \frac{F}{\sqrt{EG}} \quad (2.7)$$

### Example

For a shell of revolution, the main directions (meridional and parallel) are perpendicular to each other, hence:  $F = 0$ . This result can alternatively be obtained by the definition of such a shell:

$$\mathbf{S}(\theta, \phi) = \{a(\theta) \cos \phi, a(\theta) \sin \phi, b(\theta)\} \quad \text{with } \theta, \phi \in \mathfrak{R} \quad (2.8)$$

Substitution of (2.8) into (2.6) leads to  $F = 0$ :

$$E = a(\theta)^2, \quad F = 0, \quad G = a'(\theta)^2 + b'(\theta)^2 \quad (2.9)$$

However, an arbitrary regular three-dimensional surface is generally characterised by  $\{G, F, E\} \neq \{0, 0, 0\}$ .

As the name for  $\{G, F, E\}$  indicates, one can expect that there is also a group of expressions called “coefficients of the second fundamental form”. Although their geometrical interpretation is not directly visible, they play, together with their counterparts of the first fundamental form, an important role in the derivation of curvatures. These coefficients are defined as follows:

$$g = \frac{\det \begin{bmatrix} \mathbf{S}_{\theta\theta} \\ \mathbf{S}_\theta \\ \mathbf{S}_\phi \end{bmatrix}}{\sqrt{EG - F^2}} = \mathbf{n}(\theta, \phi) \cdot \mathbf{S}_{\theta\theta}$$

$$f = \frac{\det \begin{bmatrix} \mathbf{S}_{\theta\phi} \\ \mathbf{S}_\theta \\ \mathbf{S}_\phi \end{bmatrix}}{\sqrt{EG - F^2}} = \mathbf{n}(\theta, \phi) \cdot \mathbf{S}_{\theta\phi} \quad (2.10)$$

$$e = \frac{\det \begin{bmatrix} \mathbf{S}_{\phi\phi} \\ \mathbf{S}_\theta \\ \mathbf{S}_\phi \end{bmatrix}}{\sqrt{EG - F^2}} = \mathbf{n}(\theta, \phi) \cdot \mathbf{S}_{\phi\phi}$$

**Example**

For a shell of revolution defined according to equation (2.8), we obtain:

$$e = \frac{-|a(\theta)b'(\theta)|}{\sqrt{a'(\theta)^2 + b'(\theta)^2}}, \quad f = 0, \quad g = \frac{\text{sign}(\alpha(\theta))[a'(\theta)b''(\theta) - b'(\theta)a''(\theta)]}{\sqrt{a'(\theta)^2 + b'(\theta)^2}} \quad (2.11)$$

One can notice again that the second coefficient,  $f$ , is equal to zero.

## 2.2 Curvatures

In the example presented in figure 2.1, the curve **C** placed on the depicted surface has a certain orientation  $\alpha$  at point **P** with respect to the meridian. Depending on the angle  $\alpha$  at point **P**, the curvature  $k_n$  (normal to the surface **S**) of **C** will obtain a maximum and minimum value. These two extreme values are indicated as “principal curvatures”. In the case presented here, these curvatures are the meridian and the parallel one. It can be proven that the curvature of every continuous curve placed on a generic surface will obtain two extreme values, say,  $k_1$  and  $k_2$ . The symbol  $\alpha$  denotes the in-plane angle between the curve and the direction of  $k_1$  at a particular point, measured on that surface.

The principal curvatures and the coefficients of the first and second fundamental form are directly coupled to the so-called Gaussian ( $K$ ) and mean curvature ( $H$ ) [ $\mu 6, \mu 9, \mu 12, \mu 14$ ]:

$$K = k_1 k_2 = \frac{eg - f^2}{EG - F^2}, \quad H = \frac{1}{2}(k_1 + k_2) = \frac{eG - 2fF + gE}{2(EG - F^2)} \quad (2.12)$$

From equation (2.12) we can directly conclude that the principal curvatures are the roots of:

$$k^2 - 2Hk + K = 0 \quad (2.13)$$

where “=” stands for “set equal”. The roots are:

$$k_1 = H + \sqrt{H^2 - K}, \quad k_2 = H - \sqrt{H^2 - K} \quad (2.14)$$

With the description provided in the first paragraph of this section, the normal curvature of **C** at point **P** can be expressed as follows (figure 2.2):

$$k_n|_{at P} = (k_1 \cos^2 \alpha + k_2 \sin^2 \alpha)|_{at P} \quad (2.15)$$

where, in this example,  $k_1$  coincides with the meridian curvature ( $k_m$ ) and  $k_2$  with the parallel curvature  $k_p$ ; their corresponding radii are denoted by  $R_m$  and  $R_p$ , respectively (figure 2.2):

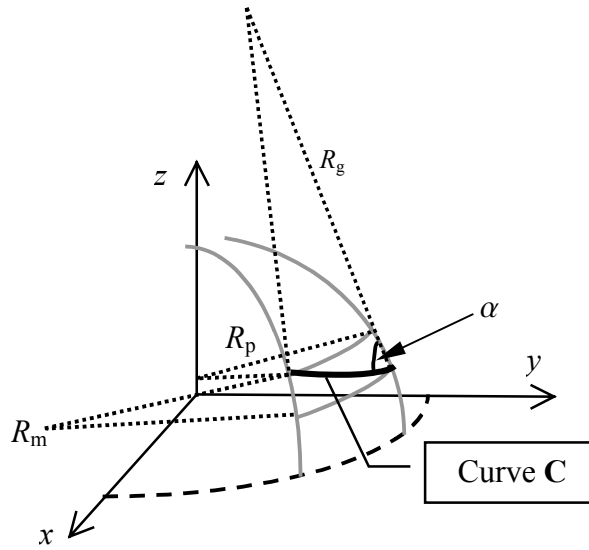


Fig. 2.2: The two principal radii of curvature (meridional  $R_m$  and parallel  $R_p$ ) for a shell of revolution. In addition, the in-plane radius of curvature ( $R_g$ , referred to as geodesic curvature) is here depicted

The curvature measured normal to the supporting surface,  $k_n$ , is of major importance for the design of thin composite shells bearing loads perpendicular to their surface. After determining  $\{E, F, G\}$  and  $\{e, f, g\}$  with equations (2.5) and (2.10) respectively, the values for  $K$  and  $H$  can be obtained with the aid of equations (2.12). Substitution of  $K$  and  $H$  into equation (2.14) leads to  $k_1$  and  $k_2$ . For a given value of  $\alpha$ , the normal curvature can be calculated with (2.15).

An additional parameter, presented in figure 2.2, is the so-called radius of geodesic curvature  $R_g$ ; this corresponds to the in-plane curvature of the path under consideration. An example enhancing the physical interpretation of the geodesic curvature can be found in the process of driving a car on the globe: when the front wheels are pointing straight ahead, the geodesic curvature  $k_g$  is equal to zero. When the steering wheel is not in the neutral position, the car will perform a turn according to an in-plane radius  $R_g$ . However, in both cases, the travelled path remains curved in the direction normal to the earth surface. The total curvature  $k_t$  (usually referred to as “curvature”) of the travelled path is given by:

$$k_t^2 = k_n^2 + k_g^2 \tag{2.16}$$

In this sub-section we just indicate the existence of the geodesic curvature. For the description of a method for calculating this parameter we refer to chapter 6. The curvatures are summarised in table 2.1.

## Part A: Fundamentals

Symbol	Name	Distinctive property
$k_1, k_2$	Principal	Maximum and minimum curvature a path can obtain at a particular locus on a surface
$H$	Gaussian	Directly coupled to $\{E, F, G\}$ and $\{e, f, g\}$
$K$	Mean	Directly coupled to $\{E, F, G\}$ and $\{e, f, g\}$
$k_n$	Normal	Curvature normal to the supporting surface
$k_g$	Geodesic	In-plane curvature, tangential to the supporting surface
$k_t$ or $k$	Total	Total curvature, quadratic summation of $k_n$ and $k_g$

Table 2.1: Summary of the presented curvatures

### 2.3 Frenet frames

The construction of a curve on a surface requires a coupling between the two independent parameters generating that surface. In our case we can either choose for a direct dependence or a parametric coupling of  $\theta$  and  $\phi$ . For example, the corresponding formulations can respectively be:

$$\begin{aligned} \mathbf{C}(\theta) &= \{x(\theta, \phi(\theta)), y(\theta, \phi(\theta)), z(\theta, \phi(\theta))\} = \{x(\theta), y(\theta), z(\theta)\} \\ \mathbf{C}(s) &= \{x(\theta(s), \phi(s)), y(\theta(s), \phi(s)), z(\theta(s), \phi(s))\} = \mathbf{C}(\theta(s), \phi(s)) \end{aligned} \quad (2.17)$$

The most common fibre path description related to filament winding is to represent its coordinates as a function of the arc length along that path. As outlined in part C, the choice to represent the path coordinates in such a way provides several advantages; by dividing the fibre path into constant length increments  $\Delta L$ , we obtain a favourable point distribution for both the kinematic and the dynamic calculations.

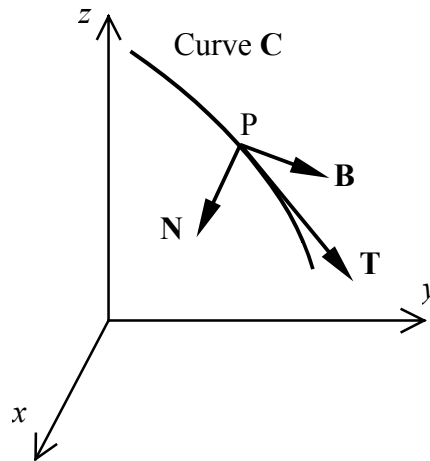


Fig. 2.3: The Frenet frame containing the tangential, normal and binormal vector

Let a curve be defined according to the first of equations (2.17) where  $\theta$  is a real parameter. Similarly to equation (2.2), the length differential is:

$$\frac{dL}{d\theta} = \sqrt{\left(\frac{dx}{d\theta}\right)^2 + \left(\frac{dy}{d\theta}\right)^2 + \left(\frac{dz}{d\theta}\right)^2} \quad (2.18)$$

According to Frenet, the unity tangent vector at a point P, is [ $\mu 12$ ]:

**Part A: Fundamentals**

$$\mathbf{T} = \frac{d\mathbf{C}}{dL} = \frac{\frac{d\mathbf{C}}{d\theta}}{\frac{dL}{d\theta}} = \frac{\mathbf{C}'}{L'} = \frac{\frac{d\mathbf{C}}{d\theta}}{\left\| \frac{d\mathbf{C}}{d\theta} \right\|} \quad (2.19)$$

where the length differential can be calculated according to equation (2.18). Since the tangent vector  $\mathbf{T}$  is a unity one, a shorter way of expressing equation (2.18) is:

$$\frac{dL}{d\theta} = \sqrt{\mathbf{C}' \cdot \mathbf{C}'} \quad (2.20)$$

The (unity) normal vector can be calculated as follows [12]:

$$\mathbf{N} = R \frac{d\mathbf{T}}{dL} = R \frac{\frac{d\mathbf{T}}{d\theta}}{\frac{dL}{d\theta}} = \frac{R}{L'} \left( \frac{\mathbf{C}''}{L'} - \frac{\mathbf{C}' L''}{(L')^2} \right) \quad (2.21)$$

where  $R$  expresses the (total) curvature, a scalar sufficiently tailored for normalising the obtained vector. Note that according to definition (2.21) the normal vector points to the centre of the body-related normal curvature. Differentiation of  $L'$  according to equation (2.20) leads, after substitution in (2.21) and some simplifications, to [12]:

$$\frac{1}{R} = k_t = \frac{\sqrt{(\mathbf{C}'' \cdot \mathbf{C}'')(L')^2 - (\mathbf{C}' \cdot \mathbf{C}'')^2}}{(L')^3} \quad (2.22)$$

The definition usually presented in textbooks related to differential calculus is:

$$\mathbf{N} = \frac{\frac{d\mathbf{T}}{dL}}{\left\| \frac{d\mathbf{T}}{dL} \right\|} \quad (2.23)$$

Since in the treatment of filament winding-related fibre paths the length increment  $\Delta L$  is usually constant, the following numerical expression can be used as an alternative:

$$\frac{1}{R} = \left\| \frac{\Delta\mathbf{T}}{\Delta L} \right\| = \frac{\|\Delta\mathbf{T}\|}{\Delta L} \quad (2.24)$$

For the calculation of the fibre torsion (twist), the binormal vector has first to be defined:

$$\mathbf{B} = \mathbf{T} \times \mathbf{N} \quad (2.25)$$

After substitution of equation (2.22) into (2.21) followed by application into (2.25), the result for  $\mathbf{B}$  becomes [12]:

$$\mathbf{B} = \frac{R}{(L')^3} \mathbf{C}' \times \mathbf{C}'' \quad (2.26)$$

The definition of fibre torsion is:

$$\frac{1}{\tau} = -\mathbf{N} \cdot \frac{d\mathbf{B}}{dL} = -\mathbf{N} \cdot \frac{\frac{d\mathbf{B}}{d\theta}}{\frac{dL}{d\theta}} \quad (2.27)$$

After substitution of (2.21) in (2.27) followed by differentiation, the result becomes [12]:

$$\frac{1}{\tau} = -R^2 \frac{\mathbf{C}'' \cdot (\mathbf{C}' \times \mathbf{C}''')}{(L')^6} \quad (2.28)$$

Since  $\mathbf{N}$  is a unity vector, under the restriction of implementing a non-zero length increment  $\Delta L$ , the torsion can numerically be approximated as follows:

$$\frac{1}{\tau} = \left\| \frac{\Delta \mathbf{B}}{\Delta L} \right\| = \frac{\|\Delta \mathbf{B}\|}{\Delta L} \quad (2.29)$$

The parameter torsion describes basically the twist of the fibre with respect to its own longitudinal direction and becomes only of importance when winding with a rigid broad tape.

It should be noted that the demand of applying a constant length increment  $\Delta L$  in equations (2.24) and (2.29) is introduced for reasons of rapid evaluation and avoidance of numerical instability. Obviously, the only requirement from a mathematical point of view is  $\Delta L \neq 0$ .

To achieve a proper balance between accuracy and calculation time it is generally preferable to quantify the tangent vector according to equation (2.19) followed by the determination of the curvature with (2.24). With this procedure, the (numerical) normal vector becomes:

$$\mathbf{N} = R \frac{\Delta \mathbf{T}}{\Delta L} \quad (2.30)$$

After application of equation (2.25), the torsion is given by (2.29).

## Part A: Fundamentals

The only important restriction on this strategy is the existence of a differentiable function, able to parametrically describe the curve of interest, as we assumed for equation (2.17).

In the last part of this section we provide here the complete set of the Frenet equations:

$$\begin{Bmatrix} \mathbf{T}'(\theta) \\ \mathbf{N}'(\theta) \\ \mathbf{B}'(\theta) \end{Bmatrix} = \left\| \frac{d\mathbf{C}}{d\theta} \right\| \begin{bmatrix} 0 & k(\theta) & 0 \\ -k(\theta) & 0 & \tau(\theta) \\ 0 & -\tau(\theta) & 0 \end{bmatrix} \begin{Bmatrix} \mathbf{T}(\theta) \\ \mathbf{N}(\theta) \\ \mathbf{B}(\theta) \end{Bmatrix}, \text{ where } \left\| \frac{d\mathbf{C}}{d\theta} \right\| = \frac{dL}{d\theta} \quad (2.31)$$

It is important to realise that the parameter  $k$  presented in the Frenet equations denotes the total curvature of the path under consideration, and not the normal one. The total and normal curvatures coincide only in the case of geodesic curves. The total curvature will prove to be a very important quantity, facilitating the numerical solution of the kinematic equations. Furthermore, as previously mentioned, the parameter torsion is playing an important role for the placement of relatively broad tapes.

## 2.4 Curves on shells of revolution

The class of shells of revolution corresponds to the most implemented collection of shapes when considering filament winding. This is the reason for providing special attention to this category. Due to the repetitive character of the associated fibre placement process, a considerable saving in calculation time can be achieved. Let a shell of revolution be defined as follows:

$$\mathbf{S}(\theta, \phi) = \{a(\theta) \cos \phi, a(\theta) \sin \phi, b(\theta)\} \quad \text{with } \theta, \phi \in \mathfrak{R} \quad (2.32)$$

As known from differential calculus textbooks, the unity derivative vectors in the meridian and parallel directions respectively, are (figure 2.4):

$$\begin{aligned} \mathbf{e}_m(\theta, \phi) &= \frac{1}{\sqrt{G(\theta)}} \frac{\partial}{\partial \theta} (\mathbf{S}(\theta, \phi)) \\ \mathbf{e}_p(\theta, \phi) &= \frac{1}{\sqrt{E(\theta)}} \frac{\partial}{\partial \phi} (\mathbf{S}(\theta, \phi)) \end{aligned} \quad (2.33)$$

where  $G(\theta)$  and  $E(\theta)$  are determined according to equation (2.5) and given in equation (2.9). Notice that in this case  $F(\theta)$  is equal to zero; this implies that the coordinate lines corresponding to  $\theta$  and  $\phi$  are perpendicular to each other. The associated principal curvatures are denoted by  $k_m$  (meridian) and  $k_p$  (parallel) and are also perpendicular to each other. Under the assumption of exclusively implementing right-handed coordinate systems, the unity normal vector becomes (fig. 2.4):

$$\mathbf{e}_n(\theta, \phi) = \mathbf{e}_m(\theta, \phi) \times \mathbf{e}_p(\theta, \phi) \quad (2.34)$$

Contrary to the Frenet frame, the normal vector of the resulting frame is pointing outwards. The obtained vectors form an orthogonal unity coordinate system having its origin at a locus P belonging to the fibre path (figure 2.4). Such a coordinate system is usually referred to as ‘‘Gaussian reference system’’. The angle between the curve at point P and the corresponding meridian at that point, is denoted by  $\alpha$  (see also figures 2.1 and 2.2). This angle is referred to as ‘‘winding angle’’ and is nearly the most important parameter for filament winding applications. The winding angle is measured in the plane formed by  $\mathbf{e}_m$  and  $\mathbf{e}_p$ .

**Part A: Fundamentals**

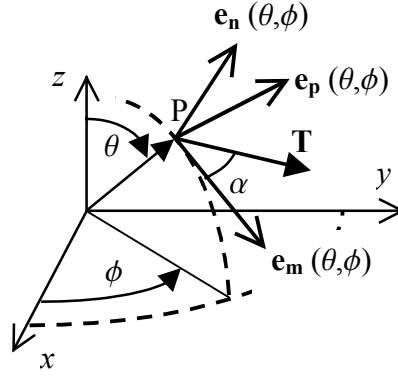


Fig. 2.4: Local Gaussian reference system at a particular fibre locus P

The vector  $\mathbf{T}$  tangent to the curve  $\mathbf{C}$  at locus P is given by:

$$\mathbf{T} = \{\cos\alpha, \sin\alpha, 0\} \cdot \begin{bmatrix} \mathbf{e}_m(\theta, \phi) \\ \mathbf{e}_p(\theta, \phi) \\ \mathbf{e}_n(\theta, \phi) \end{bmatrix} \quad (2.35)$$

With equations (2.33) and (2.34) we obtain:

$$\mathbf{T} = \left\{ \begin{array}{l} -\text{sign}(a) \sin\alpha \sin\phi + \frac{a'(\theta)}{\sqrt{G(\theta)}} \cos\alpha \cos\phi \\ \text{sign}(a) \sin\alpha \cos\phi + \frac{a'(\theta)}{\sqrt{G(\theta)}} \cos\alpha \sin\phi \\ \frac{b'(\theta)}{\sqrt{G(\theta)}} \cos\alpha \end{array} \right\} \quad (2.36)$$

The binormal vector  $\mathbf{B}$  is situated in the plane formed by  $\mathbf{e}_m$  and  $\mathbf{e}_p$ , and must satisfy equation (2.25) with  $\mathbf{N}$  replaced by  $\mathbf{e}_n$ . These considerations lead to [y6]:

$$\mathbf{B} = \{-\sin\alpha, \cos\alpha, 0\} \cdot \begin{bmatrix} \mathbf{e}_m(\theta, \phi) \\ \mathbf{e}_p(\theta, \phi) \\ \mathbf{e}_n(\theta, \phi) \end{bmatrix} \quad (2.37)$$

The complete expression for  $\mathbf{B}$  can be obtained by replacing in equation (2.36) the “cos” terms with “-sin” and the “sin” terms with “cos”. With the obtained expressions for  $\mathbf{T}$  and  $\mathbf{B}$  we can calculate the total curvature  $k$  and the torsion  $\tau$  according to equations (2.24) and (2.29), respectively.

For a properly defined curve on a shell of revolution, the angular parameters  $\alpha$  and  $\phi$  must be functions of  $\theta$  exclusively. However, since the curve is continuous, there is a particular relation between these angle-describing functions. In figure 2.5, we represent an elementary piece of such a curve:

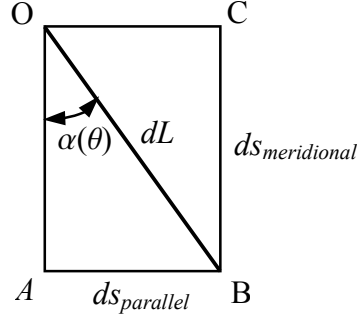


Fig. 2.5: An elementary piece of a curve on a shell of revolution

As usual, the symbol  $\alpha$  represents the angle between the meridian and the curve at the locus under consideration. From figure 2.5 and equation (2.6) we obtain [γ6]:

$$\frac{AB}{CB} = \frac{ds_{parallel}}{ds_{meridional}} = \sqrt{\frac{E}{G}} \frac{d\phi}{d\theta} = \tan(\alpha(\theta)) \quad (2.38)$$

Hence:

$$\frac{d\phi}{d\theta} = \sqrt{\frac{G(\theta)}{E(\theta)}} \tan(\alpha(\theta)) \quad (2.39)$$

In a similar way, the length differential  $dL$  can be expressed as follows:

$$\frac{dL}{d\theta} = \frac{\sqrt{G(\theta)}}{\cos(\alpha(\theta))}, \quad \frac{dL}{d\phi} = \frac{\sqrt{E(\theta)}}{\sin(\alpha(\theta))} \quad (2.40)$$

The relations presented in equations (2.39) and (2.40) are coordinate system-independent. From a mathematical point of view, for the formulation of a curve on a shell of revolution we can either define  $\alpha(\theta)$  or  $\phi(\theta)$ . In filament winding practice however, the parameter  $\alpha(\theta)$  is usually subjected to considerable restrictions; this implies that the function  $\phi(\theta)$  can not freely be chosen and will generally be represented as a functional of  $\alpha(\theta)$ . These considerations lead to following curve definition [γ6]:

$$\begin{aligned} \mathbf{C}(\theta) &= \{a(\theta) \cos(\phi(\theta)), a(\theta) \sin(\phi(\theta)), b(\theta)\} \\ \text{where } \phi(\theta) &= \int_{t=\theta_{initial}}^{\theta} \sqrt{\frac{G(t)}{E(t)}} \tan(\alpha(t)) dt \end{aligned} \quad (2.41)$$

## Part A: Fundamentals

With this definition, the tangent vector  $\mathbf{T}$  can alternatively be calculated as follows:

$$\mathbf{T} = \mathbf{T}(\theta) = \frac{\frac{d}{d\theta}[\mathbf{C}(\theta)]}{\left\| \frac{d}{d\theta}[\mathbf{C}(\theta)] \right\|} \quad (2.42)$$

With the definition presented in equation (2.41), the obtained expression becomes the same as given in equation (2.36).

For the calculation of the principal curvatures we substitute  $\{E, F, G\}$  (equation (2.9)) and  $\{e, f, g\}$  (equation (2.10)) into (2.12). With the obtained  $K$  and  $H$  values, the principal curvatures can be determined with equation (2.14). The meridional curvature is then given by:

$$k_m(\theta) = \frac{g}{G} = \frac{\text{sign}(a(\theta))(a''(\theta)b'(\theta) - a'(\theta)b''(\theta))}{(a'(\theta)^2 + b'(\theta)^2)^{3/2}} \quad (2.43)$$

The parallel curvature is:

$$k_p(\theta) = \frac{e}{E} = \frac{-b'(\theta)}{|a(\theta)|\sqrt{a'(\theta)^2 + b'(\theta)^2}} \quad (2.44)$$

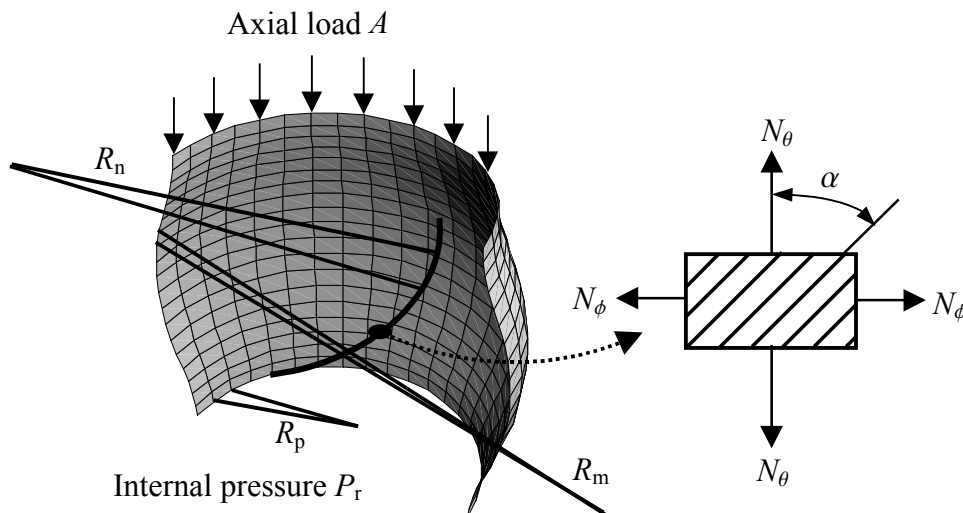
The normal curvature can be obtained by equation (2.15) with  $k_1 = k_m$  and  $k_2 = k_p$ .

## 3

## Thin anisotropic shells of revolution

Compared to thick shells, the structural analysis of thin-walled structures is considerably easier. The reason for this is that the shell under consideration can be modelled as a membrane. Since a membrane has no flexural rigidity, the complete set of the involved load and stress vectors will remain in plane. However, even this reduction is not sufficient for providing a simple theory for modelling their mechanical behaviour. As a result of this, the discussion presented here is strictly limited to shells of revolution.

The basic concepts (related to differential geometry) outlined in the previous chapter, are serving here as a basis for the derivation of the governing equations. In the next section, we emphasise on the influence of the curvatures on the resulting shell stresses distribution. In the last section we derive the differential equation describing the optimal shell meridian and we relate it to previously obtained expressions. The majority of the derivations presented here can be found in several publications and textbooks. The reason for presenting them here is to demonstrate how the mechanical performance of a thin-walled structure depends on the basic geometric parameters of the supporting shell.



**Impression of several typical quantities governing the mechanical performance of a thin shell: curvatures, external loads and fibre orientation versus principal shell stresses directions**

## Part A: Fundamentals

### 3.1 Governing equations

An elementary piece of a shell of revolution is bounded by two meridians and two parallel circles, infinitesimally close to each other, see figure 3.1. The implemented local reference system consists of three directions:  $\theta$  (meridian),  $\phi$  (parallel) and  $r$  (normal to the surface element). The external loads are denoted by  $P$  and the shell forces by  $N$ ; both are defined per unit of surface.

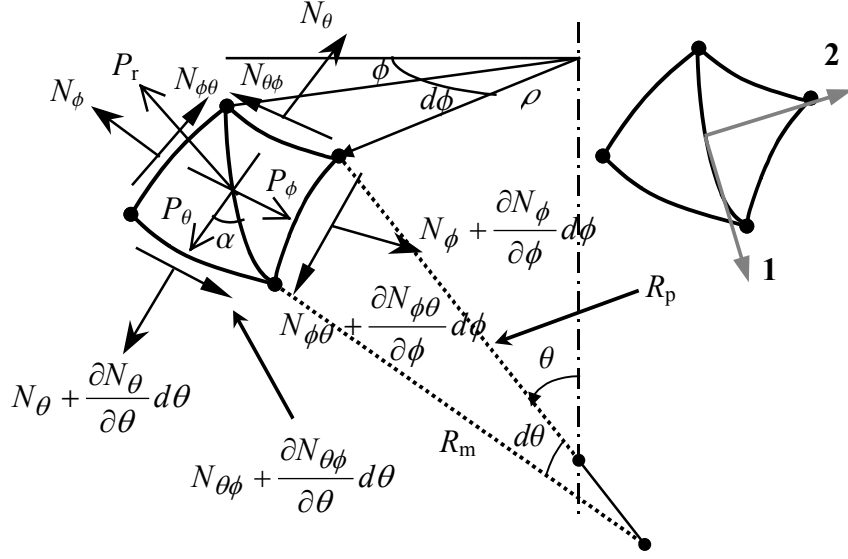


Fig. 3.1: External loads and shell forces on an elementary shell element

According to  $[\epsilon_1, \epsilon_2]$ , the equilibrium conditions are:

$$\begin{aligned} \sum F_\theta &= 0 \Rightarrow \frac{\partial}{\partial \theta}(\rho N_\theta) + R_m \frac{\partial}{\partial \phi}(N_{\phi\theta}) - R_m \cos \theta + P_\theta \rho R_m = 0 \\ \sum F_\phi &= 0 \Rightarrow \frac{\partial}{\partial \theta}(\rho N_{\theta\phi}) + R_m \frac{\partial}{\partial \phi}(N_\phi) + R_m N_{\phi\theta} \cos \theta + P_\phi \rho R_m = 0 \quad (3.1) \\ \sum F_r &= 0 \Rightarrow \frac{N_\theta}{R_m} + \frac{N_\phi}{R_p} = P_r \end{aligned}$$

For simplicity we assume here that  $P_\theta$  and  $P_\phi$  are equal to zero. In addition, since the applied loads are rotationally symmetric, the derivative of  $N_\phi$  with respect to  $\phi$  must vanish (situated in the second expression presented in equation (3.1)). This consideration leads to  $N_{\theta\phi} = 0$ . Furthermore, the shell element is covered with thin orthotropic layers whose materials axes  $\{1, 2\}$  are oriented according to an angle  $\alpha$  with respect to the meridian (see figure 3.1). The shell stresses  $N_\theta$  and  $N_\phi$  are related to the lamina stresses  $\sigma_1$ ,  $\sigma_2$  and  $\tau_{12}$  according to  $[\zeta_{14}, \zeta_{15}, \zeta_{34}, \zeta_{35}, \zeta_{36}]$ :

## Part A: Fundamentals

$$\begin{aligned} N_\theta &= \sigma_1 \cos^2 \alpha + \sigma_2 \sin^2 \alpha - \tau_{12} \sin 2\alpha \\ N_\phi &= \sigma_1 \sin^2 \alpha + \sigma_2 \cos^2 \alpha + \tau_{12} \sin 2\alpha \end{aligned} \quad (3.2)$$

For the calculations of the stresses  $\sigma_1$ ,  $\sigma_2$  and  $\tau_{12}$  of an individual layer we need an additional equation. This can be derived as follows: the strains of a single layer with respect to the material axes are given by [ζ34,κ4,κ5,κ9]:

$$\begin{aligned} \varepsilon_1 &= \varepsilon_\theta \cos^2 \alpha + \varepsilon_\phi \sin^2 \alpha \\ \varepsilon_2 &= \varepsilon_\theta \sin^2 \alpha + \varepsilon_\phi \cos^2 \alpha \\ \gamma_{12} &= (\varepsilon_\phi - \varepsilon_\theta) \sin 2\alpha \end{aligned} \quad (3.3)$$

Combination of these expressions leads to the third equation:

$$\varepsilon_1 - \varepsilon_2 + \gamma_{12} \cotan \alpha = 0 \quad (3.4)$$

To translate this expression into stresses we use the constitutive equations of a single orthotropic layer [κ1,κ4,κ5,κ9,κ10,κ11,α30]:

$$\begin{Bmatrix} \varepsilon_1 \\ \varepsilon_2 \\ \gamma_{12} \end{Bmatrix} = \begin{bmatrix} \frac{1}{E_1} & -\frac{\nu_{12}}{E_1} & 0 \\ -\frac{\nu_{21}}{E_2} & \frac{1}{E_2} & 0 \\ 0 & 0 & \frac{1}{G_{12}} \end{bmatrix} \cdot \begin{Bmatrix} \sigma_1 \\ \sigma_2 \\ \tau_{12} \end{Bmatrix} \quad (3.5)$$

where  $E_1/\nu_{12} = E_2/\nu_{21}$  (Maxwell's law). In combination with this expression, we finally obtain the third equation:

$$\begin{aligned} \frac{\sigma_1}{e_1} - \frac{\sigma_2}{e_2} + \frac{\tau_{12}}{G_{12}} \cotan 2\alpha &= 0 \\ \text{with } e_1 &= \frac{E_1}{1 + \nu_{12}}, \quad e_2 = \frac{E_2}{1 + \nu_{21}} \end{aligned} \quad (3.6)$$

Solving the system of equations (3.2) together with (3.6) leads to [ζ34]:

$$\begin{aligned}
 \sigma_1 &= \frac{1}{2c} \left[ (N_\theta + N_\phi) \left( 1 + \frac{2G_{12}}{e_2} \tan^2 2\alpha \right) + \frac{N_\theta - N_\phi}{\cos 2\alpha} \right] \\
 \sigma_2 &= \frac{1}{2c} \left[ (N_\theta + N_\phi) \left( 1 + \frac{2G_{12}}{e_1} \tan^2 2\alpha \right) - \frac{N_\theta - N_\phi}{\cos 2\alpha} \right] \\
 \tau_{12} &= \frac{G_{12} \tan 2\alpha}{c \cos 2\alpha} \left[ N_\phi \left( \frac{\sin^2 \alpha}{e_1} + \frac{\cos^2 \alpha}{e_2} \right) - N_\theta \left( \frac{\cos^2 \alpha}{e_1} + \frac{\sin^2 \alpha}{e_2} \right) \right]
 \end{aligned} \tag{3.7}$$

with:

$$c = 1 + G_{12} \left( \frac{1}{e_1} + \frac{1}{e_2} \right) \tan^2 2\alpha \tag{3.8}$$

Various researchers [ $\zeta$  group] have shown that the strength of the fibres is completely utilised when the participating laminate individual layers are aligned according to the direction of the maximum principal stress. This implies that the shear stress  $\tau_{12}$  must be equal to zero (equation (3.7)) or, in an equivalent fashion,  $\epsilon_\theta = \epsilon_\phi$  (equation (3.3)). From the last expression in equation (3.7), we obtain:

$$\tau_{12} = 0 \Rightarrow \frac{N_\phi}{N_\theta} = \frac{\sin^2 \alpha + k_e \cos^2 \alpha}{\cos^2 \alpha + k_e \sin^2 \alpha} \tag{3.9}$$

where:

$$k_e = \frac{e_2}{e_1} = \frac{E_2(1 + \nu_{12})}{E_1(1 + \nu_{21})} \tag{3.10}$$

Equations (3.9) and (3.10) provide useful information for the optimal layer orientation in a laminate covering the shell under consideration. The orientation depends completely on the ratio of the main stresses in the shell and the anisotropy of the basic laminae used for covering that shell. For an isotropic shell ( $k_e = 1$ ), it becomes directly evident that the optimal solution can only be achieved for  $N_\theta = N_\phi$ , whereby the value of  $\alpha$  does not play a role anymore. As outlined in the next section, the corresponding optimal meridian profile is then a circle. We should note here however, that the derived orientations are exclusively optimal for pressure vessels. The statement that the alignment of the fibres according to equation (3.9) is automatically leading to an optimal result in terms of laminate strength utilisation is generally not true [ $\kappa 10$ ].

## Part A: Fundamentals

To enhance simplicity for the corresponding calculations, we assume here that the mechanical matrix properties of the involved layers are negligible when compared to the fibres. This assumption immediately leads to  $k_e = 0$ . The equation for the optimal lamina orientation becomes:

$$\frac{N_\phi}{N_\theta} = \tan^2 \alpha \quad (3.11)$$

From a structural analysis-related point of view, the angle  $\alpha$  represents the lamina orientation with respect to the meridian of the shell, while, from a geometrical point of view, the parameter  $\alpha$  describes the orientation of the curve representing a fibre bundle belonging to that lamina.

### 3.2 Influence of the curvatures on the load distribution

We consider here an infinitesimally small piece of a fibre bundle placed on the surface of a convex shell of revolution (fig. 3.2). The normal fibre force per length unit acting on the shell surface, is given by [ζ14,ζ15]:

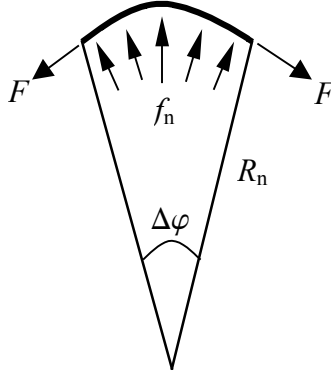


Fig. 3.2: Elementary fibre force equilibrium

$$f_n R_n \Delta\varphi = 2F \sin\left(\frac{\Delta\varphi}{2}\right) \approx F\Delta\varphi \Rightarrow f_n = \frac{F}{R_n} \quad (3.12)$$

where  $R_n$  is the radius of normal curvature (section 2.2). The shell under consideration is covered with  $N_f$  fibre bundles and is subjected to an internal pressure  $P_r$ . Every axial section (ring element, figure 3.3) of the shell must be in static equilibrium. Along the meridional direction of the ring element, we obtain:

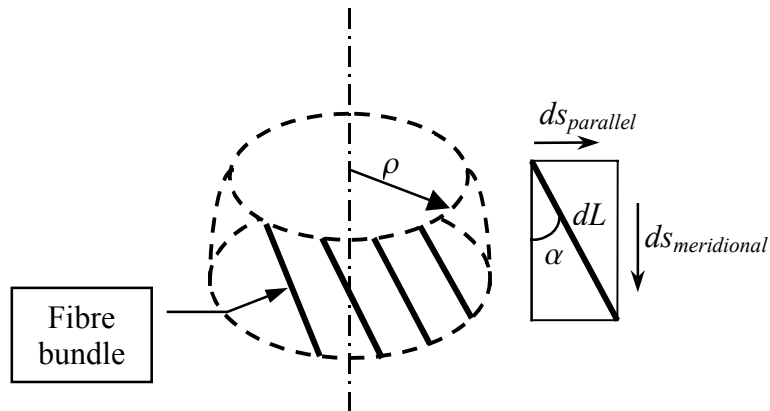


Fig. 3.3: Basic ring element belonging to a shell of revolution

$$N_f f_n dL = 2\pi\rho ds_{meridional} P_r \quad (3.13)$$

With  $ds/dL = \cos\alpha$  and equation (3.12), the equilibrium condition becomes:

**Part A: Fundamentals**

$$F = P_r \frac{2\pi\rho}{N_f} R_n \cos\alpha \quad (3.14)$$

This expression provides a direct relation between the fibre force, internal pressure, shell geometry and number of fibre bundles around the shell.

In addition to equation (3.14), the meridional and parallel curvature distributions play an important role for the determination of the shell stresses. For the mathematical description of these influences we recall equations (3.1) and (3.11); the third expression in equation (3.1) formulates the equilibrium of forces, normal to the shell surface. In addition, equation (3.11) relates the participating shell stresses  $N_\theta$  and  $N_\phi$  to each other (notice that we neglect the stiffness properties of the laminate matrix). For the calculation of the axial stress, we consider now the equilibrium of such a shell in the  $z$ -direction, see fig. 3.4:

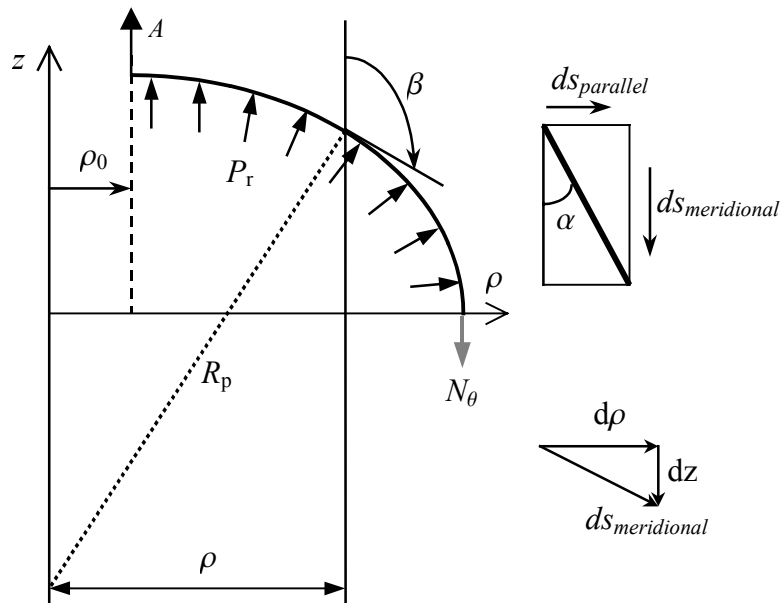


*Fig. 3.4: A shell of revolution loaded by an axial force  $A$  and an internal pressure  $P_r$*

An important geometric equation, directly extractable from fig. 3.4 is:

$$\cos\beta = -\frac{\rho}{R_p} = \frac{dz}{ds} \quad (3.15)$$

The equilibrium condition can be expressed as follows:

$$P_r \pi \rho^2 + A = 2\pi \rho N_\theta t \cos\beta = \frac{2\pi \rho^2 t N_\theta}{R_p} \quad (3.16)$$

Let us introduce the following dimensionless coefficients:

$$Y = \frac{\rho}{\rho_0}, \quad k_a = \frac{A}{\pi P \rho_0^2} \quad (3.17)$$

where  $\rho_0$  denotes the minimum shell radius (fig. 3.4). With the aid of these coefficients, we solve the system consisting of the third expression in (3.1) and equation (3.16) for  $N_\theta$  and  $N_\phi$ , and substitute them in equation (3.11). The result is [ζ21]:

$$\frac{N_\phi}{N_\theta} = \tan^2 \alpha = 2 \left( \frac{Y^2}{k_a + Y^2} \right) - \frac{R_p}{R_m} \quad (3.18)$$

As indicated in the previous section, for an isotropic shell, the stress ratio becomes equal to 1. For a shell without any external axial loads ( $k_a = 0$ ) the parallel and meridional radii of curvature become equal to each other, hence the resulting shape is a sphere.

For a cylindrical shell, one can easily derive that the optimal lamina orientation angle is equal to  $\arctan(\sqrt{2})$  [η2,η3,η13,η15,η17]. For an isotropic cylinder, the radial stress is equal to the double value of the axial stress, hence, the available isotropic material strength is only utilised for 50%.

### 3.3 Optimal shape determination

Assuming a polar coordinate system, the shell of revolution we are looking for is given by (fig. 3.5):

$$\mathbf{S}(\rho, \phi) = \{\rho \cos \phi, \rho \sin \phi, z(\rho)\} \quad (3.19)$$

The coefficients of the first fundamental form can be derived by equation (2.5):

$$E(\rho) = \rho^2, \quad G(\rho) = 1 + z'(\rho)^2 \quad (3.20)$$

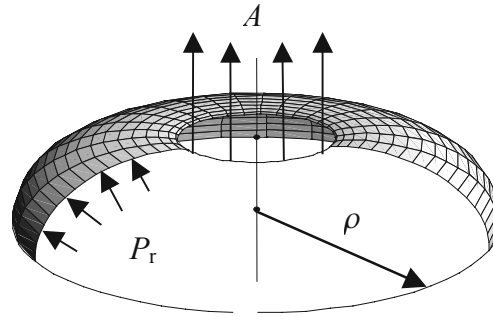


Fig. 3.5: Axial segment of a shell of revolution, loaded by internal pressure and an axial force

With the definitions of  $\alpha$  and  $\beta$  provided in fig. 3.4, the axial equilibrium of the shell is given by:

$$-FN_f \cos \alpha \cos \beta = P_r \pi \rho^2 + A \quad (3.21)$$

Similarly to equation (3.17), we introduce:

$$Z = \frac{z}{\rho_0}, \quad a = \frac{FN_f}{\pi P_r \rho_0^2} \quad (3.22)$$

According to equations (3.15), (2.6) and (3.20), the term  $\cos \beta$  can be related to the  $z(\rho)$  function as follows:

$$\cos \beta = \frac{z'(\rho)}{\sqrt{1 + z'(\rho)^2}} = \frac{Z'(Y)}{\sqrt{1 + Z'(Y)^2}} \quad (3.23)$$

Substituting equations (3.23) and (3.22) into (3.21) and solving for  $Z'(Y)$ , leads to [ $\zeta 19$ ,  $\zeta 20$ ,  $\zeta 27$ ]:

$$Z'(Y) = -\frac{k_a Y + Y^3}{\sqrt{a^2 Y^2 \cos^2 \alpha - (k_a Y + Y^3)^2}} \quad (3.24)$$

According to equations (2.43) and (2.44), the meridional and parallel radii of curvature are:

$$R_m(\rho) = \frac{1}{k_m(\rho)} = -\frac{(1 + z'(\rho)^2)^{3/2}}{z''(\rho)} = -\rho_0 \frac{(1 + Z'(Y)^2)^{3/2}}{Z''(Y)} \quad (3.25)$$

$$R_p(\rho) = \frac{1}{k_p(\rho)} = -\frac{\rho \sqrt{1 + z'(\rho)^2}}{z'(\rho)} = -\rho_0 \frac{\sqrt{1 + Z'(Y)^2}}{Z'(Y)}$$

With these expressions, the stress ratio becomes:

$$\frac{N_\phi}{N_\theta} = \tan^2 \alpha = 2 \left( \frac{Y^2}{k_a + Y^2} \right) - \frac{YZ''(Y)}{Z'(Y) + Z'(Y)^3} \quad (3.26)$$

On a way similar to equations (3.17) and (3.22), for the calculation of the fibre force we introduce:

$$R_v = \frac{R_n}{\rho_0} \quad (3.27)$$

where  $R_n$  (radius of normal curvature) can be calculated by substituting equation (3.25) into (2.15). The obtained function for  $R_v$  is represented by [ $\zeta 21$ ]:

$$R_v = \frac{Y(1 + Z'(Y)^2)^{3/2}}{\sin^2 \alpha [Z'(Y) + Z'(Y)^3] + \cos^2 \alpha [YZ''(Y)]} \quad (3.28)$$

Substitution of (3.28) and (3.22) into (3.14) leads to [ $\zeta 21$ ]:

$$a = 2Y^2 R_v \cos \alpha \quad (3.29)$$

To verify the obtained results, one can plug equation (3.24) into (3.28) and evaluate (3.29); the result becomes  $a \equiv a$ . A similar procedure can be followed for the verification of (3.26).

## Part A: Fundamentals

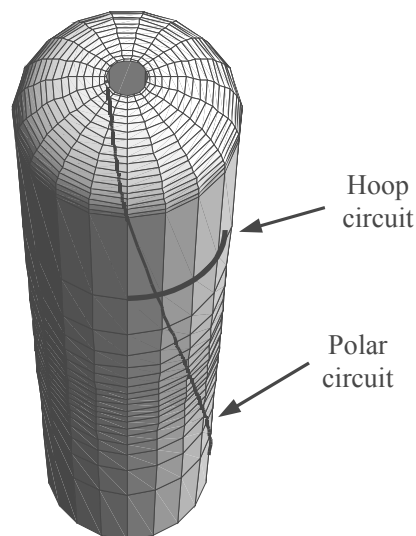
# 4

## Application: composite pressure vessels

*The governing equations derived in the previous chapter are here applied to the design procedure of an isotensoidal pressure vessel, optionally including a cylindrical part. The vessel under consideration is subjected to internal pressure and an external axial load that is applied on the polar opening of the vessel.*

*In the first section presented here we combine the differential equation for the meridian profile of the vessel with some fundamental parameters presented in chapter 2. This combination results in several expressions for the parameterisation of the fibre trajectories and the calculation of their length. Additional features include the quantification of the vessel surface and the volume contained in it. The second section describes a method for capturing the design procedure of a composite pressure vessel into three parameters:  $q$ ,  $r$  and  $s$ . With this parameterisation, we provide in the last section the complete set of required equations for determining the vessel and fibre trajectories geometry, and for calculating their performance in terms of the stored energy versus the weight of the resulting structure.*

*The theory for the design of composite pressure vessels has been improved and published by numerous authors. However, it is believed that this chapter contains a user-friendly parameterisation that provides, in a unified manner, the complete set of the required equations.*



**The shape of a typical composite pressure vessel. To achieve strain compatibility between the end dome and the cylinder, the latter is additionally covered by hoop windings**

## Part A: Fundamentals

## 4.1 Shape properties

The equation describing the meridian profile of a composite pressure vessel (equation (3.24)) depends mainly on two parameters: the dimensionless fibre force  $a$  (equation (3.22)) and the dimensionless axial load  $k_a$  (equation (3.17)). With an exception for the dimensionless coordinate  $Y$ , the resulting shape is also depending on the parameter  $\alpha$ , which describes the winding angle. As outlined in chapter 6, this angle is a function of the position on the surface supporting the fibre bundle and the available friction between them. In the case we consider here, the position is given by the  $Y$  parameter. With the assumption that the available friction is also a function of  $Y$ , the entire vessel shape can then be described. The denominator of equation (3.24) however, should provide positive real values. As a result of this, the (positive) winding angle should satisfy:

$$\cos \alpha \geq \frac{k_a + Y^2}{a} \quad (4.1)$$

To ensure the transition of one wound circuit to the other, at the locus corresponding with the smallest radius, the winding angle should be equal to  $\pi/2$  [rad] (figures 4.1 and 5.1). According to equation (4.1), the creation of an optimal pressure vessel for the complete definition range of  $Y$  is only possible when the axial load  $k_a$  on the polar opening (smallest radius) gains a certain value; the derivation of this value is given in the next section. In every other case, the construction of an entirely optimal vessel is theoretically impossible.

For simplicity we assume now that the implemented wound circuits are geodesic. According to Clairaut [a43,γ10,ζ14,ζ15], the winding angle becomes:

$$\alpha(Y) = \arcsin\left(\frac{1}{Y}\right) \quad (4.2)$$

With this information, equation (3.24) reduces to:

$$Z'(Y) = -\frac{k_a Y + Y^3}{\sqrt{a^2(Y^2 - 1) - (k_a Y + Y^3)^2}} \quad (4.3)$$

The denominator has two pairs of real, and one pair of imaginary roots. Without proceeding into details, we denote the minimum and maximum real root by  $Y_{\min}$  and  $Y_{\max}$ , respectively.

According to equation (2.9), the coefficients of the first fundamental form are given by:

**Part A: Fundamentals**

$$E = Y^2 \quad F = 0 \quad G = 1 + Z'(Y)^2 = \frac{a^2(Y^2 - 1)}{a^2(Y^2 - 1) - (k_a Y + Y^3)^2} \quad (4.4)$$

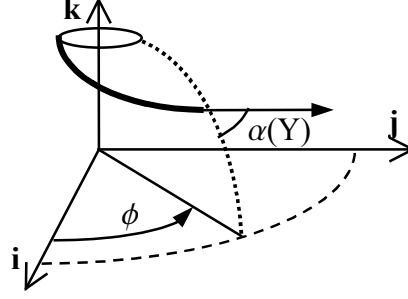


*Fig. 4.1: Winding angle  $\alpha$  and angular position  $\phi$  of a fibre locus*

Since the winding angle is a function of  $Y$ , the parallel fibre curve position  $\phi$  will also exclusively depend on  $Y$ . According to equation (2.41), we obtain:

$$\frac{d\phi}{dY} = \sqrt{\frac{G}{E}} \tan \alpha = \frac{a}{Y} \frac{1}{\sqrt{a^2(Y^2 - 1) - (k_a Y + Y^3)^2}} \quad (4.5)$$

With the aid of equation (2.40), the dimensionless length (length /  $\rho_0$ ) of the fibre placed on the mandrel is given by:

$$\frac{dL}{dY} = \frac{\sqrt{G}}{\cos \alpha} = \frac{aY}{\sqrt{a^2(Y^2 - 1) - (k_a Y + Y^3)^2}} \quad (4.6)$$

The dimensionless mandrel surface (surface /  $\rho_0^2$ ) differential is provided by:

$$\frac{dS}{dY} = 2\pi\sqrt{EG} = 2\pi aY \frac{\sqrt{Y^2 - 1}}{\sqrt{a^2(Y^2 - 1) - (k_a Y + Y^3)^2}} \quad (4.7)$$

For the differential of the dimensionless mandrel volume (volume /  $\rho_0^3$ ) we obtain:

$$\frac{dV}{dY} = \pi Y^2 Z'(Y) = \pi Y^2 \frac{k_a Y + Y^3}{\sqrt{a^2(Y^2 - 1) - (k_a Y + Y^3)^2}} \quad (4.8)$$

When  $Y$  is given as a function of a parameter  $\theta$ , the required differentials can be derived by application of the chain rule.

## 4.2 qrs-parameterisation

The derivatives presented in the previous section can easily be integrated by standard numerical procedures. With the proper parameterisation of  $Y$  however, one may obtain several elegant solutions in terms of elliptic integrals [ζ14,ζ15]. In the previous section we indicated the existence of two real roots for the denominator of equation (4.3),  $Y_{\min}$  and  $Y_{\max}$ , where the vessel reaches its maximum radius. For this reason we will change notation for the maximum dimensionless radius into  $Y_{eq}$ . Accordingly, since the slope of the meridian at that point becomes vertical, the derivative presented in (4.3) becomes infinite. Referring to fig. 3.4, the angle  $\beta$  becomes equal to  $\pi$  radians. At the same time, this point is the beginning of the cylindrical section belonging to the vessel (fig. 4.2). This section is assumed to have a length equal to  $2H_{\max} \times \rho_0$ . The existence of such a cylindrical part however, is optional.

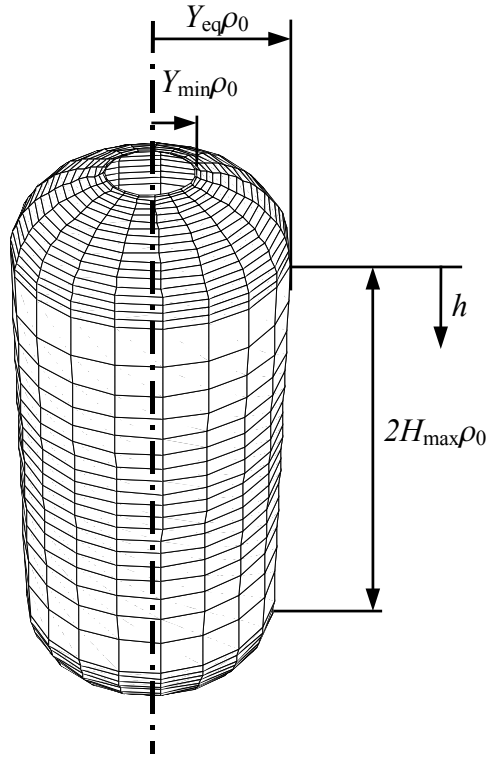


Fig. 4.2: Schematic representation of a cylindrical pressure vessel

These meridian slope-related considerations about the angle  $\beta$  at the equator together with the Clairaut relation (equation (4.2)), modify equation (3.21) as follows:

$$a \sqrt{1 - \frac{1}{Y_{eq}^2}} = Y_{eq}^2 + k_a = Y_{eq}^2 (1 + r) \quad (4.9)$$

where:

## Part A: Fundamentals

$$r = \frac{k_a}{Y_{eq}^2} = \frac{A}{\pi P_r (\rho_0 Y_{eq})^2} \quad (4.10)$$

In addition, we introduce:

$$q = \left( \frac{Y_{eq}}{Y_{\min}} \right)^2, \quad s = \frac{H_{\max}}{Y_{eq}} = \frac{h_{\max}}{Y_{eq}} \quad (4.11)$$

Furthermore, we express  $Y$  as a function of an independent parameter  $\theta$ , according to [ $\zeta 14$ ,  $\zeta 15$ ]:

$$Y = \sqrt{Y_{eq}^2 \cos^2 \theta + Y_{\min}^2 \sin^2 \theta} \quad 0 \leq \theta \leq \pi/2 \quad (4.12)$$

When setting the denominator of (4.3) equal to zero, (after substitution of equations (4.9), (4.10), (4.11) and (4.12)), the following solutions for  $Y_{eq}$  and  $Y_{\min}$  can be obtained:

$$Y_{eq}(q, r) = \frac{1}{\sqrt{q}} Y_{\min}(q, r) = \frac{1}{\sqrt{q}} \sqrt{\frac{1 + q + 2qr + q^2(1 + r^2)}{1 + q + 2qr}} \quad (4.13)$$

In addition, substitution of the derived value for  $Y_{eq}$  into equation (4.9) leads to:

$$a(q, r) = \frac{[1 + q + 2qr + q^2(1 + r^2)]^{3/2}}{q(1 + q + 2qr)} \quad \left( = \frac{FN_f}{\pi P_r \rho_0^2} \right) \quad (4.14)$$

As stated in the previous section, to achieve a perfect transition to the next wound circuit, the winding angle at the polar opening should be exactly equal to  $\pi/2$ ; this implies that  $Y_{\min}$  should be equal to 1 (equation (3.41)). This requirement leads to  $r = -1/q$ . This result can alternatively be obtained by setting equation (4.1) equal to zero. Furthermore, we indicate here that the dimensionless axial load  $r$  is limited according to the following statement [ $\zeta 27$ ], dictated by the numerator contained in the root argument of equations (4.13) and (4.14):

$$Y_{\min} \in \mathfrak{R} \Leftrightarrow r \geq -\frac{1+q}{2q} \quad (4.15)$$

With a sufficient increase of its absolute value, the maximum load can transform the pressure vessel into a torus (see part D of this dissertation). Another important aspect of vessel design is related to the determination of the required number of hoop circuits on the cylindrical part of the vessel for achieving strain compatibility between the end dome and the previously mentioned cylindrical part. According to [ζ14,ζ15] and [ζ19,ζ20], this ratio is given by:

$$\frac{N_{hoop}}{N_f} = \frac{2}{a} Y_{eq}^2 \left( 1 - \frac{1}{2} \tan^2 \alpha_{eq} \right), \quad \text{with } \alpha_{eq} = \arcsin \left( \frac{1}{Y_{eq}} \right) \quad (4.16)$$

Substitution of equation (4.2), (4.13) and (4.14) into (4.16) leads to:

$$\frac{N_{hoop}}{N_f} = \frac{-(1+q+2qr) + 2q^2(1+r^2)}{q(1+r^2)\sqrt{1+q+2qr+q^2(1+r^2)}} = R_{hp}(q,r) \quad (4.17)$$

As  $q$  tends to infinity and  $r$  to zero, the ratio expressed by equation (4.17) approaches the value 2. The result of (4.17) is depicted below:

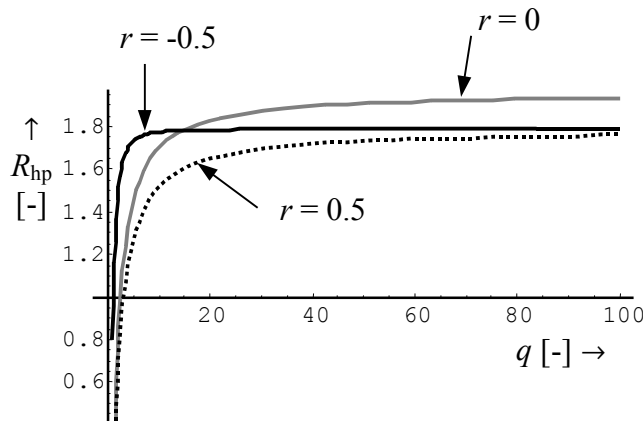


Fig. 4.3: The ratio  $N_{hoop} / N_{polar}$  as a function of the shape parameter  $q$

Summarising, the set of equations (4.10), (4.11), (4.12), (4.13), (4.14) and (4.17) provides the theory for completely designing a pressure vessel. The initial parameter set consists of  $q$  (quadratic ratio of the extreme values for the radii),  $r$  (dimensionless axial load),  $s$  (dimensionless cylindrical length) and  $F$  (strength of the applied filaments).

### 4.3 Design rules & performance

With the equations provided in the previous section, the differential equation describing the meridian becomes (equation (4.3)):

$$\frac{dZ}{d\theta} = \frac{dZ}{dY} \frac{dY}{d\theta} = Y_{\min} \frac{qr + q \cos^2 \theta + \sin^2 \theta}{\sqrt{1 + 2q(1+r) + (1-q) \sin^2 \theta}} \quad (4.18)$$

where:

$$\frac{dY}{d\theta} = \frac{(Y_{\min}^2 - Y_{eq}^2) \sin \theta \cos \theta}{Y} \quad (4.19)$$

Integration of (4.18) yields:

$$Z(q, r, \theta) = \frac{Y_{\min}}{\sqrt{1 + 2q(1+r)}} \left[ (1 + 2q(1+r)) \text{ellE} \left( \theta, \frac{q-1}{1 + 2q(1+r)} \right) - (1 + q + qr) \text{ellF} \left( \theta, \frac{q-1}{1 + 2q(1+r)} \right) \right] \quad (4.20)$$

where  $\text{ellF}(\#_1, \#_2)$  and  $\text{ellE}(\#_1, \#_2)$  denote incomplete elliptic integrals of the first and second kind, respectively [ $\mu_1, \mu_3, \mu_4, \mu_5$ ]. With a similar procedure, we express equation (4.5) as a function of  $\theta$ :

$$\frac{d\phi}{d\theta} = \frac{\sqrt{q} \sqrt{1 + q + 2qr}}{(q \cos^2 \theta + \sin^2 \theta) \sqrt{2 + q + 2qr(q-1) \cos^2 \theta}} \quad (4.21)$$

Integration yields:

$$\phi(q, r, \theta) = \sqrt{\frac{1 + q + 2qr}{q[1 + 2q(1+r)]}} \text{ell}\Pi \left( \frac{q-1}{q}; \theta \middle| \frac{q-1}{[1 + 2q(1+r)]} \right) \quad (4.22)$$

where  $\text{ell}\Pi(\#_1; \#_2 | \#_3)$  stands for an incomplete elliptic integral of the third kind. On a similar fashion, the dimensionless length of the applied fibre bundle (equation (4.6)) as a function of  $\theta$  can be described by:

$$\frac{dL}{d\theta} = Y_{\min}^2 \sqrt{\frac{q(1 + q + 2qr)}{2 + 2q(1+r) + (q-1) \cos^2 \theta}} \quad (4.23)$$

Hence:

$$L(q, r, \theta) = Y_{\min}^2 \sqrt{\frac{q(1 + q + 2qr)}{1 + 2q(1+r)}} \text{ellF} \left( \theta, \frac{q-1}{1 + 2q(1+r)} \right) \quad (4.24)$$

With equation (4.7), the dimensionless surface differential can be obtained:

$$\frac{dS}{d\theta} = 4\pi \frac{1+q+2qr+q^2(1+r^2)}{q(1+q+2qr)} \times \sqrt{\frac{(1+qr)^2 + (q-1)[1+q+2qr+q^2(1+r^2)]\cos^2\theta}{2+q+2q(1+r)\cos^2\theta}} = 4\pi S'(q,r,\theta) \quad (4.25)$$

Similarly, the volume differential (dimensionless) can be derived from equation (4.8):

$$\frac{dV}{d\theta} = 2\pi[1+(q-1)\cos^2\theta][1+qr+(q-1)\cos^2\theta] \times \sqrt{\frac{[1+q+2qr+q^2(1+r^2)]^3}{q^3(1+q+2qr)^3[2+2q(1+r)+(q-1)\cos^2\theta]}} = 2\pi V'(q,r,\theta) \quad (4.26)$$

The expressions given in (4.25) and (4.26) can not easily be integrated on an analytical way. Their numerical evaluation however, does not show any particular difficulty. The same property applies on equation (4.21) and (4.23).

The corresponding expressions ( $\phi$ ,  $L$ ,  $S$ ,  $V$ ) for the cylindrical part are considerably easier. We introduce here an independent parameter  $h$  running from the upper edge of the cylinder towards the lower edge, and define its dimensionless form as  $H = h / \rho_0$  (fig. 4.2). With equations (4.10) and (4.11) we obtain:

$$\phi_{cylinder} = \frac{H}{Y_{eq}} \frac{1}{\sqrt{Y_{eq}^2 - 1}} \quad (4.27)$$

$$L_{cylinder} = \frac{HY_{eq}}{\sqrt{Y_{eq}^2 - 1}}$$

For the design of a cylindrical pressure vessel, the resulting winding pattern will strongly depend on the total  $\phi$ -propagation generated by a complete wound circuit (referred to as turn around angle). This angular propagation of a single completed circuit can be calculated as follows:

$$\phi_{total}(q,r,s) = 4 \left( \phi(q,r,\pi/2) + \frac{s}{\sqrt{Y_{eq}^2(q,r) - 1}} \right) \quad (4.28)$$

## Part A: Fundamentals

Elaboration of equation (4.14) results in the determination of the number  $N_f$  of required wound circuits. In combination with equations (4.23) and (4.27) we obtain the required tow length for the polar circuits (notice that  $F$  is the strength of the applied fibre bundle). The number of required hoop circuits  $R_{hp}(q,r)$  is presented in equation (4.17). The total fibre length is then given by:

$$\begin{aligned}
 L_{total}(q,r,s,F) &= 4(L_{polar}^{enddome} + L_{polar}^{cylinder}) + L_{hoop}^{cylinder} = \\
 &= a(q,r)\pi\rho_0^3 \frac{P_r}{F} \left[ 4 \left( L(q,r,\pi/2) + \frac{sY_{eq}^2(q,r)}{\sqrt{Y_{eq}^2(q,r)-1}} \right) + 2R_{hp}(q,r)Y_{eq}(q,r) \right]
 \end{aligned} \tag{4.29}$$

The surface of the vessel is:

$$S_{total}(q,r,s) = 4\pi\rho_0^2 \left[ 2S'(q,r,\pi/2) + sY_{eq}^2 \right] \tag{4.30}$$

The enclosed volume is given by:

$$V_{total}(q,r,s) = 2\pi\rho_0^3 \left[ 2V(q,r,\pi/2) + sY_{eq}^3 \right] \tag{4.31}$$

The pressure vessel is created by placing the fibre bundles on a mandrel. The weight per length unit of the (impregnated) fibre bundles is  $d_f$  and is in most cases considerably higher than the mandrel density. Hence the weight contribution of the mandrel can be neglected. The performance of the resulting product is then given by [ $\zeta 14, \zeta 19, \zeta 20$ ]:

$$performance = \frac{P_r V_{total}}{weight} \approx \frac{2\pi P_r \rho_0^3 Const_1}{d_f \frac{a\pi\rho_0^3 P_r}{F} Const_2} \propto \frac{F}{d_f} \tag{4.32}$$

where  $\propto$  stands for ‘‘linearly proportional to’’. Obviously, the best performance is achieved by implementation of a light and strong fibre. This result however, is based on the assumption that the failure mode of the vessel is fibre breakage. For some applications, matrix failure might be the critical factor. Since we are dealing here with the netting theory, it is not possible to implement such failure modes in our model.

# B

## Reinforcing layer architecture

*The main subject of part B is the construction of the reinforcing layer that will finally cover the mandrel. Beginning with an outline of geodesic trajectories in chapter 5, we propose here an alternative integration scheme and provide an overview of several known solutions.*

*In chapter 6, the theory of non-geodesic fibre trajectories is extensively analysed and followed by some path evaluations on common shells of revolution. In addition, the idea is here proposed to transform the associated differential equation for the winding angle into an analytically solvable one by a proper choice of the friction distribution function.*

*The measurement techniques for the determination of the available coefficient of friction are outlined in chapter 7, where we introduce a novel mandrel shape that shows the ability to significantly facilitate the measuring procedure. In addition, in regard to the quantification of the available coefficient of friction, several results and rules of thumb are here presented.*

*The fully automatic creation of suitable winding patterns is presented in chapter 8 and followed by optimisation in terms of optionally minimising the required number of rovings, achieving the desired number of layers, or minimising undesired roving overlap.*

*The results and methodologies created in these chapters are integrated in chapter 9, where we present the theory for the description of transitional circuits (hoop→polar→hoop) on cylindrical pressure vessels, and a procedure that matches the number of the rovings (dictated by the strength calculations) to the pattern-related integer parameters. The result of this procedure is the creation of truly optimal vessels, both in the sense of mechanical performance and most economical mandrel coverage. Furthermore, we outline a methodology for the quantification of the mechanical performance reduction as a result of fibre bed stacking at the polar areas. This is achieved by firstly creating a proper description for the resulting effective meridian profile, and secondly by providing a simplified analysis tool for the estimation of the structural performance reduction. This is the first revisiting procedure of the central example throughout the thesis: the generic pressure vessel.*

### Keywords per chapter

- 5: (Non-) Geodesic, Euler-Lagrange equation, Error analysis
- 6: Christoffel symbols, Curvatures, Friction distribution
- 7: Coefficient of friction, Error analysis, Linearity
- 8: Turn-around angle, Diophantine, Laminate thickness
- 9: Transitional circuits, Optimal design, Strength reduction

## **Part B: Reinforcing layer architecture**

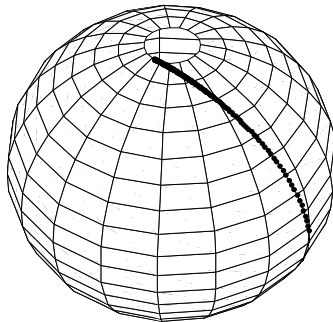
## 5

## Geodesic trajectories

*Perhaps the most elegant class of curves on surfaces is formed by geodesic trajectories that connect two arbitrary points on a continuous surface by means of the shortest possible way. This is comparable to driving a car on the earth surface without cornering at all. Due to this characteristic property, geodesic paths lead to the most stable and economical technique for covering filament wound structures*

*Beginning with the determination of geodesic paths by minimising their arc length, we proceed to the subsequent section that describes curves on shells of revolution. The reason for restricting ourselves to shells of revolution is that the determination of non-rotationally symmetric geodesics is rather complex and can only be attacked by sophisticated numerical techniques. Consequently, it is not possible to directly couple the obtained results to filament winding-related design issues. Nevertheless, in section 5.3 we propose and outline a method for determining geodesic paths on shells of revolution by numerical techniques with sufficient accuracy. The last section of this chapter provides some basic analytical solutions that can easily be implemented in simple routines.*

*A major part of the theory presented here can be found in several textbooks and papers. The main objective of this chapter is to give a comprehensive overview, introduce some numerical improvements and provide known analytical solutions in a unified way.*



**Geodesic trajectory on a sphere; from a filament winding-related point of view, a useless creation since every subsequent circuit will remain exactly on the same place**

## **Part B: Reinforcing layer architecture**

## 5.1 Curves of minimum length

As indicated in chapter 2, the expression providing the arc length of a continuous differentiable curve placed on an arbitrary surface is given by:

$$L = \int \left( \sqrt{G + 2F \frac{d\phi}{d\theta} + E \left( \frac{d\phi}{d\theta} \right)^2} \right) d\theta = \int \left( \sqrt{G \left( \frac{d\theta}{d\phi} \right)^2 + 2F \frac{d\theta}{d\phi} + E} \right) d\phi \quad (5.1)$$

where:

$$\begin{aligned} G &= \left( \frac{\partial x}{\partial \theta} \right)^2 + \left( \frac{\partial y}{\partial \theta} \right)^2 + \left( \frac{\partial z}{\partial \theta} \right)^2 = \mathbf{S}_\theta \cdot \mathbf{S}_\theta \\ F &= \frac{\partial x}{\partial \theta} \frac{\partial x}{\partial \phi} + \frac{\partial y}{\partial \theta} \frac{\partial y}{\partial \phi} + \frac{\partial z}{\partial \theta} \frac{\partial z}{\partial \phi} = \mathbf{S}_\theta \cdot \mathbf{S}_\phi \\ E &= \left( \frac{\partial x}{\partial \phi} \right)^2 + \left( \frac{\partial y}{\partial \phi} \right)^2 + \left( \frac{\partial z}{\partial \phi} \right)^2 = \mathbf{S}_\phi \cdot \mathbf{S}_\phi \end{aligned} \quad (5.2)$$

The main objective here is to determine a function relating the two independent parameters  $\theta$  and  $\phi$  (that describe the surface) to each other in such a way that the arc length integral becomes minimal. From equation (5.1) one can conclude that the arc-length will depend either on  $\{\theta, d\phi/d\theta\}$  or on  $\{\phi, d\theta/d\phi\}$ . We choose here for the parameter combination  $\{\theta, d\phi/d\theta\}$  and denote the curve origin and endpoint with  $\{\theta_b, \phi_b\}$  and  $\{\theta_e, \phi_e\}$ , respectively. The general length integral expression is:

$$L = \int f(\theta, \phi, \frac{d\phi}{d\theta}) d\theta \quad (5.3)$$

The beginning point and endpoint are fixed, so the length is exclusively depending on the function  $\phi(\theta)$ . Equation (5.3) has a stationary value if:

$$\begin{aligned} \delta L &= \delta \int_{\theta_b}^{\theta_e} f(\theta, \phi, \phi') d\theta = \int_{\theta_b}^{\theta_e} \left( \frac{\partial f}{\partial \phi} \delta \phi + \frac{\partial f}{\partial \phi'} \delta \phi' \right) d\theta \\ &= \int_{\theta_b}^{\theta_e} \left( \frac{\partial f}{\partial \phi} \delta \phi + \frac{\partial f}{\partial \phi'} \frac{d}{d\theta} (\delta \phi) \right) d\theta = 0 \end{aligned} \quad (5.4)$$

where:

$$\phi' = \frac{d\phi}{d\theta} \quad (5.5)$$

Integration by parts yields:

## Part B: Reinforcing layer architecture

$$\delta L = \int_{\theta_b}^{\theta_e} \frac{\partial f}{\partial \phi} \delta \phi d\theta + \left. \frac{\partial f}{\partial \phi'} \delta \phi \right|_{\theta_b}^{\theta_e} - \int_{\theta_b}^{\theta_e} \delta \phi \frac{d}{d\rho} \left( \frac{\partial f}{\partial \phi'} \right) d\theta = 0 \quad (5.6)$$

Since the endpoints are fixed, the second term in equation (5.6) is equal to zero. This observation results in:

$$\delta L = \int_{\theta_b}^{\theta_e} \left( \frac{\partial f}{\partial \phi} - \frac{d}{d\rho} \left( \frac{\partial f}{\partial \phi'} \right) \right) \delta \phi d\theta = 0 \quad (5.7)$$

The integral must vanish for every small  $\delta \phi$ ; hence:

$$\frac{\partial f}{\partial \phi} - \frac{d}{d\theta} \left( \frac{\partial f}{\partial \phi'} \right) = 0 \quad (5.8)$$

which is the Euler-Lagrange equation [μ6,μ8,μ15]. Replacement of the function  $f$  with the expression for the curve length (equation (5.1)) gives:

$$\frac{\frac{\partial G}{\partial \phi} + 2\phi' \frac{\partial F}{\partial \phi} + \phi'^2 \frac{\partial E}{\partial \phi}}{2\sqrt{G + 2F\phi' + E\phi'^2}} - \frac{d}{d\theta} \left( \frac{F + E\phi'}{\sqrt{G + 2F\phi' + E\phi'^2}} \right) = 0 \quad (5.9)$$

In the most general case, the involved coefficients  $E$ ,  $F$  and  $G$  are functions of both  $\theta$  and  $\phi$ . Consequently, the derived equation becomes rather difficult to solve. In [μ6] a numerical solution method is outlined, based on Christoffel symbols. However, presentation of this method lies beyond the scope of this section.

## 5.2 Geodesics on shells of revolution

For a shell of revolution, the coefficients  $E$  and  $G$  depend exclusively on  $\theta$ , while  $F$  is equal to zero (chapter 2). Consequently, the Euler-Lagrange equation becomes:

$$\frac{d}{d\theta} \left( \frac{F + E\phi'}{\sqrt{G + 2F\phi' + E\phi'^2}} \right) = 0 \Rightarrow \frac{F + E\phi'}{\sqrt{G + 2F\phi' + E\phi'^2}} = \text{constant} = c \quad (5.10)$$

The solution is:

$$\phi(\theta) = \int \sqrt{\frac{G}{E}} \frac{\frac{c}{\sqrt{E}}}{\sqrt{1 - \left(\frac{c}{\sqrt{E}}\right)^2}} d\theta \quad (5.11)$$

The geometrical meaning of equation (5.11) is depicted in figures 2.5 and 5.1 where we replaced the notation ‘meridional’ and ‘parallel’ with the corresponding coefficients of the first fundamental form, respectively  $\sqrt{G}$  and  $\sqrt{E}$ .

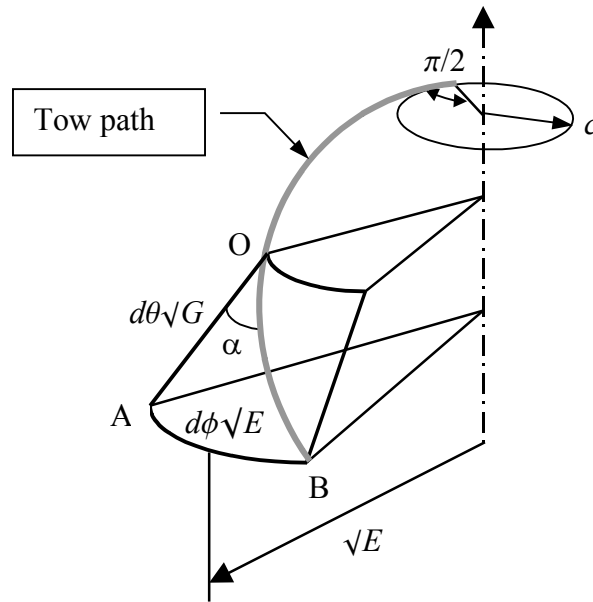


Fig. 5.1: Geodesic tow path on an elementary surface element belonging to a shell of revolution

Comparison of equation (5.11) with (2.39) leads to:

## Part B: Reinforcing layer architecture

$$\tan(\alpha(\theta)) = \frac{\frac{c}{\sqrt{E}}}{\sqrt{1 - \left(\frac{c}{\sqrt{E}}\right)^2}} \Rightarrow \alpha(\theta) = \arcsin\left(\frac{c}{\sqrt{E}}\right) \quad (5.12)$$

For filament winding applications, the winding angle should be equal to  $\pi/2$  at the locus corresponding to the smallest radius (the polar opening, see fig. 5.1) [γ6,ζ14]. This leads to the conclusion that the constant  $c$  must be equal to the radius of the polar opening. Notice that when the smallest radius is equal to zero, the created fibre path will coincide with the meridian. Consequently, the mandrel can not be covered on a geodesic manner since the winding angle will remain everywhere equal to zero.

One should recall that the solution for a curve on a shell of revolution is easily achievable because  $F = 0$  and  $E$  and  $G$  are functions of a single parameter (in our case  $\theta$ ). An arbitrary, regular and continuous three-dimensional surface however, is generally characterised by  $\{G, F, E\} \neq \{0, 0, 0\}$ . Especially the second term implies that the main curvature directions are not perpendicular to each other (section 2.1, especially figure 2.1). In this case, it is rather difficult to define a particular winding angle on a locus belonging to a curve on that surface. In practice, this angle is usually introduced in the same way as the Clairaut one, namely the angle between the path and its projection on a plane crossing that path at the treated locus, figure 5.2. The crossing plane is attached at the origin of the implemented coordinate system and is parallel to one of the axes. The choice of that plane depends mainly on the morphology of the treated object. As an example, for a box-shaped structure, the crossing plane intersects the fibre locus and coincides with the (Cartesian) axis parallel to the biggest dimension, as depicted in figure 5.2:

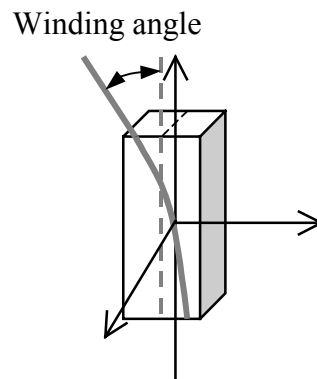


Fig. 5.2: The common definition for a winding angle on a box structure

### 5.3 Numerical evaluation

Integration of equation (5.11) leads to the determination of a geodesic fibre path on a shell of revolution. Despite the simple appearance of this expression however, the resulting integral is in most cases not suitable for analytical evaluation. As a result of this, the activation of numerical techniques seems inevitable.

The numerical evaluation of (5.11) is characterised by two difficulties: firstly, as the independent parameter approaches the minimum radius  $c$ , the integrand will tend to infinity. However, this is not really a problem for modern mathematical software, which is easily and widely available [μ3,μ14,μ15].

The second possible problem reflects on the distribution of the resulting coordinate pair values  $\{\theta, \phi\}$ . Depending on the parameterisation of the supporting meridian profile, this distribution might become rather inhomogeneous [γ6,γ10]; the resulting integration intervals are far from constant. As an example, the representation of a sphere in polar coordinates provides a dense point distribution near the equator, while the opposite case occurs at the polar areas. In general, the choice for a particular shape parameterisation will either lead to a dense distribution at the equator and relatively big intervals at the polar area, or the opposite case. To overcome this problem we propose here the combination of straightforward and recursive integration (for example, the method of Heun).

Let a shell of revolution be defined according to equation (2.8); the basic metrics are given by equation (2.9). Substitution of the latter into (5.11) leads to:

$$\phi(\theta) = \int_{t=\theta_b}^{t=\theta} \frac{c}{a(t)^2} \frac{\sqrt{(a'(t))^2 + (b'(t))^2}}{\sqrt{1 - \left(\frac{c}{a(t)}\right)^2}} dt = \int_{t=\theta_b}^{t=\theta} \psi(t) dt \quad \theta_b \leq \theta \leq \theta_e \quad (5.13)$$

where:

$$a(\theta_b) = c, \quad a(\theta_e) = \max[E] = \max.\text{radius} \quad (5.14)$$

The function  $\psi(t)$  tends to infinity when  $t$  approaches  $\theta_b$ . The numerical evaluation of equation (5.13) usually involves, despite the possible existence of convergence, significantly large numbers. Depending on the integration step size, different results may occur, although an accuracy of  $10^{-4}$  [rad] is easily achievable for “smooth” meridian profiles. We introduce now the following function:

$$\Gamma(t) = \frac{1}{\psi(t)} = \frac{1}{\left. \frac{d\phi}{d\theta} \right|_{\theta=t}} \Rightarrow d\theta = \Gamma(\theta) d\phi \quad \theta_b \leq t \leq \theta_e \quad (5.15)$$

## Part B: Reinforcing layer architecture

An example of a graph representing the function  $\Gamma(t)$  is given below:

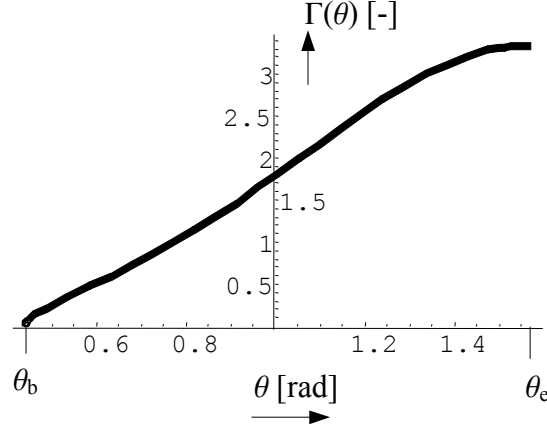


Fig. 5.3: A Typical graph of  $\Gamma(\theta)$ , associated with the differential description of geodesic tracks on a shell of revolution

The function  $\Gamma(\theta)$  results always in real and limited values for the entire definition interval  $[\theta_b, \theta_e]$ . Because a straightforward integration is not possible, we introduce now the following recursive procedure, for example based on the Heun method [μ7]:

$$\begin{aligned}
 \Delta\phi &= \frac{-\theta_e}{N} \quad \text{with } N \in \mathbb{N}^+ / 0 \\
 \phi(0) &= 0 \\
 \phi(k) &= \phi(0) + k\Delta\phi \quad \text{with } k = 1, 2, 3, \dots, N \\
 \theta(0) &= \theta_h(0) = \pi / 2 \\
 \theta_h(k) &= \theta(k-1) + \Gamma(\theta(k-1))\Delta\phi \\
 \theta(k) &= \theta(k-1) + \frac{\Delta\phi}{2} [\Gamma(\theta(k-1)) + \Gamma(\theta_h(k))]
 \end{aligned} \tag{5.16}$$

Notice that for  $\theta = \theta_b$ , the function  $\Gamma(\theta)$  becomes equal to zero. This is the reason for beginning with the scheme at  $\theta = \theta_e$ . The procedure is based on a predefined  $\Delta\phi$  step size and ends when  $\theta(k_{\text{end}})$  becomes smaller than  $\theta_b$ . The smaller the step size, the closer the last  $\theta$ -value will get to  $\theta_b$ . To enhance this approximation, it is recommendable to divide the last step  $[\phi(k_{\text{end}}-1), \phi(k_{\text{end}})]$  into smaller ones, until  $\theta(k_{\text{end}})$  will become close enough to  $\theta_b$ .

An alternative method for sufficiently approaching  $\theta_b$  can be constructed as follows (figure 5.4): for the last step of the integration procedure, the fibre bundle will get very close to the polar opening of the vessel. The metric distance between the mandrel surface points corresponding with  $\{\phi(k_{\text{end}}), \theta(k_{\text{end}})\}$  and  $\{\phi(\theta_b), \theta_b\}$  will become very small as compared to other

dimensions like the fibre bundle bandwidth. Hence, it becomes physically defendable that in this small region the fibre bundle will behave like a straight line, see figure 5.4:

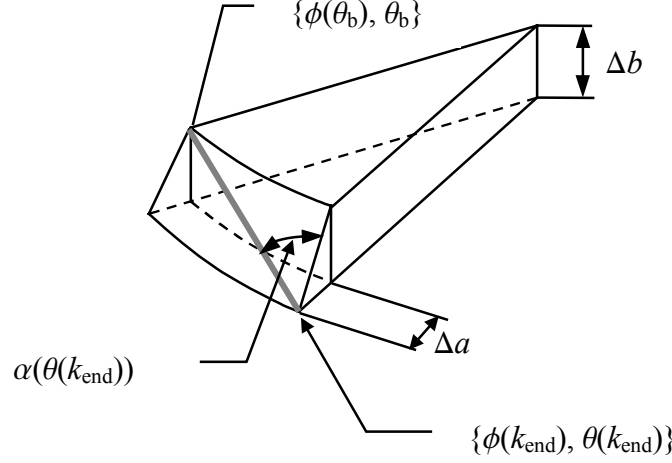


Fig. 5.4: Fibre bundle in the vicinity of the smallest radius, reflecting on the last integration step

From the figure we can immediately derive the following approximation [γ10]:

$$|\phi(\theta_b) - \phi[f(k_{end})]| \approx \frac{\tan[\alpha(\theta(k_{end}))] \sqrt{(\Delta a)^2 + (\Delta b)^2}}{a_m} \quad (5.17)$$

with

$$a_m = \frac{a(\theta_b) + a(\theta(k_{end}))}{2}$$

$$\Delta a = a(\theta(k_{end})) - a(\theta_b)$$

$$\Delta b = b(\theta(k_{end})) - b(\theta_b)$$

It can be shown that when  $\theta(k_{end})$  approaches  $\theta_b$ , equation (5.17) tends to zero. The local error associated with every integration step is of the order  $(\Delta\phi)^n$ , where  $n$  is equal to 2,3 or 5 for the methods of Euler, Heun and Runge-Kutta, respectively [μ7]. The corresponding cumulative error is generally of the order  $(\Delta\phi)^{n-1}$ . An equation providing a rough approximation for the cumulative error is [μ7]:

## Part B: Reinforcing layer architecture

$$\phi(\theta_b) - \phi(k_{end}) \approx \frac{\left(\frac{1}{2}\right)^n}{\left(1 - \left(\frac{1}{2}\right)^n\right)} (\phi(2k_{end}) - \phi(k_{end})) \quad (5.18)$$

with  $\Delta\phi(2k_{end}) = \frac{1}{2} \Delta\phi(k_{end})$

The integration scheme based on  $\Gamma(\theta)$  provides data points over constant  $\Delta\phi$ -intervals. A straightforward integration procedure (equation (3.15)) generates data points over constant  $\Delta\theta$ -intervals. A combination of the results produced by both methods is given below:

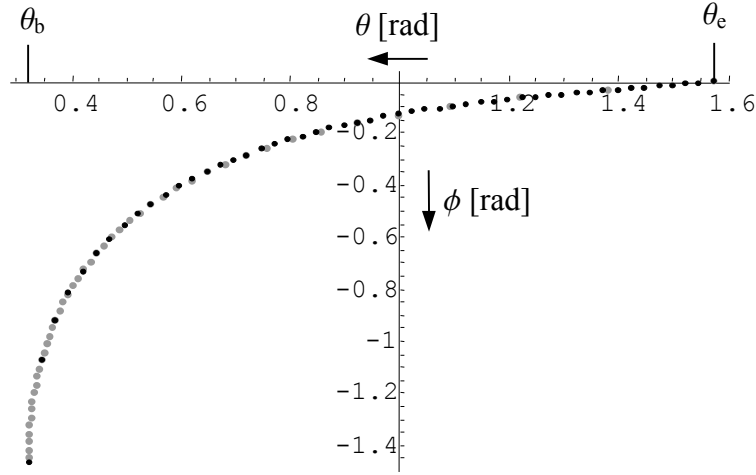


Fig. 5.5: Combination of the straightforward (black dots) and recursive (grey dots) integration method

With a proper selection of the data points provided here, a set of more or less equally distributed points can be constructed for the approximation of the geodesic path function  $\phi(\theta)$ . In the ideal case, the points belonging to the path under consideration should correspond to a constant length increment  $\Delta L$  [γ6]. This distribution leads to a representative set of data for the evaluation of the kinematic equations associated with filament winding. From equation (2.40) we obtain:

$$\Delta L = \frac{\sqrt{G(\theta)}}{\cos(\alpha(\theta))} \Delta\theta = \frac{\sqrt{E(\theta)}}{\sin(\alpha(\theta))} \Delta\phi \quad (5.19)$$

## Part B: Reinforcing layer architecture

The obtained equation leads automatically to the conclusion that the relations  $(\Delta L \leftrightarrow \Delta \theta)$  and  $(\Delta L \leftrightarrow \Delta \phi)$  behave entirely different (an exception on this statement is the sphere, described in spherical coordinates). Hence, a reliable representation approximating the criterion  $\Delta L \approx \text{constant}$  can only be constructed by interpolating over points obtained with both integration methods (for a sufficiently dense distribution of the nodes). An simple alternative method is to chose the  $\theta(k)$ -points according to:

$$\theta(k+1) = \theta(k) + \Delta\theta(k) \quad \text{with} \quad \Delta\theta(k) = \frac{\cos[\alpha(\theta(k))]}{\sqrt{G(\theta(k))}} \Delta L \quad (5.20)$$

For a higher order approximation we refer here to section 10.2.

## 5.4 Basic geodesics

Through this dissertation we represent a fibre path in such a way that the initial  $\phi$ -position is negative and becomes equal to zero when the fibre passes the maximum radius (equator) for the first time.

### Generic cone

The geometry of a conical shell of revolution in polar coordinates is given in figure 5.6:

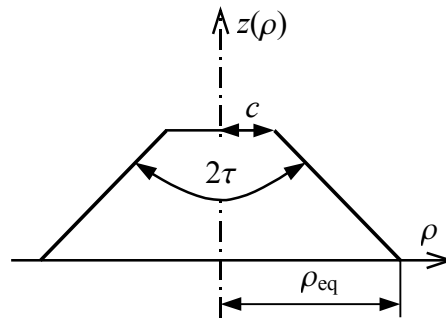


Fig. 5.6: Definition of conical shell of revolution

With a top angle  $2\tau$ , and a polar opening (minimum radius)  $c$ , the geodesic path is given by [γ7,δ2]:

$$\phi(\rho) = \frac{1}{\sin \tau} \left[ \arcsin\left(\frac{c}{\rho_{eq}}\right) - \arcsin\left(\frac{c}{\rho}\right) \right] \quad (5.21)$$

For  $\tau = 0$  we obtain a cylinder; in this case, a description in polar coordinates becomes impossible. To overcome this problem, we can use the first expression of equation ((4.27)) where the angle  $\phi$  is given as a function of the metric along the meridian of the cylinder. In addition, one may alternatively use a representation in spherical coordinates (section 6.4). Notice that for  $\tau = \pi/2$  we obtain an annulus. In this case, the total  $\phi$ -interval over  $[c, \rho_{eq}]$  is equal to  $\pi/2 - \alpha_{eq}$  [rad]. The  $\phi$  propagation (from the pole to the equator) is here denoted by  $T$ .

As an alternative to the integration procedure presented in the previous section, a solution can be created by the approximation of a given shell of revolution with a sequence of conical rings [α15]; this method is very common for filament winding applications.

### Spheroids

An example of a spheroid is depicted in figure 5.7. Let a spheroid be defined as follows [μ15]:

$$\mathbf{S}(\theta, \phi) = \{a \sin \theta \cos \phi, a \sin \theta \sin \phi, b \cos \theta\}, \quad 0 \leq \theta \leq \pi/2 \quad (5.22)$$

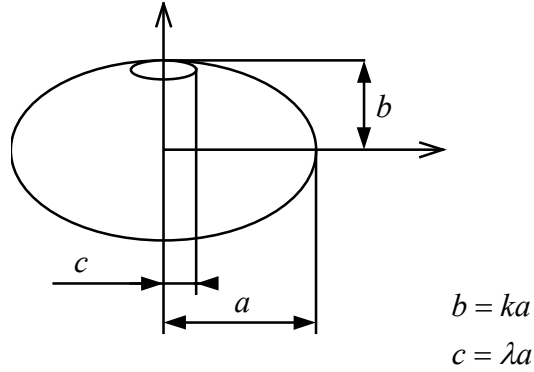


Fig. 5.7: Schematic representation of a spheroid

The differential equation describing a geodesic path on a general spheroid is [μ15]:

$$\frac{d\phi}{d\theta} = \frac{1}{\sin \theta} \sqrt{\frac{1 + (k^2 - 1) \sin^2 \theta}{\left(\frac{\sin \theta}{\lambda}\right)^2 - 1}} \quad (5.23)$$

For  $k = 1$  we obtain a sphere where:

$$\phi(\lambda, \theta) = -\arctan \left( \sqrt{\frac{\cos \theta}{\left(\frac{\sin \theta}{\lambda}\right)^2 - 1}} \right) + \frac{\pi}{2} \quad (5.24)$$

The  $\phi$ -propagation from the pole to the equator of a sphere is always equal to  $\pi/2$  [rad]. As a result of this, a geodesic path on a sphere reduces to a ring. A complete circuit will not result to any propagation in the parallel direction, therefore it is impossible to cover a sphere with geodesic trajectories.

Summarising, for  $k = 1$  we obtain a sphere ( $T = \pi/2$ ) and for  $k = 0$  an annulus ( $\pi/2 - \arcsin(\lambda)$ ). For the turn-around angle ( $\phi$ -propagation from the pole to the equator) of a spheroid, we may construct the following expression:

$$T(k, \lambda) = \frac{\pi}{2} + (k^{\delta(k, \lambda)} - 1) \arcsin \lambda, \quad \begin{matrix} 0.1 \leq k \leq 2 \\ 0.05 \leq \lambda \leq 0.85 \end{matrix} \quad (5.25)$$

## Part B: Reinforcing layer architecture

where, according to a least squares approximation:

$$\begin{aligned} \delta(k, \lambda) = & 1.63314 - 0.265057 k + 0.323549 k^2 - 0.1893 k^3 + 0.03922 k^4 + 1.5835 \lambda - 1.997 k \lambda + \\ & 1.27564 k^2 \lambda - 0.316283 k^3 \lambda + 0.0154989 k^4 \lambda - 7.82695 \lambda^2 + 9.54362 k \lambda^2 - 6.22511 k^2 \lambda^2 + \\ & 1.58703 k^3 \lambda^2 - 0.0962056 k^4 \lambda^2 + 13.4596 \lambda^3 - 16.4102 k \lambda^3 + 10.0761 k^2 \lambda^3 - 2.37023 k^3 \lambda^3 + \\ & 0.107485 k^4 \lambda^3 - 7.60142 \lambda^4 + 8.43539 k \lambda^4 - 4.54767 k^2 \lambda^4 + 0.784391 k^3 \lambda^4 + 0.0341265 k^4 \lambda^4 \end{aligned} \quad (5.26)$$

For the indicated  $k$  and  $\lambda$ -intervals, the accuracy of this approximation is 99.95%. During the procedure for determining the winding pattern of an ellipsoidal shell of revolution (chapter 8), the direct calculation of the turn-around angle can outstandingly be performed by the approximation outlined in equations (5.25) and (5.26). For the turn-around angle  $\Phi_{\text{total}}$  of an isotensoid pressure vessel we refer here to section 4.3.

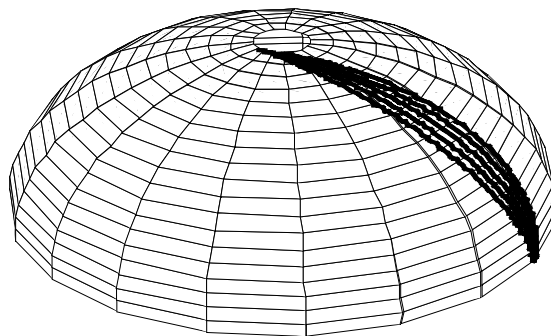
## 6

## Non-geodesic trajectories

*The application of non-geodesic filament winding significantly enlarges the design space for composite structures. The formulation and evaluation of these trajectories however, is a rather complicated issue. The key parameter in the derivations presented here is the geodesic curvature. Setting the latter equal to zero will result into a geodesic path. In this chapter we present the basic equations supporting such a path description and evaluate some solutions for curves on shells of revolution.*

*After the outline of some basic concepts in the first section, we derive the differential equation describing the winding angle distribution along the resulting path. With this information we discuss in section 6.3 the parameterisation and evaluation of a non-geodesic path. The last section provides some typical examples where the role of the coefficient of friction is highlighted.*

*The equations for the determination of non-geodesic trajectories are already known but the emphasis of the derivation presented here is mainly oriented towards the relation between the earlier presented basic geometric operators (metrics and curvatures) and the resulting fibre path orientation (winding angle distribution). In addition, we propose here the idea of formulating the friction distribution along the tow on such a way that the resulting path can analytically be described.*



**Several fibre trajectories on a shell of revolution, from geodesics to strongly non-geodesics. This discrepancy is exclusively the result of the friction, situated between the rovings and the supporting surface**

## **Part B: Reinforcing layer architecture**

## 6.1 Basic geometry

We consider here an elementary piece of a convex surface being part of a shell of revolution. As outlined in section 2.2, the fibre path attached on the presented surface element is generally characterised by two radii of curvature (figure 6.1): the normal one  $R_n$ , (perpendicular to the surface element), and the so-called geodesic curvature, (located in plane of that surface).

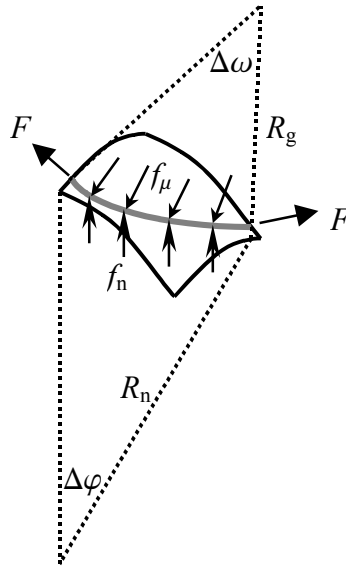


Fig. 6.1: Normal and geodesic radii of curvature describing a curved fibre path

The fibre is subjected to a longitudinal force  $F$ , a normal force per unit length  $f_n$  and a lateral force per unit length  $f_\mu$ . The static equilibrium of the forces in the direction perpendicular to the surface can be expressed as follows (section 3.2, equation (3.12)):

$$f_n R_n \Delta\varphi = 2F \sin\left(\frac{\Delta\varphi}{2}\right) \approx F \Delta\varphi \Rightarrow f_n = \frac{F}{R_n} \quad (6.1)$$

The same reasoning applies on the lateral forces equilibrium:

$$f_\mu R_g \Delta\omega = 2F \sin\left(\frac{\Delta\omega}{2}\right) \approx F \Delta\omega \Rightarrow f_\mu = \frac{F}{R_g} \quad (6.2)$$

The lateral fibre force is generated by friction that is situated between the placed fibre bundle and the supporting surface. The condition for fibre placement stability is  $[\gamma_1, \gamma_2, \gamma_5, \gamma_7, \gamma_8, \gamma_{13}, \gamma_{15}, \gamma_{20}, \gamma_{21}, \delta_1, \delta_2]$ :

## Part B: Reinforcing layer architecture

$$\mu \geq \left| \frac{f_\mu}{f_n} \right| = \left| \frac{F/R_g}{F/R_n} \right| = \left| \frac{R_n}{R_g} \right| = \left| \frac{k_g}{k_n} \right| \quad (6.3)$$

where  $k_n$  and  $k_g$  represent the normal and geodesic curvatures (dimension: 1 / length unit) respectively, and  $\mu$  stands for the coefficient of friction. In the case of applying geodesic trajectories, the geodesic curvature becomes equal to zero; this immediately leads to the conclusion that geodesic fibre paths do not require any friction between mandrel and roving.

Let a unit speed curve  $C$  ( $|C'(s)|=1$ , see [12,6,9,12]), be parametrically defined as a vector function of a single scalar parameter  $s$ , figure 6.2.

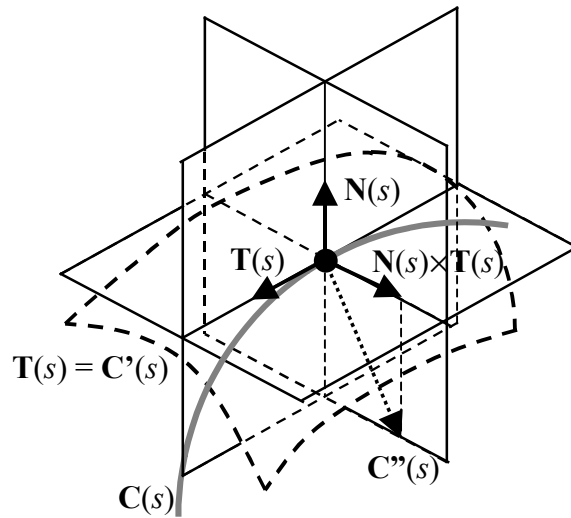


Fig. 6.2: Reference frame at a point belonging to a curve supported by a surface

As stated in chapter 3, the total curvature is directly related to the derivative of the tangent vector  $T'(s)$  ( $= C''(s)$ ). The direction of the total curvature  $k_t(s)$  ( $= |C''(s)|$ ) can be decomposed into a component perpendicular to the surface at that point, and a lateral component [12,82]:

$$\begin{aligned} k_n(s) &= N(s) \cdot C''(s) \\ k_g(s) &= (N(s) \times T(s)) \cdot C''(s) = \det[C'(s), C''(s), N(s)] \end{aligned} \quad (6.4)$$

In addition to equation (2.16), the total curvature, and the obtained values for the geodesic and normal curvatures, are related to each other as follows [12]:

$$C''(s) = k_n(s) \cdot N(s) + k_g(s) \cdot (N(s) \times T(s)) \quad (6.5)$$

## Part B: Reinforcing layer architecture

For an arbitrary speed curve ( $|\mathbf{C}'(s)| \neq 1$ , see [12,μ6,μ9,μ12]), we have to divide the first expression contained in equation (6.4) by  $|\mathbf{C}'(s)|^2$  and the second expression by  $|\mathbf{C}'(s)|^3$ , respectively. However, the complete expressions for the normal curvature are already provided in chapter 2. Nevertheless, the calculation of the geodesic curvature is significantly more elaborated.

## 6.2 General path equation

Let a continuous three-dimensional curve on a regular surface be defined as follows:

$$\mathbf{C} : s \rightarrow \mathbb{R}^3 : \mathbf{C}(s) = \mathbf{C}(\phi(s), \theta(s)) \quad (6.6)$$

The curve has an orientation  $\alpha(\theta)$  with respect to the meridian (figures 2.1, 2.2 and 2.4). The derivatives of  $\theta$  and  $\phi$  with respect to  $s$  are given by equation (2.40) with  $L$  replaced by  $s$ :

$$\begin{aligned} \frac{d\phi}{ds} &= \frac{\sin \alpha(\theta)}{\sqrt{E(\theta)}} \\ \frac{d\theta}{ds} &= \frac{\cos \alpha(\theta)}{\sqrt{G(\theta)}} \Rightarrow \frac{1}{ds} = \frac{\cos \alpha(\theta)}{\sqrt{G(\theta)}} \frac{1}{d\theta} \end{aligned} \quad (6.7)$$

The quantities  $E$  and  $G$  are outlined in section 2.1, and their formulation is given in equation (2.5) The second derivatives of  $\phi$  and  $\theta$  with respect to  $s$  can be expressed as follows (after substitution of  $1/ds$ , equation (6.7)):

$$\begin{aligned} \frac{d^2\phi}{ds^2} &= \frac{d}{ds} \left( \frac{\sin \alpha(\theta)}{\sqrt{E(\theta)}} \right) = \frac{d}{d\theta} \left( \frac{\sin \alpha(\theta) \cos \alpha(\theta)}{\sqrt{E(\theta)G(\theta)}} \right) = \\ &= \frac{d\alpha(\theta)}{d\theta} \frac{\cos 2\alpha(\theta)}{\sqrt{E(\theta)G(\theta)}} - \frac{\sin \alpha(\theta) \cos \alpha(\theta)}{2\sqrt{E(\theta)G(\theta)}^3} - \frac{\sin \alpha(\theta) \cos \alpha(\theta)}{2\sqrt{E(\theta)}^3 G(\theta)} E_{\theta}(\theta) \end{aligned} \quad (6.8)$$

$$\begin{aligned} \frac{d^2\theta}{ds^2} &= \frac{d}{ds} \left( \frac{\cos \alpha(\theta)}{\sqrt{G(\theta)}} \right) = \frac{d}{d\theta} \left( \frac{\cos^2 \alpha(\theta)}{G(\theta)} \right) = \\ &= -\frac{d\alpha(\theta)}{d\theta} \frac{2 \sin \alpha(\theta) \cos \alpha(\theta)}{G(\theta)} - \frac{\cos^2 \alpha(\theta)}{G^2(\theta)} G_{\theta}(\theta) \end{aligned}$$

where  $E_{\theta}(\theta) = \frac{dE(\theta)}{d\theta}$  and  $G_{\theta}(\theta) = \frac{dG(\theta)}{d\theta}$ . Note that equations (6.8) depend exclusively on the parameter  $\theta$ .

With a regular surface described by equation (2.32) and a curve defined according to equation (6.6), the geodesic curvature can be determined. Elaboration of the expression for  $k_g$  (presented in equation (6.4)) leads to [ $\mu_6, \mu_9, \mu_{12}, \mu_{15}$ ]:

$$k_g = \sqrt{EG - F^2} \left[ \Gamma_{11}^2 \left( \frac{d\phi}{ds} \right)^3 - \Gamma_{22}^1 \left( \frac{d\theta}{ds} \right)^3 + (2\Gamma_{12}^2 - \Gamma_{11}^1) \left( \frac{d\phi}{ds} \right)^2 \left( \frac{d\theta}{ds} \right) - (2\Gamma_{12}^1 - \Gamma_{22}^2) \left( \frac{d\phi}{ds} \right) \left( \frac{d\theta}{ds} \right)^2 - \left( \frac{d^2\phi}{ds^2} \right) \left( \frac{d\theta}{ds} \right) + \left( \frac{d^2\theta}{ds^2} \right) \left( \frac{d\phi}{ds} \right) \right] \quad (6.9)$$

where the so-called Christoffel symbols  $\Gamma_{ij}^k$  of the second kind are given by [ $\mu 6, \mu 9, \mu 12, \mu 15$ ]:

$$\begin{aligned} \Gamma_{11}^1 &= \frac{E_\phi}{2E} & \Gamma_{12}^1 &= \frac{E_\theta}{2E} & \Gamma_{22}^1 &= -\frac{G_\phi}{2E} \\ \Gamma_{11}^2 &= -\frac{E_\theta}{2G} & \Gamma_{12}^2 &= \frac{G_\phi}{2G} & \Gamma_{22}^2 &= \frac{G_\theta}{2G} \end{aligned} \quad (6.10)$$

Substitution of equations (2.5) into (6.10) followed by differentiation results in:

$$\begin{aligned} \Gamma_{11}^1 &= 0 & \Gamma_{12}^1(\theta) &= \frac{E_\theta(\theta)}{2E(\theta)} & \Gamma_{22}^1 &= 0 \\ \Gamma_{11}^2(\theta) &= -\frac{E_\theta(\theta)}{2G(\theta)} & \Gamma_{12}^2 &= 0 & \Gamma_{22}^2(\theta) &= \frac{G_\theta(\theta)}{2G(\theta)} \end{aligned} \quad (6.11)$$

The implemented Christoffel symbols depend exclusively on the parameter  $\theta$ ; this property reflects also on the coefficients of the first fundamental form ( $E$ ,  $F$  and  $G$ ). Additionally, according to equation (6.8), the involved derivatives  $\phi'(s)$ ,  $\phi''(s)$ ,  $\theta'(s)$  and  $\theta''(s)$  can also be treated as functions of  $\theta$  only. These exclusive dependencies lead to the conclusion that the geodesic curvature  $k_g$  will also depend on the parameter  $\theta$  only. Substitution of equations (6.11) and (6.8) into (6.9) leads, after some simplifications, to [ $\gamma 7, \gamma 8, \gamma 15, \delta 2$ ]:

$$k_g(\theta) = -\frac{d\alpha(\theta)}{d\theta} \frac{\cos \alpha(\theta)}{\sqrt{G(\theta)}} - \frac{1}{2} \frac{E_\theta(\theta)}{E(\theta)} \frac{\sin \alpha(\theta)}{\sqrt{G(\theta)}} \quad (6.12)$$

As stated in sections 2.2 and 6.1, a curve on a surface is geodesic when the associated geodesic curvature is equal to zero. This condition immediately results in:

$$\frac{d\alpha(\theta)}{d\theta} = -\frac{1}{2} \frac{E_\theta(\theta)}{E(\theta)} \tan \alpha(\theta) \quad (6.13)$$

The following equality is now introduced:

## Part B: Reinforcing layer architecture

$$\frac{d}{d\theta}(\sin \alpha(\theta)) = \cos \alpha(\theta) \frac{d\alpha(\theta)}{d\theta} \quad (6.14)$$

Substitution of equation (6.14) into (6.13) results in:

$$\frac{1}{\sin \alpha(\theta)} \frac{d}{d\theta}(\sin \alpha(\theta)) = -\frac{1}{2} \frac{E_\theta(\theta)}{E(\theta)} \quad (6.15)$$

Integration yields:

$$\ln(\sin \alpha(\theta)) = \ln\left(\frac{c}{\sqrt{E(\theta)}}\right) \Rightarrow \sin \alpha(\theta) = \frac{c}{\sqrt{E(\theta)}} \quad (6.16)$$

The obtained equation is the well-known Clairaut relation that has been derived in the previous chapter using the Euler-Lagrange equation. We recall here that the constant  $c$  in equation (6.16) is the pole-opening radius of the shell under consideration. According to equation (6.3), the fibre placed over the mandrel surface does not require any friction for maintaining its position. This is the reason for the excellent stability characterising geodesic filament winding. For some intuitive reason however, some designers do not take the “risk” of placing dry fibres on a mandrel.

In section 6.1 we showed that the available friction between fibre and supporting surface should not be less than the ratio  $k_g / k_n$ . To evaluate this ratio, we first replace  $k_1$  and  $k_2$  in equation (2.15) with  $k_m$  and  $k_p$ , respectively (these quantities are given by equations (2.43) and (2.44)). In addition, by recalling equation (6.12) we obtain:

$$\begin{aligned} \frac{d\alpha(\theta)}{d\theta} = & -\frac{1}{2} \frac{E_\theta(\theta)}{E(\theta)} \tan \alpha(\theta) \\ & \pm \mu \left( \frac{\sqrt{G(\theta)}}{\cos \alpha(\theta)} \left( k_p(\theta) \sin^2 \alpha(\theta) + k_m(\theta) \cos^2 \alpha(\theta) \right) \right) \end{aligned} \quad (6.17)$$

The “ $\pm$ ” sign refers to the fact that the presence of friction can either relatively increase or decrease the resulting winding angle. Finally, substitution of equality (6.14) into (6.17) leads to:

$$\begin{aligned} \frac{d}{d\theta}(\sin \alpha(\theta)) = & -\frac{1}{2} \frac{E_\theta(\theta)}{E(\theta)} \sin \alpha(\theta) \\ & \pm \mu \sqrt{G(\theta)} \left[ (k_p(\theta) - k_m(\theta)) \sin^2 \alpha(\theta) + k_m(\theta) \right] \end{aligned} \quad (6.18)$$

The first part of (6.18) provides the differential form of the Clairaut equation and the second part represents the frictional influence. The following expressions are now introduced [ $\gamma 7, \gamma 8$ ]:

$$\begin{aligned}
 A_0(\theta) &= \sqrt{G(\theta)}k_m(\theta) \\
 A_1(\theta) &= -\frac{1}{2} \frac{E_\theta(\theta)}{E(\theta)} \\
 A_2(\theta) &= \sqrt{G(\theta)}(k_p(\theta) - k_m(\theta))
 \end{aligned} \tag{6.19}$$

The combination of equations (6.18) and (6.19) leads to:

$$\frac{d}{d\theta}(\sin \alpha(\theta)) = A_1(\theta) \sin \alpha(\theta) \pm \mu \left( A_2(\theta) \sin^2 \alpha(\theta) + A_0(\theta) \right) \tag{6.20}$$

A nice property of equations (6.19) and (6.20) is the exclusive implementation of basic geometrical quantities like metrics and curvatures, which are independent of the coordinate system they are related to (intrinsic coordinates). In addition, the derived first order differential equation (6.20) is an ordinary one that can be evaluated with standard numerical  $[\mu 4, \mu 7, \mu 8]$  methods. In regard to the characteristic functions  $A_i(v)$ , the following statements can be formulated:

- $A_1(\theta)$  depends only on the parallel metric  $E(\theta)$  and not on the actual shape of the treated shell of revolution. This is an explanation for the Clairaut relation being exclusively dependent of the local radius perpendicular to the rotational-symmetry axis (this radius is equal to  $E^{1/2}$ ).
- Both  $A_0(\theta)$  and  $A_2(\theta)$  are linearly proportional to  $\sqrt{G(\theta)}$  (metric along the meridian).
- When the friction coefficient is equal to zero, the distribution of the curvature radii does not directly affect the resulting winding angle  $\alpha(\theta)$ . The latter depends then exclusively on  $E(\theta)$ .
- The only possibility for neutralising the frictional influence on the resulting fibre path is  $k_p(\theta) = k_m(\theta) = 0$ . This condition reflects on an entirely flat surface.

### 6.3 Parameterisation & evaluation

#### Polar coordinates

The definition of a shell of revolution in polar coordinates is:

$$\mathbf{S} : (\phi, \rho) \rightarrow \mathfrak{R}^3 : \mathbf{S}(\phi, \rho) = \{\rho \cos \phi, \rho \sin \phi, z(\rho)\} \quad (6.21)$$

According to equation (2.5), the associated metrics are:

$$\begin{aligned} E(\rho) &= \rho^2 \\ F(\rho) &= 0 \\ G(\rho) &= 1 + z'^2(\rho) \end{aligned} \quad (6.22)$$

The corresponding radii of curvature can be obtained by elaboration of equations (2.43) and (2.44):

$$\begin{aligned} k_m(\rho) &= -\frac{z''(\rho)}{(1 + z'^2(\rho))^{3/2}} \\ k_p(\rho) &= -\frac{z'(\rho)}{\rho\sqrt{1 + z'^2(\rho)}} \end{aligned} \quad (6.23)$$

Note that  $\rho$  is a positive real number while  $z'(\rho)$  and  $z''(\rho)$  are usually negative. The characteristic equations  $A_i(\rho)$  become:

$$\begin{aligned} A_0(\rho) &= -\frac{z''(\rho)}{1 + z'^2(\rho)} \\ A_1(\rho) &= -\frac{1}{\rho} \\ A_2(\rho) &= -\frac{z'(\rho) + z'^3(\rho) - \rho z''(\rho)}{\rho(1 + z'^2(\rho))} \end{aligned} \quad (6.24)$$

The general non-geodesic equation can be obtained by substitution of equations (6.22) and (6.24) into (6.20):

$$\begin{aligned} \frac{d}{d\rho}(\sin \alpha(\rho)) &= -\frac{1}{\rho} \sin \alpha(\rho) \pm \\ &\mu \left( \frac{z'(\rho) + z'^3(\rho) - \rho z''(\rho)}{\rho(1 + z'^2(\rho))} \sin^2 \alpha(\rho) + \frac{z''(\rho)}{1 + z'^2(\rho)} \right) \end{aligned} \quad (6.25)$$

It should be noted here that a cylindrical shell of revolution can not be described in the hereby-presented coordinate system since  $z(\rho)$  cannot be defined as a function (infinite slope).

### Spherical coordinates

A shell of revolution in spherical coordinates can be described as follows [μ2]:

$$S : (\phi, \theta) \rightarrow \mathfrak{R}^3 : \bar{S}(\phi, \theta) = \{g(\theta) \sin \theta \cos \phi, g(\theta) \sin \theta \sin \phi, g(\theta) \cos \theta\} \quad (6.26)$$

Application of equation (2.5) results in the determination of the coefficients of the first fundamental form:

$$\begin{aligned} E(\theta) &= g^2(\theta) \sin^2 \theta \\ F(\theta) &= 0 \\ G(\theta) &= g^2(\theta) + g'^2(\theta) \end{aligned} \quad (6.27)$$

The main curvatures become (equations (2.43) and (2.44)):

$$\begin{aligned} k_m(\theta) &= \frac{2g'^2(\theta) - g(\theta)g''(\theta) + g^2(\theta)}{(g^2(\theta) + g'^2(\theta))^{3/2}} \\ k_p(\theta) &= \frac{g(\theta) \sin \theta - g'(\theta) \cos \theta}{g(\theta) \sin \theta \sqrt{g^2(\theta) + g'^2(\theta)}} \end{aligned} \quad (6.28)$$

The characteristic equations  $A_i(\theta)$  can be obtained by substitution of expressions (6.27) and (6.28) into equation (6.20):

$$\begin{aligned} A_0(\theta) &= \frac{2g'^2(\theta) - g(\theta)g''(\theta) + g^2(\theta)}{g^2(\theta) + g'^2(\theta)} \\ A_1(\theta) &= -\frac{g'(\theta)}{g(\theta)} - \cot \theta \\ A_2(\theta) &= -\frac{1}{g(\theta)(g^2(\theta) + g'^2(\theta))} \left( g(\theta)g'^2(\theta) \right. \\ &\quad \left. + g'^3(\theta) \cot \theta - g^2(\theta)(g''(\theta) - g'(\theta) \cot \theta) \right) \end{aligned} \quad (6.29)$$

The general non-geodesic equation becomes:

## Part B: Reinforcing layer architecture

$$\begin{aligned} \frac{d}{d\theta}(\sin \alpha(\theta)) &= -\left(\frac{g'(\theta)}{g(\theta)} - \cot \theta\right) \sin \alpha(\theta) \pm \\ \mu \left( -\frac{g(\theta)g'^2(\theta) + g'^3(\theta) \cot \theta - g^2(\theta)(g''(\theta) - g'(\theta) \cot \theta)}{g(\theta)(g^2(\theta) + g'^2(\theta))} \sin^2 \alpha(\theta) + \right. & \quad (6.30) \\ \left. \frac{2g'^2(\theta) - g(\theta)g''(\theta) + g^2(\theta)}{g^2(\theta) + g'^2(\theta)} \right) \end{aligned}$$

Despite the relatively complicated appearance, equation (6.30) is suitable for application on a more extensive collection of shapes; a typical example is the description of a cylinder, where equation (6.21) fails (see also section 5.4). Additionally, when ellipsoidal or spherical shapes are treated, the above-mentioned equation in spherical coordinates will enable a considerable simplification. For “straight” shells of revolution e.g. a cone, a shape definition according to equation (6.21) is preferable.

### Integration procedure

For a “smooth” surface of revolution, the characteristic functions  $A_0(\theta)$ ,  $A_1(\theta)$  and  $A_2(\theta)$  are continuous and do not show any singularities. An exception on this statement is when  $E^{1/2}$  becomes equal to zero; the corresponding  $A_1(\theta)$  function becomes then infinite. This implies that the winding angle will remain equal to zero for every locus on the treated shell of revolution (see also equations (5.12) and (6.16)).

For the integration of equation (6.17) we assume here that the starting point of the fibre path is adjacently located to the polar opening of the shell under consideration ( $\alpha_{\text{initial}} = \pi/2$ ). According to equation (6.17), the derivative of the winding angle with respect to the  $\theta$ -parameter will tend to  $-\infty$ . This problem can be solved by a slight reduction of the initial winding angle value ( $\alpha_{\text{initial}} = \pi/2 - \epsilon$  where  $\epsilon$  is very small).

An example of a suitable integration method for equation (6.17) or (6.20) is the fourth order Runge-Kutta procedure [ $\mu 4, \mu 7, \mu 8$ ]. As a thumb rule, it can be stated that for an initial value of  $0.9999 \times \pi/2$ , the required number of steps will become approximately  $50 \times 10^3$  over the integration interval [ $0.9999 \times \pi/2, \alpha_{\text{equator}}$ ]. It should be noted that the minimal possible value for  $\alpha_{\text{equator}}$  is equal to zero.

The stability and calculation time obviously depend on the behaviour of the characteristic equations  $A_0(\theta)$ ,  $A_1(\theta)$  and  $A_2(\theta)$  and show generally favourable characteristics. However, when the winding angle  $\alpha$  becomes equal to 0, the integrand vanishes and the resulting fibre path will follow the meridional direction (see also the remarks in section 5.2 after equation (5.12)). In addition, for  $\alpha = \pi/2$ , the integrand becomes infinite (as previously indicated) and the fibre path will follow the circumferential direction of the shell (constant latitude).

## Part B: Reinforcing layer architecture

By approximating the obtained integration data with an interpolating function  $\alpha_p(\theta)$ , a proper expression for  $\alpha(\theta)$  can be derived [μ14,μ15]. Substitution of the latter into the second row of equation (2.41) will provide the function  $\phi(\theta)$ :

$$\phi(\theta) = \int_{s=\theta_b}^{\theta} \sqrt{\frac{G(s)}{E(s)}} \tan \alpha_p(s) ds \quad (6.31)$$

where  $\theta_b$  denotes the initial value for  $\theta$ . On a similar way, the length along the resulting curve can be found by integrating the first expression, contained in equation (2.40):

$$L(\theta) = \int_{s=\theta_b}^{\theta} \frac{\sqrt{G(s)}}{\cos(\alpha_p(s))} ds \quad (6.32)$$

With equation (6.31), the resulting path becomes a three-dimensional curve that depends on a single parameter, e.g.  $\phi$  as a function  $\rho$  when considering polar coordinates (equation (6.21)) or, in the case of spherical coordinates,  $\phi$  as a function of  $\theta$  (equation (6.26)).

## 6.4 Examples

### Conical shells

The class of “straight” shells of revolution is characterised by the equality of the meridian curvature with zero. When using polar coordinates, the complete range from annulus to almost a cylinder can be determined. The latter is inappropriate for a polar description, since in this case the shell-generating profile cannot be expressed as a function of the local radius. In the same spirit as in chapters 3 and 4, for a cone with a minor pole radius  $c$ , we introduce the following dimensionless coordinates:

$$\begin{aligned} Y &= \frac{\rho}{c} & Z(Y) &= \frac{z(\rho)}{c} \\ \Rightarrow Z'(Y) &= z'(\rho) & \& \quad \alpha'(\rho) &= \frac{\alpha'(Y)}{c} \end{aligned} \quad (6.33)$$

Assuming a top angle  $2\tau$  (figure 5.6), the equation describing the meridian becomes:

$$Z(Y) = (Y_{eq} - Y) \cot \tau \quad 1 \leq Y \leq Y_{eq} \quad (6.34)$$

where  $Y_{eq}$  is the dimensionless equatorial radius. Substitution of equation (6.34) into (6.25) results in:

$$\frac{d}{dY}(\sin \alpha(Y)) = -\frac{\sin \alpha(Y)}{Y} (1 + \mu \cot \tau \sin \alpha(Y)) \quad (6.35)$$

In combination with the boundary condition  $\alpha(1) = \pi/2$ , equation (6.35) gains the following solution:

$$\alpha(Y) = \arcsin\left(\frac{1}{\mu(Y-1) \cot \tau + Y}\right) \quad 1 \leq Y \leq Y_{eq} \quad (6.36)$$

For  $\mu = 0$  we obtain the Clairaut equation (see also equations (5.12) and (6.16)). Furthermore, for an annulus ( $\tau = \pi/2$ ), the friction is not able to create any path deviation since  $\cot(\pi/2) = 0$ . The reason for this inability can be found in the simultaneous equality of  $k_m(\rho)$  and  $k_p(\rho)$  with zero (equation (6.23) with  $z'(\rho) = z''(\rho) = 0$ ). Evaluation of equation (6.31) results in the wound trajectory description:

$$\frac{d\phi}{dY} = \frac{\operatorname{cosec} \tau}{Y \sqrt{(Y + \mu(1-Y) \cot \tau)^2 - 1}} \quad (6.37)$$

where “cosec” stands for “1 / sin”. As an example, we consider here a cone with the following characteristic parameters:

$$\begin{aligned} \tau &= \pi/8 \\ Y_{\text{eq}} &= 10 \\ \mu &= \{-0.2, -0.1, 0, 0.1, 0.2\} \\ \phi(Y_{\text{eq}}) &= 0 \end{aligned}$$

The trajectories presented in figure 6.3 correspond with  $\mu = \{-0.2, -0.1, 0, 0.1, 0.2\}$ , referring from the right to the left:

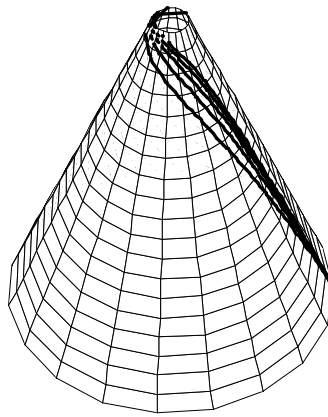


*Fig. 6.3: Fibre trajectories on a cone*

It can generally be stated that if the  $Y_{\text{eq}}$ -value is fixed, the effect of friction application increases when the top angle becomes smaller; this is generated by the relative increase of the total fibre length as a function of  $Y$ .

The basic cone-related fibre trajectories can easily be used for discretisation of rotational symmetric objects into conical ones. This technique is particularly useful for the determination of the fibre orientation in a finite element analysis or panel method.

## **Cylinder**

The formulation of a cylinder in spherical coordinates (equation (6.26)) is:

$$\begin{aligned} g(\theta) &= \frac{c}{\sin \theta} & \theta_c \leq \theta \leq \pi - \theta_c \\ \theta_c &= \arctan \frac{1}{\xi} & \xi > 0 \end{aligned} \tag{6.38}$$

## Part B: Reinforcing layer architecture

where  $c$  is the basic radius and  $\xi = 0.5 \times (\text{length of the cylinder})/c$ . The initial winding angle is here determined as follows:

$$\sin \alpha|_{\theta_c} = \frac{1}{\lambda} \quad \lambda > 1 \quad (6.39)$$

The general winding equation in spherical coordinates (6.30) becomes:

$$\frac{d}{d\theta}(\sin \alpha(\theta)) = \mu \frac{\sin^2 \alpha(\theta)}{\sin^2 \theta} \quad \theta_c \leq \theta \leq \pi - \theta_c \quad (6.40)$$

In combination with the initial condition (6.39), the solution is then given by:

$$\alpha(\theta) = \arcsin\left(\frac{1}{\lambda \pm \mu(\cot \theta - \xi)}\right) \quad (6.41)$$

Substitution of the obtained expression into equation (6.31) leads to:

$$\frac{d\phi}{d\theta} = \frac{1}{\sin^2 \theta \sqrt{(\lambda \pm \mu(\cot \theta - \xi))^2 - 1}} \quad (6.42)$$

To illustrate the results of the obtained expressions, we define here the following cylinder:  $\xi = 10$ ,  $\lambda = 10$ ,  $\mu = \{0.2, 0.1, 0, -0.1, -0.2\}$ ,  $\phi(\pi/2) = 0$ . In the figure below, the results are presented, where the applied coefficient of friction ( $\mu$ ) is equal to respectively  $\{-0.2, -0.1, 0, 0.1, 0.2\}$ , from the right to the left:

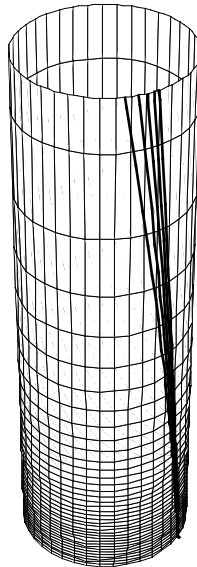


Fig. 6.4: Fibre trajectories on a cylinder

Depending on the magnitude of  $\mu$ ,  $\lambda$  and  $\xi$ , we can create transitional windings for connecting several polar and hoop circuits to each other (particularly important for the winding process of cylindrical pressure vessels in a continuous fashion). The creation of such circuits is outlined in chapter 9.

### Sphere

For a sphere, the meridian function  $g(\theta)$  is a constant and equal to the basic radius  $R$ . The non-geodesic trajectory equation becomes:

$$\frac{d}{d\theta}(\sin \alpha(\theta)) = \mu - \cot \theta \sin \alpha(\theta) \quad \theta_c \leq \theta \leq \pi / 2 \quad (6.43)$$

where  $\theta_c$  is the value corresponding to the pole opening. As an initial condition, the winding angle at the pole is set equal to  $\pi/2$ . The solution of equation (6.43) becomes:

$$\alpha(\theta) = \arcsin\left(\frac{\sin \theta_c + \mu(\cos \theta_c - \cos \theta)}{\sin \theta}\right) \quad (6.44)$$

Substitution of this result into equation (2.39) provides the description of the fibre trajectories:

$$\frac{d\phi}{d\theta} = \frac{\csc^2 \theta [\mu(\cos \theta_c - \cos \theta) + \sin \theta_c]}{\sqrt{1 - \operatorname{cosec}^2 \theta [\mu(\cos \theta_c - \cos \theta) + \sin \theta_c]^2}} \quad (6.45)$$

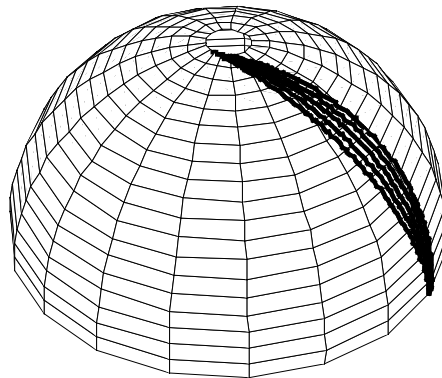


*Fig. 6.5: Fibre trajectories on a sphere*

## Part B: Reinforcing layer architecture

The sphere-related trajectories treated in our example are defined as follows:  $R = 1$ ,  $\theta_c = 0.1$ ,  $\mu = \{-0.2, -0.1, 0, 0.1, 0.2\}$ ,  $\phi(\pi/2) = 0$ . The result is depicted in figure 6.5 where, as usual, the corresponding implemented coefficient of friction is respectively equal to  $\{-0.1, -0.1, 0, 0.1, 0.2\}$  when viewing from the right to the left.

### Isotensoids

The basic equation for determining isotensoid meridians without external axial loads is given by equation (3.18) where  $k_a = 0$ :

$$\tan^2 \alpha(\rho) = 2 - \frac{k_m(\rho)}{k_p(\rho)} \quad (6.46)$$

Substitution of this relation and equation (6.23) into (6.18) leads to:

$$\frac{d}{d\rho} (\sin \alpha(\rho)) = -\frac{(\sin \alpha(\rho))}{\rho} + 2\mu \frac{z'(\rho)}{\rho} \cos^2 \alpha(\rho) \quad (6.47)$$

The coefficient of friction must belong to the interval  $[-\mu_{\max}, \mu_{\max}]$  where  $\mu_{\max}$  is the maximally achievable friction value. To obtain an analytical winding angle expression, we define a continuous function  $\mu(\rho)$  remaining between the indicated friction boundaries and satisfying the following condition:

$$\mu(\rho) = \frac{1}{2} \frac{\rho}{z'(\rho)} \frac{B'(\rho)}{B(\rho)} \frac{\tan \alpha(\rho)}{\cos \alpha(\rho)} \quad (6.48)$$

where  $B(\rho)$  is an arbitrary continuous function, able to generate  $\mu$ -values belonging to the previous mentioned range. Assuming the existence of such a function, equation (6.47) can be rewritten as follows:

$$\frac{(\sin \alpha(\rho))'}{\sin \alpha(\rho)} = -\frac{\rho'}{\rho} + \frac{B'(\rho)}{B(\rho)} \quad (6.49)$$

The solution becomes:

$$\alpha(\rho) = \arcsin\left(\frac{cB(\rho)}{\rho}\right) \quad (6.50)$$

where  $c$  is the pole radius. Indicating the equator radius with  $R$ , the following function for  $B(\rho)$  can be assumed:

$$B(\rho) = 1 + \mu_{\max} \sin\left(\pi \frac{\rho - c}{R - c}\right) \quad (6.51)$$

Substitution of equation (6.51) into (6.48) automatically leads to the creation of a winding angle equal to  $\pi/2$  at the poles. The friction function (equation (6.50)) becomes:

$$\mu(\rho) = \frac{c\pi\mu_{\max} \cos\left(\pi \frac{\rho-c}{R-c}\right)}{2z'(\rho)(R-c) \left[ 1 - \left( c \frac{1 + \mu_{\max} \sin\left(\pi \frac{\rho-c}{R-c}\right)}{\rho} \right)^2 \right]} \quad (6.52)$$

As an illustration of the obtained expressions, we consider here the following case:  $c = 1$ ,  $R = 10$ ,  $\mu = \{-0.2, -0.1, 0, 0.1, 0.2\}$ . The graphs of the obtained  $\alpha(\rho)$  solutions are given in the figure below:

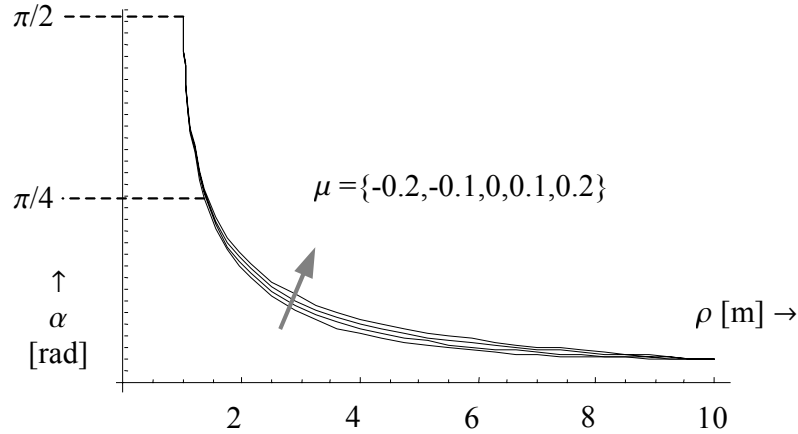


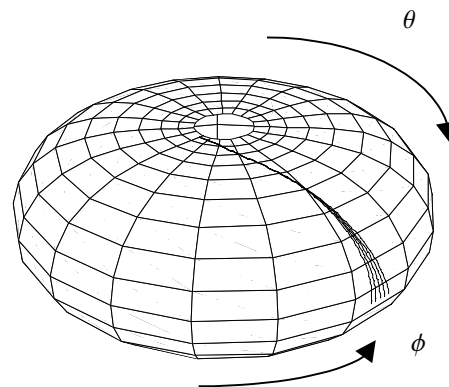
Fig. 6.6: Fibre trajectories on an isotensoidal shell of revolution

It should be noted that the friction function (6.48) is strongly depending on the meridian profile morphology ( $z'(\rho)$ ). When determining the isotensoidal shape, particular cases may occur where  $z'(\rho) = 0$ . Consequently, the desired limitation for  $\mu(\rho)$  might not be possible. However, investigation of these singularities is beyond the scope of this paper; the introduced  $B$ -function is exclusively serving the aim of creating an example.

### Oblate spheroid with flat polar areas

The last example presented here is a quantitative demonstration of the curvature influence on the ability of friction to modify a certain given geodesic path. In the figure below we show that increased curvature values will result in intensified fibre path trajectory modifications (when compared to geodesic paths):

## Part B: Reinforcing layer architecture



$$\mu = \{-0.1, -0.05, 0, 0.05, 0.1\}$$

from the left to the right

Fig. 6.7: Fibre trajectories on a shell of revolution combining flat and curved areas

Obviously, there is no path-modification possible on the flat areas. The corresponding winding angle developments are given in the figure below:

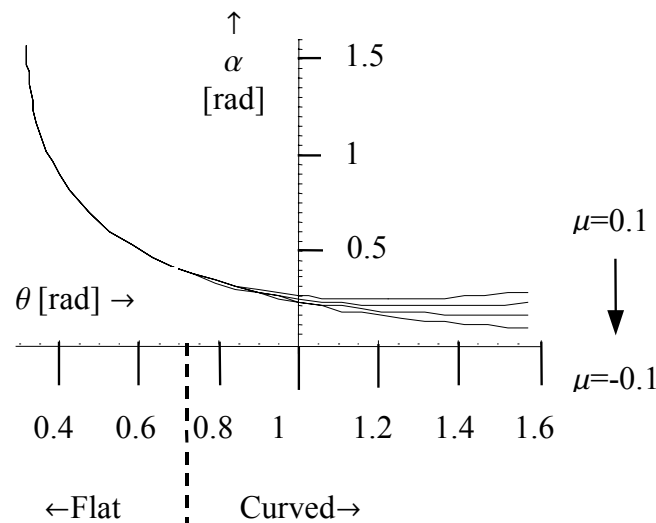


Fig. 6.8: Winding angle behaviour on a shell combining flat- and curved areas

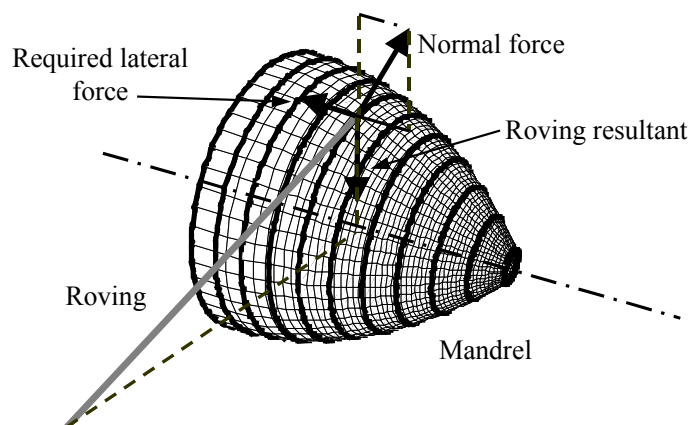
Note the initial roving path coincidence at the pole. These common trajectories are located on the left side of the presented graph, where the supporting surface is entirely flat (see also figure 6.7).

## 7

## Friction determination

The design procedure of non-geodesically filament wound products requires well-determined values for the available friction that is situated between the applied rovings and the supporting surface. In this chapter, we propose a mandrel shape with a specially designed meridian profile that enables a linearly proportional relation between the feed eye carriage translation and the measured values for the coefficients of friction. With the proposed mandrel, we performed (on a lathe-configured filament winding machine) several experiments corresponding to the variation of typical filament winding-related process parameters: fibre speed, roving tension, roving dimensions, wet vs. dry winding and surface quality of the mandrel. The results indicate that the surface quality of the mandrel and the type of winding process (wet vs. dry fibres) have a considerable influence on the obtained data. The influence of the fibre speed, roving tension and fibre material on the other hand, is negligible.

After a brief overview of the available friction-measuring methods, we outline the determination of the dedicated mandrel shape. This section concludes with an error analysis for inaccuracies, mainly induced by using the simplified solution for the required meridian profile. Section (7.2) provides several tools for the determination of the winding machine movements and the control of the roving speed. A brief description of the experiments (series and error analysis) is given in section 7.3. The experimental results are presented and discussed in section 7.4. The current chapter ends with the formulation of several conclusions regarding the applicability and advantages generated by the proposed mandrel geometry, and provides some rules of thumb for the estimation of the available coefficient of friction.



**Impression of the forces acting on a roving; in order to create static equilibrium, a lateral force (generated by friction) is here required**

## **Part B: Reinforcing layer architecture**

## 7.1 Mandrel design

The basic idea supporting the development of the experiments presented here is that the measurements for the friction coefficient should be as realistic as possible. This is mainly achieved by performing these experiments on a filament-winding machine, using a rotationally symmetric mandrel. A linear relation between the coefficients of friction and the translation of the feed eye carriage of the winding machine must ensure stability for the obtained measurements. After a short overview of the available experimental methods, the final choice is motivated and followed by the geometrical description of the resulting mandrel shape. The section concludes with an error analysis regarding the reliability of the results to be obtained.

### Overview & selection of experimental set-up

The available experimental methods are briefly presented below [ $\gamma_9, \gamma_{15}, \gamma_{17}$ ]:

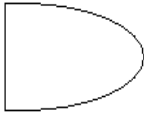
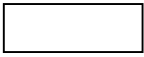
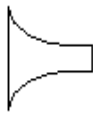
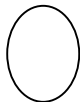
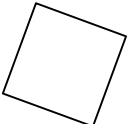
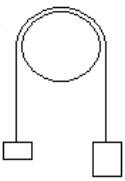
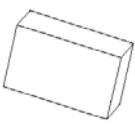
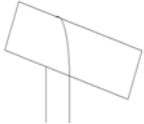
Auxiliary apparatus	Winding machine		Tilting apparatus		Arbitrary fixation of gliding plane
<b>GLIDING PLANE</b>	Specially shaped mandrel 	Cylindrical mandrel 	Trumpet-shaped mandrel 	Arbitrary mandrel 	Flat plane 
<b>PROCEDURE</b>	Winding with $\alpha \approx \text{constant}$ till fibre slips	Winding with $\alpha \neq \text{constant}$ till fibre slips	Two different forces, increase one till fibre slips 	Block with roving on the underside; will slip at a certain inclination angle 	One roving will slip at a certain inclination angle 
<b>ROVING SLIP DETECTION</b>	Via fibre tension, optically or chronometer	Via fibre tension or optically	Optically	Optically	Optically

Table 7.1: Overview of experimental methods for the determination of the coefficient of friction

## Part B: Reinforcing layer architecture

The demands on the experiments to be performed are:

- Realistic simulation of slippage during filament winding
- Inclusion of the consumed roving speed as an experimental parameter
- Ability for investigating the influence of the roving tension
- Simple and reliable acquisition of the experimental results

Despite the simplicity of various methods presented in table 7.1, the decision is taken in favour of the specially shaped convex mandrel, attached on a lathe-configured filament winding machine; this combination is the only one satisfying the complete set of requirements. A schematic overview of the chosen configuration is presented below (figure 7.1):

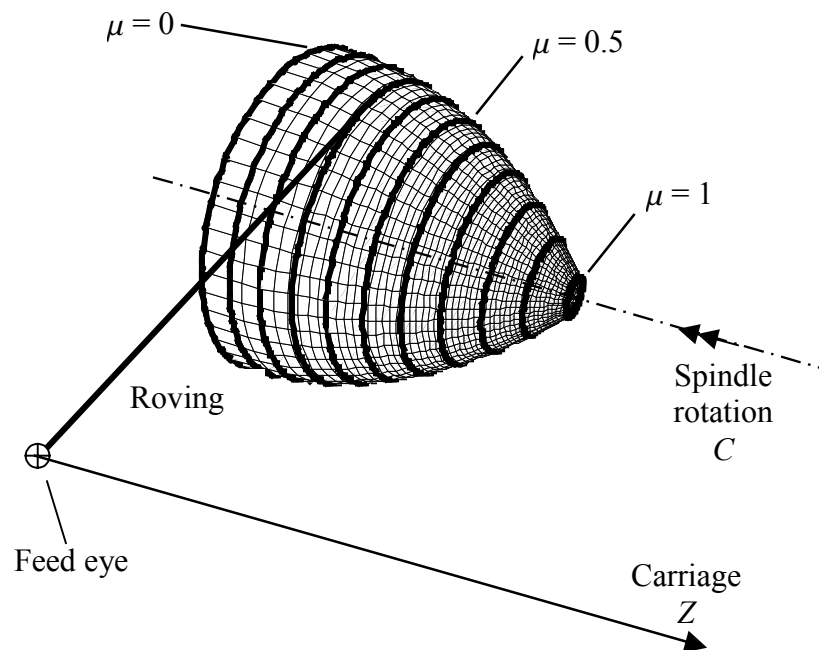


Fig. 7.1: Schematic view of the experimental lay-up (the bold lines on the mandrel represent a coefficient of friction increment equal to 0.1)

The movements required for the performance of the experiments are the spindle rotation  $C$ , the carriage translation  $Z$  and the feed eye roller inclination  $A$  [ $\alpha_3$ ] (for the definition of  $A$  we refer here to figure 11.2). The latter ensures a tangential placement of the fibre bundle on the mandrel. However, since this movement is not of primary importance for the underlying kinematic model, it is not presented in figure 7.1.

The slippage can be determined by optical methods, for example a high shutter speed video camera. When the mandrel is equipped with a benchmark indicating the  $Z$ -coordinate (figure 7.9), the corresponding coefficient of friction at the moment of roving slippage can accurately be determined. The increments on the  $Z$ -benchmark can be subdivided by placing an additional  $C$ -benchmark on the biggest periphery of the mandrel (figures 7.8 and 7.9).

An alternative method is to measure the time the roving needs to reach its slippage point when departing from the cylindrical part (in figure 7.9: left side). This method however, might not be very accurate. Nevertheless, since no video camera is needed, it is more economical.

### **Mandrel shape**

Although any convex meridian profile can generate a proper mandrel shape for the friction experiments, we introduce here an additional requirement; the increase of friction along the meridian profile must be linearly proportional to the translation of the carriage  $Z$  by a constant winding angle. The advantages provided by this demand are:

- Facilitated determination of the coefficient of friction by measurement of  $Z$
- Stability of the measurements
- Simple machine control

The fibre bundle is placed on the mandrel and has a constant winding angle (figures 7.1 and 7.9): the fibre orientation is practically perpendicular to the axis of rotational symmetry of the mandrel). This implies that the carriage is directly coupled to the shape coordinate  $z(\rho)$ . The linearity requirement for the coefficient of friction  $\mu$  can now be formulated:

$$\mu(\rho) = c_0 + c_1 z(\rho) \quad (7.1)$$

The expected coefficients of friction belong to the range  $\mu = [0, 1]$  corresponding to  $z = [0, z_r]$ . These intervals result in:

$$c_0 = 0, \quad c_1 = \frac{1}{z_r} \quad (7.2)$$

For reasons to be explained later, we assume here:  $z_r = 235$  [mm]. Depending on the width of the tested fibre bundle, the winding angle becomes:

$$\alpha(\rho) = \frac{\pi}{2} - \varepsilon, \quad 0 \leq \varepsilon \leq 0.1 \text{ [rad]}, \quad \varepsilon = \text{constant} \quad (7.3)$$

The friction required for keeping the roving stable is given by equation (6.3). We assume now that the shell is defined in polar coordinates (equation (6.21)). The meridional and parallel curvatures are then given by equation (6.23). Substitution of these curvatures into equation (2.15) results in the determination of the normal curvature:

## Part B: Reinforcing layer architecture

$$k_n(\rho) = -\frac{\sin^2 \alpha(\rho) \left[ \frac{z'(\rho)(1+z'^2(\rho))}{\rho} \right] + \cos^2 \alpha(\rho) [z''(\rho)]}{(1+z'^2(\rho))^{3/2}} \quad (7.4)$$

For the geodesic curvature, substitution of equation (6.22) into (6.21) gives:

$$\begin{aligned} k_g(\rho) &= -\alpha'(\rho) \frac{\cos \alpha(\rho)}{\sqrt{G(\rho)}} - \frac{1}{2} \frac{E'(\rho)}{E(\rho)} \frac{\sin \alpha(\rho)}{\sqrt{G(\rho)}} = \\ &= -\frac{\alpha'(\rho) \rho \cos \alpha(\rho) + \sin \alpha(\rho)}{\rho \sqrt{1+z'^2(\rho)}} \end{aligned} \quad (7.5)$$

For a convex meridian profile, the first and second derivatives (respectively  $z'(\rho)$  and  $z''(\rho)$ ) are negative. As a result of this, the curvature quotient  $k_g(\rho) / k_n(\rho)$  will become negative (equations (7.4) and (7.5)). In addition, the basic static equilibrium equation does not provide any information regarding the sign of the coefficient of friction (chapter 6). In order to generate positive friction values (as dictated by equation (6.3)) we multiply the curvature coefficient ( $k_g/k_n$ ) by -1. Substitution of equation (7.3) into equations (7.4) and (7.5) results in:

$$\mu(\rho) = -\frac{k_g(\rho)}{k_n(\rho)} = -\frac{\cos \varepsilon [1+z'(\rho)^2]}{\cos^2 \varepsilon [z'(\rho) + z'^3(\rho)] + \rho \sin^2 \varepsilon z''(\rho)} \quad (7.6)$$

Since  $\varepsilon$  does represent a small angular value, it is justified to neglect the last term in the denominator of equation (7.6). The simplified ODE for the meridian profile can then be formulated by the combination of expressions (7.1) and (7.6):

$$\begin{aligned} \mu_s(\rho) &= -\frac{\cos \varepsilon [1+z'(\rho)^2]}{\cos^2 \varepsilon [z'(\rho) + z'^3(\rho)]} = -\frac{1}{z'(\rho) \cos \varepsilon} \\ &= c_0 + c_1 z(\rho) \quad \text{with } z(r) = z_r \end{aligned} \quad (7.7)$$

where  $r$  is the minimum mandrel radius ( $c_0$  and  $c_1$  are presented in equation (7.2)). The solution for equation (7.7) becomes:

$$z_s(\rho) = \sqrt{z_r [z_r + 2(r - \rho) \sec \varepsilon]} \quad (7.8)$$

The measured coefficient of friction is then given by (equations (7.1) and (7.2)):

$$\mu_m(\rho) = \frac{\sqrt{z_r [z_r + 2(r - \rho) \sec \varepsilon]}}{z_r} \quad (7.9)$$

## Part B: Reinforcing layer architecture

For the mandrel design, we assume here  $\epsilon$  as equal to zero. Except the convex part, the mandrel includes an axle for attachment at the winding machine, and a cylindrical part for providing sufficient space to the fibre bundle to obtain its targeted velocity for the performance of the experiments. The minimum radius is equal to 15 [mm]. At  $z_s(\rho) = 0$ , the maximum radius becomes equal to  $r + z_r/2 = 132.5$  [mm].

The experiments are designed for performance by one person. According to the Dutch labour regulations, the total weight of the mandrel should not exceed the value of 25 [kg] [ $\alpha 16, \gamma 17$ ]. With  $z_r = 235$  [mm] and an aluminum alloy as construction material, the total weight becomes equal to 24.9 [kg]. The shape of the resulting mandrel is depicted below (figure 7.2):

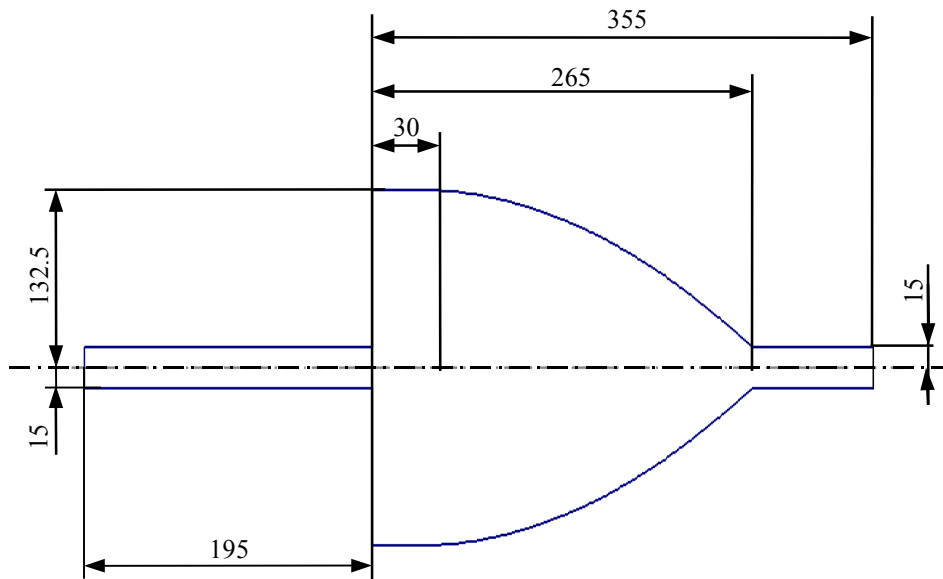


Fig. 7.2: Dimensions of the resulting mandrel shape in [mm]

The cylindrical part has a length of 30 [mm]; the total length of the axle is 550 [mm]. The surface of the mandrel is polished. For a three dimensional impression of the convex mandrel part we refer to figures 7.1, 7.8 and 7.9 (notice in figure 7.1 the rings at several  $z$ -values indicating the coefficient of friction with incremental steps of 0.1, starting at  $\mu = 0$  and ending at  $\mu = 1$ ).

### Error analysis

In the previous section we presented the simplified solution for the mandrel geometry. We assumed a constant winding angle  $\alpha = \pi/2 - \epsilon$ , where  $\epsilon \in [0, 0.1]$  [rad]. The final shape is designed with  $\epsilon = 0$  [rad]. In reality however, the winding angle is equal to:

$$\alpha(\rho) = \arctan\left(\frac{2\pi\rho}{b}\right) \quad (7.10)$$

## Part B: Reinforcing layer architecture

where  $b$  is the width of the tested fibre bundle. Substitution of equation (7.10) into equations (7.4) and (7.5) results in:

$$\mu(\rho) = -\frac{k_g(\rho)}{k_n(\rho)} = -\frac{4\pi[b^2 + 2\pi^2\rho^2][1 + z'^2(\rho)]}{\sqrt{1 + \frac{4\pi^2\rho^2}{b^2}\{4\pi^2b\rho[z'(\rho) + z'^3(\rho)] + b^3z''(\rho)\}}} \quad (7.11)$$

To obtain the real friction values  $\mu_r(\rho)$ , we substitute equation (7.8) into (7.11). The result is:

$$\begin{aligned} \mu_r(\rho) = & \left( \frac{2\pi(b^2 + 2\pi^2\rho^2)\cos\varepsilon[4(\rho - r)\cos\varepsilon - z_r(3 + \cos 2\varepsilon)]}{\sqrt{b^2 + 4\pi^2\rho^2}\{[b^2 + 8\pi^2(\rho - r)\rho]\cos\varepsilon - 2\pi^2z_r\rho(3 + \cos 2\varepsilon)\}} \right) \times \\ & \times \left( \frac{\sqrt{z_r[z_r + 2(r - \rho)\sec\varepsilon]}}{z_r} \right) = K(\rho, b, \varepsilon)\mu_m(\rho) \end{aligned} \quad (7.12)$$

The second term in equation (7.12) represents the measured friction  $\mu_m(\rho)$ . Consequently, the first term indicates the introduced measurement error. This term should be equal to 1, which is only valid for the case given by  $b = 0$  and  $\varepsilon = 0$ . Nevertheless, in the extreme case represented by  $b = 51$  [mm] and a test on a mandrel designed with  $\varepsilon = 0$ , the maximum difference between  $\mu_r$  and  $\mu_m$  becomes less than  $7 \times 10^{-3}$ .

In an attempt to further reduce the measurement error, we assume now that the realistic range of expected friction values is given by  $[\mu_{\min}, \mu_{\max}] = [0.05, 0.5]$  [ $\gamma 9$ ]. The corresponding  $\rho$ -values are  $[r_{\max}, r_{\min}] = [132.206, 103.125]$  [mm] (calculated with the aid of equation (7.9)). The measurement error is one-sided: the real friction is always slightly bigger than the measured one (although this difference should be considered negligible). For very accurate measurements, one can use a modified mandrel, based on a particular  $\varepsilon$ -value (equation (7.8)). This parameter  $\varepsilon_t$  depends on the fibre bundle width  $b$ , and is given by the solution of:

$$|K(r_{\min}, b, \varepsilon_t)| = |K(r_{\max}, b, \varepsilon_t)| \quad (7.13)$$

The parameter  $\varepsilon_t(b)$  is practically linearly proportional to  $b$ ; this is illustrated in figure 7.3:

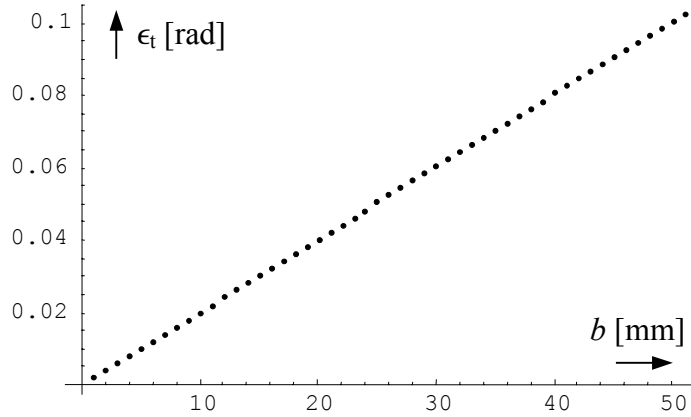


Fig. 7.3: The modified mandrel shape parameter  $\epsilon_t(b)$  as a function of the fibre bundle width

In the figure below, we provide an illustration of the error reduction achieved for a fibre bundle having a width equal to 51 [mm]:

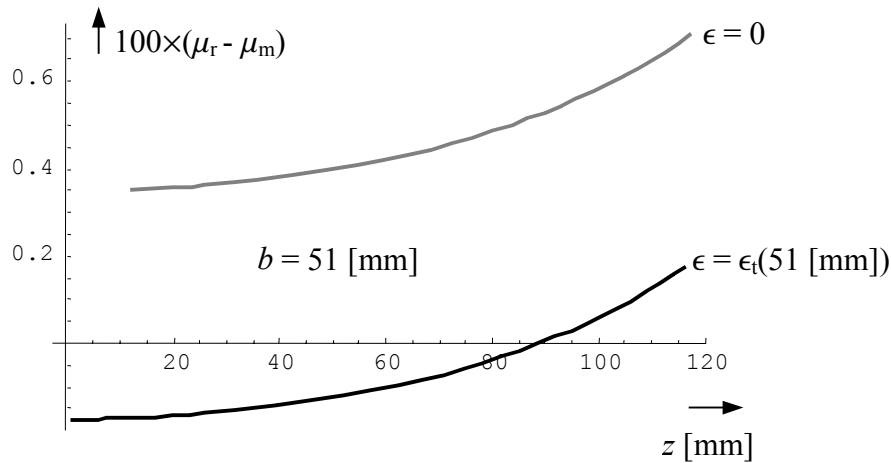


Fig. 7.4: Measurement error for the uncorrected mandrel shape (grey line) and the corrected one (black line)

Due to the significantly small error magnitude, the corresponding mandrel shapes show hardly any differences, see figure 7.5.

Summarising, the solution of the simplified ODE (equation (7.12)) provides a sufficiently accurate mandrel shape; the error remains always below  $7 \times 10^{-3}$  for  $b \in [1, 51]$  [mm]. Only in the case of requiring an absolute measurement error below 0.002, the mandrel shape should be designed according to equation (7.8) where  $\epsilon$  is given by the solution of (7.13) for a particular roving width  $b$ .

## Part B: Reinforcing layer architecture

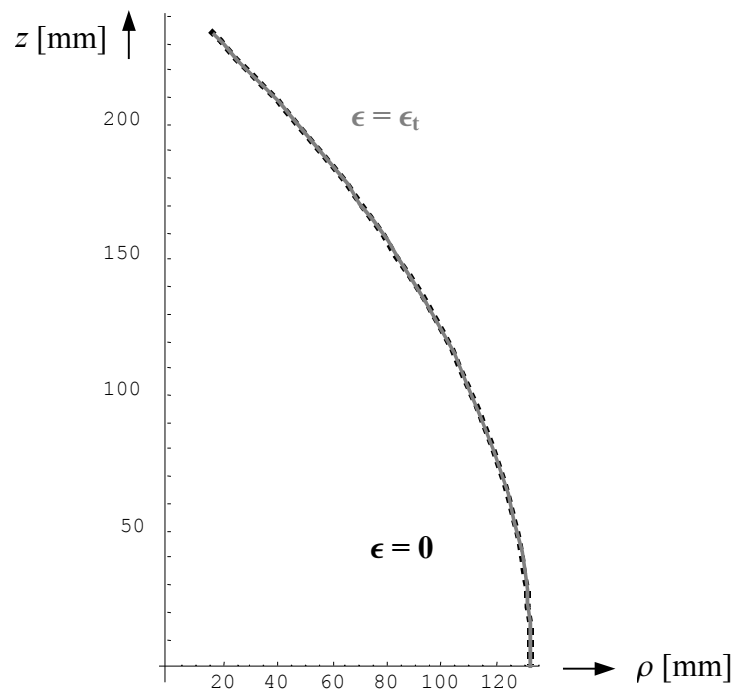


Fig. 7.5: Mandrel shapes corresponding with  $\epsilon = 0$  (black dashed line) and  $\epsilon = \epsilon_t$  (grey continuous line) for  $b = 51$  [mm]

## 7.2 Machine control

This section is associated with the determination of the required machine movements for the realisation of the friction experiments. After the description of the couplings between spindle rotation, carriage translation and feed eye inclination, we provide two equations ((7.14) and (7.16)) for relating the spindle rotation  $C$  to the translation of the feed eye carriage  $Z$ , and maintaining the fibre speed at a constant level. The time the roving needs to slip off can also serve as an alternative measuring parameter for the determination of the coefficient of friction.

### Movement couplings

Due to the special mandrel shape, the measured friction is practically linear to the  $z$ -coordinate. With the assumed constant winding angle, the carriage  $Z$  is directly coupled to the corresponding  $z$ -coordinate of the mandrel. During the experiments, the spindle rotates with a speed  $C'$  [rad/s]. The cross carriage  $X$  is set on a fixed value, sufficiently large to avoid collision between the mandrel and the feed eye. With the fibre bundle width denoted by  $b$ , the carriage  $Z$  position becomes:

$$Z = \left( \frac{b}{2\pi} \right) C \quad (7.14)$$

The feed eye inclination  $A$  (figure 11.2) must ensure a tangential placement of the tow on the rotating mandrel:

$$A = \arctan\left(\frac{d\rho}{dz}\right) = \arctan\left(\frac{1}{z'(\rho)}\right) \quad (7.15)$$

The horizontal feed eye inclination is given by  $A = 0$  [rad]. According to equation (7.7) with  $\epsilon = 0$  and equations (7.14) and (7.15), we obtain:

$$A = \arctan[c_1 z(\rho)] = \arctan\left(\frac{z(\rho)}{z_r}\right) = \arctan\left(\frac{Z}{z_r}\right) = \arctan\left(\frac{bC}{2\pi z_r}\right) \quad (7.16)$$

The required machine movements are simple and can easily be programmed in a spreadsheet. The resulting data can then be imported as a text file into the CNC controller [ $\alpha 3, \alpha 14, \alpha 19, \alpha 20, \alpha 31$ ]. A great advantage provided by the introduced mandrel shape is that the corresponding machine movements can easily be determined without the aid of expensive filament winding simulation programs.

## Part B: Reinforcing layer architecture

### Fibre speed

Application of a constant rotational speed for the spindle will result in a slight decrease of the consumed fibre speed  $S'$  [mm/s], when proceeding from the maximum radius ( $\mu = 0$ ) to the radius corresponding with the measured coefficient of friction  $\mu_m$ . The maximum value for the coefficient of friction is usually below  $\mu = 0.5$ . At this point, the relative consumed fibre speed reduction is equal to  $-21.5\%$ . The question arising now is how to vary the spindle rotation speed as a function of the feed eye position (note that  $C'$  and  $Z'$  remain coupled to each other according to equation (7.14)) to ensure constant fibre speed. From equation (7.9) we obtain:

$$\rho(\mu) = \frac{z_r}{2} \cos \varepsilon (1 - \mu^2) + r \quad (7.17)$$

Due to the linearity between  $\mu$  and  $z$ , (or  $Z$ ), the parameter  $\mu$  can be treated as the dimensionless carriage coordinate  $\zeta$  ( $= Z / z_r$ ) proceeding from 0 to 1. The aimed constant consumed fibre speed is denoted by  $S'(t)$ . With the relation  $S'(t) = \rho(\mu)C'(t)$ , the required  $C'(\zeta)$  profile in [rpm] is given by (note that  $r$  and  $z_r$  are given in [mm]):

$$C'(\zeta) = \frac{30 S'(t)}{\pi \rho(\zeta)} \quad [rpm] \quad (7.18)$$

An alternative formulation for  $C'$  is to use discrete  $\zeta$ -values given by  $i\Delta Z/z_r$ . The  $C'(\zeta)$  profile for  $r = 15$  [mm] and  $z_r = 235$  [mm] and  $S'(t) = 500$  [mm]/s is given below:

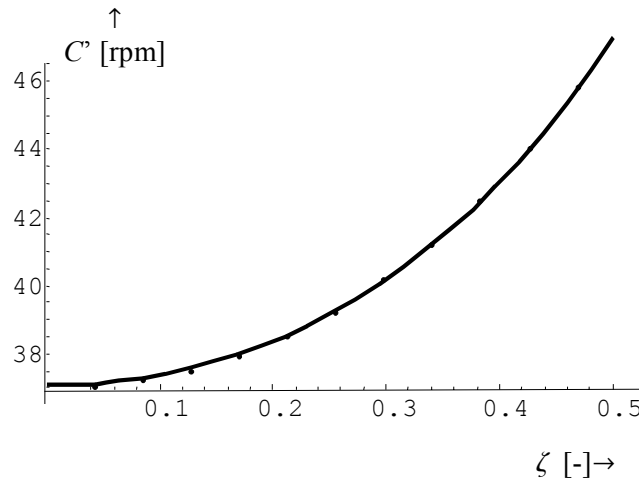


Fig. 7.6: Spindle speed profile as a function of the dimensionless carriage

The set of CNC control data is based on a constant  $\Delta Z$  increment. The corresponding  $\Delta C$  increment is given by equation (7.14). With the dimensionless cumulative value for  $Z$  ( $= i\Delta Z / z_r$ ) and equation (7.18), the

required rotational speed  $C'$  for every increment can be determined. The corresponding feed eye inclination is given by equation (7.16).

An alternative roving speed control strategy can be derived from the proper determination of the corresponding time increments as a function of  $\zeta$  (some controllers may require such an input format). With a constant fibre speed  $S'$ , and a roving width  $b$ , the time increment to complete the  $i$ -th circuit is given by:

$$\Delta t(i) = \frac{2\pi\rho(i \frac{b}{z_r})}{S'} \quad (7.19)$$

The required time for reaching the  $n^{\text{th}}$  circuit corresponding to the measured coefficient of friction, is:

$$t(b, \mu_m) \approx \sum_{i=0}^n \frac{2\pi\rho(i \frac{b}{z_r})}{S'} \quad \text{with} \quad n = \text{IP}\left(\frac{\mu_m z_r}{b}\right) \quad (7.20)$$

where “IP” denotes the extraction of the maximum integer number, contained in the argument. We assume the maximum expectable coefficient of friction as equal to 0.5. The dimensionless carriage  $\zeta$  will run from 0 to 0.5. For a simple approximation (for example to be used in spreadsheets) of the time as a function of  $\zeta$ , one may proceed to the elaboration of equation (7.20). The discrete character of equation (7.20) provides a non-zero time value for the initial parameter  $i = 0$ , so a correction has to be added. The result is:

$$t_{appr}(b, \zeta) = -\frac{\pi(b + z_r \zeta)[b\zeta + 2z_r(\zeta^2 - 3) - 12r]}{6bS'} - \frac{\pi(2r + z_r)}{S'}(1 - \zeta^{a(b)})$$

$$\text{where} \begin{cases} b < 10 \text{ [mm]} : a = 1 \\ b > 10 \text{ [mm]} : a = b/10 \end{cases} \quad (7.21)$$

The exact value for the time required to reach  $\zeta$  is given by [y11]:

$$t_{exact}(b, \zeta) = \frac{1}{S'} \int_{l=\rho(\zeta)}^{l=r_{\max}} \frac{\sqrt{1 + z'^2(l)}}{\cos \alpha(b, l)} dl \quad (7.22)$$

where  $\alpha(b, l)$  is presented in equation (7.10). The implementation of this integral however, involves rather complicated evaluations. In figure 7.7 we provide the relative error generated by equation (7.21) when compared to the exact solution (7.22):

## Part B: Reinforcing layer architecture

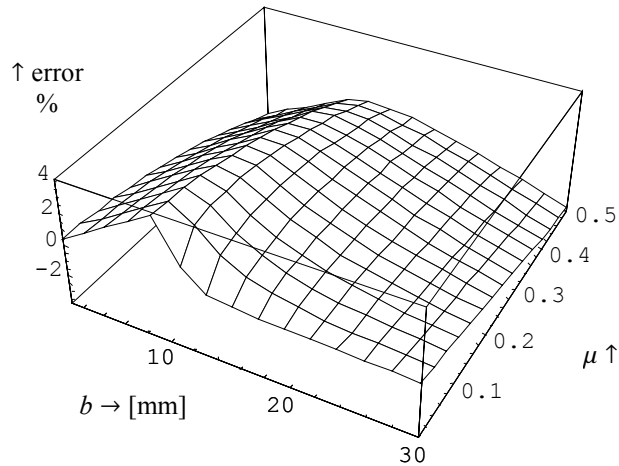


Fig. 7.7: Relative error of the approximated experiment time versus the exact one for the expected range of coefficients of friction

For typical filament winding applications with roving width and friction ranges corresponding to  $b = [5, 30]$  [mm] and  $\mu = [0.1, 0.5]$  respectively, the error remains below 3%. For a certain  $\zeta$  (or  $Z / z_r$ ) value, under the restriction of a practically constant fibre speed (within a deviation of  $\pm 3\%$ ), the required time increments can be obtained by equation (7.21). As indicated in the previous section, the time from the beginning of the experiment until slippage of the roving can be translated into the corresponding  $\zeta$ -coordinate (which can directly be interpreted as the measured coefficient of friction). For this translation however, we should take into account that the application of equation (7.21) may introduce an error of (maximally) 3%. Consequently, it is preferable to use equation (7.22) for that purpose.

## 7.3 Experiments

### Apparatus

For the acquisition of the coefficients of friction that are related to various winding process parameter combinations, we use here the specially designed mandrel as outlined in section 7.1 and depicted in figures 7.1 and 7.2. Due to the implemented meridian profile, the coefficient of friction is linearly proportional to the carriage position  $Z$ . The left side of the mandrel is characterised by  $\{\rho, Z\} = \{132.5, 0\}$  [mm] and  $\mu = 0$ . The curved mandrel part ends at  $\{\rho, Z\} = \{15, 235\}$  [mm] and  $\mu = 1$ . The aluminum mandrel surface is polished. The mandrel is attached on a CNC-controlled lathe-configured filament-winding machine (figure 7.8):

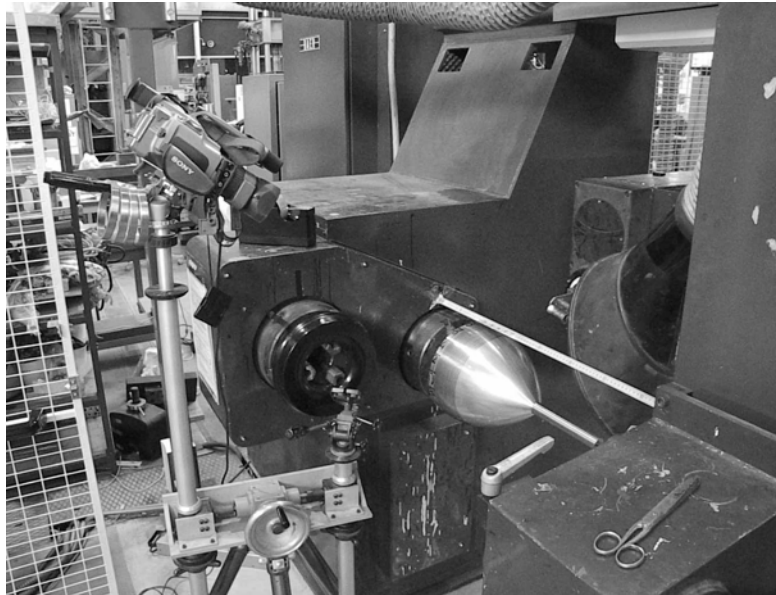


*Fig. 7.8: The complete test set-up, including video camera and suction unit*

To determine the point where slipping starts, we have used a video camera with high shutter speed (600), see figures 7.8 and 7.9. The mandrel is utilised with a fixed benchmark indicating the carriage position  $Z$  (marking: 5 [mm]). In addition, a second benchmark on the mandrel indicates its rotational position with a marking of  $20^\circ$  (figure 7.9). A carriage stroke equal to the roving width  $b$  corresponds with a spindle rotation of  $360^\circ$ . Hence, a  $20^\circ$ -propagation on the angular benchmark corresponds with a carriage stroke equal to  $b / 18$ .

## Part B: Reinforcing layer architecture

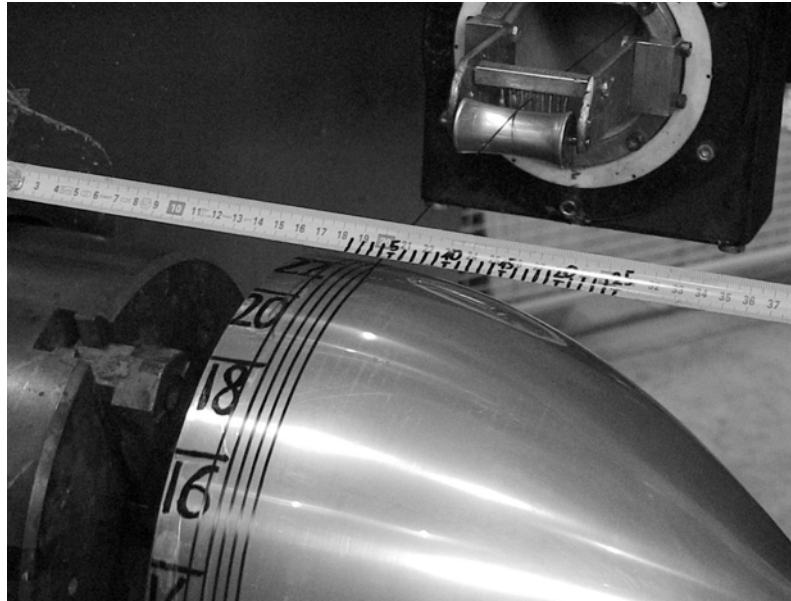


Fig. 7.9: The mandrel with benchmarks for the feed eye carriage translation  $Z$  and the spindle rotation  $C$

At a certain point, the tow will start slipping on the mandrel; this point provides the initial value for the coefficient of friction to be measured. This phenomenon is followed by a complete separation of the tow from the mandrel surface. This separation is referred to as “catastrophic slipping” [γ17].

### Measurement error estimation

The high shutter speed camera provides sufficient accuracy for the determination of the slippage point. However, the judgement of whether slipping occurs is rather subjective. We assume here that the observer of the experiment is able to provide this judgement within an accuracy of 50% on the angular benchmark, placed on the mandrel. This uncertainty corresponds with  $10^\circ$  on the benchmark, thus  $1/36$  of the roving width. An additional error is introduced by the shape of the mandrel; as explained in section 7.1, the linearity error is maximally 0.7%. The maximum expected value for the measured coefficient of friction is 0.5. This value, in combination with the shape inaccuracy, leads to an absolute error of  $\Delta\mu = 0.0035$ . Furthermore, the mandrel is manufactured with an accuracy of  $\pm 0.01$  [mm]. The influence of this tolerance on the measurements however, can be neglected. At the beginning of the experiment, the carriage position must be referenced. For this procedure we assume a tolerance  $\Delta Z_0$  of  $\pm 1$  [mm]. Hence, the total absolute error becomes:

$$E_{abs}(b) = \left( \frac{\Delta Z_0}{z_r} + \Delta\mu \right) + \frac{b}{36z_r} \quad (7.23)$$

With  $z_r = 235$  [mm], the result is depicted below (figure 7.10):

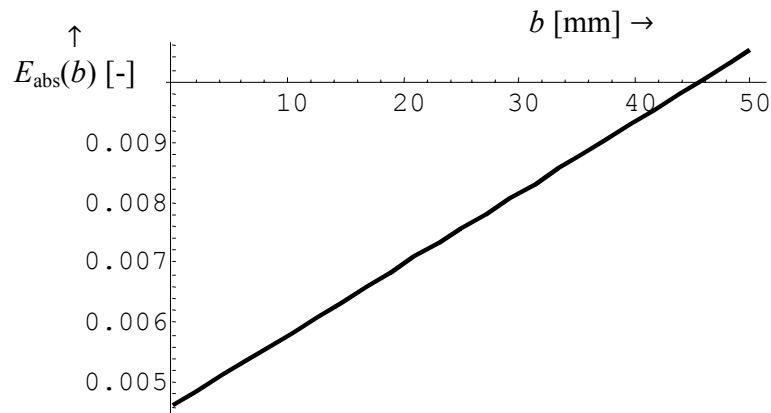


Fig. 7.10: *Estimated absolute error for the measured coefficient of friction as a function of the roving width*

### Performed series

Several winding parameters can possibly influence the available friction between placed roving and mandrel. Although some of these parameters are not expected to have substantial impact on the measured coefficients of friction, we include them here to cover the complete set of typical filament winding process parameters. The investigated series are based on the following variables:

- Winding speed (spindle rotation: 3.6, 12 and 60 [rpm])
- Fibre tension (narrow rovings: 1-5 [N], broad rovings: 5-15 [N])
- Roving morphology: width {0.5, 1, 1.5, 2, 3} [mm] and twisted / untwisted yarns
- Fibre materials (Glass, Carbon)
- Wet / dry winding
- Surface roughness of the mandrel

The expected values for the coefficients of friction lay in the range [0.1, 0.5]. In regard to the roving speed, we apply here for the experiments a constant value for the rotational speed of the spindle  $C'$ . As outlined in section 7.2, when proceeding with the roving towards higher  $Z$ -values, a roving speed reduction is expected. The roving speed values are given in table 7.2:

## Part B: Reinforcing layer architecture

Coefficient of friction	Carriage $Z$ [mm]	Mandrel radius $\rho$ [mm]	Fibre speed [m/s] at $C' = 3.6$ [rpm]	Fibre speed [m/s] at $C' = 12$ [rpm]	Fibre speed [m/s] at $C' = 60$ [rpm]
0.1	23.5	131.32	0.0495	0.165	0.825
0.2	47.0	127.800	0.0482	0.161	0.803
0.3	70.5	121.925	0.0460	0.153	0.766
0.4	94.0	113.700	0.0429	0.143	0.714
0.5	117.5	103.125	0.0389	0.130	0.648

Table 7.2: Expected friction values and their corresponding roving speeds for various  $C'$ -values

## **7.4 Results & discussion**

For every parameter combination (winding speed, tension etc.) we carried out three experiments. The provided results show the calculated mean values. The results are presented per examined parameter. In order to isolate a parameter, e.g. speed, we calculated the average friction value of the complete set of experiments for a certain winding speed. The influence of e.g. the winding speed on the resulting friction however, may strongly be affected by the fibre tension or mandrel surface quality. Consequently, the results per examined parameter provide only a general idea about the effect that an input parameter can have on the final result.

### **Winding speed**

The tests corresponding to the winding speed-related series have been carried out with  $C=\{3.6, 12, 60\}$  [rpm] (when an absolutely constant fibre speed is desired, the rotational speed of the spindle must be varied according to the corresponding radii (section 7.2)). The obtained friction values for catastrophic slipping are practically the same as the values for initial slippage of the fibres. The mean standard deviations are in the order of [0.01, 0.02]. The averaged result of the experiments clearly indicates that the influence of the winding speed on the measured friction is generally negligible and remains in the order of [0, 0.02]; this observation is valid for both dry and wet winding. In conclusion, the influence of the winding speed on the friction between tow and mandrel is negligible.

### **Roving tension**

Depending on the dimensions of the examined fibre bundles, the tension has been limited in several cases for avoiding tow failure. As observed by the winding speed series, catastrophic slipping occurs at practically the same place as the initial slippage. The differences between the obtained experimental data are negligible (in the order of 0.015). The standard deviation is in the order of [0.014, 0.018]. From these series we can conclude that the roving tension does not noticeably affect the obtained friction values.

## Part B: Reinforcing layer architecture

### Fibre materials

To ensure the usability of the generated results, we selected some typical Carbon and Glass fibres. The carbon rovings are summarised in table 7.3:

Manufacturer	Torayca	Soficar Torayca	Soficar Torayca
Type	T300	T300	T300
Twisted / untwisted	Twisted	Untwisted	Untwisted
Nr of filaments	1,000	3,000	6,000
Lot-nr	080045	F113013	F110083
Approx. width	0.5 [mm]	1.5 [mm]	2.5 [mm]

Table 7.3: The examined Carbon fibre bundles

The examined Glass fibre bundles are given in table 7.4:

Manufacturer	PPG Fibre Glass	PPG Fibre Glass	PPG Fibre Glass	Vetrotex	Scott Bader
Type / Lot	ECDE 75 1/0 0.7Z 610	ECDE 150 1/0 1.0Z 631	611 EC 11 136 Z20	EC-13-136 TD22 V379	320 Tex. Roving
Twisted / untwisted	Twisted	Twisted	Twisted	Untwisted	Untwisted
Approx. width	0.3 [mm]	0.5 [mm]	1 [mm]	1-1.5 [mm]	2-3 [mm]

Table 7.4: The examined Glass fibre bundles

To isolate the influence of the fibre material on the coefficient of friction, the experimental series have been limited to dry fibre bundles. The results indicate that the difference between Carbon fibres and Glass fibres is negligible (in the order of 0.003). The standard deviation remains in the order of [0.008, 0.01] and the obtained values belong to the [0.178, 0.181]-range. However, Di Vita et al. [2] obtained  $0.1 \leq \mu_{\text{carbon}} \leq 0.125$  and  $0.275 \leq \mu_{\text{glass}} \leq 0.3$ , which is a significant difference. Since the cited experimental study is comparable with the method presented here, the difference is probably caused by the surface treatment of the fibres used here or the surface quality of the involved mandrel.

### Roving morphology

The fibre bundle width and the characterisation twisted / untwisted are closely related to each other. In the tests performed here, the rovings having a width from 0.3 to 1 [mm] are twisted, while the broader ones are untwisted. The results for slipping start are presented in figure 7.11. The depicted results do not include the case of wet winding, since this is expected to flatten out the influence of the roving width on the measured coefficient of friction.

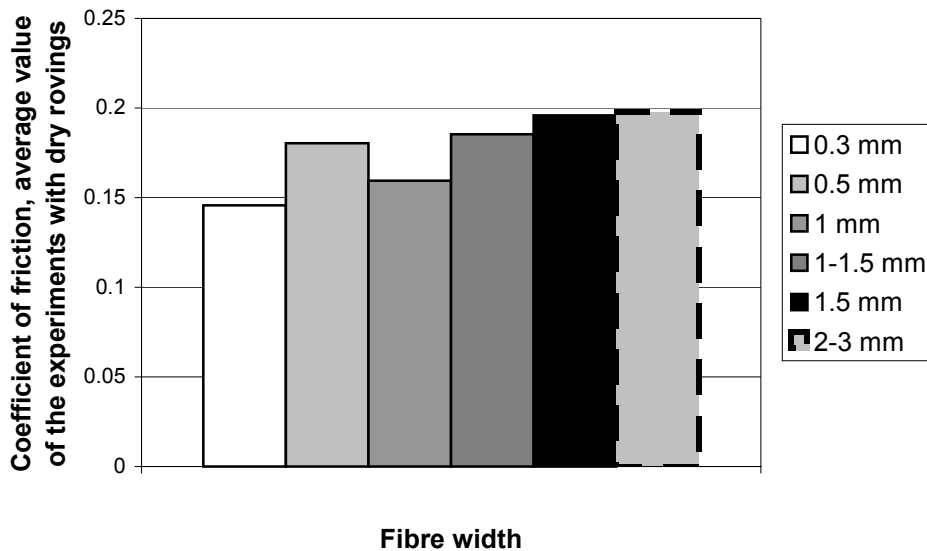


Fig. 7.11: Averaged influences of the roving width on the measured coefficients of friction at slipping start (polished surface)

The depicted results indicate that an increased roving width tends to raise the coefficient of friction. A possible explanation for this phenomenon is outlined in section 7.1, formulated in equation (7.12) and indirectly depicted in figure 7.4. Nevertheless, the results generated by equation (7.12) are too small for explaining the measured differences. Consequently, the tendency towards higher friction values can probably be explained by an increased interaction between the yarns. Since every yarn is subjected to a different normal curvature across the roving width, interference between them is very likely to occur; the broader the tape, the bigger the total velocity difference between the inner and outer yarns. This scenario however, has not been verified. Furthermore, the mean standard deviation for the presented values remains in the range [0.01, 0.02].

### Wet vs. dry winding

For the performance of the wet winding experiments, the mandrel has been covered with epoxy resin of the type VE 2908 KA/VE 4908 KB, manufactured by Bakelite AG. The potlife is 5-6 hours. It is believed that this mandrel coverage has resulted in an acceptable simulation of winding with impregnated fibres. As a result of the tests performed here, the obtained coefficients of friction did not show any time dependency. Consequently, it is assumed that the resin viscosity has no considerable impact on the coefficient of friction, at least in this particular case. The results are depicted in figure 7.12:

## Part B: Reinforcing layer architecture

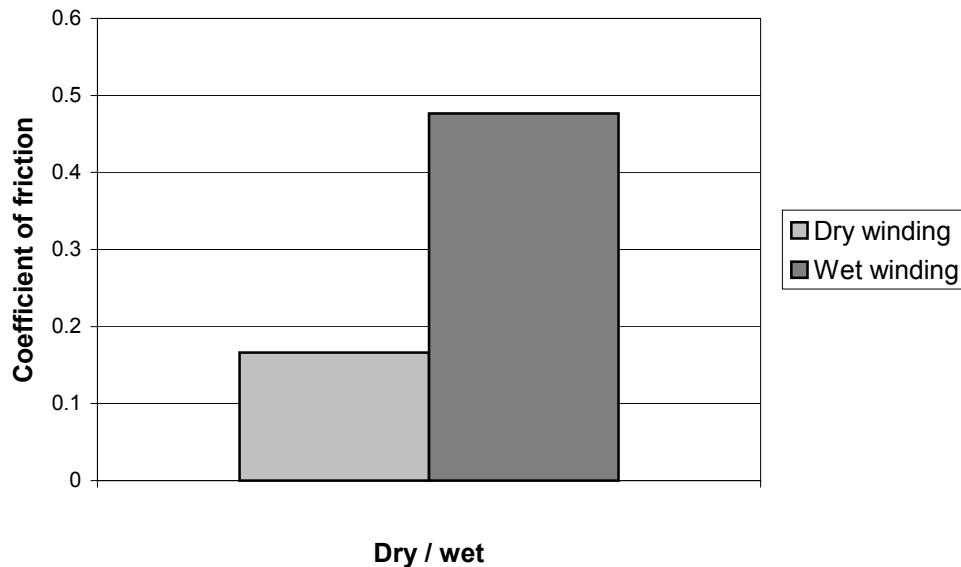


Fig. 7.12: Dry winding vs. wet winding (averaged results)

The tests have been performed on the polished surface of the aluminum mandrel. The comparison between dry and wet winding reflects on identical {winding speed / tension / roving dimensions / fibre materials} sets. In general, we can conclude that the coefficients of friction for wet fibres are approximately three times as high as for dry fibres. The values for catastrophic slipping are even (slightly) higher. Nevertheless, the observed differences between slip initiation and roving separation are rather small. The standard deviation for the presented results is within the order of 0.006 for dry winding and 0.03 for wet winding.

The results obtained here do not completely agree with [γ21] reporting  $0.24 \leq \mu_{\text{dry}} \leq 0.39$  and  $0.29 \leq \mu_{\text{wet}} \leq 0.37$ . In addition, Lossie and Van Brussel [ζ24] report  $0.2 \leq \mu_{\text{wet}} \leq 0.34$  while Scholliers and Van Brussel [γ18] report  $0.2 \leq \mu_{\text{wet}} \leq 0.4$ . Furthermore, Park et al. [ζ13] (who is referring to [γ18]) report  $\mu_{\text{wet}} = 0.2$  and  $\mu_{\text{dry}} = 0.39$ . In conclusion, the determination of whether dry or wet winding will provide elevated values for the coefficient of friction, is probably dependent on more parameters like the quality, potlife and manufacturer of the resin, mandrel surface quality, fibre materials etc. Perhaps standardisation of friction tests would provide more reliable data.

### Mandrel surface

The surface quality of the mandrel is obviously a parameter having great impact on the measured coefficients of friction. In the experiments performed here, we examined three characteristic surfaces: polished aluminum, mandrel smoothly covered with a dry epoxy layer (Araldite LY 5052 / HY 5052) and roughened epoxy layer (achieved by a sandpaper with grain size 120). The obtained results are depicted in figure 7.13:

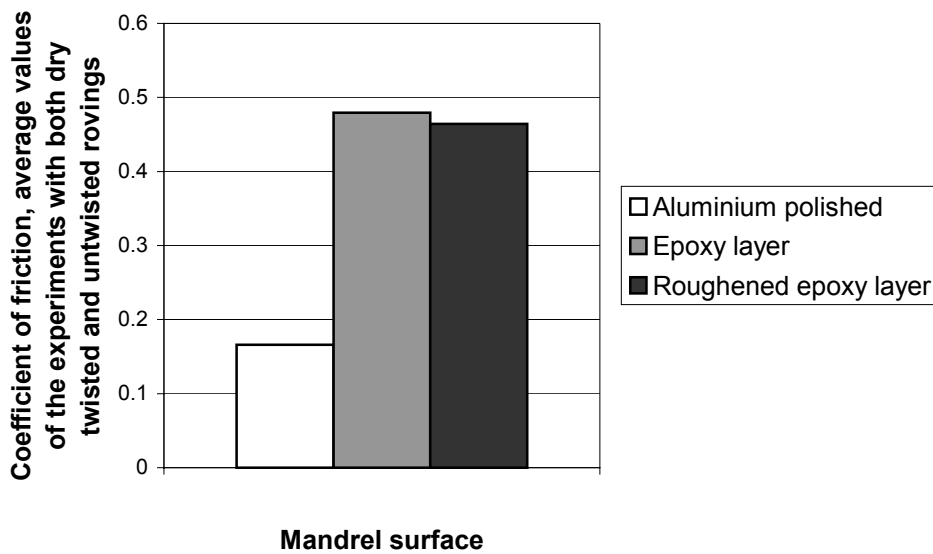


Fig. 7.13: Measured coefficients of friction for various mandrel surface qualities (roughness)

As expected, the epoxy layers provide considerably higher friction values. A remarkable aspect presented in the figure is that the averaged difference between the smooth and roughened epoxy surface data is very small. As observed from the comparison between wet and dry winding, the friction becomes for both epoxy layers approximately three times higher. The related standard deviations remain in the order of [0.008, 0.03].

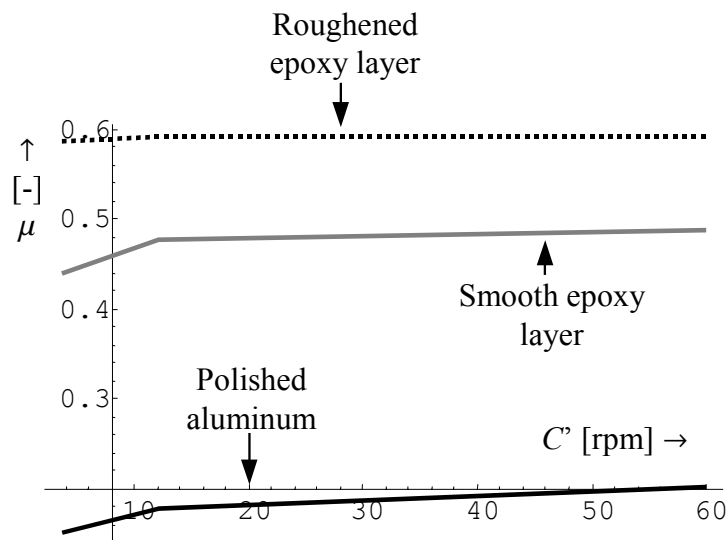


Fig. 7.14: Measured friction for various mandrel surface qualities (dry untwisted carbon roving with  $b = 1.5$  [mm])

## Part B: Reinforcing layer architecture

A more reliable way to depict the data should involve the presentation of the measured coefficients of friction as a function of the average surface roughness ( $R_a$ ). This representation format however, does still not provide reliable conclusions. An important parameter influencing the sensitivity of the friction for the surface roughness is the roving morphology. In figure 7.14 we provide the average friction values for the untwisted carbon fibre roving T300 with 3000 filaments and a total width of 1.5 [mm].

As expected, the measured friction values increase with the mandrel surface roughness. For a twisted fibre bundle however, this statement might not be realistic. In figure 7.15 we present the surface roughness response of a twisted Glass fibre bundle (ECDE 75,  $b = 0.3$  [mm]):

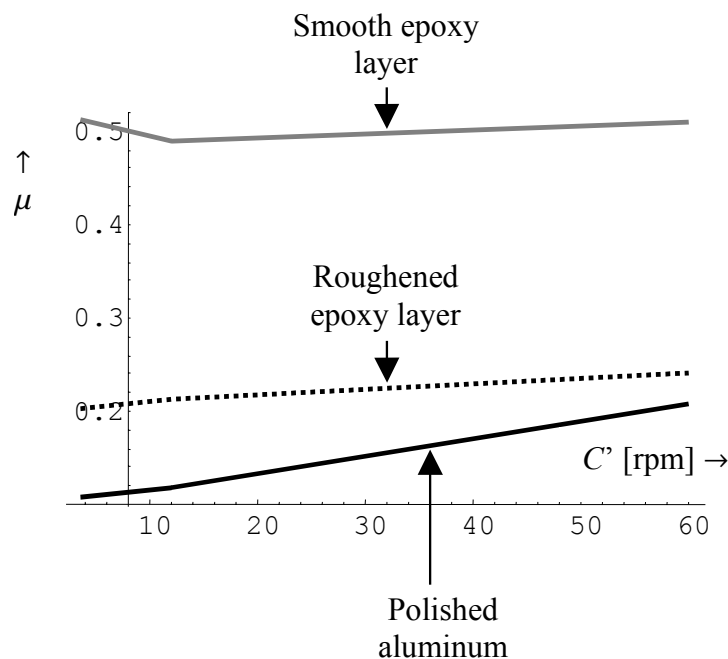


Fig. 7.15: Measured friction for various mandrel surface qualities (dry twisted glass roving with  $b = 0.3$  [mm])

The value for the coefficient of friction corresponding to the smooth epoxy layer is considerably higher than the original one (polished aluminium). On the roughened epoxy layer however, the friction drops significantly. This can possibly be explained by rolling of the roving over the surface instead of slipping. Nevertheless, this statement has to further be examined. The combination of friction values related to both sliding and rolling results in the small differences (smooth epoxy vs. roughened epoxy) depicted in figure 7.13, where we present the averaged results for both twisted and untwisted yarns.

## **7.5 CONCLUDING REMARKS**

In this chapter we have presented an extensive treatment of friction experiments for filament winding applications. The main objective here has been the description of the method and presentation of the results related to experiments for the determination of the coefficient of friction, situated between the mandrel and the applied roving. The involved mandrel surface is specially designed for providing a linear relation between the measured coefficient of friction and the feed eye carriage translation of the winding machine. The roving slippage point has been located with the aid of a high shutter speed video camera. The performed experiments correspond to various filament winding process-related parameters like fibre speed, roving tension, roving dimensions and materials, wet vs. dry winding, and surface quality of the mandrel.

The advantages provided by the implementation of the proposed mandrel geometry on a filament-winding machine are:

- Realistic simulation of the fibre behaviour during filament winding processes
- Facilitated determination of the coefficient of friction (optical or by means of a chronometer)
- Improved stability and accuracy for the measurements (due to the linearly proportional relation between the coefficient of friction and the carriage translation)
- Simple machine control (suitable for spreadsheet programming)

The most important property of the proposed method is that the linearity (carriage vs. expected coefficient of friction) ensured by the mandrel shape makes a low cost experimental friction determination procedure feasible, without the need of advanced filament winding simulation programs. The complete set of errors generated by simplifications in the mandrel geometry and machine control remains considerably small. The costs for performing the friction experiments are rather low; this is mainly caused by the general applicability and reusability of the mandrel.

The measurements clearly indicate that the most important parameters influencing the coefficient of friction are the surface quality, fibre bundle morphology (twisted / untwisted) and the eventual fibre impregnation. The influence of the winding speed, roving tension and fibre bundle materials can be considered as negligible. The effect of surface quality on the resulting friction is significant; the coefficient of friction tends to increase with increasing surface roughness. For rather rough surfaces however, the resulting coefficient of friction depends strongly on the fibre bundle morphology: broad untwisted rovings tend to slide, while the twisted bundles prefer to roll over the surface.

## Part B: Reinforcing layer architecture

An unexpected observation is that the coefficient of friction for impregnated fibres is clearly higher than for dry fibres. These observations do not completely agree with previously reported results [2,18,23,24]. Nevertheless, it is believed that these discrepancies are probably caused by differences in the surface quality of the mandrel, the surface treatment of the involved fibres and / or the resin quality and potlife. This statement however, is rather subjective.

The results obtained here represent only general tendencies; for a more reliable determination of the available coefficient of friction, one should perform experiments with the specific winding parameter combinations that are expected to be applied at the production stage. For the design of non-geodesically wound objects however, we can provide the following rules (for a conservative estimation, one should subtract 0.05 from the presented values):

- Dry fibre bundles on a polished aluminium surface:  $\mu = 0.15$
- Dry fibre bundles on smooth dry epoxy surface:  $\mu = 0.5$
- Twisted dry fibre bundles on a roughened dry epoxy surface:  $\mu = 0.2$
- Untwisted dry fibre bundles on a roughened epoxy surface:  $\mu = 0.6$
- Impregnated fibre bundles on a polished aluminium surface:  $\mu = 0.4$

The standard deviation for every measured series is smaller than the estimated error; this property indicates that the measurements can generally be considered as reliable, without the presence of a systematic error.

It is strongly advisable to separately obtain friction data for thermoplastic composites, since their physiology is rather different when compared to rovings impregnated with thermoset matrix materials. At the same time, contrary to thermoset materials, the measured coefficient of friction might be strongly dependent on the viscosity of the matrix (hence, the temperature). Furthermore, we strongly recommend further experimental investigations, preferably with additional methods to clarify the coefficient differences reported by several authors.

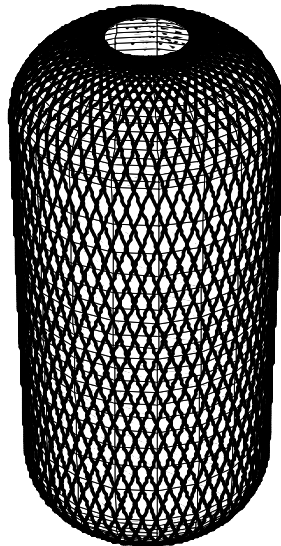
## 8

## Winding patterns &amp; fibre stacking

*The creation of a suitable winding pattern inevitably leads to a charming game with integer numbers formulated in the so-called first order Diophantine equation. With the roving dimensions and especially the roving width as a control parameter, we present here an algorithm for the automatic generation of suitable patterns, including the determination of the resulting fibre layer thickness distribution.*

*After the outline of the theory supporting the creation of winding patterns, we proceed to the construction of an algorithm for creating them (section 8.2). The subsequent section provides the tools for estimating and describing the resulting laminate thickness. The last section includes examples of both the usual pattern design strategies (from a range of applicable bandwidths to a pattern) as well as the reverse cases (how to distribute  $n$  bundles of prescribed dimensions with the least sacrifice of homogeneity).*

*An aspect of great importance included in this chapter is the demonstration of the fact that the decisions taken during the design stage might have a great impact on the quality of the resulting product, especially in terms of the resulting laminate coherence and thickness distribution.*



**Filament wound composite pressure vessel, where, in this case, the exclusive usage of geodesic trajectories automatically leads to a perfect coverage; this is achieved by a proper choice of the roving dimensions**

## **Part B: Reinforcing layer architecture**

## 8.1 Basic theory

### Requirements

We consider here a three-dimensional, rotationally symmetric body, subjected to filament winding. The body under consideration has two polar openings, which can occasionally be unequal to each other. An example of such a body is given in the figure below:

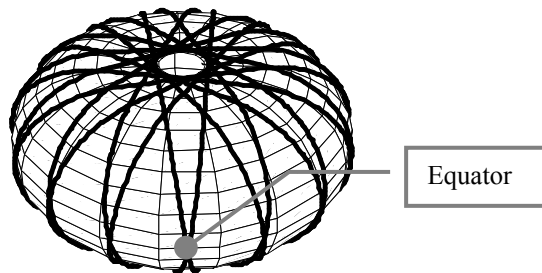


*Fig. 8.1: A typical filament wound body covered by one round of circuits*

An important property of the filament winding process is its repetitive character. Regardless of the eventual rotational symmetry of the body and the physiology of the applied circuits, a necessary condition for the creation of a winding pattern is the existence of repetition. In figure 8.1, the depicted body is covered by a certain number of circuits extending over the complete equatorial periphery of that body. The next round of circuits should be placed exactly adjacent to the first one. This process should be repeated until the periphery is fully covered with fibre bundles. In the case the mandrel has to be covered by e.g. two layers, the shift between two consequent rounds should preferably provide a 50% overlap of the fibre bundles at the equatorial periphery. In the case of four layers, this overlap should be 25% and so on. A suitable winding pattern is characterised by:

- Full and rotationally symmetric coverage
- Homogeneous thickness in circumferential (constant latitude) direction
- Roving overlap according to the desired number of fully completed layers

Assuming that we want to cover the body with one complete layer, this set of demands can be translated into a situation where an integer number  $n$  of fibre bundle widths is fitted in the equatorial periphery, exactly adjacent to each other. In the case of e.g. two layers ( $d = 2$ ), the number of widths fitted in the equator is equal to  $d \times n$ . The dimension of the fibre width at the equator (effective width) will obviously depend on the winding angle at that point (figures 8.1 and 8.2). With  $\alpha_{eq}$  denoting the winding angle at the equator, we obtain:

## Part B: Reinforcing layer architecture

$$b_{eff} = \frac{b}{\cos \alpha_{eq}} \quad (8.1)$$

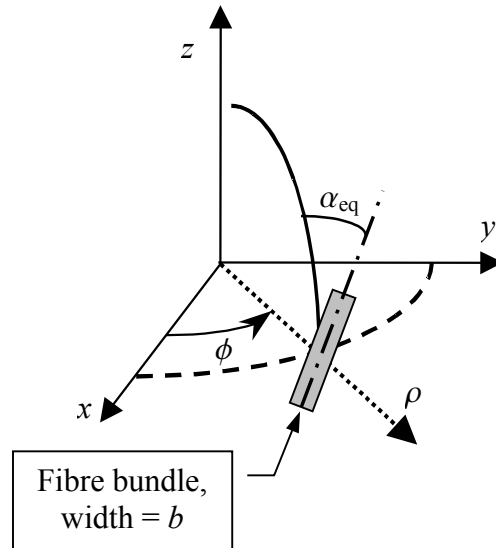


Fig. 8.2: Determination of the effective fibre width at the equator

The condition for full coverage is given by (the subscript “eq” denotes the equator):

$$n b_{eff} == 2\pi\rho_{eq} \quad (8.2)$$

### Roving dimensions

In most engineering applications, the meridian profile of the body is dictated by strength calculations (as demonstrated in chapters 3 and 4). By neglecting the thickness build-up of the wound layers, one may assume that this profile remains unchanged. An additional practical consideration is the fact that the applied fibre bundle has certain dimensions: a width  $b$  and a thickness  $\delta$ . These dimensions are usually neglected during the design process of the body, but have a significant influence on the resulting pattern; in fact, for geodesic fibre trajectories, the construction of a suitable winding pattern depends entirely on the fibre bundle dimensions. One should notice that this rule applies only in the case of having an exactly predetermined fibre path (for instance, entirely geodesic winding) or by implementing some prescribed slippage tendency distribution. Summarising, we assume here that there is no possibility to correct the pattern by alternating the fibre path geometry or by activating some additional turn-around at the polar areas.

To illustrate the influence of the fibre bundle dimensions on the resulting pattern, we assume here geodesic trajectories. This limitation however is not necessary, but greatly facilitates the required calculations. The body under consideration is defined in polar coordinates and includes two polar openings. We focus now on the upper pole of the body (figure 8.3) where a broad fibre bundle is placed (grey thick line).

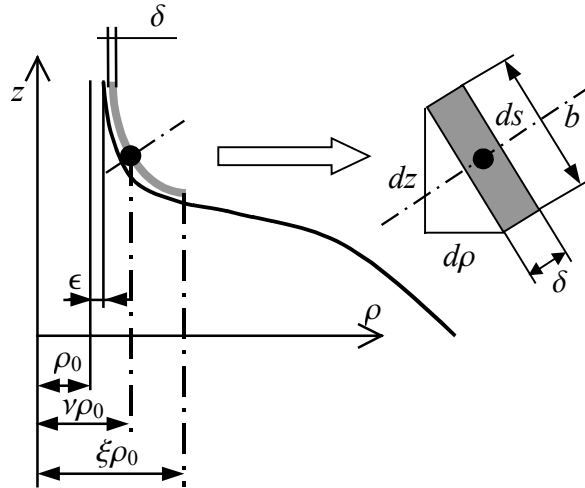


Fig. 8.3: Cross section of the applied fibre bundle at the polar area

The polar opening has a radius  $\rho_0$ . To ensure some flexibility for fitting the polar caps at the top and bottom of the vessel, the inner edge of the fibre bundle may optionally not be placed exactly tangential to the polar opening, but slightly away from it. We denote this eccentricity by  $\epsilon$ . On a way similar to chapter 3, the following dimensionless parameters are now introduced [β2,ζ21]:

$$B = \frac{b}{\rho_0}, \quad E = \frac{\epsilon}{\rho_0}, \quad \Delta = \frac{\delta}{\rho_0}, \quad Y = \frac{\rho}{\rho_0}, \quad Z = \frac{z}{\rho_0} \quad (8.3)$$

The length differentials presented in the right side of figure 8.3 are given by (equations (2.6) and (3.20), in dimensionless form):

$$\begin{aligned} dZ &= Z'(Y)dY \\ dY &= 1dY \\ dS(Y) &= \sqrt{1 + Z'^2(Y)}dY \end{aligned} \quad (8.4)$$

The parameter  $\nu$  represents the dimensionless distance between the centreline of the fibre bundle (black dot) and the axis of rotational symmetry; this can now be considered as the real polar radius of the wound body.

## Part B: Reinforcing layer architecture

From figure 8.3 and the presented differentials we can immediately determine the real polar radius  $\nu$  by solving (notice the negative sign of  $Z'(Y)$ ):

$$\nu = \left. \frac{\varepsilon + \left(\frac{d\rho}{ds}\right)\frac{b}{2} + \left(\frac{dz}{ds}\right)\frac{\delta}{2}}{\rho_0} \right|_{\rho=\nu\rho_0} = E + \left(\frac{1}{\sqrt{1+Z'^2(\nu)}}\right)\frac{B}{2} - \left(\frac{Z'(\nu)}{\sqrt{1+Z'^2(\nu)}}\right)\frac{\Delta}{2} \quad (8.5)$$

With this equation, the radial position of the fibre centreline  $\nu$  is completely determined by  $b$ ,  $\delta$  and  $\varepsilon$ . The linearised parameter  $\nu$  can be approximated as follows:

$$\nu = 1 + E + \nu_B B + \nu_\Delta \Delta \quad (8.6)$$

The effects of eccentricity and fibre bundle thickness can usually be neglected; this leads to:

$$\nu = 1 + \nu_B B \quad (8.7)$$

When applying a particular slippage tendency distribution (which may also be zero) along a complete circuit, the fibre path geometry becomes fully defined. Consequently, the winding pattern will fully depend on  $\nu$ . As an example, for geodesic fibre placement, the winding angle at the equator is given by (equation (5.12)):

$$\alpha_{eq} = \arcsin\left(\frac{\nu}{Y_{eq}}\right) \quad (8.8)$$

where  $Y_{eq}$  is the dimensionless equator radius of the body (as defined in equation (3.15)). Substitution of equation (8.8) into (8.1) and evaluation of (8.3) leads to:

$$B = \frac{2\pi}{d^2 n^2 + 4\pi^2} \left( -2\pi\nu_B + \sqrt{d^2 n^2 (Y_{eq}^2 - 1) + 4\pi^2 Y_{eq}^2 \nu_B^2} \right) \quad (8.9)$$

With this equation, we are able to define a set of suitable  $B$ -values resulting in a perfect occupation of the equatorial periphery, according to a predetermined number of layers.

### Turn-around angle

The next step consists of the calculation of the fibre trajectory along a complete winding. We denote the parallel angle at some point belonging to the wound circuit by  $\phi$  (figure 8.4).

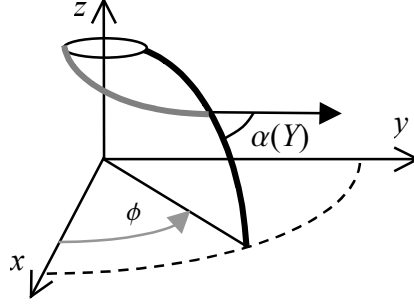


Fig. 8.4: Basic wound fibre geometry

With a given distribution (generally non-geodesic) of the winding angle as a function of the independent coordinate (in this case:  $Y$ ), the differential equation providing the fibre path description becomes:

$$\frac{\partial \phi(Y, \nu)}{\partial Y} = \frac{\sqrt{1 + Z'^2(Y)} \tan \alpha(Y, \nu)}{Y} \quad (8.10)$$

This result is derived from equation (6.31) by substituting the proper expressions for the coefficients of the first fundamental form, presented in section 2.1. The turn-around angle (the angular  $\phi$ -propagation corresponding to a complete wound circuit) is obtained by integrating (8.10) along a single circuit. As an example, we recall here equation (4.28) providing the turn-around angle for an arbitrary cylindrical-isotensoid pressure vessel ( $\Phi_{total}$ ). Furthermore, for an oblate spheroid covered by geodesic trajectories, the obtained  $\Phi_{total}$ -value is less than  $2\pi$  [rad]; the opposite applies on a prolate spheroid. To highlight these differences, we define:

$$\Delta K(\nu) = \text{mod}[\Phi(\nu)_{total} - 2\pi] \quad (8.11)$$

As previously stated, the angular propagation parameter depends completely on  $\nu$ . This expression however, can usually not be obtained by analytical methods. In [β4], the authors show that for a fairly small interval for  $b$ , the  $\Delta K(\nu)$  function is strongly linear, see figure 8.5:

**Part B: Reinforcing layer architecture**

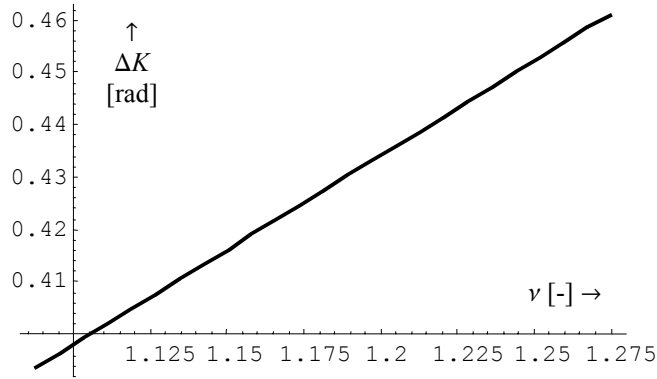


*Fig. 8.5: A typical graph of  $\Delta K$  [rad] as function of  $\nu$  [dimensionless] for an isotenoidal pressure vessel*

For the evaluation of a series of suitable fibre bundles, it is strongly recommended to construct such an approximation. This will greatly facilitate the associated winding pattern-determining calculations.

**Diophantine equations**

The construction of a suitable winding pattern may be expressed by the solution of the first order Diophantine equation  $[\beta_1, \beta_2, \beta_3, \beta_5, \mu, 15]$ . Before proceeding to the elaboration of these expressions, we present here the basic winding pattern terminology (figure 8.6):

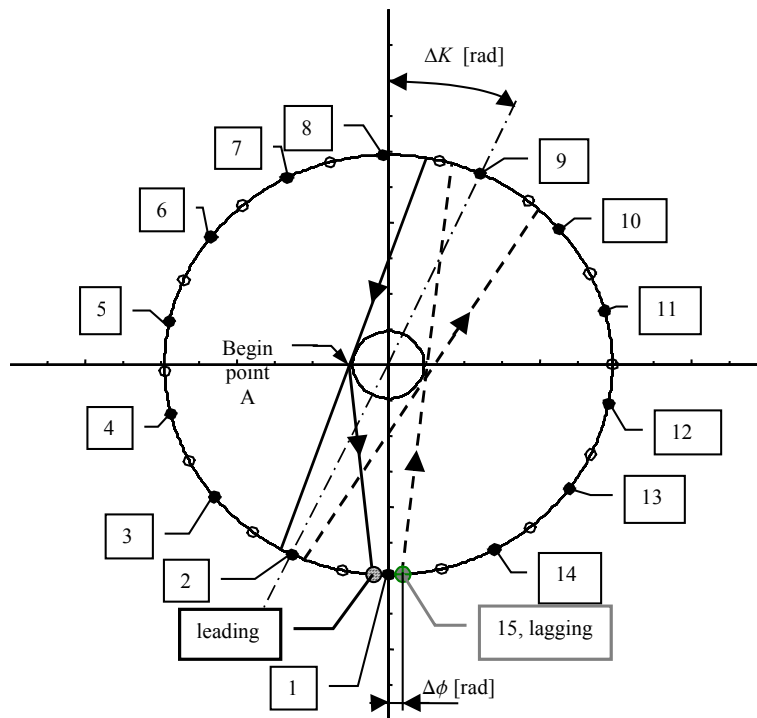


*Fig. 8.6: Winding pattern terminology*

## Part B: Reinforcing layer architecture

In the presented figure, we schematically depict the equator of a rotationally symmetric body, for instance covered with 15 circuits. The two first circuits are schematically indicated by straight lines. The continuous lines reflect on fibre trajectories placed on the upper surface of the body (say, north hemisphere) and the dotted lines denote the trajectories on the south hemisphere. In addition, the black dots indicate fibre passages from the upper polar surface to the lower one (north  $\rightarrow$  south); the opposite situation applies on the white dots. The wound object is divided into  $p$  angular partitions (in this case,  $p = 15$ ) of  $\Delta K$  [rad].

When the body is covered by a single complete layer ( $d = 1$ ), an integer number  $k$  of fibre bundles should fit in every partition  $\Delta K$ . In the case of e.g. two layers ( $d = 2$ ), this number should be  $2k$ . After completing  $p$  circuits, the fibre bundle may be placed before (leading) or after the first winding (lagging). In the example resented here, for  $d = 1$ , the placement of circuit nr. 15 should be exactly adjacent to the neighbouring circuit (nr. 1); for  $d = 2$  a 50% overlap is desirable; for  $d = 3$  we aim to construct an overlap of 33.3 % and so on. The total number of the fibre bundles fitting in the equatorial circumference of the body is indicated by  $n$ . To create a suitable pattern consisting of  $d$  layers, the following conditions must be satisfied [ $\beta_1, \beta_2, \beta_3, \beta_4$ ]:

$$\begin{aligned} (p+1)dk - dn &= 1 && \textit{leading pattern} \\ pdk - dn &= -1 && \textit{lagging pattern} \end{aligned} \tag{8.12}$$

where all participating products must be integer numbers. The obtained solution in terms of determining at least one unknown parameter is characterised by the absence of a common divisor for the involved integer quantities [ $\beta_1, \mu 15$ ]. This equation is also known as the first order Diophantine equation. Its fifth order variant leads to the famous Fermat's last theorem.

## 8.2 Pattern generating algorithm

### Input parameters

Since the construction of a suitable pattern is here assumed as exclusively dictated by  $\nu$ , we temporarily consider this scalar as an independent control parameter. Furthermore, we assume that the eccentricity value  $\epsilon$  and the fibre bundle thickness  $\delta$  are fixed (figure 8.3). Consequently, the control parameter  $\nu$  is exclusively associated with  $B$  (dimensionless fibre bundle width). On the equatorial circumference of the body under consideration, the fibre bundle occupies an arc corresponding to an angle  $\Delta\varphi$ . From equation (8.1), we obtain:

$$\Delta\varphi(\nu) = \frac{B(\nu)}{\cos \alpha(\nu)_{equator}} \quad (8.13)$$

This angle, together with  $\Delta K(\nu)$  (equation (8.11)), is completely determining the pattern parameters which are temporarily real numbers:

$$p(\nu) = \frac{2\pi}{\Delta K(\nu)}, \quad k(\nu) = \frac{\Delta K(\nu)}{\Delta\varphi(\nu)}, \quad n(\nu) = \frac{2\pi}{\Delta\varphi(\nu)} \quad (8.14)$$

A perfect pattern is achieved when, for a particular  $\nu$ -value, the Diophantine equations (8.12) become satisfied [β1,β5]. Except this requirement, the involved products should all be integers. Obviously, simultaneous satisfaction of these conditions is generally not possible. Consequently, a special strategy must be here developed, serving two aims: first to localise the potential solution intervals for  $\nu$ , and second to select the best solutions in terms of e.g. achieving a feasible pattern with minimised undesired fibre bundle overlap.

### Search strategy

Designers of filament wound products usually specify a range of acceptable fibre bundle thickness values,  $[B_{min}, B_{max}]$  [β2]. Assuming that the values for  $\epsilon$  and  $\delta$  are fixed, the design parameter  $\nu$  becomes exclusively dependent on  $B$ . Consequently, the corresponding range for  $\nu$  can now be specified:  $\{\nu_{min}, \nu_{max}\}$  (equation 8.5). This  $\nu$ -range leads to a practically linear  $\Delta K(\nu)$  relationship (equation (8.11) and figure 8.5). Although not guaranteed, the obtained  $\Delta K(\nu)$ -range in combination with the corresponding  $B$ -values should lead to a collection of acceptable winding patterns.

The existence of suitable winding patterns for  $\nu \in [\nu_{min}, \nu_{max}]$  is determined by equation (8.12). The pattern-related participating values  $p(\nu)$  and  $dk(\nu)$  should be integers; this is obtained by respectively taking the integer part (maximum integer, contained in the argument) of  $p(\nu)$ , and the ceiling

(smallest integer containing  $dk(v)$ ) of the second. The reason for this choice is the avoidance of gaps in the resulting wound layer; partial overlap of the fibre bundles at the equator is then allowed. The parameter  $dn(v)$  will temporary remain real (for reasons of demonstration). The existence of suitable winding patterns can then be investigated with:

$$\begin{aligned}
 \text{Leading:} \quad & C[dk(v)]\{IP[p(v)]+1\} \stackrel{?}{=} dn(v)+1 \\
 \text{Lagging:} \quad & C[dk(v)]IP[p(v)] \stackrel{?}{=} dn(v)-1
 \end{aligned}
 \tag{8.15}$$

where “C[#]” stands for ceiling and “IP[#]” for integer part. The symbol “ $\stackrel{?}{=}$ ” expresses the checking condition of whether the presented equality is satisfied. The criterions for the leading and lagging cases are depicted below (figures 8.7 and 8.8, respectively):

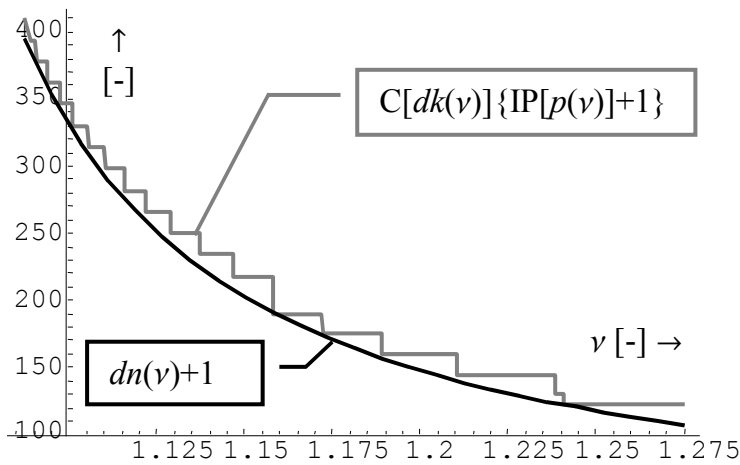


Fig. 8.7: The leading pattern criterion

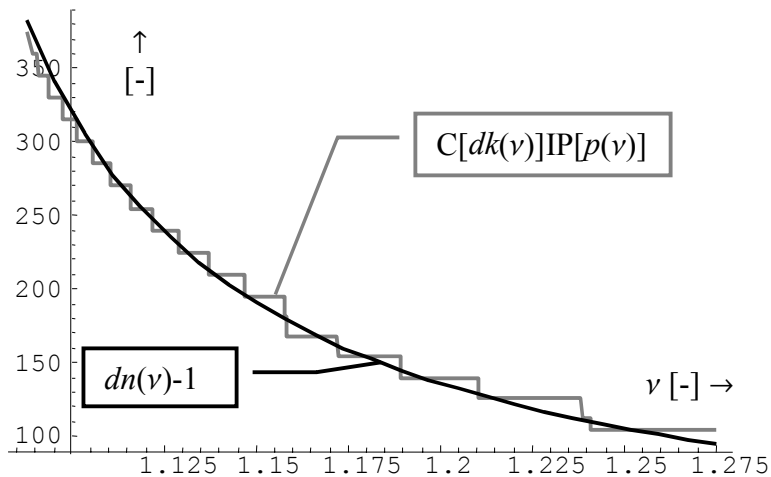


Fig. 8.8: The lagging pattern criterion

## Part B: Reinforcing layer architecture

For the given  $\nu$ -range, the possibilities to construct a proper winding pattern occur at the areas where the stepped lines cross the black continuous curve; at these points the conditions expressed in equation (8.15) become satisfied. The first step in the solution strategy is the localisation of the  $\nu$ -values providing integer numbers for  $p(\nu)$ ,  $k(\nu)$  and  $n(\nu)$ ; these are the points where the value of the stepped lines changes. We denote these values by respectively  $\nu_p(i)$ ,  $\nu_k(i)$  and  $\nu_n(i)$ . Together with the bounds  $[\nu_{\min}, \nu_{\max}]$ , the intervals that are possibly containing a solution are now defined. This is achieved by sorting the obtained values from smaller to bigger.

The second step of the strategy is the localisation of the intervals containing a possible winding pattern. Suppose an interval is given by  $[\nu_q, \nu_r]$ ; if for example at  $\nu = \nu_q$  the stepped line points a greater value than the curved line does, while at  $\nu = \nu_r$  the opposite situation occurs, then we can conclude that this interval is containing a possible winding pattern. In mathematical terms, the interval bounds should satisfy:

$$\begin{aligned} \text{Leading : } & \left\langle C[dk(\nu_q)]\{IP[p(\nu_q)]+1\} - [dn(\nu_q)+1] \right\rangle \times \\ & \times \left\langle C[dk(\nu_r)]\{IP[p(\nu_r)]+1\} - [dn(\nu_r)+1] \right\rangle < 0 \end{aligned} \quad (8.16)$$

$$\begin{aligned} \text{Lagging : } & \left\langle C[dk(\nu_q)]IP[p(\nu_q)] - [dn(\nu_q)-1] \right\rangle \times \\ & \times \left\langle C[dk(\nu_r)]IP[p(\nu_r)] - [dn(\nu_r)-1] \right\rangle < 0 \end{aligned}$$

Every interval satisfying condition (8.16) contains three integers; those satisfy the Diophantine equation automatically (for the assumed number of layers). We denote the leading solution by  $\{p^+, k^+, dn^+\}$  and the lagging one by  $\{p^-, k^-, dn^-\}$ . The corresponding required  $\Delta K$ -angles can then be found by (equations (8.11) and (8.12)):

$$\Delta K^+ = \frac{2\pi}{p^+ + 1} \left( 1 + \frac{1}{dn^+} \right), \quad \Delta K^- = \frac{2\pi}{p^-} \left( 1 - \frac{1}{dn^-} \right) \quad (8.17)$$

The exact values for  $\nu^+$  and  $\nu^-$  respectively can be determined by the solution of (equations (8.10) and (8.11)):

$$\Phi(\nu^+) - 2\pi = \Delta K^+, \quad \Phi(\nu^-) - 2\pi = \Delta K^- \quad (8.18)$$

In the general case, the solutions for  $\nu$  do not exactly correspond to an integer number of fibre bundles along the equatorial circumference. However, due to the proper truncation of  $p(\nu)$  and  $dk(\nu)$  (equation (8.15)) we obtain the warranty for having only a slight fibre bundle overlap. The exact values for  $\nu$  (leading:  $\nu^{b^+}$ , lagging:  $\nu^{b^-}$ ) that generate zero roving overlap are:

$$\frac{2\pi}{dn^+} = \frac{\Delta\phi(v^{b+})}{d}, \quad \frac{2\pi}{dn^-} = \frac{\Delta\phi(v^{b-})}{d} \quad (8.19)$$

The fibre overlap at the equator is accordingly given by [β2]:

$$\begin{aligned} \text{Leading} : \rho_0 & \left( \frac{B(v^+)}{\sqrt{1 - \left(\frac{v^+}{Y_{equator}}\right)^2}} - \frac{B(v^{b+})}{\sqrt{1 - \left(\frac{v^+}{Y_{equator}}\right)^2}} \right) \\ \text{Lagging} : \rho_0 & \left( \frac{B(v^-)}{\sqrt{1 - \left(\frac{v^-}{Y_{equator}}\right)^2}} - \frac{B(v^{b-})}{\sqrt{1 - \left(\frac{v^-}{Y_{equator}}\right)^2}} \right) \end{aligned} \quad (8.20)$$

The result of these calculations is a collection of feasible patterns and their corresponding fibre bundle dimensions, which can optionally be judged on the amount of undesired roving overlap they create at the equator.

**The reverse problem: predetermined  $b$  and  $n$**

In several filament-winding applications, the dimensions of the available fibre bundles are already determined in an early stage of the design process. In addition, the number of circuits is usually fixed. In the case these data do not lead to an acceptable winding pattern, an alternative solution can be created in terms of pseudo patterns. In this situation, we calculate patterns corresponding to smaller roving width values and allow excessive fibre bundle overlap at the equator. With this method, the inhomogeneity of the wound layer is completely smeared out and reduced into the available space provided by a single fibre bundle. The best result can be obtained in terms of least fibre bundle overlap or a resulting pattern having the parameter  $dn$  as close as possible to the aimed value.

### 8.3 Laminate thickness variation

As outlined in section 8.1, the dimensionless radial coordinate of the fibre bundle centreline is denoted by  $\nu$  (figure 8.3), while the dimensionless radius of the outer bundle edge is represented by the symbol  $\xi$ . On a way similar to the calculation of  $\nu$  (equations (8.3) and (8.5)) we obtain:

$$\xi = \frac{\varepsilon + \left(\frac{d\rho}{ds}\right)b + \left(\frac{dz}{ds}\right)\delta}{\rho_0} \Bigg|_{\rho=\xi\rho_0} = E + \left(\frac{1}{\sqrt{1+Z'^2(\xi)}}\right)B - \left(\frac{Z'(\nu)}{\sqrt{1+Z'^2(\xi)}}\right)\Delta \quad (8.21)$$

We introduce:

$$c = \frac{ndB\Delta}{\pi} \quad (8.22)$$

By completing the required number of circuits, the averaged fibre bed thickness across the meridian may be described as follows [ζ13,ζ16,ζ28,ζ34,ζ35]:

$$T_{complete} = \frac{c}{\sqrt{Y^2 - \nu^2}} \quad (8.23)$$

For  $Y \rightarrow \nu$ , the thickness will tend to infinity. This property introduces the need to construct another approach for the thickness description at the polar area [β6]. The corresponding situation is depicted in figure 8.9:

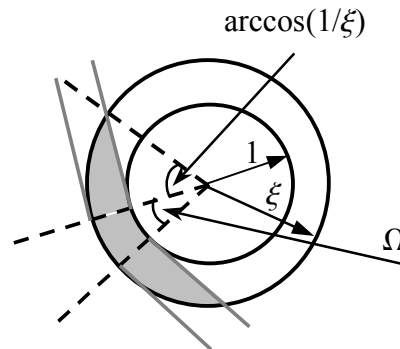


Fig. 8.9: Fibre bundle geometry at the pole

The grey surface, multiplied by  $nd\Delta$ , should be equal to  $\pi(\xi^2-1)T_{polar}$ . This consideration leads to [ζ21]:

$$T_{polar} = nd\Delta \frac{-2\sqrt{\xi^2 - 1} + (\xi^2 - 1)\Omega + 2\xi^2 \operatorname{arcsec} \xi}{2\pi(\xi^2 - 1)} \quad (8.24)$$

where “arcsec” stands for “arc secant”. The coordinate  $\nu^*$  where  $T_{\text{complete}} = T_0$ , is given by (figure 8.10):

$$\nu^* = \sqrt{\nu^2 + \left( \frac{2B(\xi^2 - 1)}{-2\sqrt{\xi^2 - 1} + (\xi^2 - 1)\Omega + 2\xi^2 a \sec \xi} \right)^2} \quad (8.25)$$

The thickness distribution presented here is in general characterised by satisfactory accuracy. However, for the proper calculation of the curvatures related to a particular fibre layer, the thickness distribution should provide continuity up to the second derivative ( $C^2$  continuity). For this reason, we introduce the following approximation (figure 8.10):

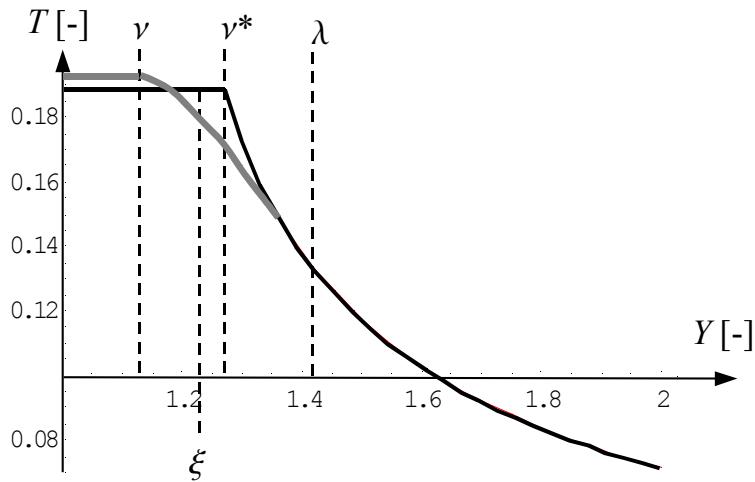


Fig. 8.10: The original thickness distribution (black) and its smoothed approximation (grey)

The smoothing process can be realised by a fourth degree polynomial:

$$p(Y) = \sum_{i=0}^4 a_i Y^i \quad (8.26)$$

The coefficients must satisfy:

**Part B: Reinforcing layer architecture**

$$\begin{aligned}
 \int_{\nu}^{\nu^*} p(Y)dY + p(\nu)(\nu - 1) &= T_{polar}(\nu^* - 1) \\
 p'(\nu) &= 0 \\
 p''(\lambda) &= T''_{complete}(\lambda) \\
 p'(\lambda) &= T'_{complete}(\lambda) \\
 p(\lambda) &= T_{complete}(\lambda)
 \end{aligned} \tag{8.27}$$

with  $\lambda = \nu^* + (\nu^* - \nu)$ . The obtained coefficients are linearly proportional to  $c$  and  $T_{polar}$ . Every collection of  $p$  circuits is denoted by  $i$ . By repeating this collection  $kd$  times, the required number of fully closed layers will achieve its maximum value ( $d$ ). Hence, we define:

$$\begin{aligned}
 T(i, Y) &= \frac{i}{nd} \left( p - \frac{1}{kd} \right) p(\nu), & 1 \leq Y \leq \nu \\
 T(i, Y) &= \frac{i}{nd} \left( p - \frac{1}{kd} \right) p(Y), & \nu \leq Y \leq \lambda \\
 T(i, Y) &= \frac{i}{nd} \left( p - \frac{1}{kd} \right) \frac{c}{\sqrt{Y^2 - \nu^2}}, & \lambda \leq Y \leq Y_{\max}
 \end{aligned} \tag{8.28}$$

The results of equation (8.28) agree very well with experimental data and guarantee  $C^2$  continuity for the region of interest:  $[\nu, Y_{\max}]$ . A similar method is published by Vasiliev [ $\zeta$ 34, $\zeta$ 35].

## 8.4 Example

To illustrate the presented method, we consider here an isotensoidal pressure vessel with  $\rho_0 = 40$  [mm] and  $Y_{eq} = 7.72$ , subjected to both internal pressure and axial forces. The vessel has to be covered with geodesic fibre trajectories (chapter 5). The available design space is dictated by:  $b = [5, 25]$  [mm],  $\delta = 0.3$  [mm] and  $\epsilon = 1$  [mm]. The corresponding  $\nu$ -range becomes [1.0875, 1.3375]. Within this range, the following leading (table 8.1) and lagging (table 8.2) patterns become feasible:

$b$ [mm]	$p+1, dk, n$	overlap [mm]
5.103	16, 14, 383	0.038
11.27	15, 12, 179	0.432

Table 8.1: The resulting leading patterns

$b$ [mm]	$p, dk, n$	overlap [mm]
10.45	15, 21, 316	4.302
10.43	15, 20, 301	3.981
10.42	15, 19, 286	3.627
10.40	15, 18, 271	3.234
10.38	15, 17, 256	2.795
10.35	15, 16, 241	2.301
10.33	15, 15, 226	1.741
10.30	15, 14, 211	1.103
10.27	15, 13, 196	0.367
16.88	14, 12, 169	5.387
16.83	14, 11, 155	4.299
16.76	14, 10, 141	2.994
16.68	14, 9, 127	1.404
24.25	13, 8, 105	5.742

Table 8.2: The resulting lagging patterns

The least fibre bundle overlap solution corresponds with the first leading pattern. However, since the width of the applied bundle is rather small, a considerable number of windings are needed (383). When choosing for a wider fibre bundle, the best solutions are the lagging patterns {14, 9, 127} (minimum number of circuits) and {15, 13, 196} (least bundle overlap). A disadvantage of the lagging patterns derived here is the slightly increased fibre overlap when compared to the leading ones.

## Part B: Reinforcing layer architecture

### Predetermined $b$ and $n$

With predetermined values for  $b$  and  $n$ , the reverse strategy has to be followed. Suppose that  $b = 10$  [mm] and  $dn = 200$ . The tolerance interval for  $n$  is assumed as  $\{198, 220\}$ . With  $dn$  running from 198 to 220, various combinations of integers satisfying the Diophantine equations can then be constructed [ $\beta 1, \beta 4$ ].

The obtained results are presented in table 8.3; the first column represents the theoretical dummy roving width that is able to provide a  $\Delta K$  corresponding to the pattern given in the next column of the table. The third column represents the roving width at the equator, and the last one represents how well the obtained roving width can fit  $dn$  times in the equatorial circumference of the body:

$b_{\text{dummy}}$ [mm]	$p+1, dk, n$	$b_{\text{equator}}$ [mm]	$b_{\text{equator}} - 2\pi\rho_{\text{equator}} / dn$ [mm]
5.245	16, 13, 207	10.101	0.7297
17.730	14, 15, 209	10.133	0.8511
11.068	15, 14, 209	10.116	0.8336
$b$ [mm]	$p, dk, n$	$b_{\text{equator}}$ [mm]	$b_{\text{equator}} - 2\pi\rho_{\text{equator}} / dn$ [mm]
24.396	13, 16, 209	10.152	0.8699
16.782	14, 15, 211	10.131	0.9365
10.184	15, 14, 211	10.113	0.9194

Table 8.3: Possible winding patterns for fixed  $dn$  and  $b$ -values

The best solution is in this case represented by the last row; the dummy fibre bundle width  $b_{\text{dummy}}$  is very close to  $b_{\text{equator}}$ . The only disadvantage of this solution is the increase of the number of circuits from 200 to 211 (5.5%).

### Maximum thickness

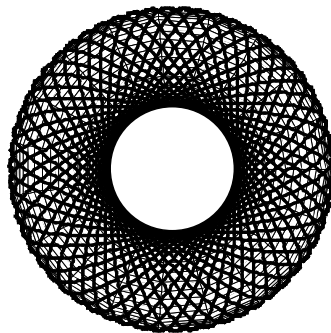
The pressure vessel considered here is subjected to geodesic winding without any fibre bundle overlap at the equator ( $d = 1$ ) and without any additional turn-around ( $\Omega = 0$ , figure 8.9). The maximum thickness of the reinforcing fibre layer becomes at the polar area approximately equal to  $2\delta$ . For overlapping bundles, the maximum thickness can even reach  $10\delta$  to  $20\delta$ . The main reason for this phenomenon is that the hereby-created laminate might include fibre bridging. The thickness can further be increased by applying additional turning around ( $\Omega$ ) at the polar areas. These observations agree well with [ $\beta 6$ ] and [ $\zeta 34, \zeta 35$ ].

## 9

## Pressure vessels revisited (1)

*The theory of isotenoid pressure vessels, as outlined in chapters 3 and 4 in its simplified version (netting theory), is leading to optimal pressure vessels. At least, from a structural analysis-related point of view. A step usually forgotten in the design procedure is that depending on the applied roving dimensions and the vessel geometry, the required number of circuits might not lead to acceptable mandrel coverage. In addition, the thickness of the resulting reinforcing layer might be excessive as the fibres tend to pile up near the polar areas. Furthermore, since the construction of a cylindrical vessel will require both hoop and polar windings, the transitions between these circuits might cause problems in terms of insufficient friction for the path modification, or an excess of applied roving length.*

*These considerations lead to the suspicion that an “optimal” vessel is probably not optimal in the sense of completely utilising the available strength of the involved materials in combination with the achievement of minimal production costs. In this chapter we first provide the description of the geometry of “real” fibre bundles on a mandrel, followed by the theory and design rules for the construction of transitional circuits (section 9.2). Section 9.3 provides perhaps the most important issue of this thesis: matching the pattern-related integer numbers to the number of rovings dictated by structural analysis. We show here that a product obeying these rules is the real optimal one. The last section will reduce our optimism by showing the effect of the laminate thickness distribution on the resulting mechanical performance. Since the constructed laminate has a dimension in thickness direction (where the thickness distribution along that profile is not constant), the participating layers can not simultaneously be isotenoidal. This section outlines a simplified method for estimating the reduction of structural efficiency.*



**Top view of filament wound pressure vessel: notice the increasing roving density as proceeding inwards, to the polar area**

## **Part B: Reinforcing layer architecture**

## 9.1 Trajectories of a finite dimensioned roving

In the previous chapter we demonstrated that compared to the ideal fibre bundle, the “real” fibre bundle (having a certain thickness and width) will always result in a modified wound trajectory. The main reason for this modification is that the centreline of the fibre bundle is not exactly tangent to the polar opening of the mandrel. For geodesically wound pressure vessels, on a way similar to equation (8.8), we denote the dimensionless radius with  $Y$  and the dimensionless effective polar opening with  $\nu$ . Accordingly, the Clairaut equation becomes:

$$\alpha = \arcsin\left(\frac{\nu}{Y}\right) \quad (9.1)$$

As a result of the modified winding angle distribution, the parallel angle  $\phi$  will also be affected. Substitution of (9.1) into (4.5) leads to:

$$\phi'(Y, \nu) = \frac{a\nu}{Y\sqrt{Y^2 - \nu^2}} \sqrt{\frac{Y^2 - 1}{a^2(Y^2 - 1) - (k_a Y + Y^3)^2}} = \frac{\nu}{\sqrt{Y^2 - \nu^2}} [\phi'(Y)]_{\nu=1} \quad (9.2)$$

With the parameters  $\{q, r\}$  and the elliptical coordinate system presented in chapter 4 (equation (4.12)), we obtain [ζ21]:

$$\begin{aligned} \phi'(q, r, \nu, \theta) = & \frac{2\sqrt{2}\nu}{1 + q + (q - 1)\cos(2\theta)} \sqrt{\frac{q(1 + q + 2qr)}{3 + q(3 + 4r) + (q - 1)\cos(2\theta)}} \times \\ & \times \sqrt{\frac{1 + q\{2r + q[r^2 + q(1 + r^2)]\} + c(q - 1)\cos(2\theta)}{-2q\nu^2(1 + q + 2qr) + c(q + 1) + c(q - 1)\cos(2\theta)}} \end{aligned} \quad (9.3)$$

where:

$$c = 1 + q + 2qr + q^2(1 + r)^2 \quad (9.4)$$

We recall here that the original validity range for the elliptical coordinate  $\theta$  is  $[0, \pi/2]$  [ζ14,ζ15,ζ19,ζ20ζ21,ζ27]. Due to the modified polar opening radius however, the definition range is now changed into  $[0, \theta_p]$  where  $\theta_p$  is slightly smaller than  $\pi/2$  and corresponds with the dimensionless polar opening radius  $\nu$ . At the vicinity of the polar opening the parallel angle differential will tend to infinity. Accordingly, for  $\theta = \theta_p$ , the denominator of (9.3) becomes equal to zero. This consideration leads to the solution:

## Part B: Reinforcing layer architecture

$$\theta_p(q, r, \nu) = \frac{1}{2} \arccos \left( \frac{-2q(1+q+2qr)\nu^2 + c(q+1)}{c(q-1)} \right) \quad (9.5)$$

To evaluate the roving length differential we substitute (9.1) into (4.6):

$$L'(Y, \nu) = \frac{aY}{\sqrt{Y^2 - \nu^2}} \sqrt{\frac{Y^2 - 1}{a^2(Y^2 - 1) - (k_a Y + Y^3)^2}} = \sqrt{\frac{Y^2 - 1}{Y^2 - \nu^2}} [L'(Y)]_{\nu=1} \quad (9.6)$$

Or, in elliptical coordinates:

$$L'(q, r, \nu, \theta) = \frac{c\sqrt{2}}{\sqrt{q(1+q+2qr)}} \sqrt{\frac{1}{3+q(3+4r)+(q-1)\cos(2\theta)}} \times \sqrt{\frac{1+q\{2r+q[r^2+q(1+r^2)]\}+c(q-1)\cos(2\theta)}{-2q\nu^2(1+q+2qr)+c(q+1)+c(q-1)\cos(2\theta)}} \quad (9.7)$$

The case  $\nu = 1$  corresponds to rovings with zero width and thickness (figure 8.3), where the presented expressions for  $\phi'$  and  $L'$  reduce to equations (4.21) and (4.23) respectively. These equations can analytically be integrated (equations (4.22) and (4.24)). For  $\nu \neq 1$ , the integration of (9.3) and (9.6) can only be performed by numerical evaluation:

$$\phi(q, r, \nu, \theta) = \int_{t=0}^{\theta} \phi'(q, r, \nu, t) dt, \quad L(q, r, \nu, \theta) = \int_{t=0}^{\theta} L'(q, r, \nu, t) dt, \quad (9.8)$$

where  $0 \leq \theta \leq \theta_p$

With the definitions for  $q$ ,  $r$  and  $s$  presented in chapter 4, the turn-around of a single circuit becomes:

$$\Phi(q, r, s, \nu) = 4 \left( \phi(q, r, \nu, \theta_p) + \frac{s}{\sqrt{Y_{eq}^2(q, r) - 1}} \right) \quad (9.9)$$

The total length of a complete circuit can similarly be calculated by replacing the term  $L(q, r, \pi/2)$  in equation (4.29) with  $L(q, r, \nu, \theta_p)$ . Obviously, the mandrel surface and volume remain unchanged.

## 9.2 Transitional circuits

As outlined in chapter 4, the cylindrical part of a composite pressure vessel with isotensoid end domes is covered by both polar and hoop circuits. The transition from polar to hoop windings or vice versa is usually done by cutting the applied fibre bundle and reattaching it on the mandrel. However, An alternative method that is enhancing the continuity of the production process, is to gradually change the winding angle on such a way that the desired transition becomes feasible. This alteration obviously requires some non-geodesic winding. Depending on the initial winding angle, the length of the cylinder and the available friction, the desired transition can usually not be completed in one run over the cylindrical part. This attempt will force the roving to repeatedly enter the dome area (at the equator) with various winding angles. In this section we provide the basic equations for the design of such circuits and demonstrate them in an example.

### Transitional circuit geometry

An example of polar and hoop windings is given in the first page of chapter 4. The definition of the cylindrical part is schematically given below:

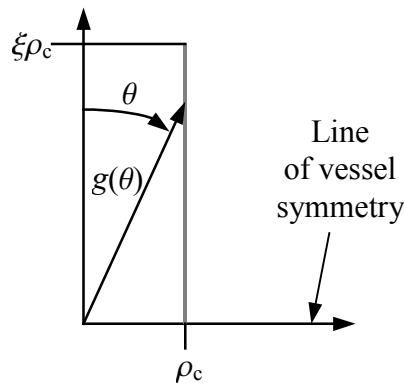


Fig. 9.1: Definition of the cylindrical part belonging to a pressure vessel

The cylindrical part is defined in spherical coordinates (equation (6.26)) where the function  $g(\theta)$  is given in equation (6.38):

$$g(\theta) = \frac{\rho_c}{\sin \theta} \quad \theta_c \leq \theta \leq \pi - \theta_c \quad (9.10)$$

$$\theta_c = \arctan\left(\frac{1}{\xi}\right)$$

Notice that the parameter  $\xi$  is similar to the parameter  $s$  that is used in the previous section and in chapter 4. The reason for this double notation is purely alphabetical.

## Part B: Reinforcing layer architecture

For reasons of compatibility with upcoming derivations, we relate the initial winding angle (at  $\theta = \theta_c$ ) to a parameter  $\lambda$  as follows (see also chapter 6):

$$\sin \alpha|_{\theta_c} = \frac{1}{\lambda} \quad (9.11)$$

As previously indicated, the transitional circuits are here constructed by changing the roving direction according to a constant coefficient of friction  $\mu$ . The resulting winding angle distribution is given by equation (6.41) [ $\gamma_{11}, \delta_2$ ]:

$$\alpha(\theta) = \arcsin\left(\frac{1}{\lambda \pm \mu(\cot \theta - \xi)}\right) \quad (9.12)$$

The resulting path description can be obtained by integration of equation (6.42) [ $\gamma_{11}$ ]:

$$\begin{aligned} \phi(\theta) = \frac{1}{\mu} \left\{ \ln[\lambda - \mu\xi + \sqrt{(\lambda - \mu\xi)^2 - 1}] \right. \\ \left. - \ln[\lambda + \mu(\cot \theta - \xi) + \sqrt{[\lambda + \mu(\cot \theta - \xi)]^2 - 1}] \right\} + c_\phi \end{aligned} \quad (9.13)$$

where  $c_\phi$  is an arbitrary angular constant [rad]. The consumed fibre length differential is (equation (2.40)):

$$\frac{dL}{d\theta} = \frac{\sqrt{G(\theta)}}{\cos \alpha(\theta)} = \frac{\rho_c}{\sin^2 \theta \sqrt{1 - \frac{1}{\lambda + \mu(\cot \theta - \xi)}}} \quad (9.14)$$

Integration yields:

$$L(\theta) = -\frac{\rho_c \sqrt{[\lambda + \mu(\cot \theta - \xi)]^2 - 1}}{\mu} + c_l \quad (9.15)$$

where  $c_l$  is an arbitrary metric constant [m].

### Transition strategies

Once the transition from polar to hoop is completed, the winding angle  $\alpha$  becomes equal to  $\pi/2$ . This implies that the denominator of the arcsine argument that is presented in equation (6.12) must become equal to 1:

$$\lambda + \mu(\cot \theta - \xi) = 1 \quad (9.16)$$

## Part B: Reinforcing layer architecture

This equation expresses the criterion for completing the aimed transition. When the transformation “polar → hoop” must be realised in a single run (from  $\theta_c$  to  $\pi-\theta_c$ ), a certain minimum length for the cylindrical part of the vessel will be required. From equation (9.16) we obtain:

$$\lambda + \mu[\cot(\pi - \theta_c) - \xi_{hoop}] = 1 \Rightarrow \xi_{hoop} = \frac{\lambda - 1}{2\mu} \quad (9.17)$$

In the opposite case, when  $\lambda$ ,  $\mu$  and  $\xi$  are given, the required number of passages on the cylindrical part is given by:

$$\xi_{hoop} = n_{req}\xi \Rightarrow n_{req} = C\left[\frac{\xi_{hoop}}{\xi}\right] = C\left[\frac{\lambda - 1}{2\mu\xi}\right] \quad (9.18)$$

where  $C[\#]$  stands for ceiling (smallest integer containing the argument). Once the construction of these passages is initiated, every subsequent circuit will start with a modified initial winding angle  $\alpha_{tr}(j)$ :

$$\alpha_{tr}(j) = \arcsin\left(\frac{1}{\lambda - 2j\mu\xi}\right) \quad (9.19)$$

The associated effective  $\lambda$ -value ( $\lambda_{tr}(j)$ ) is (equation (9.11)):

$$\lambda_{tr}(j) = \lambda - 2j\mu\xi \quad (9.20)$$

The corresponding isotensoidal end-dome should obviously have the same winding angle at its equator, and the same radius. These considerations lead to:

$$\rho_c = \rho_0 Y_{eq} \quad \& \quad \frac{1}{Y_{eq}} = \frac{1}{\lambda} \quad (9.21)$$

where  $\rho_0$  is the polar opening radius. With the  $r$ -value given (equation (4.13)), the proper value for  $q$  ( $= q_m$ ) is given by:

$$Y_{eq}(q_m, r) = \lambda \Rightarrow \quad (9.22)$$

$$q_m = \frac{(\lambda^2 - 1)(2r + 1)\sqrt{\lambda^2 - 1}\sqrt{3 + \lambda^2 + 4r^2\lambda^2 + 4r(\lambda^2 + 1)}}{2(1 + r)^2}$$

The end dome is now fully defined;  $q_m$  and  $\rho_0$  are “frozen”. As previously mentioned, every modified transitional winding enters the dome with  $\alpha_{tr}(j)$ . Hence, the effective dimensionless value for the polar opening radius can be quantified as follows:

## Part B: Reinforcing layer architecture

$$\alpha_{tr}(j) = \arcsin\left(\frac{1}{\lambda_{tr}(j)}\right) = \arcsin\left(\frac{v(j)}{\lambda}\right) \Rightarrow v(j) = \frac{\lambda}{\lambda_{tr}(j)} \quad (9.23)$$

### Example

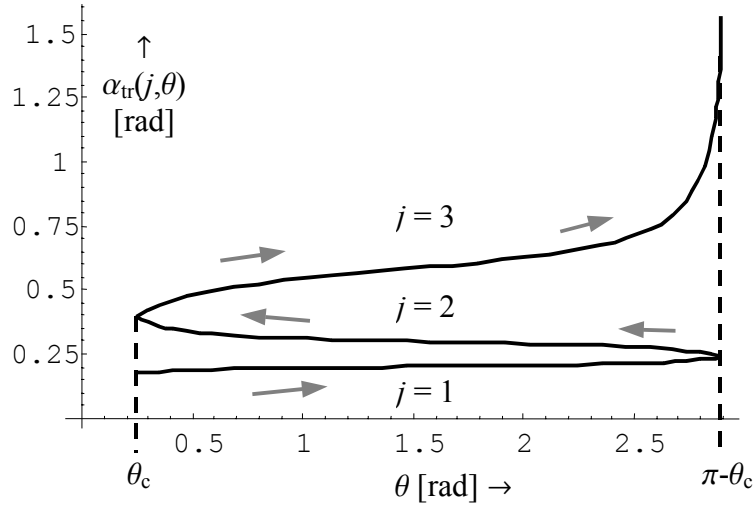


Fig. 9.2: Winding angle development during the three required transitional windings

We consider here a cylindrical vessel with  $\lambda = 5.8$ ,  $\mu = 0.2$ ,  $\xi = 4$  and  $\rho_c = 1$  [m]. Equation (9.18) immediately leads to  $n_{req} = 3$ ; this implies that we need three transitional windings. The corresponding isotensoidal end dome is assumed to have a zero  $r$ -value. Equations (9.21) and (9.22) lead to:  $q_m = 33.6111$  and  $\rho_0 = 0.172414$  [m]. The result is depicted in figure 9.2.

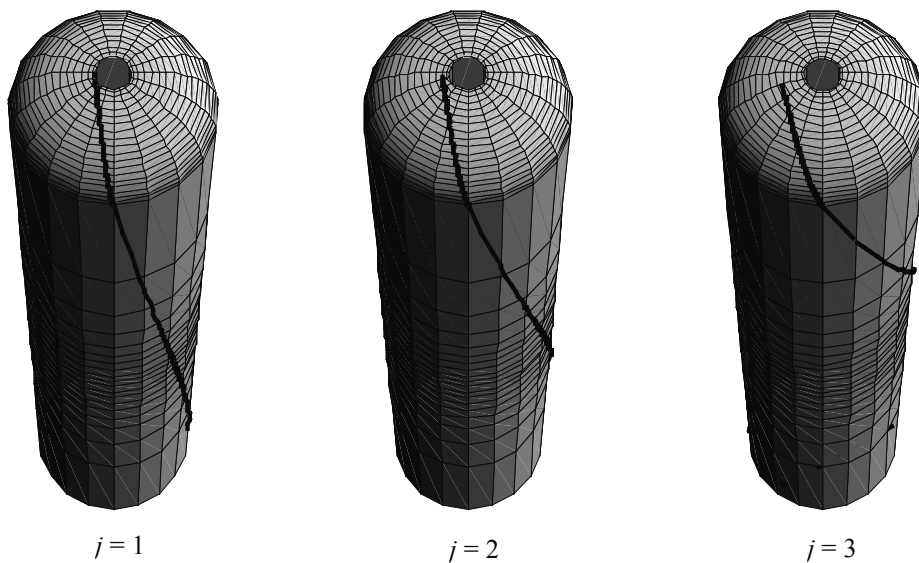


Fig. 9.3: Visualisation of the transitional circuits

## Part B: Reinforcing layer architecture

Application of equation (9.23) leads to the determination of the required  $\nu(j)$  values. The result is shown in figure 9.3. Integration of equation (9.7) and evaluation of (9.15) with the proper  $\nu(j)$ ,  $\lambda_{tr}(j)$ ,  $\theta_p$  and  $c_1$  values leads to an additional wound roving length of 33.6837 [m]; this is comparable with the length of three unmodified half circuits (32.2141 [m]). The total number of circuits is typically much higher (in the order of hundreds), so the added weight can be neglected [γ11].

### 9.3 Maximum strength versus optimal pattern

The most important steps in the design procedure of a composite pressure vessel are the shape determination and the derivation of suitable winding patterns. Both can be expressed in terms of the required number of wound circuits. This section presents a methodology for matching the number of circuits dictated by strength calculations (chapter 4) to these dictated by winding patterns (chapter 8). The main key for this matching procedure can be found in terms of the main characteristic properties of the fibre bundle: cross sectional dimensions and tensile strength. The fibre trajectories here are geodesic, and they are not subjected to any additional turn around ( $\Omega$ ) at the polar areas of the treated vessel. In this sense, the solution may be regarded as optimal since it guarantees minimal fibre length, minimal fibre stacking, minimal number of required circuits, minimal undesired fibre bundle overlap and maximal utilisation of the fibre bundle strength.

#### Matching the mechanical and pattern-related properties

For a pressure vessel that is dimensioned according to the “ $qrs$ ” parameterisation (section 4.2), the required number of fibre bundles is given by equation (4.13):

$$a(q,r) = \frac{[1 + q + 2qr + q^2(1 + r^2)]^{3/2}}{q(1 + q + 2qr)} \left( = \frac{FN_f}{\pi P_r \rho_0^2} \right) \quad (9.24)$$

where  $F$  is the maximum allowable tensile force for the fibre bundle,  $N_f$  the total number of fibre bundles passing the equator,  $P_r$  the internal pressure, and  $\rho_0$  the radius of the polar opening. We assume now that the strength of the applied fibre bundle per unit of cross sectional area is  $\sigma$ . Furthermore, the fibre bundle has a square section with a width  $b$  and a thickness  $\delta$ . Every completed wound circuit creates (per layer) two fibre bundles passing the equatorial cross section (black and white dots in figure 8.6). Accordingly,  $N_f = 2nd$  where  $n$  is the number of windings and  $d$  the number of fully closed layers (as defined in chapter 8). With these considerations we obtain:

$$\left. \begin{array}{l} a\pi P_r \rho_0^2 = FN_f \\ F = \sigma b \delta \\ N_f = 2nd \end{array} \right\} \Rightarrow nd = \frac{\pi P_r a \rho_0^2}{2 F b \delta} = \frac{\pi P_r a}{2 \sigma B \Delta} \quad (9.25)$$

where  $B$  and  $\Delta$  denote the dimensionless width, respectively thickness. The required effective number of filaments clearly depends on the “load/strength” ratio  $P_r / \sigma$ , and a dimensionless geometric parameter  $a / B\Delta$ .

For the construction of a suitable winding pattern, the applied circuits must satisfy the conditions presented in equation (8.17) where, according to (8.18), the parameter  $\Delta K$  depends directly on the turn around angle  $\Phi(q, r, s, \nu)$  (equation (9.11)). Substituting (9.25) into (8.17) and solving (8.18) for  $\Phi$  leads to:

$$\begin{aligned} \frac{\sigma}{P_r} \frac{B\Delta}{a} &= \frac{p}{2} - \frac{1+p}{\pi} \Phi && \text{Leading pattern} \\ \frac{\sigma}{P_r} \frac{B\Delta}{a} &= \frac{1-p}{2} + \frac{p}{\pi} \Phi && \text{Lagging pattern} \end{aligned} \quad (9.26)$$

where, as outlined in section 8.1:

$$\left. \begin{aligned} \Phi &= \Phi(q, r, s, \nu) \\ \nu &= \nu(B, E, \Delta) \end{aligned} \right\} \Rightarrow \Phi = \Phi(q, r, s, B, E, \Delta) \quad (9.27)$$

In conclusion, the left part of (9.26) depends on  $\{q, r, \sigma, B, \Delta\}$  and the right part on  $\{q, r, s, E, B, \Delta\}$ . The complete matching procedure can be summarised as adjusting these parameter combinations to each other. Notice that non-common parameters are  $E, s$  and  $\sigma$ . In practice, the eccentricity value  $E$  is limited up to a few tenths of millimetres. In addition, the fibre strength  $\sigma$  is usually predetermined as a typical value for e.g. glass or carbon fibres. The roving thickness  $\delta$  should be, in order to avoid excessive fibre stacking at the polar areas, as small as possible. An increased thickness value  $B$  is generally advantageous for limiting the required production time. Nevertheless, too large values may introduce significant strength problems since the fibre topology will considerably deviate from the theoretical one; this situation can lead to the requirement for applying additional circuits on the vessel. Moreover, the available fibre spools are limited to certain width ranges. Within these ranges, an optimal solution should be found in terms of minimal strength reduction and minimal production costs, under one important constraint:  $nd$  should at least be equal to the value provided by equation (9.25). If the latter can not be fulfilled, a certain fibre overlap at the equator has to be accepted.

A remarkable observation is that when we neglect  $E$ , the successful design of a cylindrical pressure vessel can be reduced to a proper combination of  $s$  and  $\sigma$ . Apparently, for a cylindrical pressure vessel of undetermined length, there is always an optimal solution in terms of perfectly matching the required number of fibre bundles to a feasible pattern by modifying the length of the cylindrical mandrel part.

### Example

We consider here a pressure vessel with  $a = 50$  and  $k_a = -10$  (as defined in equations (4.10) and (4.14)). These parameters lead to:  $Y_{\min} = 1.01648$  and  $Y_{\text{eq}} = 7.71872$  (equation (4.13)).

## Part B: Reinforcing layer architecture

The corresponding  $q$  and  $r$ -values are respectively 57.6625 and  $-0.168$ . The design pressure  $P_r$  is set equal to 20 [MPa] and the applicable fibre bundle width range is [5, 20] [mm]. The radial offset  $\epsilon$  at the polar area is set equal to 1 [mm]. We further assume that the available fibre spools contain rovings with a thickness of 0.3 [mm] and a tensile strength  $\sigma$  within the range [4000, 4500] [MPa].

### Objectives

- Maximal utilisation of the mechanical fibre properties
- Preferably one wound layer
- Minimal number of required circuits

### Constraints

- Roving overlap at the equator: less than 1 [mm]
- Fixed roving width
- Fixed polar radius offset ( $\epsilon$ )

The given width range generates a spectrum of corresponding  $\Phi$ -values (equation (9.9)). These  $\Phi$ -values lead to a collection of pattern constants  $p$  and  $n$  (equation (8.14)). The suitable patterns are (solution of equations (8.17) for the obtained  $p$  and  $n$  values and for  $d = 1$ ):

### Lagging patterns

$p, dk, n$	$\Delta K / 4$ [rad]	$\sigma$ [MPa]	overlap [mm]
15, 21, 316	$21\pi / 632$	2566.8	4.307
15, 20, 301	$10\pi / 301$	2698.5	3.986
15, 19, 286	$19\pi / 572$	2844.5	3.632
15, 18, 271	$9\pi / 271$	3007.2	3.238
15, 17, 256	$17\pi / 512$	3189.6	2.798
15, 16, 241	$8\pi / 241$	3395.6	2.304
15, 15, 226	$15\pi / 452$	3630.0	1.744
15, 14, 211	$7\pi / 211$	3899.3	1.104
15, 13, 196	$13\pi / 392$	4211.6	0.366
14, 12, 169	$6\pi / 169$	2974.8	5.402
14, 11, 155	$11\pi / 310$	3253.9	4.311
14, 10, 141	$5\pi / 141$	3590.7	3.003
14, 9, 127	$9\pi / 254$	4005.4	1.408
13, 8, 105	$4\pi / 105$	3340.3	5.770

Table 9.1: Evaluation of the resulting lagging patterns

**Leading patterns**

$p+1, dk, n$	$\Delta K / 4$ [rad]	$\sigma$ [MPa]	overlap [mm]
16, 24, 383	$12\pi / 383$	4330.9	0.037
15, 12, 179	$6\pi / 179$	4201.0	0.432

Table 9.2: Evaluation of the resulting leading patterns

**Optimal solution**

The best solution in terms of the above presented desired properties is the second leading pattern: the required  $\nu$ -value for generating a parallel angle propagation of  $\Delta K/4 = 6\pi / 179$  is  $\nu = 1.16426$ , leading to  $b = 11.141$  [mm]. The required tensile strength for the fibre to be applied is equal to 4201 [MPa] while the necessary number of circuits becomes equal to 179. The result is depicted below:

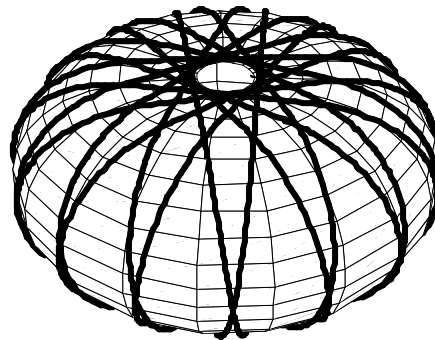


Fig. 9.4: The resulting pattern, after the completion of 15 circuits (pattern {15, 12, 179}, as defined in chapter 8)

## **9.4 Influence of the fibre layer geometry on the mechanical properties**

The common design methodologies for composite pressure vessels usually neglect the influence of the laminate thickness variation along the meridian profile. In addition, the original fibre path orientation is assumed to remain preserved by neglecting the fibre bundle dimensions. This section attempts to describe the influence of the fibre bundle geometry and thickness build up on the structural performance of the composite vessel under consideration. The outlined theory is demonstrated by an example. The results indicate that the effect of reinforcement layer geometry should generally not be overlooked, as the strength of the final product might be lower than the assumed one [ζ13,ζ32].

### **Fibre stacking vs. path orientation**

We assume here that the meridian profile of the vessel under consideration is described in polar coordinates. Hence, in accordance to chapter 3, the original meridian profile is given by a dimensionless function  $Z(Y)$ . As motivated in chapter 8 and section 9.1, the dimensions of the applied fibre bundle force the geodesic path to undergo winding angles as formulated in equation (9.1); this is the first modification of the fibre path geometry [ζ13,ζ32].

The second modification is caused by fibre stacking, especially around the poles [ζ13,ζ32,ζ34,ζ35]. For a vessel covered according to a pattern  $\{p, kd, nd\}$ , we derived the function  $T(i, Y)$  that provides the thickness build up for every collection  $i$  of  $p$  circuits. The counter  $i$  is running from 1 to  $k$ .

The obtained thickness distribution is perpendicular to the vessel surface. Hence, in order to describe the resulting meridian profile  $P(i, Y)$ , every obtained  $T(i, Y)$ -value should be projected on the  $Z$ -axis. This consideration leads to the following expression:

$$P(i, Y) = Z(Y) + \frac{T(i, Y)}{\sqrt{1 + Z'^2(Y)}} \quad (9.28)$$

where  $Z'(Y)$  is presented in equation (4.3). Differentiation leads to:

$$P'(i, Y) = Z'(Y) + \frac{T'(i, Y)}{\sqrt{1 + Z'^2(Y)}} - \frac{T(i, Y)Z'(Y)Z''(Y)}{[1 + Z'^2(Y)]^{3/2}} \quad (9.29)$$

Contrary to [ζ13], we assume here that the thickness build up itself does not influence the winding angle, since these deviations are in general sufficiently small.

However, the influence of the thickness build-up on the second characteristic angle  $\beta$  (as depicted in figure 3.4 and defined in equation (3.23)) can not be neglected:

$$\cos \beta(i, Y) = \frac{P'(i, Y)}{\sqrt{1 + P'^2(i, Y)}} \quad (9.30)$$

**Deformation and load distribution**

The axial load bearing capacity (equation (3.21)) of a particular layer is given by:

$$a \sqrt{1 - \frac{1}{Y^2}} \frac{Z'(Y)}{\sqrt{1 + Z'^2(Y)}} = a \cos \alpha \cos \beta = Y^2 + k_a \quad (9.31)$$

For the  $i$ -th placement of a collection of  $p$  circuits, the left side of (9.31) is now denoted by:

$$a(i, Y) \cos \alpha(Y) \cos \beta(i, Y) \quad (9.32)$$

The validity range of  $Z(Y)$  is  $[Y_b, Y_{\max}]$  where  $Y_b$  is generally slightly bigger than  $\nu$  [ζ14,ζ15]. If the tensile fibre load  $a(i, Y)$  and the orientation  $\beta(i, Y)$  remain unchanged, there is no possibility to neutralise the externally applied load combination  $k_a + Y^2$ , see figure 9.5:

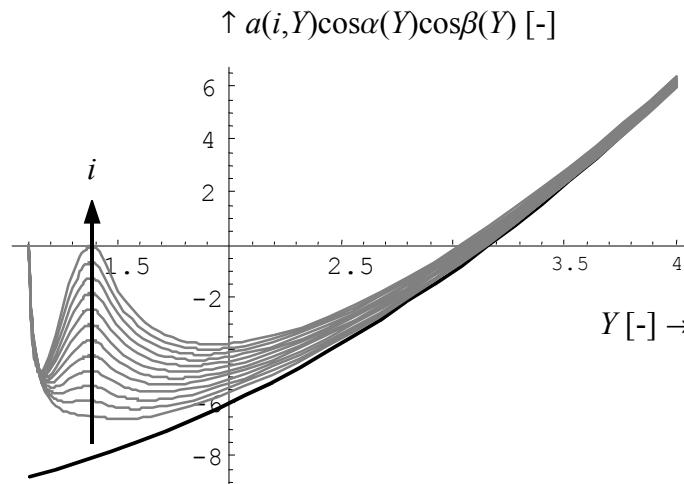


*Fig. 9.5: Load bearing capacity of several fibre layers (grey) as function of Y. The black line represents the applied loads on the vessel*

## Part B: Reinforcing layer architecture

The inability to create equilibrium can also be viewed by calculating the normal curvature of the vessel including the fibre stacking (equation (3.28)):

$$R_n = -\frac{Y^3[1+P^2(i,Y)]^{3/2}}{\nu^2[P(i,Y)+P^3(i,Y)]+Y(Y^2-\nu^2)P''(i,Y)} \quad (9.33)$$

The curvature  $R_n$  can even obtain negative values in the polar area, while, in addition, the denominator may also become equal to zero. Reconsideration of equation (3.29) leads to the conclusion that there is no real-valued tensile fibre force, able to create axial equilibrium. Furthermore, equation (3.14) leads to the observation that an eventual winding angle correction  $\Delta\alpha$  will not have considerable effect. In conclusion, both the fibre force and the  $\beta$ -angle must be modified.

For the calculation of the resulting meridian profile and fibre force distribution, we assume that every original  $\cos\beta$ -value is modified by a quantity  $\cos\Delta\beta$ . This perturbation is the same for every separate layer. Meanwhile, the resulting fibre force  $a^*$  will depend on both  $Y$  and the indicative layer number  $i$  (in other words:  $a^* = a^*(i, Y)$ ). The effect of the modified winding angle at the equator (given by equation (8.8)) on equation (9.32) can be taken into account by defining a new value for the dimensionless fibre force  $a$ :

$$a_{eq}^* = a \sqrt{\frac{Y_{\max}^2 - 1}{Y_{\max}^2 - \nu^2}} \quad (9.34)$$

The cumulative axial force equilibrium can be expressed as follows:

$$-\frac{1}{kd} \sum_{i=1}^{kd} a^*(i,Y) \cos\alpha(Y) [\cos\beta(i,Y) + \cos\Delta\beta(Y)] = k_a + Y^2 \quad (9.35)$$

In addition, an individual layer should satisfy:

$$-a^*(i,Y) [\cos\beta(i,Y) + \cos\Delta\beta(Y)] = D(i) [k_a + Y^2] \quad (9.36)$$

where  $D(i)$  expresses the load-bearing contribution of the layer under consideration. The simultaneous determination of  $a^*(i, Y)$ ,  $\Delta\beta(Y)$  and  $D(i)$  should satisfy the condition of minimum deformation energy. In this case however, the solution for this problem becomes rather complicated. Some solution methods are presented in [ $\zeta$ 13, $\zeta$ 16, $\zeta$ 28, $\eta$ 13]. In this section, the bending stiffness of the laminate is neglected. With this condition in mind, two extreme cases may be distinguished: constant fibre force  $a^*(i, Y)$ , and constant load distribution  $D(i)$  throughout the thickness direction of the layer.

**Constant fibre force**

We consider here a pressure vessel covered by unimpregnated fibre bundles and assume that there is no friction between the layers. This immediately leads to the conclusion that the fibre force  $a^*$  must remain constant and equal to  $a^*_{eq}$ . From equation (9.35), the new state of deformation  $\Delta\beta(Y)$  ( $= \Delta\beta_0(Y)$ ) can be obtained. Plugging this result into equation (9.36) leads to the determination of the load bearing contribution of each individual layer,  $D_0(i)$ .

**Homogeneous external load distribution through the thickness direction**

We assume now that every layer is able to carry the same fraction of the total load applied on the pressure vessel:  $D(i) = (k+Y^2)/kd$ . The initial guess for the deformation is:  $\Delta\beta(Y) = \Delta\beta_0(Y)$ ; from equation (9.36) we obtain the fibre force distribution  $a^*_1(i, Y)$ . The summation of the fibre forces according to the obtained distribution (for a particular coordinate ( $Y$ )) is usually slightly bigger than the original fibre force  $a^*_{eq}$  (mostly limited to 10%). In order to reduce the total fibre load, we substitute the function  $a^*_1(i, Y)$  into (9.35) and recalculate the deformation; the result is denoted by  $\Delta\beta_1(Y)$ . With the obtained state of deformation and equation (9.36), a new fibre force distribution can be determined:  $a^*_2(i, Y)$ . The corresponding fibre force summation over the participating layers is denoted  $a^*_2(Y)$  (without the index  $i$ ). This iteration may be repeated until the fibre force summation  $a^*_N(Y)$  is sufficiently close to the original one,  $a^*_{eq}$ . The final shape is indirectly given by  $\Delta\beta_N(Y)$  (equation (9.37)).

**The resulting shape**

The definition range for the obtained shape modification is  $[Y_b, Y_{max}]$ . From equation (9.30), the differential equation that describes the deformed shape can be derived:

$$P'^*_\#(i, Y) = \frac{\cos \beta_\#(i, Y) + \cos \Delta\beta_\#(i, Y)}{\sqrt{1 - [\cos \beta_\#(i, Y) + \cos \Delta\beta_\#(i, Y)]^2}} \quad (\# = 0, 1, \dots, N) \quad (9.37)$$

Integration of (9.37) leads to the geometric description of the “new” meridian profile including the thickness build up. The reduced validity interval makes it impossible to draw any conclusion for the structural performance of the shape at the vicinity of  $Y = 1$ .

## Part B: Reinforcing layer architecture

### Example

The example presented here is based on the pressure vessel and fibre geometry given in section 8.4. The winding pattern corresponds to:  $p = 15$ ,  $kd = 12$ ,  $nd = 179$  and the additional turn around angle ( $\Omega$ ) is equal to 0.

### Constant fibre force

In figure 9.6, we depict the original geometry of the implemented layers with black lines, and the resulting ones with grey lines. It is visible that the original shape is concave at some regions close to the polar opening; unless the external loads on the vessel approximately correspond with the average of the grey lines given in figure 9.5, there is no possibility to satisfy the condition of axial force equilibrium. In contrast to the original (partially concave) shape, the resulting meridian profile is convex over the entire  $[Y_b, Y_{\max}]$ -interval.

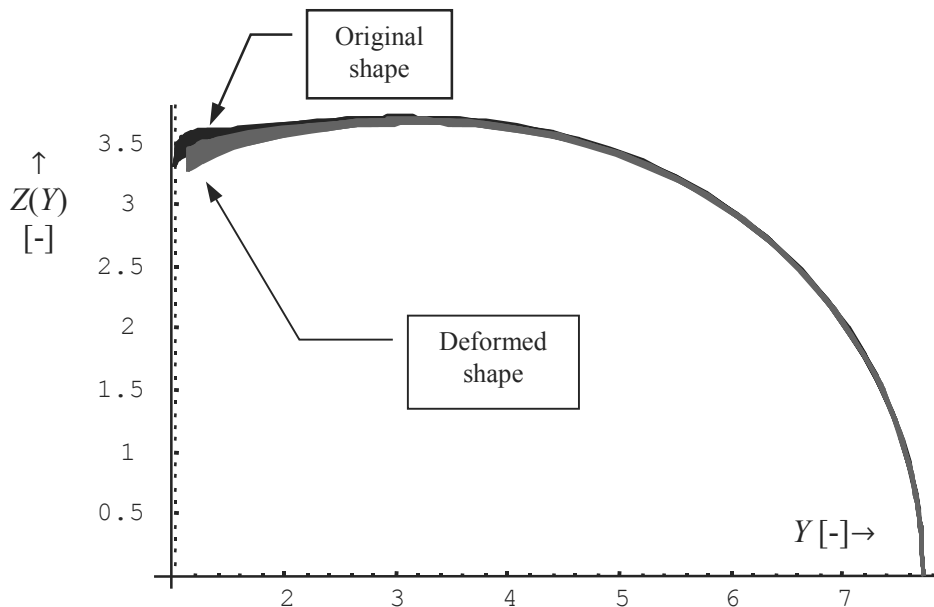


Fig. 9.6: Original (black) and deformed vessel shape (grey) for constant fibre loading

The load bearing capacity  $D(i, Y)$  through the overwound fibre layers is given in figure 9.7; the distribution is linear over the shell thickness ( $i$ -direction), but strongly non linear along the meridian profile itself ( $Y$ -direction).

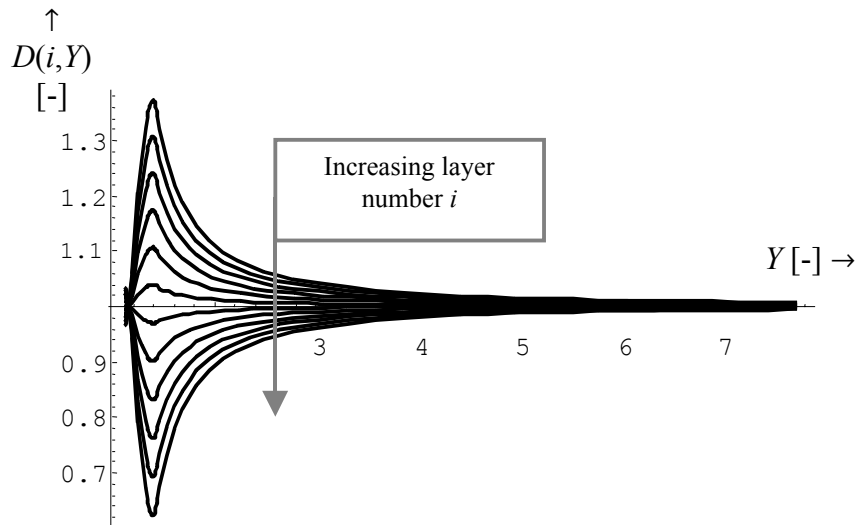


Fig. 9.7: Load bearing contribution among the fibre layers as a function of the dimensionless radius  $Y$

#### Homogeneous external load distribution through the thickness direction

The initial guess for the meridian shape modification is given by a  $\Delta\beta_0(Y)$  perturbation on the original  $\beta$  distribution. To reduce the fibre loads, we apply here the previously described iteration procedure. The result after 10 iterations is depicted in figures 9.8 and 9.9.

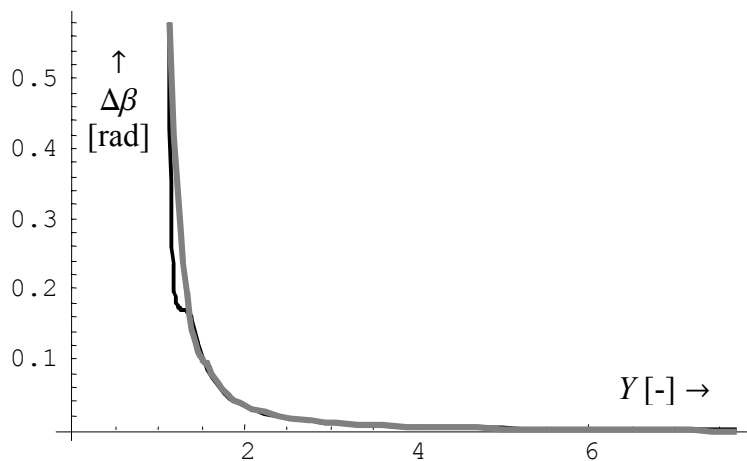


Fig. 9.8:  $\cos\Delta\beta_0(Y)$  (black) and  $\cos\Delta\beta_N(Y)$  (grey) after 10 iterations

## Part B: Reinforcing layer architecture

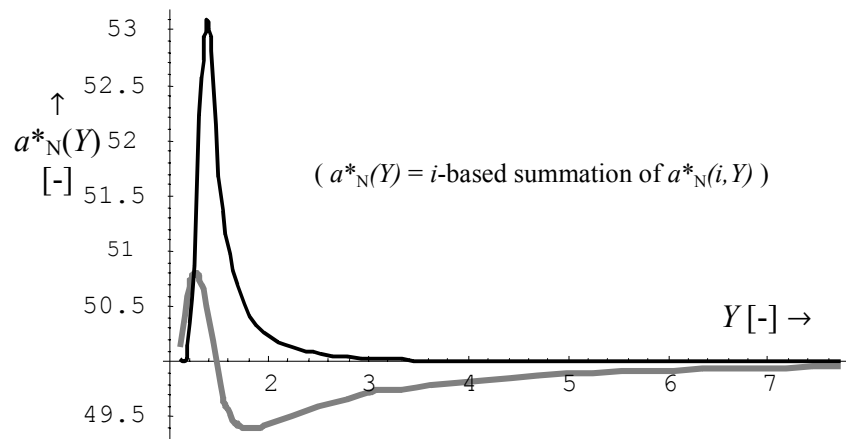


Fig. 9.9:  $a^*_2(Y)$  (black) and  $a^*_N(Y)$  (grey) after 10 iterations.

The original deviation of the fibre force summation (6.2%) is reduced to 1.4% ( $a^*_{eq} = 50.1$ ). The maximum tensile fibre load in the upper layer is reduced from 81 to 73 (dimensionless numbers). The tensile force in the lower layer remains practically unchanged (37.3). The original design value for  $a$  is 50 [-]. The resulting meridian profile shows a limited difference with the one presented in figure 9.6; the deviation is mainly concentrated on the polar region.

The results demonstrate that, when designing pressure vessels, the effect of fibre stacking should generally be taken into account. In particular, the combination of additional fibre path turn-around at the poles and considerable bundle thickness may increase the deviations in the fibre loads when compared to the design values. Both the assumptions of equal fibre loads and equal load bearing capacity per layer lead to the conclusion that the vessel performance may significantly be reduced. In the presented example, these reductions are 38% and 46%, respectively. This observation agrees well with the design rules given by European Space Agency [ζ7] for pressure vessels.

# C

## Production process

*In this part, we provide a comprehensive treatment of the kinematic equations for filament winding. Beginning in chapter 10 with the description of a generic geometric model and the economical (in terms of calculation efforts) derivation of the input parameters for the corresponding solutions, we present some typical results reflecting on shells of revolution and consequently discuss their properties.*

*The transformation of the kinematic equations into a more convenient form followed by the elaboration of their solution procedure, is presented in chapter 11. In addition, we derive here the complete set of analytical solutions for the lathe winder and provide several results for the winding process of shells of revolution on a generic machine configuration. With the description of every single machine motion as a function of the locus indicator belonging to the placed roving, and with the length quantification of the free-hanging fibre, the basis is here created for the production process optimisation procedure. Some simulation results reflecting on a tumble winder are given in appendix A.*

*The dynamic aspects of filament winding are considered in chapter 12, where we propose the application of several interpolation and numerical differentiation techniques for the creation of a proper estimation for the resulting velocities and accelerations.*

*An additional constraint for the winding process can be found in the determination of the allowable moving space for the feed eye, chapter 13. This space is bounded by the workspace limits of the machine, and is additionally dictated by collision avoidance between the feed eye structure and the mandrel. In this chapter, we provide some easily accessible techniques for determining the feed eye moving space boundaries. The obtained results are formulated in terms of a collection of feasible ranges for the length of the free-hanging fibre.*

*With the description of the collision boundaries, the dynamic machine limits (both velocities and accelerations for every participating movement), and the analytical kinematic solution for the lathe winder, we formulate in chapter 14 the production process optimisation problem. Within the dynamic and collision constraints, the objective here is to minimise the production time. Before proceeding to the optimisation problem, a rigorous reduction of the input grid for the control variables is realised. Considering an incremental production step, the optimisation problem is evaluated by the calculation of the minimum time needed to execute that step, while respecting the dynamic constraints and the available space for the movements of the feed eye. Next, the summation of these increments is minimised by a proper quantification of the control variable for every incremental step, by means of dynamic*

## **Part C: Production process**

*programming techniques. The simulation results of this method, applied on a lathe winder, are given in appendix B.*

*In a more generic fashion, we revisit in this part again the class of optimal pressure vessels (chapter 15) and provide various results for shapes of gradually varying aspect ratios. In regard to the selection of the proper machine configuration and its adjustments, several rules of thumb are here given. Furthermore, we propose some additional machine configurations for enhancing a further production time reduction.*

### **Keywords per chapter**

- 10: **Machine configuration, Input parameters, Curvature, Torsion**
- 11: **Kinematic equations, Spindle rotations, Feed eye translations, Roving speed**
- 12: **Lagrange, Splines, Fourier, Least squares, Finite differences, Multipoint approximation, Lanczos convergence factors**
- 13: **Feed eye, Machine limits, Collision bounds**
- 14: **Grid, Finite differences, Transition matrix, Transition costs, Dynamic programming**
- 15: **Isotenoid, Spheroid, Aspect ratio, Feed eye amplitude**

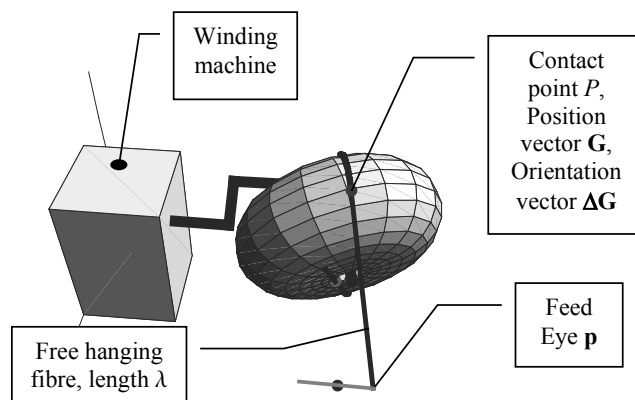
# 10

## Basic geometry

*As an introduction to the kinematic aspects of filament winding, we present in this chapter the geometry of a generic filament-winding machine configuration and subsequently determine the set of the required input parameters for the determination of the associated machine movements. For the corresponding input parameters we provide here some strategies for their efficient and accurate determination.*

*In the first section we outline the generic winding machine geometry. The associated body related quantities are expressed in their most general form as position and orientation vectors. The next section is related to the discrete determination of the body-related quantities. From this point we realise a reduction towards shells of revolution, being the most common class of objects created with filament winding techniques. The final formulation is expressed in the angular parameters  $\alpha$ ,  $\beta$  and  $\phi$  that are closely related to the design process of the shell to be wound (chapters 3 and 4, i.e. figure 3.4). The hereby-presented strategy for the derivation of the input parameters is mainly based on the theory outlined in chapter 2 (derivation of the tangent, normal and binormal vectors, curvatures and torsion). The last section (10.3) presents some typical examples of discretised paths on shells of revolution, and discusses several characteristic properties.*

*The presented quasi-analytical method for the determination of the body parameters does practically not suffer from cumulative error generation when evaluated. The accuracy of the obtained results is entirely independent of the number of discrete fibre points taken. As a result of this, the user is free in taking decisions regarding the size of the data collections involved in the solution of the kinematic winding equation(s).*



**Schematic view of a pressure vessel subjected to three rotations generated by a winding machine. In this particular case, the feed eye performs a one-dimensional translation.**

## **Part C: Production process**

## 10.1 Generic machine configuration

We consider here a three-dimensional body (indicated as mandrel), attached to a generic filament winding machine configuration, figure 10.1. The feed eye performs three translations  $\{p_x, p_y, p_z\}$  and the mandrel rotates about three axes being orthogonal to each other [15]. The rotation sequence is  $Q \rightarrow \gamma \rightarrow R$ .

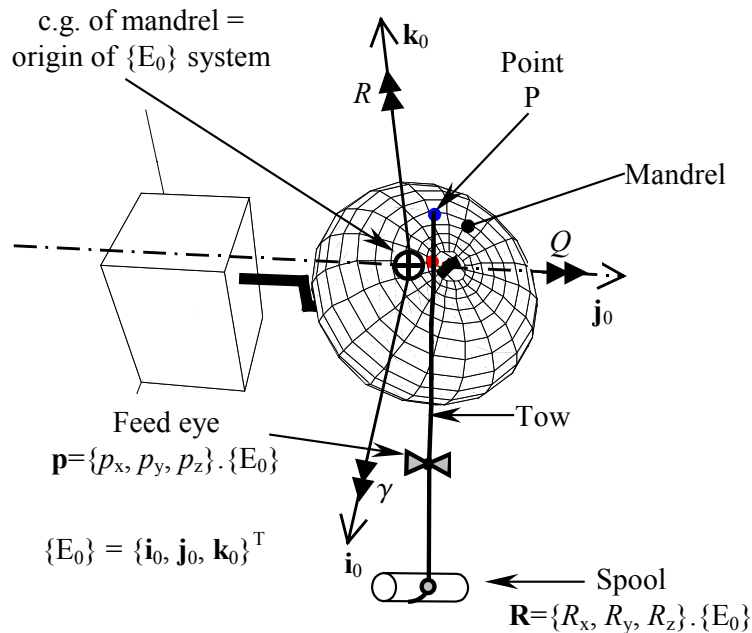


Fig. 10.1: General layout of a filament-winding machine

At the centre of gravity of the mandrel we attach a right-handed reference system  $\{E_3\}$  (figure 10.2) and an inertia reference system  $\{E_0\}$ . The orientation of  $\{E_3\}$  can be related to  $\{E_0\}$  with the aid of three consequent Euler rotations (figure 10.2) over respectively the angles  $Q$ ,  $\gamma$  and  $R$  [12,13]. More specific, the body under consideration is subjected to:

- Body rotation  $Q$  of  $\{E_0\}$  with respect to the  $\mathbf{j}_0$  axis: the resulting coordinate system is  $\{E_1\}$
- Body rotation  $\gamma$  of  $\{E_1\}$  with respect to the  $\mathbf{i}_1$  axis: the resulting coordinate system is  $\{E_2\}$
- Body rotation  $R$  of  $\{E_2\}$  with respect to the  $\mathbf{k}_2$  axis: the resulting coordinate system is  $\{E_3\}$ . The latter forms the basis for the body-related vector quantities

Additional features are (figure 10.1):

- Feed eye situated at  $\mathbf{p} = \{p_x, p_y, p_z\} \cdot \{E_0\}$

**Part C: Production process**

- Spool providing the roving at  $\mathbf{R} = \{R_x, R_y, R_z\} \cdot \{E_0\}$

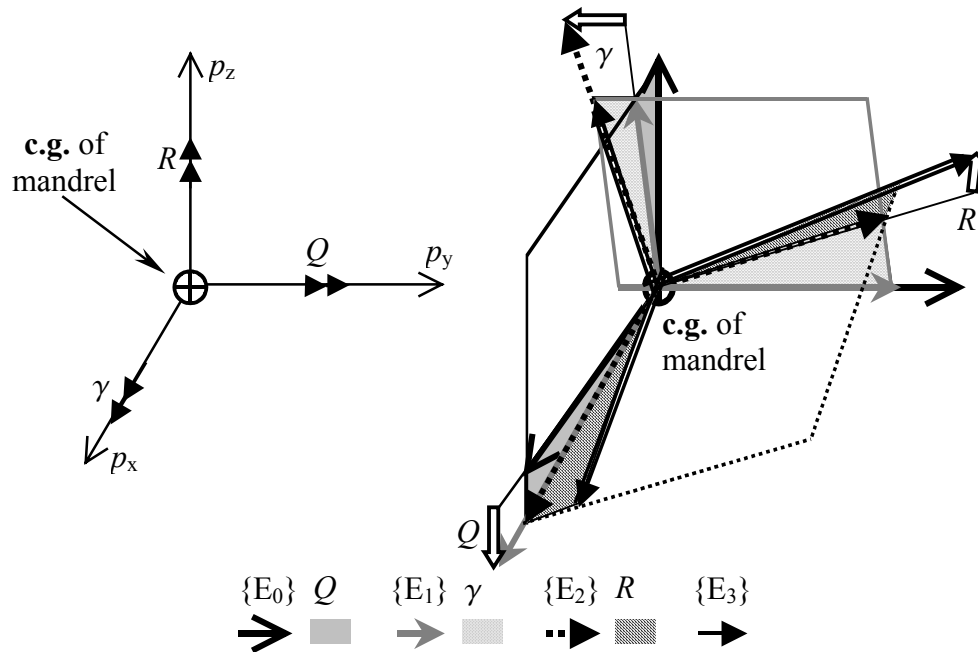


*Fig. 10.2: The three Euler rotations describing the body orientation with respect to the inertia coordinate system  $\{E_0\}$ , including the coordinates that indicate the feed eye position*

Notice that the feed eye and the spool are not subjected to any rotation; their position vectors are referred to the inertia system  $\{E_0\}$ . A two-dimensional version of the body rotations is given below:

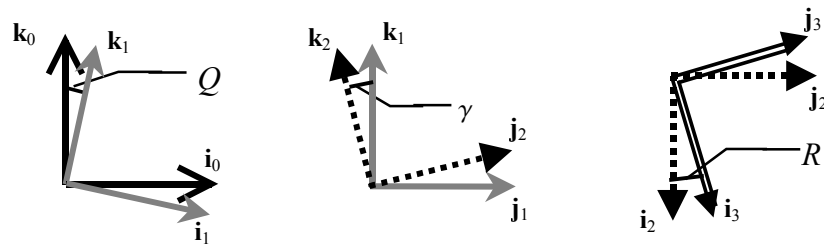


*Fig. 10.3: Rotation sequence of the body reference system*

These rotations can be expressed as follows:

$$\begin{aligned}
 \{E_1\} &= [R_{10}] \cdot \{E_0\} \\
 \{E_2\} &= [R_{21}] \cdot \{E_1\} \\
 \{E_3\} &= [R_{32}] \cdot \{E_2\}
 \end{aligned}
 \tag{10.1}$$

where  $[R_{ij}]$  are orthogonal transformation matrices:

$$[R_{10}] = \begin{bmatrix} \cos Q & 0 & -\sin Q \\ 0 & 1 & 0 \\ \sin Q & 0 & \cos Q \end{bmatrix}$$

$$[R_{21}] = \begin{bmatrix} 1 & 0 & 0 \\ 0 & \cos \gamma & \sin \gamma \\ 0 & -\sin \gamma & \cos \gamma \end{bmatrix} \quad (10.2)$$

$$[R_{32}] = \begin{bmatrix} \cos R & \sin R & 0 \\ -\sin R & \cos R & 0 \\ 0 & 0 & 1 \end{bmatrix}$$

The body related reference system  $\{E_3\}$  can directly be expressed in the inertia system  $\{E_0\}$  [12, 13]:

$$\{E_3\} = [R_{32}] \cdot [R_{21}] \cdot [R_{10}] \cdot \{E_0\} = [R_{tot}] \cdot \{E_0\} \quad (10.3)$$

where:

$$[R_{tot}] = \begin{bmatrix} cQcR + sQs\gamma sR & -cQsR + sQs\gamma cR & sQc\gamma \\ c\gamma sR & c\gamma cR & -s\gamma \\ -sQcR + cQs\gamma sR & sQsR + cQs\gamma cR & cQc\gamma \end{bmatrix} \quad (10.4)$$

with  $c\# = \cos\#$  and  $s\# = \sin\#$ . Returning to figure 10.1, the position of a locus P belonging to the roving path is given by a vector  $\mathbf{G}$  that is defined in  $\{E_3\}$ . The path orientation at that point is given by the unity vector  $\Delta\mathbf{G}$ , which is also defined in  $\{E_3\}$ , figure 10.4:

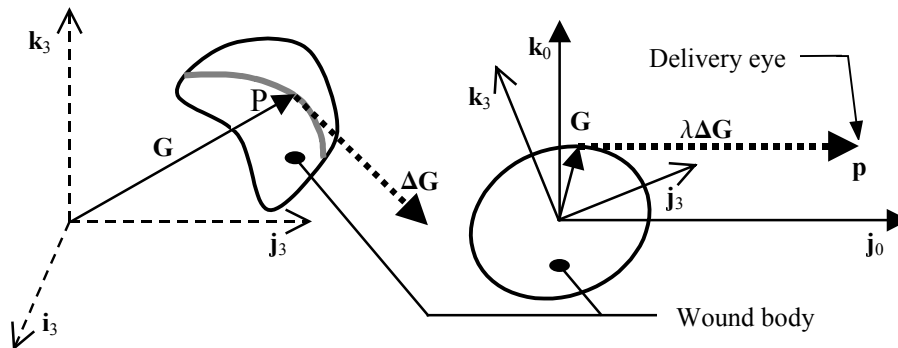


Fig. 10.4: Position vector  $\mathbf{G}$  and tangent vector  $\Delta\mathbf{G}$  (pointing to the feed eye  $\mathbf{p}$ ) at a roving locus P

## Part C: Production process

The line connecting the delivery eye with the contact locus of the roving on the surface of the wound object is referred as “free hanging fibre”. The metric distance of the latter is indicated by  $\lambda$ . Notice that  $\Delta\mathbf{G}$  is a unity vector (similar to the tangent vector  $\mathbf{T}$  as defined in chapter 2). From figures 10.1 and 10.4 it follows immediately that:

$$\mathbf{G}.\{E_3\} + \lambda\Delta\mathbf{G}.\{E_3\} = \mathbf{p}.\{E_0\} \quad (10.5)$$

With equation (10.1) we obtain the following expression (although the decision to describe the involved vectors in  $\{E_0\}$  or  $\{E_3\}$  is free, we choose here for  $\{E_0\}$ ):

$$\mathbf{G}[R_{tot}].\{E_0\} + \lambda\Delta\mathbf{G}[R_{tot}].\{E_0\} = \mathbf{p}.\{E_0\} \quad (10.6)$$

In practice, for the derivation and solution of the associated kinematic equations, the only necessary input parameters are  $\mathbf{G}$  and  $\Delta\mathbf{G}$ . However, a closer inspection of figures 10.1 and 10.4 leads to the conclusion that the radius of total curvature belonging to the path point P already provides additional information about the relation between the body rotation(s) and the propagation of that contact point along the roving path. Especially when considering complicated cases with simultaneous translations and rotations, knowledge of this curvature provides an excellent tool for predicting the angular or translation increments that satisfy equation (10.6). This property significantly shortens the calculation time (as outlined in chapter 11). For the sake of simplicity we recall here that the total curvature coincides with the normal curvature only in the case of geodesic trajectories (equation 2.16). However, due to physical limitations for the available friction, even in the case of non-geodesic winding, the normal and total curvature are rather close to each other. An additional useful parameter, especially when winding with a rigid tape, is the torsion of the fibre path. “Torsion” refers to the degree a curve on a surface fails to be planar. Consequently, it can be used for the prediction of the fibre twist along its length direction.

The winding geometry is now completely defined in terms of having the entire set of three simultaneous translations and rotations. Due to the principle of relative movement, every possible machine configuration can be covered (e.g. polar winder, racetrack winder) [15,18,19].

## 10.2 Input parameters

For shells of revolution, the determination of  $\mathbf{G}$  and  $\Delta\mathbf{G}$  can easily be realised by expressing them as functions of the basic angular quantities  $\alpha$  (winding angle),  $\beta$  (meridian slope) and  $\phi$  (parallel angle coordinate of the fibre path) [γ6,ι15]. For the position and orientation vectors, the required derivations are presented in chapter 2 where  $\mathbf{G}$  is replaced by  $\mathbf{C}$ , and  $\Delta\mathbf{G}$  by  $\mathbf{T}$ .

Contrary to  $\beta$  (which depends exclusively on the meridian profile), the parameters  $\alpha$  and  $\phi$  are additionally determined by the winding method in terms of geodesic or non-geodesic tow placement. The supporting theories are outlined in chapters 5 and 6, respectively. In this section we will assume geodesic windings to enhance simplicity for the derivations presented here. However, it should be noted that such a restriction is in general not necessary.

### Length increments

As outlined in the previous section, the set of required input parameters for the solution of the kinematic equations consists of  $\mathbf{G}$ ,  $\Delta\mathbf{G}$ ,  $k_t$  (total curvature) and occasionally  $\tau$  (roving path torsion). Before proceeding to the generation of the required input data, a proper selection of representative roving points has to be realised. Depending on the implemented coordinate system for the path description, considerable variations in the roving length increments can occur. In section 5.3 we demonstrated that these differences can become considerable. This leads to the conclusion that a representative data point selection should preferably be based on equal length increments.

Let a particular complete wound circuit be indicated by  $j$ , while a locus belonging to it is denoted by  $i$ . Every circuit has obviously two “turning” points. A fibre trajectory from the upper (at  $\theta = \theta_{up}$ ) to the lower (at  $\theta = \theta_{down}$ ) turning point of the treated circuit is assumed to contain  $p$  length increments. The corresponding counter runs from respectively 0 (at  $\theta = \theta_{up}$ ) to  $p$  (at  $\theta = \theta_{down}$ ), and the first circuit is indicated by  $j = 0$  (figure 10.5). The number of length increments can be chosen as a consequence of the required accuracy for the kinematic solution. Note that, according to these considerations, a complete circuit contains  $2p-1$  points, (the locus  $2p$  becomes the “ $i = 0$ ” indicated point of the next circuit). Recalling equation (2.40), (which is similar to (6.32)), the fibre length between the upper pole and an arbitrary  $\theta$ -value is given by:

$$L(0) = 0$$

$$L(i) = \int_{\theta_{up}}^{\theta_i} \frac{\sqrt{G(t)}}{\cos \alpha(t)} dt, \quad 1 \leq i \leq p \quad (10.7)$$

The length increment is defined as follows:

## Part C: Production process

$$\Delta L = \frac{L(p)}{p} \quad (10.8)$$

The  $\theta(i)$ -collection (roving point selection) can then be constructed:

$$\begin{aligned} \theta(i=0) &= \theta_{up} \\ \theta(i) &= \text{solution of } L(\theta) == i\Delta L, \quad 1 \leq i \leq p \\ \theta(p) &= \theta_{down} \end{aligned} \quad (10.9)$$

where “==” stands for “set equal”. As  $\theta(i)$  is the main independent parameter, it will be denoted by  $\theta_i$  to distinct it from other discrete variables. The solution of equation (10.9) usually involves numerical techniques. However, with the particular strategy presented in (10.9), the accumulation of errors is significantly reduced. An alternative method is a step-by-step solution based on either the length integral having  $\theta_{i-1}$  and  $\theta_i$  as boundary values, or an approximation based on the differential that is presented in equation (2.40). Both methods show more error accumulation while the second one additionally introduces round-off errors [μ7]. Nevertheless, when the number of data points  $p$  is sufficient high, the errors can be neglected. The expression describing the consumed fibre length simply becomes:

$$L(i, j) = L(i) + 2jL(p) \quad (10.10)$$

The method we are progressing here can be classified as quasi-analytical; the counter  $i$  results in the corresponding  $\theta_i$ -parameter which determines practically the exact values for the associated angular quantities  $\alpha(\theta)$ ,  $\beta(\theta)$  and  $\phi(\theta)$ . For the geometrical meaning of these parameters we refer here to section 2.4.

### Angular parameters

For simplicity we assume here that the mandrel is a generic shell of revolution, defined in spherical coordinates according to:

$$\begin{aligned} \mathbf{S}(\theta, \phi) &= \{g(\theta) \sin \theta \cos \phi, g(\theta) \sin \theta \sin \phi, g(\theta) \cos \theta\} \\ \text{with } \theta_{up} &\leq \theta \leq \theta_{down} \\ \text{and } 0 &\leq \phi \leq 2\pi \end{aligned} \quad (10.11)$$

According to definition (10.11), the angular parameters can only be determined in the interval  $[\theta_{up}, \theta_{down}]$ . The proper derivation of these quantities for every  $(i, j)$  locus indicator requires some additional work. To enhance this, a two-dimensional representation of a complete wound circuit is considered here (figure 10.5). The treated wound object is divided into four quadrants.

The coordinate  $\theta_{up}$  (usually significantly close to  $z$ -axis) is located in quadrant I, while  $\theta_{down}$  is found in the lower region of quadrant II.

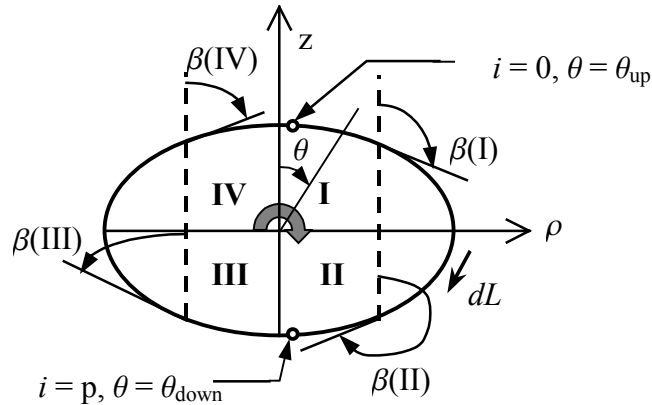


Fig. 10.5: Schematic representation of the four body-related quadrants

The winding process is assumed here to propagate in the positive  $\phi$ -direction, as depicted in figure 2.4. As a result of this assumption, it is fairly easy to conclude that the winding angle will always exhibit positive values (see equations (2.39) and (6.31)). Once again, for convenience (although not necessary), the created circuits are assumed to be geodesic ones. Since the integrand in equation (2.39) remains positive for the entire definition interval, the parameter  $\phi(\theta)$  does automatically exhibit monotonic behaviour. The same property applies on the function describing the consumed roving length (equation (10.7)). In order to ensure the continuation of the fibre placement process, the winding angle  $\alpha(\theta)$  should exhibit values substantially close to  $\pi/2$  at the upper ( $\theta = \theta_{up}$ ) and lower ( $\theta = \theta_{down}$ ) poles. Additionally, according to equation (5.12), the smallest angular value ( $\alpha_m$ ) should be found at the greatest radius of application (in figure 10.5: at  $\theta = \pi/2$ ). These considerations lead to the results presented in table 10.1:

I	II	III	IV
$\pi/2 \rightarrow \alpha_m$	$\alpha_m \rightarrow \pi/2$	$\pi/2 \rightarrow \alpha_m$	$\alpha_m \rightarrow \pi/2$

Table 10.1: Behaviour of the winding angle in the four quadrants

Returning to equation (5.12) and figure 5.1, it becomes evident that the implemented constant  $c$  must equalise the parallel radius at the pole (as derived in chapter 5). With this information, the following winding angle data can be obtained:

$$c = \sqrt{E(\theta_{up})}$$

$$\alpha(i) = \begin{cases} \arcsin\left(\frac{c}{\sqrt{E(\theta_i)}}\right) & 0 \leq i \leq p \\ \alpha(2p-i) & p < i < 2p \end{cases} \quad (10.12)$$

### Part C: Production process

Notice that the sequential circuit number  $j$  does not affect the winding angle propagation. There is no reason to include it [ $\gamma 6$ ].

The calculation of the third angular quantity  $\beta(i)$  is slightly more complicated. In chapter 3, figure 3.4, we presented the relation between  $d\rho$ ,  $dz$  and  $ds$  in terms of the meridian profile inclination angle  $\beta$ :

$$\frac{d\rho}{ds} = \sin \beta, \quad \frac{dz}{ds} = \cos \beta \quad (10.13)$$

In order to obtain the proper sign for the above-presented derivatives (see also figure 10.5), the required angle  $\beta(\theta)$  should have the characteristics presented in table 10.2:

	I	II	III	IV
$\sin\beta$	+	-	+	-
$\cos\beta$	-	-	+	+

Table 10.2: Sign requirements on  $\beta(\theta)$

Taking these requirements into account, the intervals satisfying these conditions are presented in table 10.3:

I	II	III	IV
$\pi/2 \rightarrow \pi$	$\pi \rightarrow 3\pi/2$	$\pi/2 \rightarrow 0$	$0 \rightarrow -\pi/2$

Table 10.3: Quadrant-related ranges for  $\beta(\theta)$

From the body representation (equation (10.11)) and the definition of the meridional differential  $ds$  (first expression in equation (2.6)), the following data generating procedure can be constructed:

$$\beta(i) = \begin{cases} \arccos\left(\frac{dz}{ds}\right) = \arccos\left(\frac{g'(\theta_i)\cos\theta_i - g(\theta_i)\sin\theta_i}{\sqrt{G(\theta_i)}}\right) & 0 \leq i \leq p \\ \beta(2p-i) - \pi & p < i < 2p \end{cases} \quad (10.14)$$

In the above presented equation, it is assumed that the implemented software assumes the solution interval  $(\pi/2, 3\pi/2)$  for a negative arc cosine argument. As additionally mentioned for  $\alpha(i)$ , the solution is not affected by the sequential circuit number  $j$ .

Contrary to  $\alpha(i)$  and  $\beta(i)$ , the parallel angle (second spherical coordinate)  $\phi(i, j)$  exhibits monotonic behaviour. The initial value ( $\theta = \theta_{up}$ ) is indicated by  $\phi_{up}$ , while the angular propagation  $\Delta\phi_c$  after a complete half circuit (from “up” to “down”) can be found by:

$$\Delta\phi_c = 2 \int_{\theta_{up}}^{\theta_{down}} \sqrt{\frac{G(t)}{E(t)}} \tan \alpha(t) dt \quad (10.15)$$

The pseudo function  $\phi(i, j)$  becomes:

$$\Delta\phi(i) = \int_{\theta_{i-1}}^{\theta_i} \sqrt{\frac{G(t)}{E(t)}} \tan \alpha(t) dt, \quad 1 \leq i \leq p$$

$$\phi(i, 0) = \begin{cases} \phi_{up} & i = 0 \\ \phi(i-1, 0) + \Delta\phi(i) & 1 \leq i \leq p \\ 2\phi(p, 0) - \phi(2p-i) & p < i < 2p \end{cases} \quad (10.16)$$

$$\phi(i, j) = \phi(i, 1) + j\Delta\phi_c \quad j \geq 1$$

At this point, the complete set of input data for the kinematic winding solution has been obtained. The solution of equation (10.10) creates a useful mapping from  $i$  to  $\theta$  that generates the required angular parameter values. As mentioned at the beginning of this section, the independent parameter  $\theta$  is called here to construct the link between the discrete values  $(i, j)$  and their corresponding continuous angular quantities  $\alpha(i)$ ,  $\beta(i)$  and  $\phi(i)$ .

### Curvature and torsion

With equations (10.10), (10.12), (10.14) and (10.16) the discrete position vector  $\mathbf{G}(i, j)$  becomes:

$$\mathbf{G}(i, j) = \begin{cases} g(\theta_i) \sin \theta_i \cos \phi(i, j) \\ g(\theta_i) \sin \theta_i \sin \phi(i, j) \\ g(\theta_i) \cos \theta_i \end{cases}^T \cdot \{E_3\} \quad (10.17)$$

According to equation (2.36), the discrete orientation vector  $\Delta\mathbf{G}(i, j)$  is :

$$\Delta\mathbf{G}^T(i, j) = \begin{cases} \cos \alpha(i) \sin \beta(i) \cos \phi(i, j) - \sin \alpha(i) \sin \phi(i, j) \\ \cos \alpha(i) \sin \beta(i) \sin \phi(i, j) + \sin \alpha(i) \cos \phi(i, j) \\ \cos \alpha(i) \cos \beta(i) \end{cases}^T \cdot \{E_3\} \quad (10.18)$$

On a similar way, the discrete binormal vector  $\mathbf{B}$  can be obtained by recalling equation (2.37):

### Part C: Production process

$$\mathbf{B}^T(i, j) = \begin{Bmatrix} -\sin \alpha(i) \sin \beta(i) \cos \phi(i, j) - \cos \alpha(i) \sin \phi(i, j) \\ -\sin \alpha(i) \sin \beta(i) \sin \phi(i, j) + \cos \alpha(i) \cos \phi(i, j) \\ -\sin \alpha(i) \cos \beta(i) \end{Bmatrix}^T \cdot \{E_3\} \quad (10.19)$$

An alternative method to determine  $\Delta \mathbf{G}(i, j)$  is, instead of using equation (10.18), to construct the finite differences:

$$\Delta \mathbf{G}(i, j) = \frac{\mathbf{G}(i, j) - \mathbf{G}(i-1, j)}{\|\mathbf{G}(i, j) - \mathbf{G}(i-1, j)\|} \quad (10.20)$$

Notice that the approximation for  $\mathbf{B}$  is similar to (10.20). Although this alternative method can imply a data and calculation time reduction, it virtually represents a first order approximation of the tangent vector. The accuracy is generally sufficient if the step  $\Delta L$  is small enough [19, 10, 23, 24]. An important exception on this statement reflects on the fibre path near the pole areas of the treated mandrel, where the winding angle rapidly tends towards the value of  $\pi/2$  [rad]. Even by very small incremental length steps, problems can arise in the form of rigorous direction changes of the tangent vector. If the final difference method is preferable, a data averaging procedure has to be implemented, resulting in a smooth orientation change of the tangent vector when crossing over the pole. Despite its incremental character, the method according to equations (10.17) and (10.18) provides practically the exact values for the components of  $\mathbf{G}(i, j)$  and  $\Delta \mathbf{G}(i, j)$  [76].

According to equation (2.24) with  $\Delta \mathbf{T} = \Delta(\Delta \mathbf{G})$ , the local curvature can be obtained as follows:

$$k_t(i, j) = \frac{\|\Delta \mathbf{G}(i, j) - \Delta \mathbf{G}(i-1, j)\|}{\Delta L}, \quad i \geq 1 \quad (10.21)$$

On a way entirely similar to (10.21), the torsion is given by:

$$\tau(i, j) = \frac{\|\mathbf{B}(i, j) - \mathbf{B}(i-1, j)\|}{\Delta L}, \quad i \geq 1 \quad (10.22)$$

### 10.3 Examples

In order to verify the calculation method presented in the previous section, three wound body morphologies have been selected for study: a very flat ellipsoid with an aspect ratio of “height / equatorial diameter” equal to 0.1, a cylindrical pressure vessel with isotensoidal end domes, and a sphere. The latter serves the aim of verifying the correct values for the curvature and torsion. In every example, the value of  $p$  (number of data points from the upper to the lower pole) has been set equal to 200.

The applied fibre trajectories are geodesic, so the total curvature coincides with the total curvature (equation (2.16) with  $k_g = 0$ ). Therefore, the obtained curvature values are referred to as “normal curvature”.

#### Calculation method

The shapes under consideration are shells of revolution, analytically described in spherical coordinates (definition (10.11)). Their metrics in meridional and parallel direction are given by equation (6.27). Furthermore, we assume that the objects have two equal polar openings with a radius  $c$ . In combination with the assumption of creating geodesic trajectories with a dimensionless fibre bundle, the winding angle at every point can be described by equation (10.12) (in the case of a non-zero bundle width, the parameter  $c$  has to be increased according to the fibre bundle dimensions and the meridian morphology at the area surrounding the polar openings, see section 8.1). The second (parallel) coordinate describing the roving path is given by equation (10.16), while the meridian inclination angle is obtained with the aid of equation (10.14).

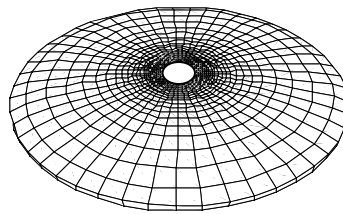
For a proper data point distribution, the total fibre length of one quadrant is calculated with equation (10.7) and divided into 200 intervals. The corresponding  $\theta(i)$ -values are then determined by numerically solving equation (10.9) (secant method). With the aid of equations (10.10), (10.12), (10.14) and (10.16), the position vector  $\mathbf{G}$  and the orientation vector  $\Delta\mathbf{G}$  become fully determined (equations (10.17) and (10.18), respectively). As a final step, the normal curvature and torsion at every point belonging to the fibre path are numerically evaluated with equations (10.21) and (10.22), respectively.

The complete set of intermediate and final results (with an exception for equation (10.9)) is analytically created. Depending on the meridian profile (which is the basic geometric input for this strategy), several steps may not be suitable for analytical determination. In the case of non-geodesic winding, the derivation of the winding angle distribution along the meridian will usually require the numerical solution of equation (6.17); this can be carried out by standard procedures like Runge-Kutta (section 6.3) [ $\mu 4, \mu 7, \mu 8$ ]. Next, the resulting winding angle distribution along the meridian can be described in the form of an interpolating polynomial. With this polynomial, the parallel coordinate  $\phi$  can be obtained by numerical integration of equation (10.16) with common methods, for instance Simpson.

## Part C: Production process

The same treatment can be applied on equation (10.7) for the determination of the fibre length. Application of e.g. the secant method on equation (10.9) will then provide the desired data point distribution. In general, the determination of  $\beta$  does not provide any reason for evaluating with numerical techniques. The complete set of the angular quantities ( $\alpha$ ,  $\beta$  and  $\phi$ ) can finally be described in the form of interpolating polynomials (as an expression of  $\theta$ ). Consequently, for a particular  $\theta(i)$ - value, the corresponding discrete angular values become immediately available. With these values, the required position and orientation vector quantities can easily be obtained. The same property applies on the determination of the normal curvature and torsion related values (equations (10.21) and (10.22)).

### Flat ellipsoid



$$\begin{aligned}\rho_{\text{pole}} &= 1 \\ \rho_{\text{max}}/\rho_{\text{min}} &= 10 \\ \text{Roving width} &= \rho_{\text{min}}/1000\end{aligned}$$

Fig. 10.6: An extremely flat ellipsoidal shell of revolution

The circuits applied on the treated shell (figure 10.6) are geodesic, while the fibre width is equalised to 0.001 length units. The obtained data collections are here presented with a continuous counter ( $i+jp$  instead of  $(i, j)$ ). The angular values for  $\alpha(i)$ ,  $\beta(i)$  are presented in figures (10.7) and (10.8) respectively, while  $\phi(i, j)$  is parametrically presented in figure (10.9) as an expression of  $\theta_i$ .

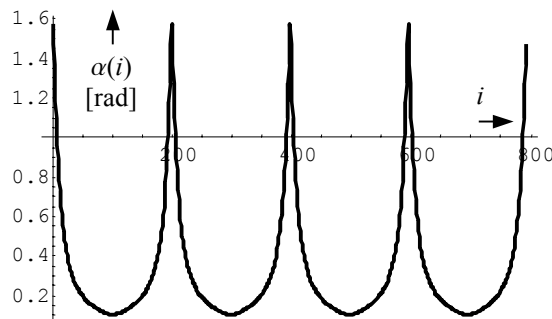


Fig. 10.7:  $\alpha(i)$  [rad] as a function of  $i$  (one circuit = 400 points)

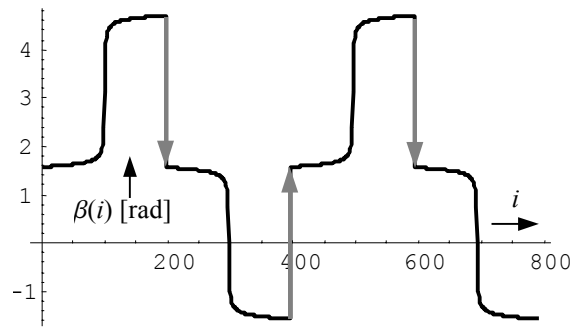


Fig. 10.8:  $\beta(i)$  [rad] as a function of  $i$  (one circuit = 400 points)

While the winding angle  $\alpha(i)$  has smooth behaviour,  $\beta(i)$  is showing an abrupt value modification when passing the equatorial area ( $i$  around 100, 300 etc). This property is associated with the sharp corner at the edge of the shell.

The expectation arises that the curvature should also exhibit large modifications. Notice the arrows in figure 10.8 representing a discontinuous “jump” from  $3\pi/2$  to  $\pi/2$  and so on, according to equation (10.14) and table 10.3.

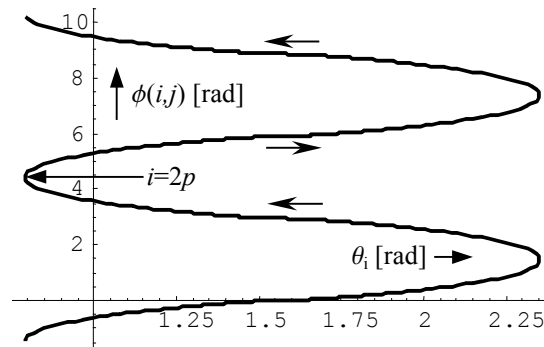


Fig. 10.9:  $\phi(i, j)$  [rad], parametrically related to  $\theta_i$  (one circuit = 400 points)

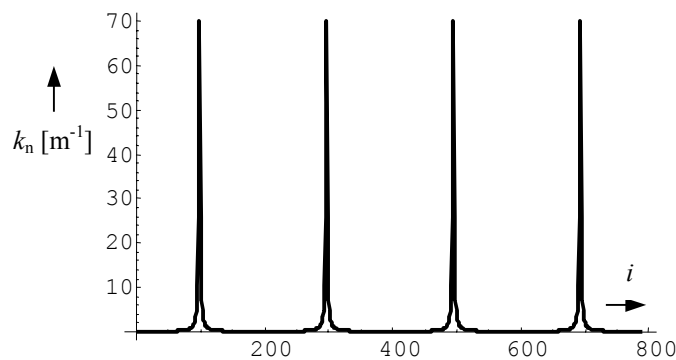


Fig. 10.10:  $\kappa(i, j)$  as a function of  $i$  (one circuit = 400 points)

Typical are the extreme normal curvature values at the equatorial plane of the ellipsoid (fig. 10.10); at that locus, the fillet radius is extremely small. The

## Part C: Production process

torsion of the fibre bundle when passing the equator is even more radical . This passage is physically comparable with folding a tape over the edge of a flat plane.

### Cylindrical pressure vessel

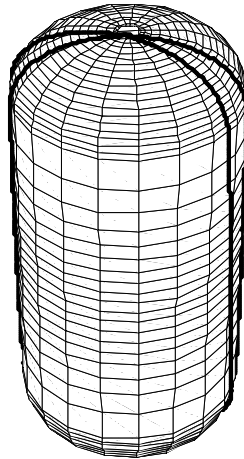


Fig. 10.11: A typical cylindrical pressure vessel ( $\rho_{\text{pole}} = 0.05$ ,  $\rho_{\text{max}} / \rho_{\text{pole}} = 10$ , cylinder height =  $30 \times \rho_{\text{pole}}$ )

Here, a geodesically wound pressure vessel is considered (figure 10.11), consisting of a cylindrical part and isotensoidal end domes (chapters 3 and 4). The winding angle (figure 10.12) at the poles becomes slightly less than  $\pi/2$ . This property is dictated by the static force equilibrium of the roving (demonstrated in the denominator of equation (4.3) where the argument of the square root nullifies before  $Y$  can reduce to 1). In practice however, in order to create a smooth transition to the subsequent wound circuit, the winding angle has to reach the value of  $\pi/2$  when passing the polar areas (section 8.2). Nevertheless, in figure 10.12, the reduced value for the winding angle has been preserved.

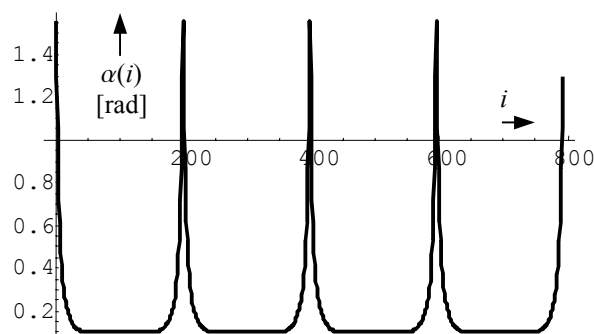


Fig. 10.12:  $\alpha(i)$  [rad] as a function of  $i$  (one circuit = 400 points)

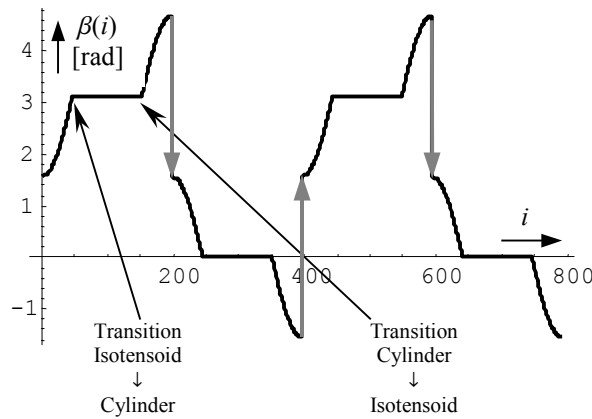


Fig. 10.13:  $\beta(i)$  [rad] as a function of  $i$  (one circuit = 400 points)

At the cylindrical part, the winding angle  $\alpha(i)$  and the inclination angle  $\beta(i)$  remain constant. The morphology of  $\beta(i)$  (figure 10.13) already provides a hint regarding the expected normal curvature discontinuities when transiting from the isotensoidal to the cylindrical region ( $i = 50, 150$  etc.). The propagation of the second spherical coordinate  $\phi$  is given in figure 10.14.

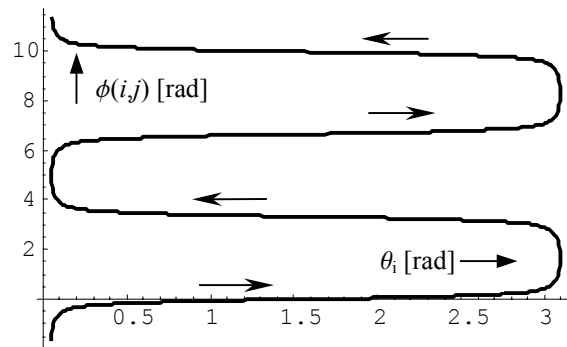


Fig. 10.14:  $\phi(i, j)$  [rad], parametrically related to  $\theta_i$  (one circuit = 400 points)

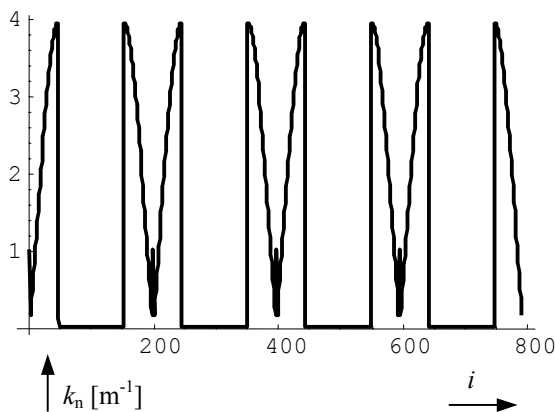


Fig. 10.15: Normal curvature distribution on a cylindrical pressure vessel (two circuits shown)

## Part C: Production process

As previously mentioned, the normal curvature exhibits discontinuities at the transitional areas ( $i = 50, 150$  and so on, figure 10.15 and section 15.3). Furthermore, the peaks on  $i = 200, 400$  etc. correspond with the pole locations. In order to assure a smooth transition from a particular circuit to the next one, the corresponding winding angle should be equal to  $\pi/2$ . This implies that the corresponding path radius should be exactly equal to the pole radius (equation 10.12). However, dictated by the theory for optimal pressure vessels, the actual minimum radius becomes slightly bigger, which is a property resulting in a reduced winding angle at the pole.

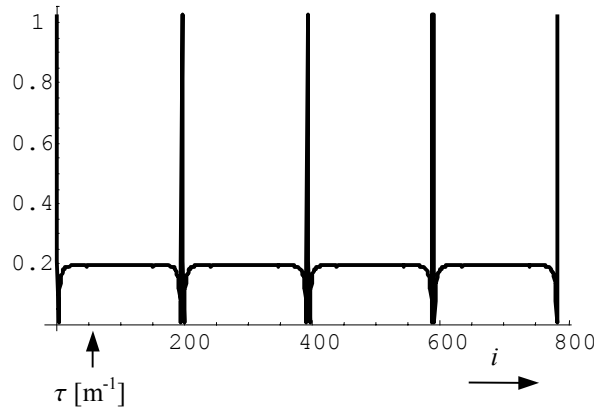


Fig. 10.16: Fibre torsion distribution on a cylindrical pressure vessel

Regarding the fibre torsion distribution (figure 10.16), notice again the peaks on  $i = 200, 400$  etc.; these are again introduced by the slightly decreased winding angle at the poles (equation (5.12)).

The discontinuous character of  $\beta(i)$  when transiting from the isotensoidal part to the cylindrical one and vice versa, affects the normal curvature significantly more when compared to the fibre torsion. The explanation for this phenomenon is as follows: at the treated loci, the winding angle is very small, so  $\cos\alpha(i)$  approaches its maximum value (in this case: 0.995). The total curvature is obtained by numerical differentiation of  $\Delta G$  (equations (10.18) and (10.21)). In the expression for  $\Delta G$ , the terms containing  $\beta(i)$  are multiplied by  $\cos\alpha(i)$  that obtains its maximum value at these loci. The opposite case applies on the fibre torsion (differentiation of equation (10.19) according to (10.22)) where the  $\beta(i)$ -containing factors are multiplied by  $\sin\alpha(i)$ , being there a small value.

## Sphere

Since a geodesic on a sphere is not able to create angular propagation between two adjacent wound circuits (see the introduction of chapter 5), this item is not particularly interesting for filament winding applications. However, since the normal curvature (= sphere radius) and fibre torsion (= 0) are constant, the sphere forms a suitable test object for the accuracy of the

determination procedure for these quantities. A sphere is assumed here with a radius equal to 1. In addition, the sphere contains two openings at the upper and lower pole; both have a radius of 0.1 units of length.

The constant normal curvature implies that the rate of change of the orientation vector is constant. The zero-torsion implies that the treated fibre remains in the same plane.

The obtained results coincide exactly with the expected values:  $\kappa_n = 1$ ,  $\tau_n = 0$ . However, when the length increment  $\Delta L$  (equations (10.21) and (10.22)) approaches the same order as that of the numerical accuracy characterising the evaluation of equations (10.7) and (10.16), instabilities in the final result may be expected. Alternatively, integration of the previous mentioned equations can be carried out analytically (section 5.4).

## **Part C: Production process**

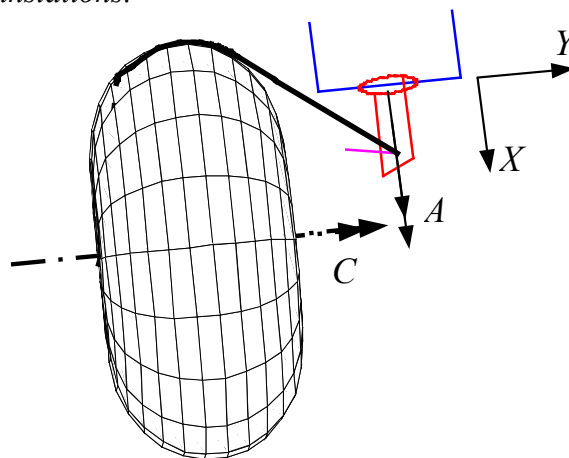
## 11

## kinematic model

With the generic machine configuration outlined in the previous chapter, we derive here the kinematic equations and provide their solution. Due to the generic machine geometry, the derived equations should be suitable to deal with every possible winding machine configuration. However, in order to create a well-determined solution, various assumptions have been made, mainly regarding the coupling between the involved machine movements (translations and rotations). These couplings should preferably be derived by optimisation techniques.

After the presentation of the basic system of kinematic equations we proceed to the outline of several characteristic expressions and parameters and formulate their solution conditions. In the section 11.2, the two most common machine configurations are considered: the lathe winder, and the tumble winder. For the lathe winder, the complete set of required movements can be derived analytically. For the tumble winder however, this is not possible. The associated numerical solution procedure for the generic machine configuration (which covers both the lathe and the tumble winder) is outlined in section 11.3 and evaluated in the last section where we present several results. These results reflect on the complete set of involved movements, as well as the velocity profiles of the applied roving.

The solution method presented here can be characterised by robustness, sufficient accuracy and short calculation times. These properties make the method suitable for optimisation purposes. The obtained results clearly indicate that for a particular wound object geometry, the most suitable winding machine configuration is not always the lathe winder. In addition, the use of a lathe winder without cross carriage is generally not feasible due to excessive feed eye translations.



Top view of a lathe winder with the feed eye translations  $X$  and  $Y$ , mandrel rotation  $C$  and feed eye roller inclination  $A$

## **Part C: Production process**

## 11.1 Winding equations

### Initial system

The generic machine configuration is outlined in section 10.1. As depicted in figure 10.1, we consider here a locus  $\mathbf{G}.\{E_3\}$  belonging to the fibre path under consideration. The orientation of the tangent vector is  $\Delta\mathbf{G}.\{E_3\}$  (figure 10.4). The body containing that path is rotated according to a particular, temporarily unknown set of values  $Q$ ,  $\gamma$  and  $R$  [rad], figures 10.2 and 10.3. This set of values corresponds to a particular position  $\mathbf{p}.\{E_0\}$  of the delivery eye. The line connecting  $\mathbf{p}$  and  $\mathbf{G}$  has a length  $\lambda$ . As derived in the previous chapter, the corresponding equation is, [19]:

$$\mathbf{G}.\{E_3\} + \lambda\Delta\mathbf{G}.\{E_3\} = \mathbf{p}.\{E_0\} \quad (11.1)$$

Translation of this equation in  $\{E_0\}$  results in (equation (10.6)):

$$\mathbf{G}.[R_{tot}].\{E_0\} + \lambda\Delta\mathbf{G}.[R_{tot}].\{E_0\} = \mathbf{p}.\{E_0\} \quad (11.2)$$

where  $[R_{tot}]$  is given in (10.4). Rearranging and dropping of  $\{E_0\}$  leads to:

$$\mathbf{G}.[R_{tot}] - \mathbf{p} + \lambda\Delta\mathbf{G}.[R_{tot}] = \mathbf{0} \quad (11.3)$$

We introduce now the following vectors:

$$\begin{aligned} \mathbf{v}_1 &= \begin{Bmatrix} v_{11} \\ v_{12} \\ v_{13} \end{Bmatrix} = [R_{tot}].\mathbf{G}^T = [R_{tot}].\begin{Bmatrix} G_x \\ G_y \\ G_z \end{Bmatrix} \\ \mathbf{v}_2 &= \begin{Bmatrix} v_{21} \\ v_{22} \\ v_{23} \end{Bmatrix} = [R_{tot}].\Delta\mathbf{G}^T = [R_{tot}].\begin{Bmatrix} \Delta G_x \\ \Delta G_y \\ \Delta G_z \end{Bmatrix} \end{aligned} \quad (11.4)$$

The winding equation becomes:

$$\mathbf{v}_1 - \mathbf{p}^T + \lambda\mathbf{v}_2 = \mathbf{0}^T \quad (11.5)$$

Expressing this in matrix form gives:

$$\begin{bmatrix} v_{11} & -p_x & v_{21} \\ v_{12} & -p_y & v_{22} \\ v_{13} & -p_z & v_{23} \end{bmatrix} \begin{Bmatrix} 1 \\ 1 \\ \lambda \end{Bmatrix} = \mathbf{M} \cdot \begin{Bmatrix} 1 \\ 1 \\ \lambda \end{Bmatrix} = \begin{Bmatrix} 0 \\ 0 \\ 0 \end{Bmatrix} \quad (11.6)$$

### Part C: Production process

This homogeneous linear system of equations involves the following unknowns:

- Row 1:  $Q, \gamma, R, p_x, \lambda$
- Row 2:  $\gamma, R, p_y, \lambda$
- Row 3:  $Q, \gamma, R, p_z, \lambda$

### Characteristic equations

Since  $\lambda \neq 0$ , the system (10) has a non-trivial solution if  $[\mu 2, \mu 7, \mu 8]$ :

$$\begin{aligned} \det[\mathbf{M}] &= p_x(v_{12}v_{23} - v_{13}v_{22}) \\ &+ p_y(v_{13}v_{21} - v_{11}v_{23}) \\ &+ p_z(v_{11}v_{22} - v_{12}v_{21}) = 0 \end{aligned} \quad (11.7)$$

Before proceeding to the detailed expression for equation (11.7), we introduce:

$$\begin{aligned} U_{xy} &= \det \begin{bmatrix} G_x & \Delta G_x \\ G_y & \Delta G_y \end{bmatrix} \\ U_{yz} &= \det \begin{bmatrix} G_y & \Delta G_y \\ G_z & \Delta G_z \end{bmatrix} \\ U_{zx} &= \det \begin{bmatrix} G_z & \Delta G_z \\ G_x & \Delta G_x \end{bmatrix} \end{aligned} \quad (11.8)$$

Writing out of equation (11.7) results in:

$$\det[\mathbf{M}] = D_x p_x + D_y p_y + D_z p_z = 0 \quad (11.9)$$

where:

$$\begin{aligned} D_x &= cQ(U_{yz}cR - U_{zx}sR) + sQ[U_{xy}c\gamma + (U_{zx}cR + U_{yz}sR)s\gamma] \\ D_y &= c\gamma(U_{zx}cR + U_{yz}sR) - U_{xy}s\gamma \\ D_z &= -sQ(U_{yz}cR - U_{zx}sR) + cQ[U_{xy}c\gamma + (U_{zx}cR + U_{yz}sR)s\gamma] \end{aligned} \quad (11.10)$$

It can easily be shown that the multipliers  $D_{\#}$  can never simultaneously be equal to zero since:

$$D_x^2 + D_y^2 + D_z^2 = U_{xy}^2 + U_{yz}^2 + U_{zx}^2 \neq 0 \quad (11.11)$$

The identification of the rows in  $\mathbf{M}$  that contain similar unknowns can create an alternative solution procedure. One can easily observe that rows 1

and 3 include  $Q$  among the other unknowns. Hence, the following reduced matrix can be constructed:

$$\begin{bmatrix} v_{11} - p_x & v_{21} \\ v_{13} - p_z & v_{23} \end{bmatrix} \begin{Bmatrix} 1 \\ \lambda \end{Bmatrix} = \mathbf{N} \cdot \begin{Bmatrix} 1 \\ \lambda \end{Bmatrix} = \begin{Bmatrix} 0 \\ 0 \end{Bmatrix} \quad (11.12)$$

The non-trivial solutions are generated by the following condition:

$$\det[\mathbf{N}] = T_x p_x - D_y - T_z p_z = 0 \quad (11.13)$$

with:

$$\begin{aligned} T_x &= -sQ(\Delta G_x cR - \Delta G_y sR) + cQ[\Delta G_z c\gamma + (\Delta G_y cR + \Delta G_x sR)s\gamma] \\ T_z &= cQ(\Delta G_x cR - \Delta G_y sR) + sQ[\Delta G_z c\gamma + (\Delta G_y cR + \Delta G_x sR)s\gamma] \end{aligned} \quad (11.14)$$

The above-presented expressions can also be viewed as inner vector products:

$$T_x = \{-sQ, cQ\} \cdot \begin{Bmatrix} A \\ B \end{Bmatrix}, \quad T_z = \{cQ, sQ\} \cdot \begin{Bmatrix} A \\ B \end{Bmatrix} \quad (11.15)$$

The row vectors involved here are orthogonal; this implies that  $T_x$  and  $T_z$  can not simultaneously be equal to zero. The same property reflects on the  $D_{\#}$  multipliers defined in equation (11.10).

### Length of the free hanging fibre

Both equations (11.9) and (11.13) can be used to obtain a solution. Notice that these equations do not require any a-priori knowledge of  $\lambda$ . Additionally, in equation (11.13) only two coordinates of the feed eye position are involved. The remaining coordinate  $p_y$  can be calculated by using row 2 of the system presented in equation (11.6). However, for the determination of  $p_y$  the value of  $\lambda$  must be known. This can be calculated by evaluating row 1 or row 3 of system (11.6).

Alternatively, a general expression for  $\lambda$  can be obtained as follows; from equation (10) we obtain:

$$\begin{aligned} \|\mathbf{p}\| &= \sqrt{\mathbf{p} \cdot \mathbf{p}} = \sqrt{(\mathbf{v}_1 + \lambda \mathbf{v}_2) \cdot (\mathbf{v}_1 + \lambda \mathbf{v}_2)} = \\ &= \sqrt{(\mathbf{G} + \lambda \Delta \mathbf{G}) \cdot (\mathbf{G} + \lambda \Delta \mathbf{G})} = \\ &= \sqrt{\mathbf{G} \cdot \mathbf{G} + 2\mathbf{G} \cdot \Delta \mathbf{G} + \Delta \mathbf{G} \cdot \Delta \mathbf{G}} = \\ &= \sqrt{g'(\theta)^2 + 2h(\theta) + 1} \end{aligned} \quad (11.16)$$

## Part C: Production process

where  $\mathbf{p} = \{p_x, p_y, p_z\}$  and  $g(\theta)$  is the function that describes the meridian profile. Note that the length of the orientation vector  $\Delta\mathbf{G}$  is equal to 1. The length of  $\mathbf{G}$  can immediately be derived from equation (10.17). In addition, with the expression for  $\Delta\mathbf{G}$  (equation (10.18)), the inner vector product  $\mathbf{G} \cdot \Delta\mathbf{G}$  ( $= h$ ) becomes:

$$h(\theta) = g(\theta) \cos \alpha(\theta) \cos(\beta - \theta) = \cos \alpha(\theta) \frac{g(\theta)g'(\theta)}{\sqrt{g(\theta)^2 + g'(\theta)^2}} \quad (11.17)$$

where  $g'(\theta) = dg(\theta)/d\theta$ . The function  $h$  expresses the verticality between the vectors  $\mathbf{G}$  and  $\Delta\mathbf{G}$  where, next to the meridian function  $g$ , the winding angle  $\alpha$  is playing an important role. As an example, for a geodesic on a sphere, the verticality function  $h(\theta)$  is equal to zero ( $g'(\theta) = 0$ ); this leads to an associated space angle equal to  $\pi/2$  radians ( $= \arccos(h(\theta)) = \arccos(0)$ ). Obviously, a fibre path placed on a sphere always exhibits a tangent vector perpendicular to the associated position vector.

From this point, we denote the involved scalar functions without the argument. For the determination of the length of the free-hanging fibre, we substitute equation (11.17) into (11.16) and solve for  $\lambda$ . After dropping the negative solution, the result is:

$$\lambda = -h + \sqrt{(p_x^2 + p_y^2 + p_z^2) - g^2 + h^2} \quad (11.18)$$

The obtained expression is rotation invariant. Consequently, the length of the free hanging fibre can be obtained without any information regarding the orientation of the body. The position of the feed eye however, must be known.

### Consumed fibre speed

Referring to figure 10.1, the fibre spool is located at  $\{R_x, R_y, R_z\} \cdot \{E_0\}$ . At the same time the feed eye location is given by  $\{p_x, p_y, p_z\} \cdot \{E_0\}$ . The involved  $z$ -coordinates are usually equal to zero. Accordingly, we define:

$$\sigma = \sqrt{(R_x - p_x)^2 + (R_y - p_y)^2} \quad (11.19)$$

For a certain locus ( $i, j$ ) of the tow path on the mandrel, the total roving length is given by:

$$S(i, j) = L(i, j) + \lambda(i, j) + \sigma(i, j) \quad (11.20)$$

where the implemented quantities are all expressed as a function of the fibre locus  $i$ , belonging to the  $j^{\text{th}}$  circuit (hence, the locus indicator is  $(i, j)$ ). Notice that the delivery eye coordinates are also depending on  $\lambda$ ; this implies that the

total fibre length can additionally be controlled by the proper variation of that parameter.

The kinematic solution usually expresses the required machine movements as a function of  $(i, j)$  and not as a function of time. Assuming for example that the primary rotation speed  $Q'$  is constant, we can obtain the consumed fibre length as a function of time  $(S(t))$  by inverse Lagrange interpolation  $[\mu 2, \mu 5]$ . In theory, the higher the order is of the interpolation degree, the better the accuracy will be. However, since the interpolation formulae of Lagrange attempt to intersect every given data point, irregular behaviour of the interpolating polynomial  $S(t)$  can be expected. The (numerical) consumed fibre speed and acceleration profiles can be derived by numerical differentiation of the constant time increment points that are generated with the aid of the obtained interpolating polynomials. These techniques are extensively discussed in chapter 12.

## 11.2 Machine configurations

As previously stated, the general expression for the system of kinematic equations (11.6) involves three unknown rotations  $\{Q, \gamma, R\}$  and three unknown translations  $\{p_x, p_y, p_z\}$ . Since there are only three kinematic equations available, a reduction of the number of unknowns must be realised. This can be achieved by firstly assuming a certain winding machine configuration and secondly by coupling various degrees of freedom to each other. This coupling is usually dictated by the machine characteristics in terms of available space and acceleration limits [α23,α24,α42]. These limits generally reflect on moving machine parts and fibre tensioning devices [ν1]. We present here the most common configurations: the lathe winder and the tumble winder.

### Lathe winder

The lathe winder configuration is given by:  $\gamma = -\pi/2$  and  $p_z = 0$ , (figure 11.1):

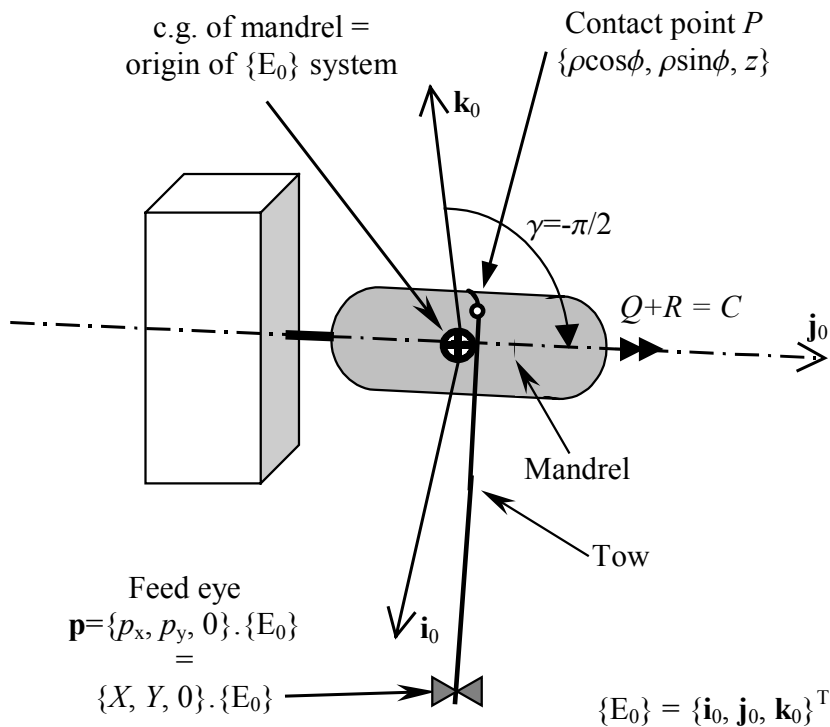


Fig. 11.1: Schematic layout of a lathe winder

For simplicity we use here a polar coordinate system for the body, which is indicated in the figure. With  $C = Q+R$ , the system of kinematic equations (11.6) becomes:

$$\begin{cases} p_x \\ p_y \\ p_z \end{cases} = \begin{cases} X \\ Y \\ 0 \end{cases} = \begin{cases} \rho \cos(C + \phi) - \lambda[\sin \alpha \sin(C + \phi) - \cos \alpha \sin \beta \cos(C + \phi)] \\ z + \lambda \cos \alpha \cos \beta \\ -\rho \sin(C + \phi) - \lambda[\sin \alpha \cos(C + \phi) + \cos \alpha \sin \beta \sin(C + \phi)] \end{cases} \quad (11.21)$$

where we assumed that  $Z = 0$ . The determinant of  $\mathbf{N}$  (equation (11.12)) becomes:

$$-\rho \sin \alpha + X[\sin \alpha \cos(C + \phi) + \cos \alpha \sin \beta \sin(C + \phi)] = 0 \quad (11.22)$$

We introduce [16]:

$$\begin{aligned} \omega &= C + \phi \quad (= Q + R + \phi) \\ \eta &= [\sin \alpha \cos \omega + \cos \alpha \sin \beta \sin \omega] \end{aligned} \quad (11.23)$$

Notice that  $\eta$  is the same as  $v_{23}$ , which is provided by equation (11.4) with  $\Delta \mathbf{G}$  determined by (10.18). With the third row of equation (11.21) and the determinant (11.22), the following system can be constructed:

$$-\begin{cases} \det[\mathbf{N}] \\ Z \end{cases} = \begin{cases} \rho \sin \alpha - X\eta \\ \rho \sin \omega + \lambda\eta \end{cases} = \begin{cases} 0 \\ 0 \end{cases} \quad (11.24)$$

From the solution of (11.24) and the second row of (11.21) we finally obtain the required machine movements:

$$\begin{aligned} C &= -\phi \pm \arcsin \left( \frac{\lambda \sin \alpha}{\sqrt{\lambda^2 \sin^2 \alpha + (\rho + \lambda \cos \alpha \sin \beta)^2}} \right) \\ X &= \sqrt{\lambda^2 \sin^2 \alpha + (\rho + \lambda \cos \alpha \sin \beta)^2} \\ Y &= \rho + \lambda \cos \alpha \cos \beta \end{aligned} \quad (11.25)$$

The proper sign for the  $C$ -rotation can be derived as follows: in equation (11.24) the factor  $\rho \sin \alpha$  is always positive; especially in the case of geodesic winding, it is equal to the radius of the polar opening. With  $X > 0$  and  $\lambda \geq 0$ , we can easily derive that  $\sin \omega$  must always be negative. Consequently the parameter  $\omega$  is subjected to:  $-\pi/2 \leq \omega \leq \pi/2$ . The third row of equation (11.21) gives:

$$\begin{aligned} \cos \omega &= -\left( \frac{\sin \omega}{\lambda \sin \alpha} \right) (\rho + \lambda \cos \alpha \sin \beta) = \text{const}_{\text{pos}} (\rho + \lambda \cos \alpha \sin \beta) \\ \Rightarrow \text{sgn}(\cos \omega) &= \text{sgn}(\rho + \lambda \cos \alpha \sin \beta) = \text{sgn}(\Xi) \end{aligned} \quad (11.26)$$



$$\begin{aligned}
 C &= -\phi \\
 A &= \arctan\left(\frac{\cos \beta}{\tan \alpha}\right) \\
 X &= \rho \\
 Y &= z
 \end{aligned} \tag{11.29}$$

### Tumble winder

Typical tumble winder configurations correspond to a fixed inclination angle  $\gamma$ , while  $p_z$  is equal to zero [ $\alpha 23, \alpha 40, \alpha 41, \iota 18, \iota 19$ ]. These choices are based on reasons associated with machine dynamics and winding antisymmetry, respectively. Additional assumptions can be found in terms of the a-priori determination of  $R$  as a function of  $Q$  and  $p_x = \text{constant}$ . With these assumptions, the problem has a well-defined solution. Summarising, we have:

$$\begin{aligned}
 p_x &= \text{const} \geq \max\|\mathbf{G}\| \\
 p_z &= 0 \\
 \gamma &= \text{const} \\
 R &= f(Q)
 \end{aligned} \tag{11.30}$$

The unknown rotation  $Q$  can be determined by solving equation (11.13) with  $T_x$  given by (11.14) and  $D_y$  by (11.10):

$$\begin{aligned}
 p_x \{ & -\sin Q[\Delta G_x \cos R(Q) - \Delta G_y \sin R(Q)] \\
 & + \cos Q[\Delta G_z \cos \gamma + (\Delta G_y \cos R(Q) + \Delta G_x \sin R(Q)) \sin \gamma] \} \\
 & == \\
 & \cos \gamma [U_{zx} \cos R(Q) + U_{yz} \sin R(Q)] - U_{xy} \sin \gamma
 \end{aligned} \tag{11.31}$$

The solution for  $Q$  can be obtained by standard procedures like Regula Falsi, Newton-Raphson or the secant method [ $\mu 1-4, \mu 7, \mu 8, \mu 14, \mu 15$ ]. The required feed eye movement can be calculated by evaluating row 2 of system (11.6):

$$p_y = \cos \gamma [S_y \cos R(Q) + S_x \sin R(Q)] - S_z \sin \gamma \tag{11.32}$$

where:

$$\begin{Bmatrix} S_x \\ S_y \\ S_z \end{Bmatrix} = \begin{Bmatrix} G_x \\ G_y \\ G_z \end{Bmatrix} + \lambda \begin{Bmatrix} \Delta G_x \\ \Delta G_y \\ \Delta G_z \end{Bmatrix} \tag{11.33}$$

### Part C: Production process

The required value of  $\lambda$  can be obtained by evaluating row 1 or row 3 of equation (11.6):

$$\lambda = -\frac{v_{13}}{v_{23}} \quad \text{or} \quad \lambda = \frac{p_x - v_{11}}{v_{21}} \quad (11.34)$$

For checking the results, equation (11.18) can be used to verify  $\lambda$ . In the case of demanding a zero feed eye translation, the corresponding rotation  $R_0$  is given by setting equation (11.32) equal to zero and solving for  $R$ :

$$R_0 = -\arccos\left(\frac{S_x \sqrt{S_x^2 + S_y^2 - S_z^2 \tan \gamma} + S_y S_z \tan \gamma}{S_x^2 + S_y^2}\right) \quad (11.35)$$

It should be noted that a solution for zero feed eye translation is not always feasible; this is mainly depending on the actual value of  $\gamma$ . In addition, the behaviour of  $R_0$  can become very irregular. The conclusion can be drawn that the zero feed eye translation is in general not a practical solution. However, this equation is very useful for determining the  $R$ -value at the beginning of the winding process: the placement of the roving tangent to the polar opening. A necessary condition for this solution is the knowledge of the corresponding  $\lambda$ -value; for a rotationally symmetric object, the solution for that  $\lambda$  can be found by evaluating equation (11.18):

$$\lambda = -h + \sqrt{(p_x^2 + 0^2 + 0^2) - g^2 + h^2} \quad (11.36)$$

When expecting relatively small feed eye movements, this equation can be used as a predictor for directly solving  $Q$  out of row 1 or row 3 of system (11.6). As a last remark, it should be noted that the model corresponding to the tumble winder also covers the lathe configuration. This is the reason for focussing in the next section on solution techniques and initial conditions reflecting on this generic, tumble winder-related model.

### 11.3 Solution procedure

The kinematic equations for the tumble winder can also be applied on the lathe winder; in this case, the angle  $\gamma$  should be set equal to  $\pm\pi/2$ . As demonstrated in the previous section, the secondary rotation  $R$  will then automatically be added to or subtracted from  $Q$ . However, in the case of  $\gamma \neq \pi/2$ , a problem arises in regard to the selection of the function that couples  $Q$  to  $R$ . In addition, a second problem is the determination of the initial values for  $Q$ ,  $R$  and  $p_y$ .

#### Initial values

The main question now is which function to assume for the coupling of  $R$  and  $Q$ . To facilitate the control of the movements of the tumble winder, we introduce here a linear relation [α23,ι18,ι19]:

$$R(Q) = R_0 + \nu(Q - Q_0) \quad (11.37)$$

where  $R_0$  and  $Q_0$  are the initial values corresponding to roving placement at the polar opening of the object under consideration. The gear ratio is given by  $\nu$ ; this value is determined by the desired winding pattern [α3,ι19] and can be expressed as a ratio of integer numbers. By adapting the implemented gears to this ratio, we can ensure the creation of a perfect winding pattern.

The initial point of the first wound circuit is given by the coordinates  $\rho_0 (= g_0 \sin \theta_0)$  and  $z_0 (= g_0 \cos \theta_0)$  that correspond to the upper polar opening of the shell to be wound (figure 10.5). The parallel angle  $\phi$  at that point in the  $\{x_3, y_3\}$  plane (figure 10.4) is denoted by  $\phi_0$ . For the definition of  $\phi$  we refer to figure 2.4 where the local reference frame  $\{\mathbf{e}_m, \mathbf{e}_p, \mathbf{e}_n\}$  coincides with the  $\{x_3, y_3, z_3\}$  frame used here. We further assume that the windings propagate in the positive  $\phi$ -direction, and that the first time the roving passes the equator, the  $\phi$  angle is equal to zero. This implies that the initial  $\phi$  value ( $= \phi_0$ ) is negative. The turn around angle is then given by  $\Phi = -4\phi_0$ . Furthermore, we have:  $\alpha_0 = \pi/2$  and  $\beta_0 = \pi/2$  (section 10.3). Therefore, equation (11.32) becomes:

$$[-\rho_0 + p_x \cos Q_0 \cos(R_0 + \phi_0)] \sin \gamma + [p_x \sin Q - z_0 \cos \gamma] \sin(R_0 + \phi_0) = 0 \quad (11.38)$$

The corresponding feed eye translation can be determined by evaluating row 2 of system (11.6):

$$p_{y0} = -z_0 \sin \gamma + \cos \gamma [\lambda \cos(R_0 + \phi_0) + \rho_0 \sin(R_0 + \phi_0)] \quad (11.39)$$

### Part C: Production process

Since the winding problem is antisymmetric with respect to  $p_y$ , we are free to choose for a “convenient” value of  $R_0$ . By assuming  $R_0 = -\pi/2 - \phi_0$ , we force the roving orientation to become parallel to the  $\{x_0, z_0\}$ -plane (figure 10.1). This property guarantees that the applied fibre will remain close to the “zero”-position of  $p_y$ . Substitution of this value into equation (11.38) leads to:

$$z_0 \cos \gamma - \rho_0 \sin \gamma - p_x \sin Q_0 = 0 \quad (11.40)$$

The solution for  $Q$  becomes:

$$Q_0 = \arcsin\left(\frac{z_0 \cos \gamma - \rho_0 \sin \gamma}{p_x}\right) = \arcsin\left(\frac{g_0}{p_x} \cos(\theta_0 + \gamma)\right) \quad (11.41)$$

The corresponding feed eye position is then given by (equation (11.39) [μ11]):

$$p_{y0} = -\rho_0 \cos \gamma - z_0 \sin \gamma = -g_0 \sin(\theta_0 + \gamma) \quad (11.42)$$

The gear ratio presented in equation (11.37) depends on the winding pattern constant (angular propagation)  $\Delta K^+$  or  $\Delta K^-$  for the case of leading, respectively lagging patterns (section 8.2). However, an important difference here is that for the determination of  $\nu$  we must take for  $\Delta K$ :  $\Delta K = \Phi - 2\pi$  instead of equation (8.11). For simplicity we denote here the pattern constant by  $\Delta K$ . With the aid of equation (8.11), the gear ratio is given by:

$$\nu = \frac{\Delta K}{2\pi} = \frac{\Phi - 2\pi}{2\pi} = -1 - 2\frac{\phi_0}{\pi} \quad (11.43)$$

Notice that if for example the second circuit is crossing the equatorial periphery of the vessel on the left side of the first one (as indicated in figure 8.6 where circuit number 2 is on the left side of number 1), the  $R$ -rotation has the opposite sign of the  $Q$ -rotation. The opposite applies on the case where the second circuit is located on the right side of the first one. These effects are automatically taken into consideration with equation (11.43). When arriving at the opposite pole (lower pole, index “1”), the  $Q$ -propagation is equal to  $-\pi$ . The corresponding  $R_1$  value becomes:

$$R_1 = R_0 + (\pi + 2\phi_0) \quad (11.44)$$

The remaining input parameters are:  $\rho_1 = \rho_0$ ,  $z_1 = -z_0$ ,  $\alpha_1 = \pi/2$ ,  $\beta_1 = 3\pi/2$ ,  $\phi_1 = -\phi_0$  (note that at  $\phi = 0$  the fibre passes the equator). With this information and equation (11.44) we obtain [μ11]:

$$p_{y1} = \rho_0 \cos \gamma + z_0 \sin \gamma = g_0 \sin(\theta_0 + \gamma) \quad (11.45)$$

From the comparison of this result with equation (11.42) we can conclude that the feed eye movement has a periodic character (at least when considering its maximum amplitude values).

The last step in formulating the begin conditions is the determination of  $\gamma$ . As previously indicated for a lathe winder, this value can be set equal to  $\pm\pi/2$ . For the tumble winder one may assume  $\gamma = -\theta_0$  as a starting value. This value results in a zero feed eye position when placing the fibre at the poles. However, depending on the object morphology, large feed eye displacements may be generated for other loci (for an extensive treatment of the proper  $\gamma$ -setting we refer here to chapter 15).

### **Numerical solver**

The solution of equation (11.31) involves two main difficulties: the derivative with respect to  $Q$  may become complicated, and there are multiple solutions corresponding to a particular set of data points  $(i, j)$  as defined in chapter 10. Even by assuming that the computation and evaluation of the derivative at every point is economical in terms of time, there is no guarantee for getting the solution value  $Q(i, j)$  that is closest to the previous solution point  $Q(i-1, j)$ . In addition, problems may occur when the derivative of (11.31) with respect to  $Q$  obtains a stationary value [μ6,μ15]. This leads to the conclusion that probably an economical and safe solution procedure is the application of the secant method [μ2,μ6,μ15]. An important condition might be that the solution interval for a particular point must be well defined; the solution search interval boundaries should generate values of opposite sign and their difference should be as small as possible. Additionally, the solution of every next point should guarantee a monotonic propagation of  $Q(i, j)$ .

As outlined in chapter 10, the selection of the data points corresponds to a constant length increment. Depending on the associated curvature, the angular solution increment  $\Delta Q$  may vary. In mathematical terms:

$$\Delta Q(i, j) \propto \left. \frac{\Delta L}{R} \right|_{(i, j)} = \Delta L k|_{(i, j)} \quad (11.46)$$

where “ $\propto$ ” stands here for “proportional to”. The next step is to determine the smallest and greatest value of the normal curvature; these values define the extreme values in the  $Q$ -propagation speed. Due to the assumed geometry of the model presented here ( $dQ/dL \leq 0$ ), the solution points  $Q(i, j)$  will exhibit monotonic behaviour towards negative values. Therefore, we define:

$$\begin{aligned} u &= -\min(k) \\ d &= -\max(k) \end{aligned} \quad (11.47)$$

The minimum normal curvature value ( $k$ ) can not be less than zero. However, in order to anticipate for eventual numerical instabilities or extreme shapes, we assume the bound for  $u$  as equal to  $\Delta L/2$ . By applying the same

## Part C: Production process

reasoning, the maximum bound is assumed as equal to  $2d$ . The initial value of  $Q_0$  is given by equation (11.41). The local search intervals are now defined as follows:

$$\{Q_g(i, j) + 2d\Delta L, Q_g(i, j) + \frac{\Delta L}{2}\} \quad (11.48)$$

$$\text{with } Q_g(i, j) = \begin{cases} Q_0 & i = 1 \\ Q_s(i-1, j) & i > 1 \end{cases}$$

where  $Q_s(i, j)$  is the solution of equation (11.31) at a particular point  $(i, j)$ . Note that in this equation, the function  $R(Q)$  is defined according to equation (11.37); the required parameters can be obtained by equations (11.41) and (11.43) while  $R_0$  is equal to  $-\pi/2 - \phi_0$ .

As an alternative to the above presented secant method (including the initial solution interval estimation), a straightforward solution algorithm is also feasible; the determinant equation (11.31) depends actually on the counter  $(i, j)$  and  $Q$  (note that  $R$  is completely defined as a function of  $Q$ ). Let us denote this determinant equation with  $D(Q, i)$  (for simplicity we temporarily neglect the wound circuit number indicator  $j$ ). Furthermore, we assume that a particular solution  $Q_s(i-1)$  is known. The main question now is how to predict the next point  $Q_s(i)$ . In figure 11.3, we depict a schematic representation of  $D(Q, i)$  for a particular point  $i$ .

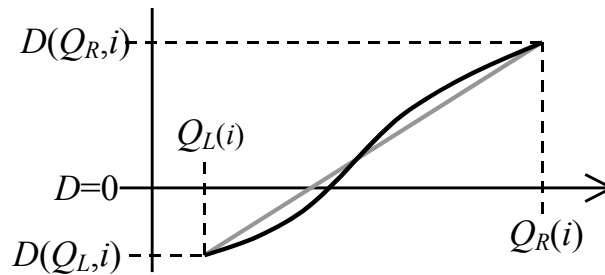


Fig. 11.3: Local solution interval for  $D(Q, i)$

The  $Q$ -interval in figure 11.3 is defined as follows:

$$\begin{aligned} Q_L(i) &= Q_s(i-1) + u\Delta L \\ Q_R(i) &= Q_s(i-1) + d\Delta L \end{aligned} \quad (11.49)$$

Hence, the approximate solution  $Q_a(i)$  becomes:

$$Q_a(i) = Q_L(i) + \frac{Q_R(i) - Q_L(i)}{D[Q_R(i), i] - D[Q_L(i), i]} D[Q_L(i), i] \quad (11.50)$$

This strategy is actually representing the first iterative step of the secant method [μ2, μ8]. By comparing the resulting approximate solution with the

“exact” one, we obtain a reliable estimation for the convergence speed of the solution process. The differences between the exact and the approximate solution are generally very small. The straightforward solution (denoted by  $Q_c(i)$ ) can now be formulated:

$$\begin{aligned} Q_c(1) &= Q_0 \\ Q_L(i) &= Q_c(i-1) + u\Delta L \\ Q_R(i) &= Q_c(i-1) + d\Delta L \end{aligned} \tag{11.51}$$

where  $Q_c(i)$  (for  $i > 1$ ) is equal to  $Q_a(i)$  (equation (11.50)). The index “c” shows that the solution is characterised by cumulative error generation. However, the accuracy of this method is very satisfactory. Even by a small number of length steps per circuit, the maximum error remains below  $0.5^\circ$ , even when treating extreme shapes with high curvature gradients. This property sets the ability for solving the winding problem by using simple programs like spreadsheets.

In conclusion, the stability and convergence speed of the solution based on the determinant (11.31) is satisfactory; the calculation time is in general smaller than the time needed for creating the input data. These properties form a suitable basis for applying optimisation techniques (chapter 14).

## 11.4 Results & discussion

The proposed solution method is applied on various objects: cylinders of various lengths with isotensoidal or ellipsoid end domes, oblate and prolate spheroids and cones. However, in order to demonstrate the influence of  $\gamma$  on the required machine movements and roving accelerations, we have chosen for an object consisting of a quasi-ellipsoidal meridian profile and flat surfaces near the poles. Because at the flat areas the roving becomes directly placed over a considerable portion of its own length, the impact on the stability of the profiles for  $Q$  and  $S''(t)$  is expected to be considerable. Some frames of the simulations carried out are given in appendices A (tumble winder) and B (lathe winder).

### The object under consideration

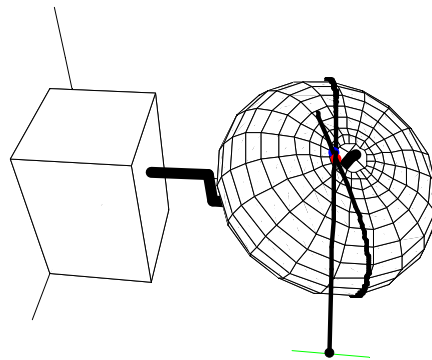


*Fig. 11.4: Geodesically overwound quasi-ellipsoidal shell of revolution with flat polar areas placed on the tumble winder configuration*

The maximum radius of the shell is equal to 0.3 [m], while the minimum one is 0.04 [m]. The maximum height is equal to 0.14 [m]. The applied fibre bundle bandwidth is 0.02 [m]. The flat surface corresponds with a radius range beginning from the pole up to  $\rho = 0.12$  [m]. The applied roving paths are geodesic and take the fibre bundle width into account (chapter 8). For the description of the shape and the trajectories we introduced a coordinate system as depicted in figure 2.4; the polar value of  $\theta$  ( $= \theta_0$ ) including the fibre bundle width becomes equal to 0.349943 [rad], while the equatorial value for  $\theta$  is equal to  $\pi/2$ . At that point, the  $\phi$ -value of the first circuit is equal to zero. The initial point of fibre placement is located at the upper pole; the corresponding  $\phi$ -value is equal to  $\phi_0 = -1.45499$  [rad].

### Winding machine geometry

We use here the general model (as depicted in figure 10.1) that is based on the tumble winder (section 11.2). In order to avoid collision between the feed eye and the shell,  $p_x$  is set equal to 0.5 [m], while  $p_z$  is equal to zero. The spool location is assumed as coinciding with the feed eye ( $R_x = p_x$ ,  $R_y = p_y$ ). Consequently, the parameter  $\sigma$  is here equal to zero. The secondary rotation  $R$  is coupled to the primary one, according to equation (11.37). The range of  $\gamma$ -values varies from  $\gamma = 0$  to  $\gamma = -\pi/2$  using steps of  $\pi/10$ . The value  $-\pi/2$  generates the lathe winder geometry. The basic idea in this set-up is to evaluate the obtained results in terms of the delivery eye movement characteristics (kinematic and dynamic) and consumed fibre accelerations. It should be noted that  $\dot{Q}$  as a function of time is always held constant and equal to  $(2\pi/3)$  [rad/s]. With  $\phi_0 = -1.45499$  [rad], the parameter  $R'$  becomes equal to 0.1544 [rad/second] or 8.8466 degrees/second (equation (11.43)). Furthermore, the average consumed fibre speed is equal to 0.4891 [m/s] (equations (10.7) and (11.20) in combination with the assumed value for  $\dot{Q}$ ). Notice that the “traditional” maximum winding speed is equal to 1 [m/s] and 0.5 [m/s] for winding with dry, respectively impregnated rovings.

### Calculation flow diagrams

With the input parameters  $\theta_0$ ,  $g_0$ ,  $\gamma$ ,  $p_x$  and  $\phi_0$  we calculate the initial kinematic values  $Q_0$ ,  $p_{y0}$  and  $R_0$  according to the diagram presented in figure 11.5.

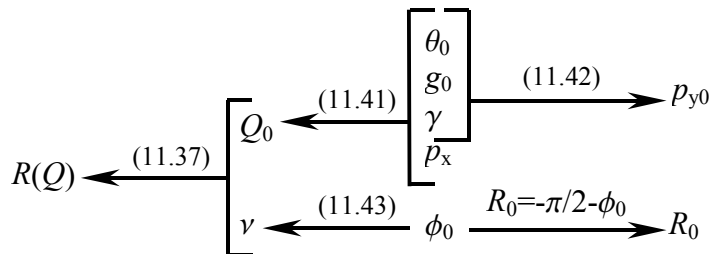


Fig. 11.5: Calculation flow diagram for the determination of the initial kinematic values

The next step is the determination of  $Q$  as an expression of the spherical coordinate  $\theta$  (which describes the implemented meridian profile of the mandrel by means of the function  $g(\theta)$ ), see figure 11.6. The main equation to be solved is (11.31), which requires the determination of the vector  $\mathbf{U}$  (equation (11.18)); in order to obtain this vector, we need additional input values in the form of  $\mathbf{G}$  and  $\Delta\mathbf{G}$ . Furthermore, in order to properly determine the solution intervals for (11.31), the values of  $k$  and  $\Delta L$  must be given (alternatively, we can determine  $k$  with equation (10.21)). An additional required input parameter is  $R(Q)$ , which is already calculated with the aid of figure 11.5.

**Part C: Production process**

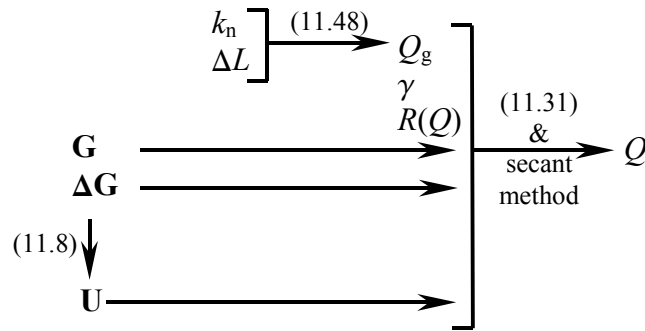


Fig. 11.6: Calculation flow diagram for the determination of  $Q$

The calculation of  $p_y$  requires the determination of the free fibre length,  $\lambda$  (see figure 11.7). The latter is obtained with the first expression that is contained in equation (11.34).

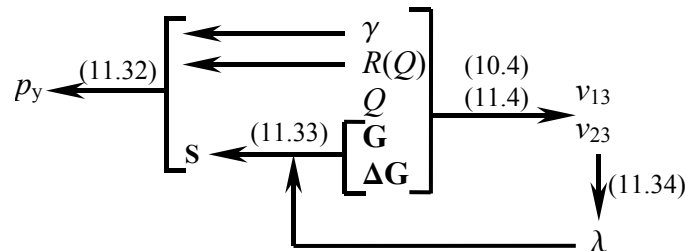


Fig. 11.7: Calculation flow diagram for  $\lambda$  and  $p_y$

The last process parameter to be determined is the acceleration of the consumed roving (figure 11.8). The consumed roving length is described as a function of the place coordinate  $\theta$ . Using  $Q(\theta)$  (figure 11.6) we express  $S$  as a function of  $Q$ . After that, and with the known value for  $Q'$  we formulate  $S$  as a function of time. The obtained discrete  $S(t)$  points are generally not evenly distributed in time. For the construction of a  $S(t)$ -points collection over constant  $\Delta t$ -intervals, we interpolate the resulting  $S(t)$  curve by a second order Lagrange polynomial (see also chapter 12). The resulting evenly distributed  $S(t)$ -values are then double differentiated by four-point formulas [μ8].

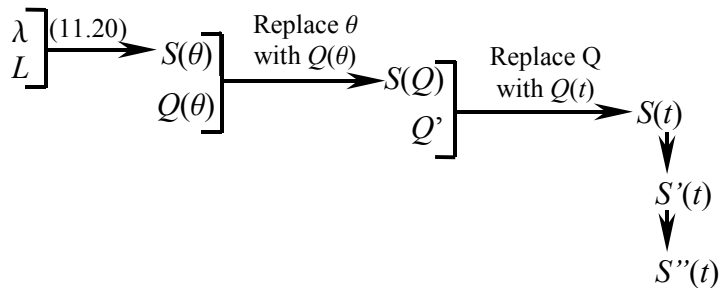


Fig. 11.8: Calculation flow diagram for the determination of the consumed roving velocity and acceleration

**The primary rotation Q**

As previously mentioned, the applied  $\gamma$ -values are:  $\{0, -0.1\pi, -0.2\pi, -0.3\pi, -0.4\pi, -0.5\pi\}$  corresponding to figures 11.9, 11.10, 11.11, 11.12, 11.13 and 11.14, respectively. These figures depict the  $Q$ -propagation as an expression of the place coordinate  $\theta$ . Beginning at a slightly positive initial value dictated by equation (11.41), the angle  $Q$  propagates towards negative values. We present here the two first windings.

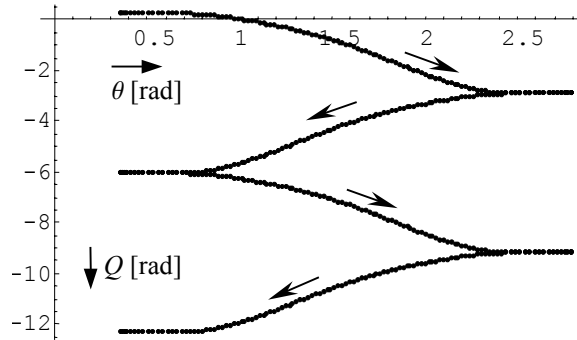


Fig. 11.9:  $Q$  [rad] as an expression of the place coordinate  $\theta$  for  $\gamma = 0$

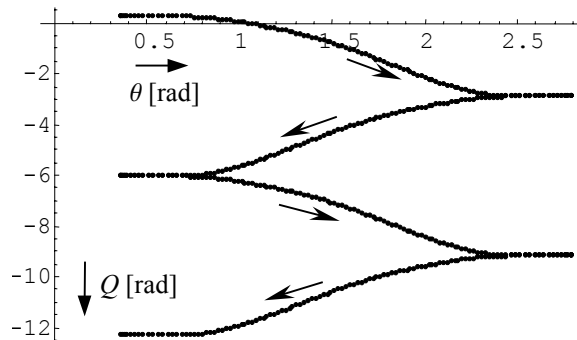


Fig. 11.10:  $Q$  [rad] as an expression of the place coordinate  $\theta$  for  $\gamma = -0.1\pi$

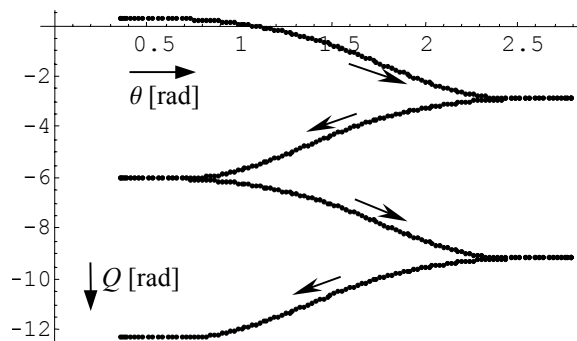


Fig. 11.11:  $Q$  [rad] as an expression of the place coordinate  $\theta$  for  $\gamma = -0.2\pi$

### Part C: Production process

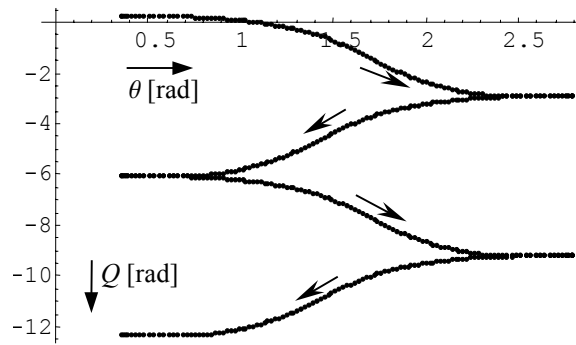


Fig. 11.12:  $Q$  [rad] as an expression of the place coordinate  $\theta$  for  $\gamma = -0.3\pi$

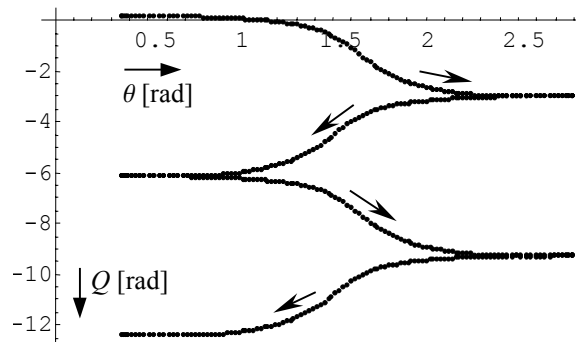


Fig. 11.13:  $Q$  [rad] as an expression of the place coordinate  $\theta$  for  $\gamma = -0.4\pi$

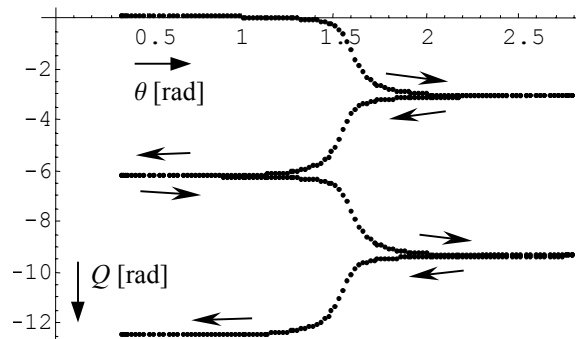


Fig. 11.14:  $Q$  [rad] as an expression of the place coordinate  $\theta$  for  $\gamma = -0.5\pi$

The horizontal parts in the presented graphs correspond with roving placement at the flat polar areas. Another remarkable aspect is that the  $Q$ -solution is antisymmetric with respect to these areas. The smoothness of  $Q(\theta)$  is reducing when the inclination angle  $\gamma$  tends towards the lathe winder configuration ( $\gamma \rightarrow -\pi/2$ , see figure 11.1). In addition, the horizontal graph parts are consequently increasing in length. The reason for this is that the amplitude of the resulting delivery eye movement becomes very large due to the small winding angle  $\alpha$  at the equatorial areas.

**The feed eye movement  $p_y$**

The feed eye movement is, as shown in equations (11.42) and (11.45), periodic. The initial value of  $p_y$  is located on the right side of the presented graphs. Consequently, the feed eye curve proceeds from the right to the left as a function of the obtained  $Q$ -values. As previously stated, the graphs describing the delivery eye movement as a function of  $Q$  are based on two consequent wound circuits and reflect on  $\gamma = \{0, -0.1\pi, -0.2\pi, -0.3\pi, -0.4\pi, -0.5\pi\}$ . The corresponding figures are respectively 11.15, 11.16, 11.17, 11.18, 11.19 and 11.20.

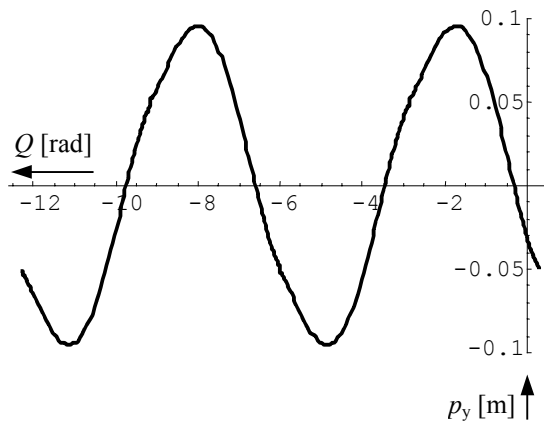


Fig. 11.15: The feed eye movement  $p_y$  [m] as a function of  $Q$  [rad] for  $\gamma = 0$

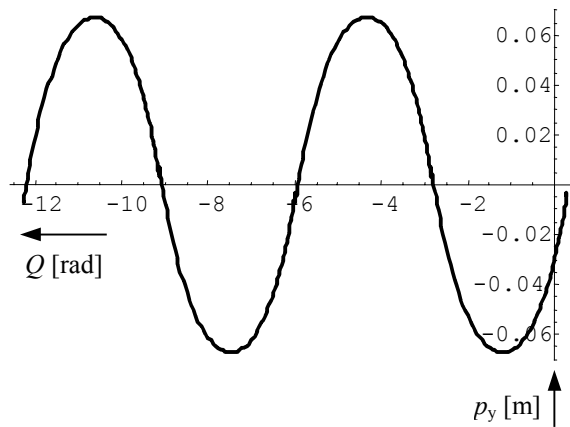
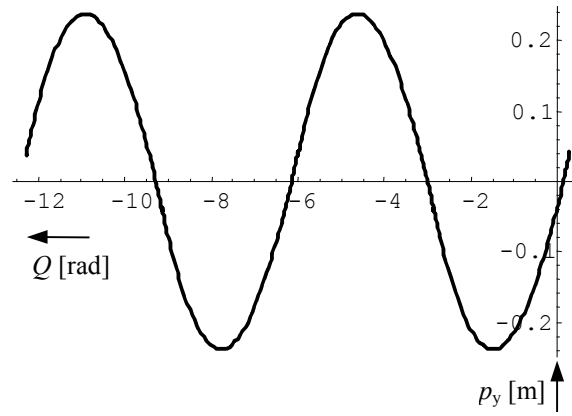
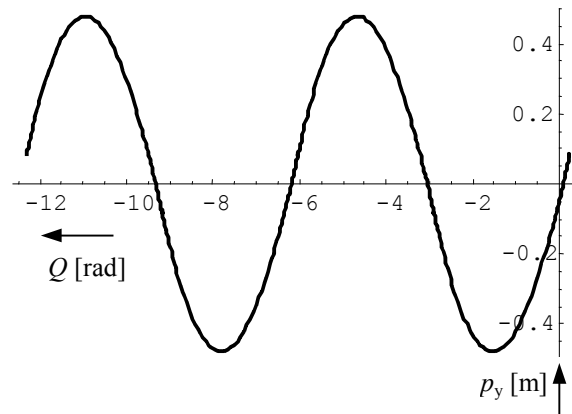


Fig. 11.16: The feed eye movement  $p_y$  [m] as a function of  $Q$  [rad] for  $\gamma = -0.1\pi$

**Part C: Production process**



*Fig. 11.17: The feed eye movement  $p_y$  [m] as a function of  $Q$  [rad] for  $\gamma = -0.2\pi$*



*Fig. 11.18: The feed eye movement  $p_y$  [m] as a function of  $Q$  [rad] for  $\gamma = -0.3\pi$*

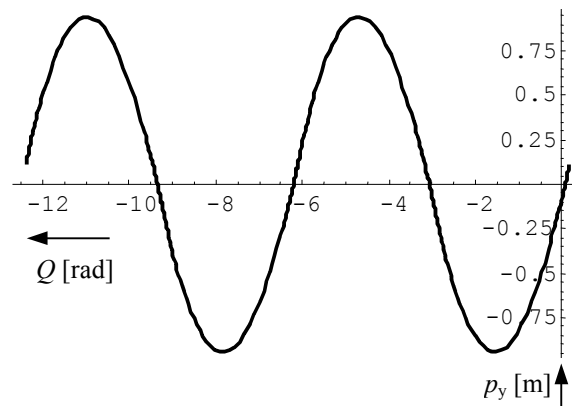


*Fig. 11.19: The feed eye movement  $p_y$  [m] as a function of  $Q$  [rad] for  $\gamma = -0.4\pi$*

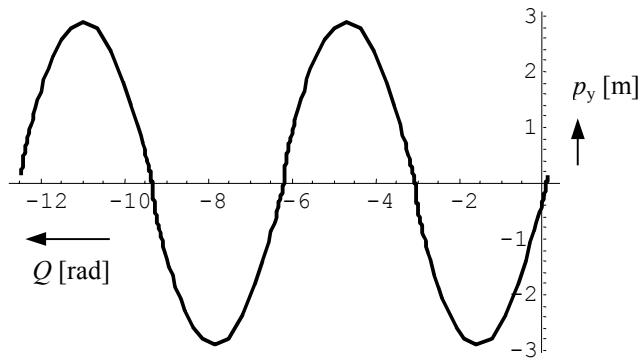


Fig. 11.20: The feed eye movement  $p_y$  [m] as a function of  $Q$  [rad] for  $\gamma = -0.5\pi$

For  $\gamma = \{-0.1, -0.2, -0.3\}$  [rad], the feed eye movement becomes almost sinusoidal. The amplitude shows a minimum for  $\gamma = -0.1$  and a maximum for the lathe winder configuration  $\gamma = -\pi/2$ . As mentioned in section 11.2 and expressed in equation (11.25), the feed eye amplitude for a lathe winder may become considerably large (especially for small  $\alpha$ -values). The only solution for this problem can be found in terms of properly reducing the cross-feed distance  $p_x$  [α3,ι19].

### Consumed roving accelerations

The derived feed eye amplitude values are directly coupled to the length of the free-hanging fibre  $\lambda$ . When obtaining a considerably large amplitude value, one may expect that the corresponding  $\lambda$ -value will also become large. Although there is no direct coupling between these two parameters, this expectation is generally true. Since the consumed roving length depends directly on  $\lambda$  (equation (11.20)), the expectation arises that in the case of e.g. the lathe winder, the generated accelerations will exhibit large values. We examine again two consequent wound circuits with  $\gamma = \{0, -0.1\pi, -0.2\pi, -0.3\pi, -0.4\pi, -0.5\pi\}$  (corresponding to figures 11.21, 11.22, 11.23, 11.24, 11.25 and 11.26, respectively).

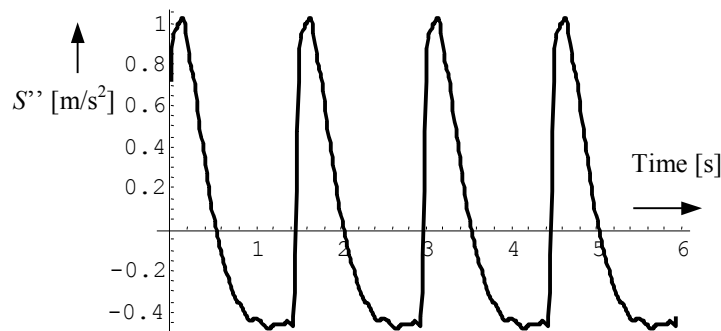
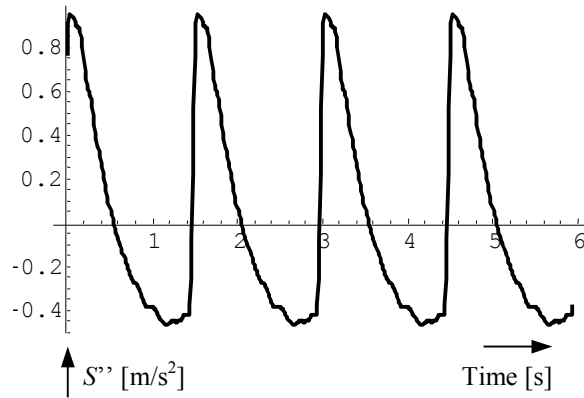
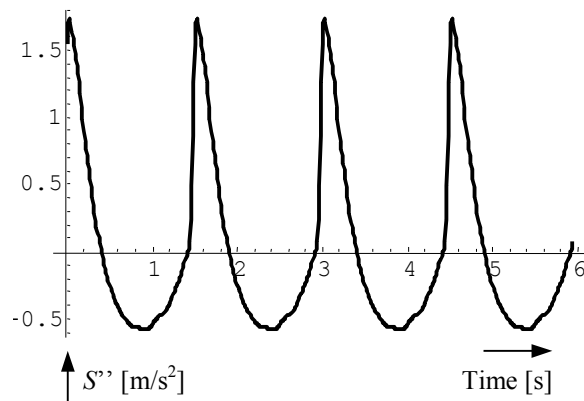


Fig. 11.21: The consumed roving acceleration [m/s<sup>2</sup>] as a function of time [s] for  $\gamma = 0$

**Part C: Production process**



*Fig. 11.22: The consumed roving acceleration [ $\text{m/s}^2$ ] as a function of time [s] for  $\gamma = -0.1\pi$*



*Fig. 11.23: The consumed roving acceleration [ $\text{m/s}^2$ ] as a function of time [s] for  $\gamma = -0.2\pi$*

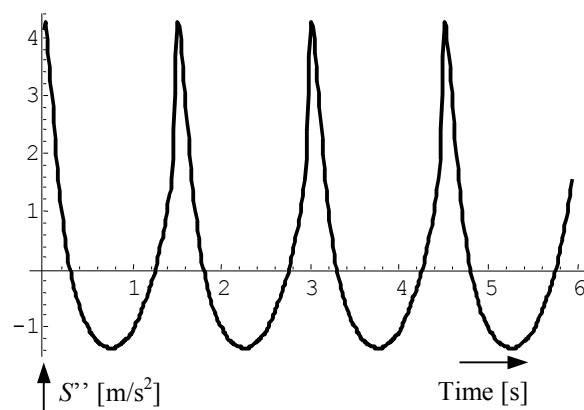


*Fig. 11.24: The consumed roving acceleration [ $\text{m/s}^2$ ] as a function of time [s] for  $\gamma = -0.3\pi$*

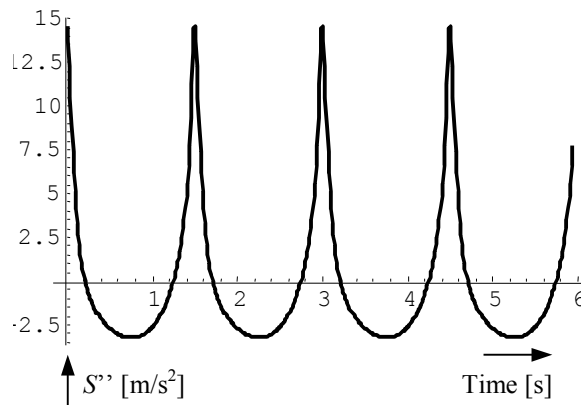


Fig. 11.25: The consumed roving acceleration [m/s<sup>2</sup>] as a function of time [s] for  $\gamma = -0.4\pi$

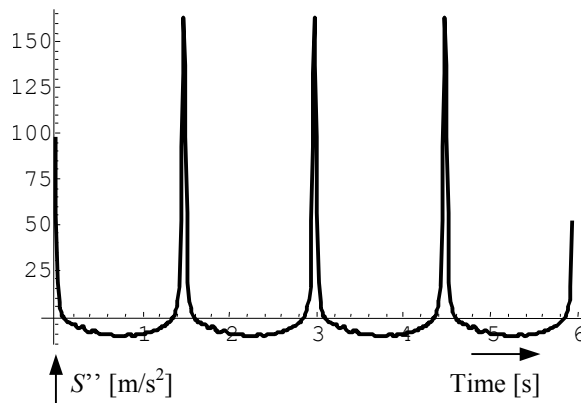


Fig. 11.26: The consumed roving acceleration [m/s<sup>2</sup>] as a function of time [s] for  $\gamma = -0.5\pi$

The results clearly indicate that the lathe winder configuration without activation of  $p_x$  will result in considerable fibre accelerations [α3,ι19], see also chapter 14. With this configuration, the rotational speed of the spindle has to be reduced. However, this speed reduction does not solve the problem of the large delivery eye amplitude (although it will reduce its acceleration).

### The best configuration

For this particular object to be wound, the best configuration is given by  $\gamma = -0.1\pi$  [rad] approximately. Since the two main rotations  $Q$  and  $R$  proceed constantly in time, the associated machine parts will not exhibit dynamic problems [α23,α24]. The main points of concern are here the accelerations for the feed eye and the consumed roving. For the first one, we assume the “traditional” limit of 0.3 g [α3], while for the second one we assume 1 g. The feed eye movement is almost sinusoidal, see figure 11.27:

### Part C: Production process

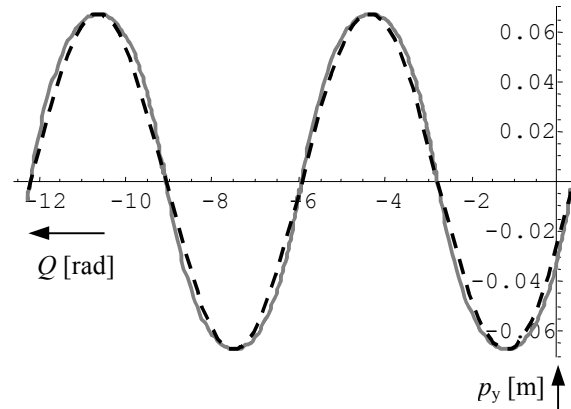


Fig. 11.27: The exact solution for the feed eye movement [m] (black dashed line) and its sinusoidal approximation (grey continuous line)

The maximum metric difference between the exact solution and the approximation is 8 [mm]; the corresponding maximum roving orientation deviation remains below 1 degree, hence this approximation is acceptable, even for the manufacturing process of high performance products. The greatest advantage of this configuration for this particular shape is that the delivery eye movement can easily be performed by mechanical control devices [α16] like camshafts or crank mechanisms.

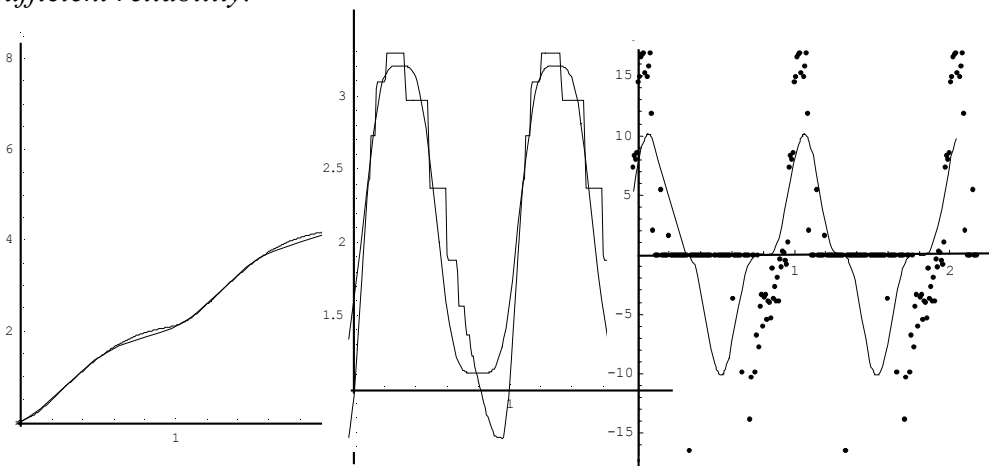
From the acceleration limits indicated above, one can calculate that the maximum rotational speed of  $Q$  should not exceed  $2.124\pi$  [rad/s] or  $382.82^\circ/\text{s}$ . The average fibre consumption speed is then equal to 1.59 [m/s].

# 12

## Dynamics of filament winding

A parameter determining the rate of success for filament wound products can be found in the manufacturing costs. As outlined in chapter 11, a proper selection of the winding machine configuration is the first action towards a competitive product. The second but of equal importance step, is the attempt to additionally reduce the costs by minimising the production time. For this purpose, the dynamic limits of the winding machine must be well defined. In order to fully utilise such a machine, we must be able to accurately determine the velocities and accelerations of the involved machine parts and the consumed roving. This quantification requires suitable and reliable methods for data interpolation and their differentiation.

After a short overview of the dynamic machine limits and the physiology of the data controlling the movements, we proceed to the description of several, common and less common interpolation techniques. While the known interpolating methods are shortly presented, we provide special attention to the approximation by a method combining least squares with prescribed values for the resulting polynomial and its derivatives at particular points. In addition, we propose here a method that combines the decomposition of the discrete signal into a linear and periodic part, followed by a Fourier series approximation of the latter. Section 12.3 contains a short consideration of differentiating discrete nodes and provides information about suppressing the resulting noise. In the last section we outline some typical results and discuss the advantages and drawbacks of the method presented here. This chapter concludes with several “design rules” for the creation of differentiated data of sufficient reliability.



The first graph in this figure presents the original data and their approximation. The second graph contains the discrete derivative of the original data points and the analytical derivative of the approximating function. The third graph represents their second derivatives. The graphs demonstrate the typical problem of differentiating discrete data: scatter versus poor approximation.

## **Part C: Production process**

## 12.1 Machine limits & control data

### Dynamic constraints

In the most general case, the process of filament winding involves three rotations  $\{Q, \gamma, R\}$  and three translations  $\{p_x, p_y, p_z\}$ . As outlined in the previous chapter, for  $\gamma = \pm\pi/2$  we obtain the lathe configuration with  $C = Q \pm R$ . In regard to the feed eye movements, the position  $p_z$  remains usually equal to zero and the translation  $p_x$  is generally only activated for the lathe winder configuration (to reduce excessive translation of the carriage  $p_y$ ).

An additional item of significant importance is the dynamic behaviour of the free-hanging roving (provided by the spool) and in particular its velocity profile ( $S'(t)$ ). The dynamics of the free hanging roving itself is a rather complicated issue that can usually only be evaluated by experimental or expensive numerical methods. In practice however, the dynamic behaviour of the roving itself is usually not a limiting factor. This statement does not apply on the velocity profile the consumed roving is forcing the spool to undergo; especially when winding with impregnated fibre bundles, controlling the roving speed is of major importance. This velocity should generally be as constant as possible. On the other hand, when applying dry fibre bundles, we are not particularly interested in constant roving velocity, but a rather high roving tension is preferable. The reason for this is that for dry winding, the elevated roving consumption speed is increasing the chance for dynamic instabilities of the free hanging fibre bundle. Possible additional problems can be found in the control systems of commercially available fibre tensioners, which tend to oscillate at elevated speeds [v1]. From studies performed on the applicability of tumble winders for the production of donut-shaped pressure vessels, it is known that the main factor limiting the production speed (thus, the costs) is the performance of fibre tensioners [ $\alpha 23, \alpha 24, \alpha 41, \alpha 42$ ]. Consequently, it is believed that the need for improved tensioners is rather evident.

In general, the dynamic limits of the involved production machine are mainly dictated by the moments of inertia of the product itself, the available torque of the servomotors, the type of control etc. Especially in regard to the machine cybernetics, the majority of lathe winders is controlled by CNC software that typically relates the involved  $A$ ,  $X$  and  $Y$  increments to the  $C$  increments according to some prescribed speed. On the basis of the prescribed speed  $C'$  (which can differ per CNC control block), the controller calculates the time needed to perform a particular  $C$ ,  $A$ ,  $X$  or  $Y$ -increment; when for example this increment is equal to zero, the time interval becomes infinite. This means that the  $C$  increments should always differ from zero; hence the rotational speed  $C'$  should always remain either positive or negative (as given in table 12.1).

## Part C: Production process

Lathe winder	#' min [#s]	#' max [#s]	#'' min [#s <sup>2</sup> ]	#'' max [#s <sup>2</sup> ]
$S$ [m]	-0.5	1.5	-5	10
$C$ [rad]	$-10\pi/6$	-0.05	$-6\pi$	$6\pi$
$A$ [rad]	$-20\pi/6$	$20\pi/6$	$-20\pi$	$20\pi$
$X$ [m]	-0.5	0.5	-3.5	3.5
$Y$ [m]	-1	1	-3.5	3.5

Table 12.1: Typical dynamic constraints for a lathe winder

For the rumble winder, it is even more difficult to provide dynamic limits with general validity. However, for a tumble winder where the rotations  $Q$  and  $R$  are coupled through a gearbox (constant ratio, equation (11.37)) we provide as an example the following values [ $\alpha 23, \alpha 24$ ]:

Tumble	#' min [#s]	#' max [#s]	#'' min [#s <sup>2</sup> ]	#'' max [#s <sup>2</sup> ]
$S$ [m]	-0.5	1.5	-5	10
$Q$ [rad]	$-6\pi$	-0.05	$-6\pi$	$6\pi$
$A$ [rad]	$-20\pi/6$	$20\pi/6$	$-20\pi$	$20\pi$
$R$ [rad]	$-6\pi$	-0.05	$-6\pi$	$-6\pi$
$Y$ [m]	-1	1	-3.5	3.5

Table 12.2: An example of possible dynamic constraints for a tumble winder

It should be noted that the values presented here are exclusively serving the aim of providing a typical example. Since the dynamic limits are additionally governed by the inertia properties of the wound product and the physiology of the applied fibre bundle (dimensions, allowable tension, dry or impregnated filaments, geodesic or non-geodesic circuits), experimental investigation of these limits is usually a necessity.

### Control data

We assume now that the dynamic limits of the involved production machine are well determined. As previously indicated, the control parameters for the winding machine are provided as a collection of discrete data points ( $S(i, j)$ ,  $C(i, j)$ ,  $A(i, j)$ ,  $X(i, j)$ ,  $Y(i, j)$ ,  $Q(i, j)$ ,  $R(i, j)$ ). To gain information about machine parts and consumed fibre velocities and accelerations, one has to respectively repeatedly differentiate the data with respect to time. Before proceeding to these operations, we should redistribute the data over constant time increments; the reason for this is that CNC controllers usually work in time blocks, defined in a few milliseconds [ $\alpha 3, \alpha 19, \alpha 20$ ].

As an example, we consider here a set of data representing the consumed roving length (provided by a spool) as a function of time. As outlined in chapter 10, the calculations performed by filament winding simulation programs are usually based on constant length increments belonging to the fibre trajectory, placed on the surface of the wound object [76,119]. Unless the wound trajectory on the body has a constant curvature at every point belonging to that trajectory, the velocity of the consumed fibre is not constant. Consequently, the data representing the consumed roving length as a function of time are characterised by irregular sample points distribution (figure 12.1).

Furthermore, the repetitive character of filament winding processes generates periodic machine movements and periodic consumed roving length profiles. As a result of this property, we need only to describe these quantities as a function of time for a single wound circuit. In several cases, the latter can also be divided into two periodic parts. In general however, this is not valid (for example when considering the kinematics of a tumble winder that exhibit an anti-symmetric character as demonstrated in figures 11.9-11.14). In the example under consideration, we can distinguish two periods (figure 12.1): from 0 to 0.5 seconds and from 0.5 to 1 second.

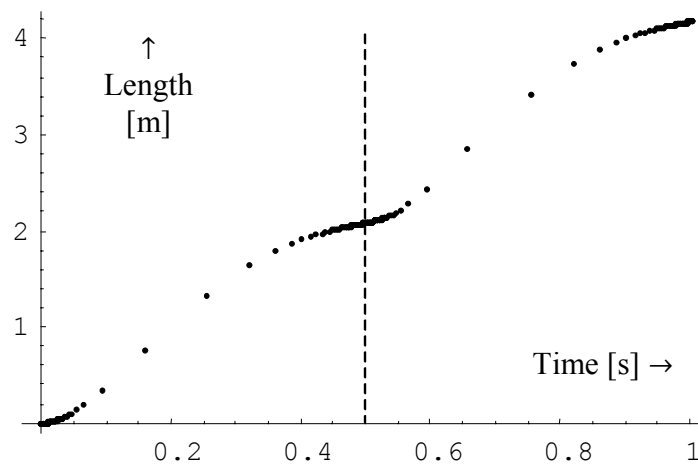


*Fig. 12.1: Data distribution representing the consumed roving length as a function of time*

Although we present here a rather extreme example, the depicted gaps can cause significant errors when, for instance interpolating with a simple first order method. Hence, the obtained values for the velocities and accelerations might not be realistic at all.

## **12.2 Interpolation techniques**

### **Lagrange**

The Lagrange interpolation method is a classical one and is available on almost every mathematical software package [μ2,μ3,μ8,μ14,μ15]. The simplest and fastest appearance of this method is the linear one, which provides great stability for obtaining results between two adjacent data points (base points). The drawback of this simplest version however, is the reduced accuracy, especially in cases where the “distance” between the nodes is rather large. Referring to figure 10.1, this method should probably lead to a strongly not reliable data description. The analytical approximation of the given points improves when the interpolation order is increased. However, if the interpolation order becomes too high, the obtained polynomial may increasingly oscillate between the nodes [μ8]. This oscillation has certainly a negative influence on the reliability of the obtained values by discrete differentiation.

For filament winding applications it is found that generally the “best” representation is given by a second or third order interpolation. This observation however, is purely empirical and assumes the almost traditional block time of 20 milliseconds for the CNC controller, while the length increments of the wound trajectory on the mandrel remain in the order of 1 to 5 millimetres (belonging to the range [0.5, 1.5] [m/s]).

### **Bezier splines**

A Bezier spline interpolates only the endpoints; the other points “control” the spline [μ8,μ15]. For the complete set of data belonging to one period, one may construct a collection of several, for example cubic Bezier splines and properly connect them to each other. To reduce the number of required polynomials, one should tend to include as much as possible nodes in one curve. In contrast, the most extreme case is the inclusion of only the first and last nodes belonging to one period; the other nodes control the curve. The complete roving length consumption profile can then be described by one cubic polynomial. Despite its facilitating properties when regarding differentiation, the information obtained by this method is not reliable. Such a curve should be constructed over a smaller number of nodes. When that number approaches the minimum required number of base points for the construction of the polynomial (for a cubic Bezier: four points), then it is probably better to use cubic splines. The implementation of Bezier curves makes in our case only sense when a significant reduction of the number of required polynomials can be achieved.

### **Cubic splines**

Interpolation by Cubic splines provides, like Lagrange polynomials do, a data description able to “catch” exactly every node  $[\mu_8, \mu_{15}]$ . Since the implemented polynomials are cubic ones, we can assume that they hardly will oscillate. In addition, the technique for determining the corresponding polynomials involves the inversion of a tri-diagonal sparse matrix that requires very short calculation times. As a result of this property, cubic splines are strongly recommended for large data sets. Contrary to the approximation by Bezier curves, modification of a subset of data points does not strongly affect the resulting curve; the influence has a local character. A disadvantage of this method is that we still end up with a considerable number of several polynomials that have separately to be differentiated. Nevertheless, a description of the data set by cubic splines seems useful for filament winding applications.

### **Partial least squares fitting**

The kinematic solution of the filament-winding problem depends both on the position vector  $\mathbf{G}$  of some point belonging to the roving path, as well as its orientation (tangent) vector  $\Delta\mathbf{G}$ . The solution of these equations can, in the most general case, only be obtained by numerical root determination. However, when considering particular points belonging to the roving path, the solution can be derived on an analytical way. Such points correspond to the smallest ( $\rho_0$ ) and biggest radius ( $\rho_{eq}$ ) of the mandrel being wound (we consider here rotationally symmetric objects). On the smallest radius, since the roving is transiting to the next circuit, the slope of the path has to be equal to zero as the meridian slope is also zero (figure 10.5). In addition, the corresponding winding angle becomes equal to  $\pi/2$  [rad] (table 10.1). On the other hand, at the equator, the winding angle obtains its smallest value and the slope of the mandrel is vertical. The associated solutions for the machine movements provide reliable information regarding not only their absolute values but also their derivatives. The same reasoning applies on the consumed roving length behaviour. Summarising, for particular points belonging to the solution data set, we already now the values themselves of their derivatives.

To serve the aim of fast implementation, one would preferably have a polynomial applying to, if possible, the whole range of the data that correspond to one period. In our example, the representation of the consumed fibre length as a function of time would consist of two similar polynomials, defined in the intervals  $[0, 0.5]$  and  $[0.5, 1]$  [s], figure 12.1. On the bounds of these intervals, the fibre is passing the polar areas of the object under consideration; these points provide the exact (analytical) values for the consumed roving length and its derivatives in time. At the same time, since we want to cover at once the complete set of nodes belonging to one period by preferably a limited degree polynomial, we should apply least squares fitting.

### Part C: Production process

The polynomials  $p(x)$  and  $q(x)$  we are looking for must satisfy two conditions:  $C^1$  continuity at the definition interval bounds and least squares data fitting. We define:

$$p(x) = \sum_{i=0}^k a_i x^i \quad (12.1)$$

Denoting the given nodes by  $\{x_i, y_i\}$  the residual is:

$$R^2 = \sum_{i=1}^n [y_i - \sum_{i=0}^k a_i x^i] \quad (12.2)$$

The least-squares solution requires:

$$\frac{\partial(R^2)}{\partial a_i} = 0 \quad i = 0,1,2,\dots,k \quad (12.3)$$

This leads to the following system of linear equations [ $\mu 7, \mu 15$ ]:

$$\begin{bmatrix} n & \sum_{i=1}^n x_i & \cdots & \sum_{i=1}^n x_i^k \\ \sum_{i=1}^n x_i & \sum_{i=1}^n x_i^2 & \cdots & \sum_{i=1}^n x_i^{k+1} \\ \vdots & \vdots & \ddots & \vdots \\ \sum_{i=1}^n x_i^k & \sum_{i=1}^n x_i^{k+1} & \cdots & \sum_{i=1}^n x_i^{k+k} \end{bmatrix} \begin{Bmatrix} a_0 \\ a_1 \\ \vdots \\ a_k \end{Bmatrix} = \begin{Bmatrix} \sum_{i=1}^n y_i \\ \sum_{i=1}^n x_i y_i \\ \vdots \\ \sum_{i=1}^n x_i^k y_i \end{Bmatrix} \Rightarrow \mathbf{A}_2 \mathbf{v} = \mathbf{u}_2 \quad (12.4)$$

where  $\mathbf{A}_2$  is the VanderMonde matrix. The continuity conditions at the interval bounds require [ $\mu 13$ ]:

$$\begin{bmatrix} 1 & x_0 & x_0^2 & x_0^3 & \cdots & x_0^k \\ 1 & x_n & x_n^2 & x_n^3 & \cdots & x_n^k \\ 0 & 1 & 2x_0 & 3x_0^2 & \cdots & kx_0^{k-1} \\ 0 & 1 & 2x_n & 3x_n^2 & \cdots & kx_n^{k-1} \end{bmatrix} \begin{Bmatrix} a_0 \\ a_1 \\ a_2 \\ \vdots \\ a_k \end{Bmatrix} = \begin{Bmatrix} y_0 \\ y_n \\ d_0 \\ \vdots \\ d_n \end{Bmatrix} \Rightarrow \mathbf{A}_1 \mathbf{v} = \mathbf{u}_1 \quad (12.5)$$

where  $[d_0, d_n]$  are the known (analytical) derivatives, and  $[y_0, y_n]$  the known boundary values. The vector we are looking for should primary satisfy equation (12.5) and, as a second demand, represent a least-squares solution for equation (12.4). We represent this vector as follows [ $\mu 13$ ]:

$$\mathbf{v} = \mathbf{P}_1 \mathbf{u}_1 + \mathbf{N}_1 \mathbf{x}^{(1)} \quad (12.6)$$

where  $\mathbf{P}_1$  is the pseudo inverse of  $\mathbf{A}_1$  (obtained by singular value decomposition of  $\mathbf{A}_1$ ) and  $\mathbf{N}_1$  is the nullspace of  $\mathbf{A}_1$ . The temporary unknown vector  $\mathbf{x}^{(1)}$  belongs to that nullspace and can be determined from equation (12.4):

$$\mathbf{x}^{(1)} = \mathbf{P}_2 (\mathbf{u}_2 - \mathbf{A}_2 \mathbf{P}_1 \mathbf{u}_1) \quad (12.7)$$

where  $\mathbf{P}_2$  is the pseudo inverse of  $\mathbf{A}_2$ . The solution for  $\mathbf{v}$  becomes:

$$\mathbf{v} = \mathbf{P}_1 \mathbf{u}_1 + \mathbf{N}_1 \mathbf{P}_2 (\mathbf{u}_2 - \mathbf{A}_2 \mathbf{P}_1 \mathbf{u}_1) \quad (12.8)$$

It can be shown that the obtained solution satisfies the least squares requirement as good as  $\mathbf{P}_1 \mathbf{u}_1$ ; the additional term presented in equation (12.8) belongs to the nullspace of  $\mathbf{A}_1$ . The selection of  $k$  (the polynomial degree) should provide a sufficiently accurate data series approximation. In addition, the decision regarding the number of polynomials to be involved is closely related with their interpolation order. The selection of this truncation parameter depends on the data behaviour and is usually fixed after some trial and error work. A great advantage of this method is that we end up with a small number of polynomials providing  $C^1$  continuity and reduced oscillation. Furthermore, the determination of pseudo inverses can be found in almost every mathematics-related package and is very stable [μ15]. The determination of the nullspace is also a standard feature.

### **Fourier series**

The periodic character of the data under consideration makes them suitable for an approximation by a Fourier series. Their accuracy however, depends strongly on the quality of the integration procedure for obtaining the multipliers of the involved sine and cosine terms. Since there is no curve-related information about the spaces between the nodes, integration over some approximation created by Lagrange interpolation is generally not reliable (oscillation).

A better method is to construct a collection of cubic splines and integrate over them (see also the remarks in the cubic splines paragraph). Before proceeding to this operation, we decompose the data into a linear  $f_l(x)$  and a discrete periodic part  $Y_i$  that is given in figure 12.2:

$$f_l(x) = \frac{y_n - y_0}{x_n - x_0} (x - x_0) \quad Y_i = y_i - f_l(x_i) \quad (12.9)$$

### Part C: Production process

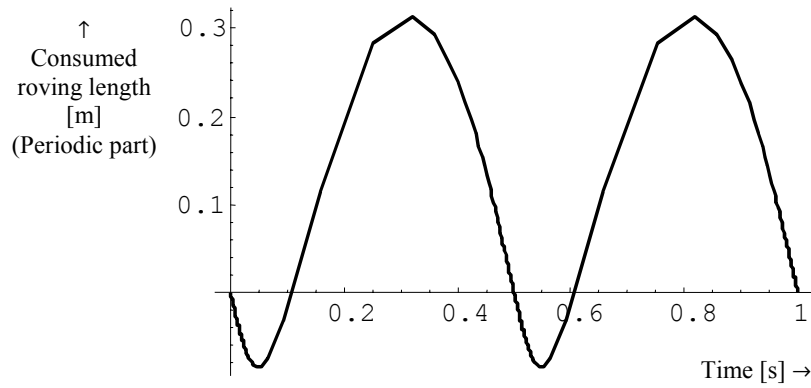


Fig. 12.2: The input data after extraction of the linear part is forming a periodic function in time

The next step consists of the determination of cubic splines  $C_i(x)$ . Every single spline describes the behaviour of the periodic part at a particular interval  $[x_i, x_{i+1}]$  with sufficient accuracy and absence of oscillations. With these splines, the series can then be obtained by:

$$f_p(k, x) = a_0 + \sum_{i=1}^k \left( a_i \cos \frac{i\pi x}{L} + b_i \sin \frac{i\pi x}{L} \right) \quad (12.10)$$

We define the profile function:

$$P(x) = C_i(x) \quad x_i \leq x \leq x_{i+1} \quad (12.11)$$

The coefficients of the series are then given by:

$$a_0 = \frac{1}{2L} \int_{x_0}^{x_n} P(x) dx, \quad a_i = \frac{1}{L} \int_{x_0}^{x_n} P(x) \cos \frac{i\pi x}{L}, \quad b_i = \frac{1}{L} \int_{x_0}^{x_n} P(x) \sin \frac{i\pi x}{L} \quad (12.12)$$

The original data (figure 12.1) are then approximated by:

$$F(k, x) = f_l(x) + f_p(k, x) \quad (12.13)$$

The Fourier series is truncated at a particular number  $k$ . If this number  $k$  is small, the approximation is poor. When  $k$  becomes too large we introduce high frequencies in equation (12.13) which may cause significant fluctuations in the calculated acceleration values.

It should be noticed that several mathematics packages provide splines in parametric form  $[\mu 3, \mu 14, \mu 15]$ . In this case we should divide  $L$  into small increments  $\Delta h$  and numerically integrate among them. When  $\Delta h$  is in the order  $2L/n$ , even the simple trapezium method will provide satisfactory results  $[\mu 2, \mu 7]$ .

## 12.3 Differentiation & filtering

### Discrete methods

Having a proper description of the data given in figure 12.1, decisions have to be taken in regard to the differentiation procedure. This can be done by single or multipoint formulas. The simplest way to obtain approximations for the derivative is:

$$\left. \frac{\Delta y}{\Delta x} \right|_i = d_i = \frac{y_i - y_{i-1}}{\Delta h}, \quad \left. \frac{\Delta^2 y}{\Delta x^2} \right|_i = \frac{d_i - d_{i-1}}{\Delta h} = \frac{d_i - 2d_{i-1} + d_{i-2}}{2(\Delta h)^2} \quad (12.14)$$

Differentiation of a higher order approximation will usually result in improved accuracy for the derivatives. As an example, we provide here finite differences that are based on a second order Lagrange interpolation. The latter is defined as follows [μ8]:

$$\begin{aligned} p_2(x) &= L_0(x)y_0 + L_1(x)y_1 + L_2(x)y_2, \quad \text{with :} \\ L_0(x) &= \frac{(x-x_1)(x-x_2)}{(x_0-x_1)(x_0-x_2)} = \frac{(x-x_1)(x-x_2)}{2(\Delta h)^2} \\ L_1(x) &= \frac{(x-x_0)(x-x_2)}{(x_1-x_0)(x_1-x_2)} = \frac{(x-x_0)(x-x_2)}{-(\Delta h)^2} \\ L_2(x) &= \frac{(x-x_0)(x-x_1)}{(x_2-x_0)(x_2-x_1)} = \frac{(x-x_0)(x-x_1)}{2(\Delta h)^2} \end{aligned} \quad (12.15)$$

Differentiation of  $p_2(x)$  results in:

$$y'(x) \approx p'_2(x) = \frac{2x-x_1-x_2}{2(\Delta h)^2} y_0 - \frac{2x-x_0-x_2}{(\Delta h)^2} y_1 + \frac{2x-x_0-x_1}{2(\Delta h)^2} y_2 \quad (12.16)$$

Evaluation of (12.16) for  $\{x_0, x_1, x_2\}$  gives:

$$\begin{aligned} y'_0 &\approx \frac{1}{2\Delta h}(-3y_0 + 4y_1 - y_2) \\ y'_1 &\approx \frac{1}{2\Delta h}(-y_0 + y_2) \\ y'_2 &\approx \frac{1}{2\Delta h}(y_0 - 4y_1 + 3y_2) \end{aligned} \quad (12.17)$$

In comparison with the first derivatives provided by equation (12.14), the corresponding finite differences presented in (12.17) are divided by a doubled increment ( $2\Delta h$ ); this should theoretically improve the stability of the obtained results. However, at the same time the values for  $f_i$  are in some cases

## Part C: Production process

multiplied by the number 3 or 4; this multiplication will generally result in amplification of the obtained finite differences. Consequently, for a node  $i$  it is generally preferable to use the second expression in (12.17):

$$\left. \frac{\Delta y}{\Delta x} \right|_i = d_i = \frac{y_{i+1} - y_{i-1}}{2\Delta h} \quad \left. \frac{\Delta^2 y}{\Delta x^2} \right|_i = \frac{d_{i+1} - d_{i-1}}{2\Delta h} \quad (12.18)$$

This repeated construction of central differences provides sufficient accuracy and noise reduction for  $\Delta h$  in the order of  $2L/n$ . Nevertheless, this statement is purely empirical and is based on data distributions that are typical in filament winding modelling. When discrete differentiation is desired, we can enlarge  $\Delta h$  (for example  $4L/n$ ) to suppress the occurring oscillations. Note that the kind of supporting interpolation functions for the construction of these finite differences is not restricted to Lagrange. For example, the creation of the differences can be based on cubic splines. However, once these splines are defined, it is preferable to take their analytical derivatives.

Additional methods for noise suppression can usually be found in mathematics programs. The most common of these methods are [μ15]: (weighted) moving average, Lowess, Loess, Savitzky-Golay etc. Nevertheless, these methods are not evaluated in the present chapter.

### Analytical differentiation

Direct differentiation of obtained splines is in several cases not recommendable, since it strongly depends on the node behaviour. For example, when some nodes are located around a sharp corner followed by nodes located on a straight line, the spline slope development between these nodes might be unrealistic (for instance, the resulting curve will have several “dents”).

When the data are described by a partial least squares fitting, oscillations in the derivatives are relatively damped out. In this case we may proceed to direct differentiation. However, when the degree of the polynomial is very high, oscillations can still occur. Contrary to this, a low polynomial degree may result to rather conservative velocity and acceleration estimations.

In the case of describing the data in spline-based Fourier series, we should be aware of the influence of the higher frequencies when differentiating. This is known as the Gibbs phenomenon, which is typically demonstrated in textbooks on a Fourier series approximating a square wave. A practical solution to this, is to truncate the series at the number  $k$  where the multipliers of the trigonometric coefficients become larger than the previous ones ( $a_{i+1} > a_i$  or  $b_{i+1} > b_i$ ). Another correction method to suppress the higher frequencies [μ15] contains the multiplication of the differentiated Fourier terms with the so-called Lanczos convergence factors. These factors are based on the sinc(#) function, usually referred to as sampling function:

$$\text{sinc}(x) = \begin{cases} 0 & x = 0 \\ \frac{\sin(x)}{x} & x \neq 0 \end{cases} \quad (12.19)$$

The Fourier series presented in equation (12.10) is multiplied with (12.19) after differentiation. The derivatives become:

$$f'_{,p}(k, x) = -\frac{k \text{sinc}\left(\frac{i\pi}{k}\right)}{L} \sum_{i=1}^k \left[ a_i \sin\left(\frac{i\pi x}{L}\right) + b_i \cos\left(\frac{i\pi x}{L}\right) \right] \quad (12.20)$$

$$f''_{,p}(k, x) = -\frac{k^2 \text{sinc}^2\left(\frac{i\pi}{k}\right)}{L^2} \sum_{i=1}^k \left[ a_i \cos\left(\frac{i\pi x}{L}\right) + b_i \sin\left(\frac{i\pi x}{L}\right) \right]$$

where, in the first derivative, the term before the summation is the Lanczos convergence factor; in the second derivative, this term is squared.

The method based on the Lanczos convergence factor is very common in the field of numerically deriving accelerations from sampled displacement data, like at impact testers. However, when the periodic data have a smooth appearance and the series are truncated at a proper  $k$ -value, these corrections might be not necessary. Nevertheless, we must not forget that an important factor affecting the degree of oscillation is the quality of the integration when determining  $a_0$ ,  $a_i$  and  $b_i$ . This is the reason for integrating the Fourier coefficients over cubic splines instead of Lagrange interpolating polynomials.

## 12.4 Results & discussion

In this section, an overview of some typical results is given. First we present the original data (black dots) and their approximations (figure 12.3). The partial least squares approximation (PLS) is based on two polynomials connected with  $C^1$  continuity. The derivatives at their endpoints as well as the corresponding  $y$ -values are analytically evaluated. The Fourier series approximation (F) is, together with PLS and the cubic splines (CS), given in a black continuous line. The grey line represents the Bezier approximation where we used only three nodes as base points (at  $x = 0$ ,  $x = 0.5$  and  $x = 1$ ). It is clearly visible that the Bezier curve with only three base points provides a poor approximation. The other methods work sufficiently well.

Following a similar colour scheme, the next graph (12.4) represents the obtained velocity profiles. Except the partial least squares (PLS, dashed black line) and Fourier (continuous black line), the data are obtained by discrete differentiation (based on (equation 12.18)).

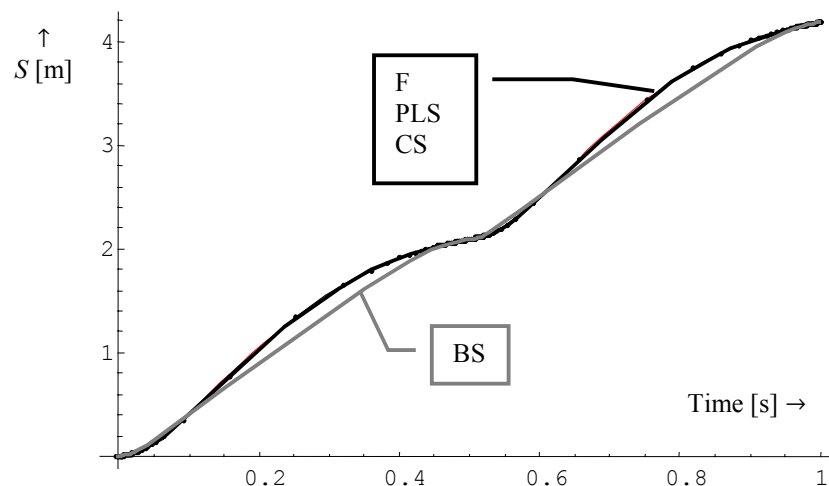


Fig. 12.3: Various approximations of the original roving length data as a function of time

The remarkable aspect of the velocity graph is that while the original profiles presented in figure 12.3 are fairly smooth, their derivatives are far from constant. The poor quality of the numerically differentiated Bezier approximation (continuous grey line) was expectable. Furthermore, the analytical derivative of the Fourier approximation agrees very well with the discrete velocity values obtained by numerical differentiation of the Cubic spline approximation. Since the Cubic splines-based approximation (CS) is also drawn with a continuous black line, there is hardly any difference with (F). As a last remark, we denote here that the derivatives of the partial least squares approximation are slightly overestimating the resulting velocity.

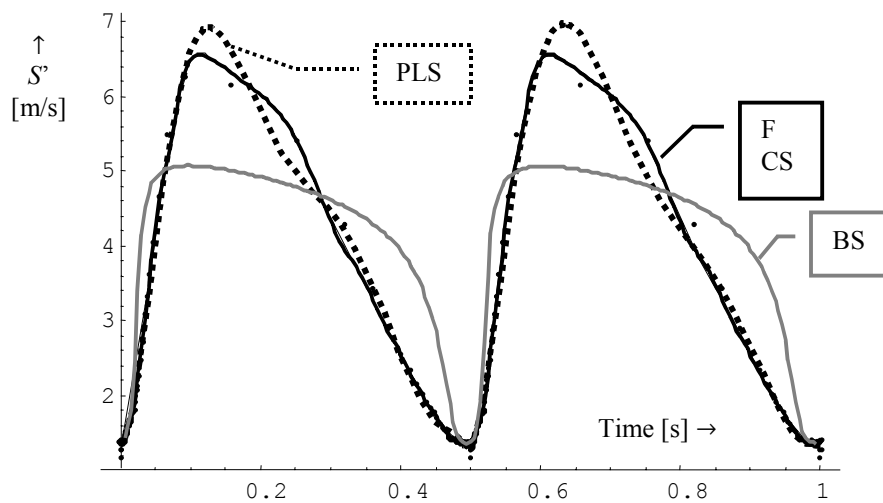


Fig. 12.4: The obtained velocity profiles as a function of time

In figure 12.5 we present the acceleration data; dashed black line = second analytical derivative of the partial least squares approximation, continuous black line = second analytical derivative of the Fourier series, thick continuous grey line = second discrete derivative of the cubic splines approximation, thin continuous grey line = second discrete derivative of the Bezier splines approximation. From the figure we can conclude that the acceleration profiles derived by the Fourier and partial least squares approximation agree very well. The same observation applies on the profile derived from the cubic splines. However, this curve shows some (limited) oscillation. The differentiated Bezier curves overestimate the acceleration. The same drawback applies on the data obtained by double discrete differentiation of the original nodes (black dots). In addition, the discrete derivatives obtained from the black dots do generate considerable scatter.

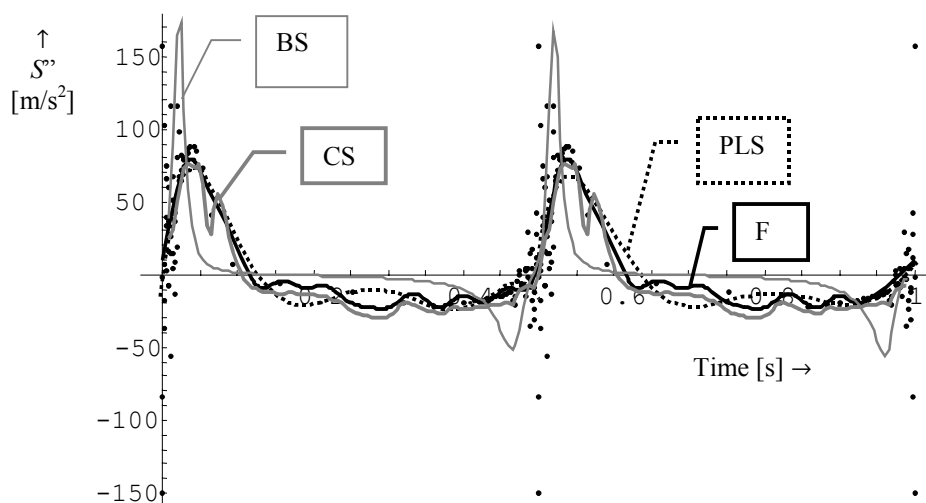


Fig. 12.5: The obtained acceleration profiles as a function of time

## Part C: Production process

The results clearly indicate that simple interpolation methods followed by numerical differentiation will in general produce noisy velocity and acceleration data. One may suppress the resulting oscillations by enlarging the differentiation increments, but this operation is usually reducing the accuracy and reliability of the obtained data. In addition, the application of the usual smoothing methods may also cause this accuracy reduction.

It is believed that the analytical approximation methods (for instance, partial least squares and Fourier) followed by analytical differentiation provide a useful tool for estimating the reliability of the obtained discrete results and the quality of eventually applied methods for their smoothing. In addition, since the partial least squares and Fourier-based methods provide a fully analytical representation of the velocity and acceleration data, they are suitable for implementation in an optimisation algorithm. In addition, the analytical approximation methods can act as input-generating parameters for machine controllers.

In conclusion however, the best performance is achieved by the Fourier series approximation. Nevertheless, for calculating the acceleration, the implementation of the partial least squares approximation may be preferable since it hardly oscillates. For the final data representation it is strongly recommended to use the combination of a (quasi)-analytical and discrete method over a sufficient range of step sizes and truncation parameters  $k$ . Depending on their sensitivity for oscillations, a final decision can then be taken.

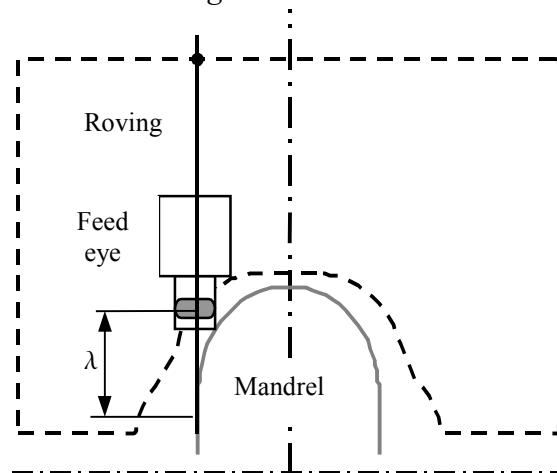
## 13

## Collision control

An important facet of the filament winding process, besides the proper quantification of the dynamic machine limits (chapter 12), is the exact determination of the space where the feed eye is allowed to move in. The curves bounding that space are dictated by two groups of geometrical constraints: the outer machine workspace limits for the carriage and cross carriage translations, and the collision avoidance of the feed eye unit with the mandrel.

The usual strategy for determining this moving space is to respect some margins of safety around the contour of the mandrel. Despite the existence of several publications tackling this problem, the need for a relatively easy to evaluate straightforward boundary-determining procedure did probably not gain the attention it deserves. As derived in chapter 11, the feed eye translations depend on the locus  $i$  of the roving on the mandrel and the free-hanging fibre length  $\lambda$ . The latter is playing an important role in the problem of minimising the production time. Consequently, a proper determination of its lower and upper bounds is highly desirable.

The chapter begins with a treatment of the procedure for obtaining the collision-related limiting contour in the vicinity of the mandrel. The resulting curves typically demonstrate the interaction between mandrel shape and feed eye unit geometry. Section 13.2 is associated with the determination of the  $\lambda$ -bounds for the outer feed eye moving space contour. These  $\lambda$ -bounds can be obtained through analytical methods. For the (usually) curved contour around the mandrel, the limiting  $\lambda$ -values can generally only be derived by numerical methods, section 13.3. In addition, we provide an example of a  $\lambda$ -intervals collection where it is demonstrated that in several cases it might not be possible to create a filament wound product, at least according to the common assumptions for the cross carriage translation  $X$ .



**Schematic top view of a lathe winder, where the moving space for the feed eye is bounded by dashed lines**

## **Part C: Production process**

### 13.1 Feed eye geometry

To avoid collision between the wound object and the feed eye, the geometry of the latter has to be well defined. With a proper determination of the dimensions for the feed eye and its supporting construction, the allowed moving area near the wound object can then be calculated, see figure 13.1:

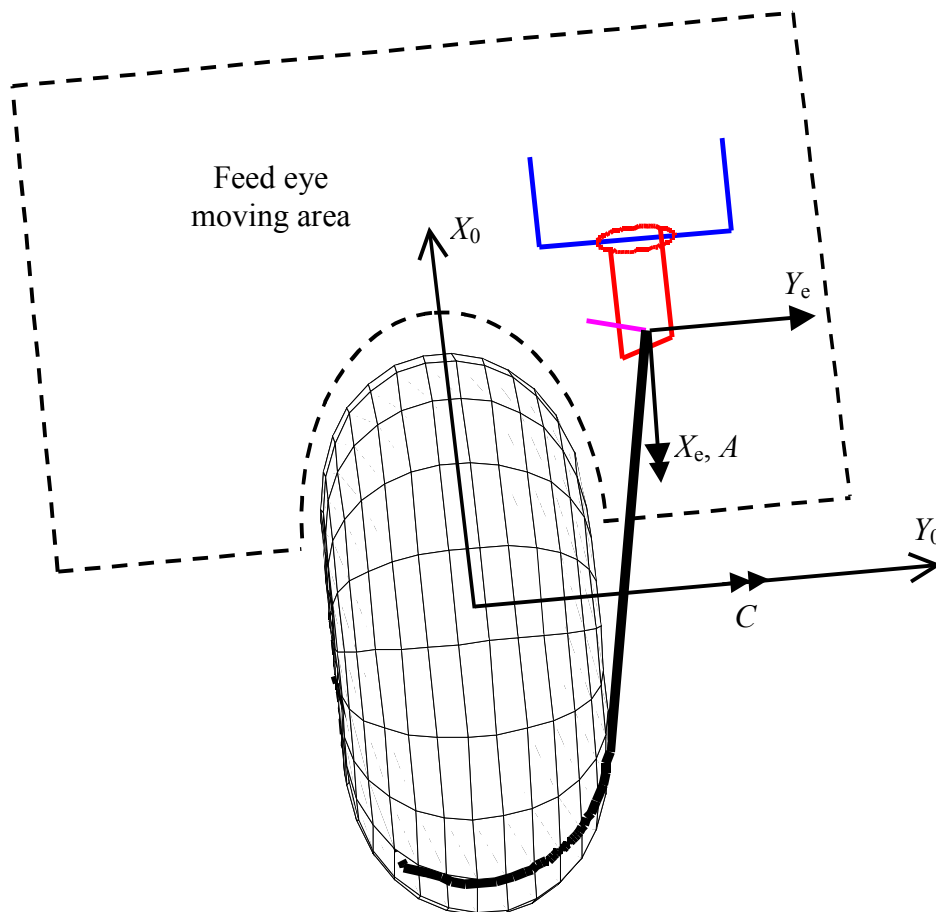


*Fig. 13.1: Top view of mandrel that is attached to a lathe winder, and feed eye unit*

In the figure, the dashed lines bound the permitted moving area for the feed eye. Obviously, the outer boundaries are determined by the machine limits for the  $X$  and  $Y$  movements. It should be noted that the common notation for the carriage is  $Z$  (as used in chapter 7). However, we use here the mathematically correct notation  $Y$ .

It is evident that minimisation of the feed eye construction will enlarge the moving area. Nevertheless, manufacturers of filament winding machines tend to create rather large supporting structures of a specific form [α3], as depicted in figure 13.2. Although not optimal, this feed eye unit shape is almost traditional, so we introduce here a parametric description for it.

### Part C: Production process

Depending on the winding machine under consideration, one can approximate the feed eye unit by a proper quantification of the parameters  $P_{\#\#}$  (figure 13.2).

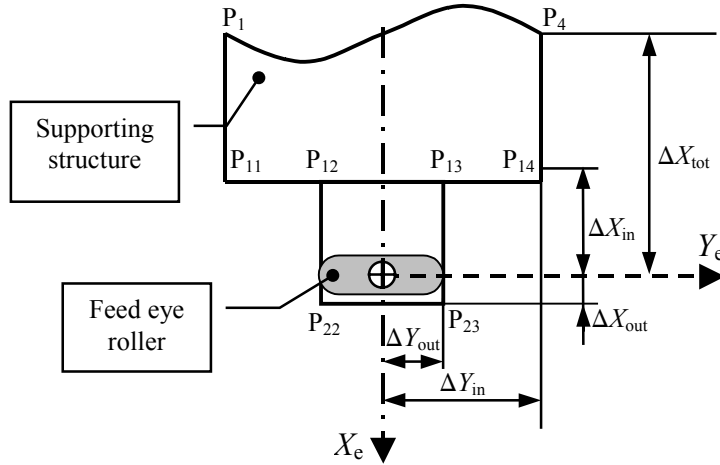


Fig. 13.2: Top view of a parametrically defined feed eye structure

The quantification of  $\Delta X_{tot}$  depends mainly on the contour of the wound body and is determined by the relevant length of the feed eye supporting structure that can possibly contact the body, figure 13.3. Another issue that affects the moving space for the feed eye is the cross carriage translation limitation that is usually part of the CNC software controlling the machine, designed for avoiding collision of the feed eye with the machine axis. Instead of this limitation we introduce here some additional space for the  $X$ -movement, denoted as  $X_{tol}$  (tolerance).

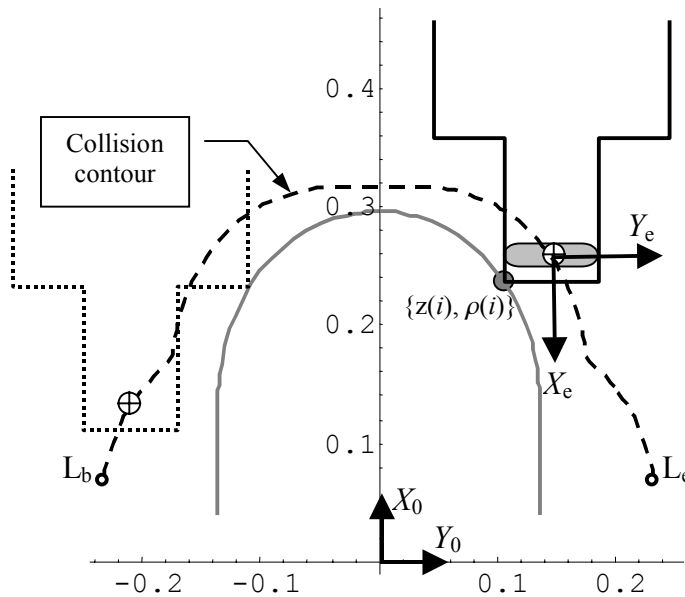


Fig. 13.3: Schematic representation of the feed eye-related collision bounds

The additional freedom for the cross carriage position  $X$  is extremely useful for adjusting the reference position of the feed eye, in order to create the ability for placing the fibre bundle exactly adjacent to the polar openings of e.g. a pressure vessel. Setting the feed eye closer to the mandrel will reduce the polar opening radius of the resulting roving layer.

For a particular locus  $i$  belonging to the roving path that is placed on the mandrel, we assume that the corresponding position vector coordinates in the  $\{X_0, Y_0\}$  system are given by  $\{z, \rho\}$  (as used in section 11.2). The inner and outer dimensions of the feed eye construction (as indicated in figure 13.2) generate two limiting contours for avoiding collision with the body under consideration (figure 13.3):

$$\begin{aligned} \mathbf{C}_{in}(i) &= \{\rho(i) - \Delta X_{in} + X_{tol}, \text{sgn}[z(i)]\Delta Z_{in} + z(i), 0\} \\ \mathbf{C}_{out}(i) &= \{\rho(i) + \Delta X_{out} + X_{tol}, \text{sgn}[z(i)]\Delta Z_{out} + z(i), 0\} \end{aligned} \quad (13.1)$$

With the proper selection of the absolute maximum coordinate values provided by these contours for a locus  $i$ , we finally obtain the limiting contour  $\mathbf{C}_{col}(i) = \{X_{col}(i), Y_{col}(i)\}$  for the feed eye translations near the body. The resulting curve is depicted in figure 13.3 as a black dashed line beginning at the point  $L_b$  and ending at  $L_e$ , defined in the  $\{E_0\}$  system. Notice that  $L_b$  and  $L_e$  depend simultaneously on the feed eye dimensions and the body contour.

### 13.2 Machine limits

The description of the outer machine limits is far easier than the determination of the boundaries in the vicinity of the wound object. The outer feed eye translation limits  $\{L_{11}, L_{12}, L_{21}, L_{22}\}$  are given in the machine coordinate system  $\{E_m\}$  (notice that  $\{L_b, L_e\}$  is defined in  $\{E_0\}$ ).

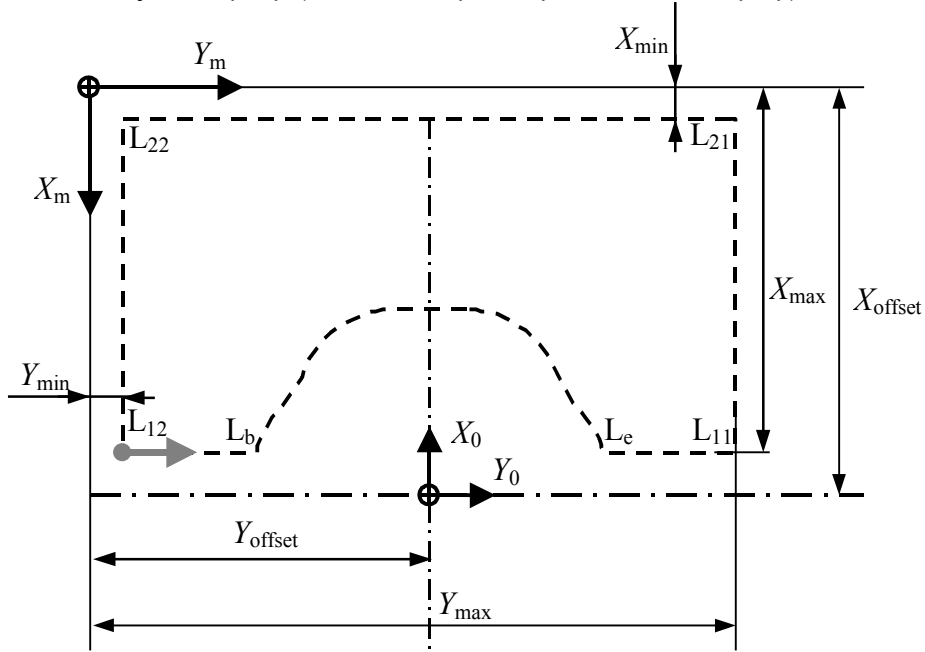


Fig. 13.4: Limits for the feed eye translations

From the figure we can immediately derive the machine limits with respect to the  $\{E_0\}$  system:

$$\begin{aligned}
 Y_{21} &= Y_{\min} - Y_{\text{offset}} = Y_{22} \\
 Y_{11} &= Y_{\max} - Y_{\text{offset}} = Y_{21} \\
 X_{12} &= X_{\text{offset}} - X_{\max} = X_{11} \\
 X_{22} &= X_{\text{offset}} - X_{\min} = X_{21}
 \end{aligned}
 \tag{13.2}$$

With the complete set of points defined in  $\{E_0\}$  and the feed eye-related contour  $C_{\text{col}}$  we construct two interpolating polynomials expressing the  $X$  and  $Y$  coordinates of the entire border as functions of the length along the contour  $\{L_{12}, L_b, C_{\text{col}}, L_e, L_{11}, L_{21}, L_{22}, L_{12}\}$  (grey arrow, as indicated in figure 13.4):

$$C_{\text{tot}}(s) = \begin{Bmatrix} X_{\text{border}}(s) \\ Y_{\text{border}}(s) \\ 0 \end{Bmatrix}, \quad 0 \leq s \leq \text{length} \left\{ \underbrace{L_{12}, L_b, L_e, L_{11}, L_{21}, L_{22}, L_{12}}_{\text{Figure 13.4}} \right\}
 \tag{13.3}$$

In section 11.2 we derived the equations for the analytical determination of the required machine movements for rotationally symmetric objects, attached on a lathe-configured winder. The complete set of provided solutions is actually underdetermined; for a particular locus  $i$  of the applied roving, the solution is additionally depending on the length  $\lambda$  of the free-hanging fibre (as depicted in figure 10.4). The obtained solutions for the feed eye translations are here repeated:

$$\begin{aligned} X(i, \lambda) &= \sqrt{\lambda^2 \sin^2 \alpha(i) + (\rho(i) + \lambda \cos \alpha(i) \sin \beta(i))^2} \\ Y(i, \lambda) &= \rho(i) + \lambda \cos \alpha(i) \cos \beta(i) \end{aligned} \quad (13.4)$$

According to these equations, with a sufficiently increased  $\lambda$ , the previously determined borders can be crossed. Denoting the  $X$ -coordinate of the border with  $X_{\text{lim}}$ , the corresponding  $\lambda$ -value is given by:

$$\lambda_{X_{\text{lim}}}(i) = \frac{-\rho \cos \alpha \cos \beta \pm \sqrt{\sin^2 \alpha (X_{\text{lim}}^2 - \rho) + \cos^2 \alpha \sin^2 \beta X_{\text{lim}}^2}}{\sin^2 \alpha + \cos^2 \alpha \sin^2 \beta} \Big|_i \quad (13.5)$$

where the negative solution is occasionally dropped. Since the value for  $X_{\text{lim}}$  is predetermined, the radial body coordinate  $\rho$  can eventually become smaller than  $X_{\text{lim}}$ . In this case, the derived expression will generate two positive solutions, indicating that for a sufficiently large  $\lambda$ -value the feed eye will re-enter the allowed working space. Consequently, for particular loci  $i$ , one can obtain a set of two  $\lambda$ -intervals corresponding to feasible feed eye positions. As depicted in figure 13.6, the trace  $\Lambda(i, \lambda) = \{X(i, \lambda), Y(i, \lambda), 0\}$  does generally not lay on a straight line.

To cross a certain  $Y$ -value ( $= Y_{\text{lim}}$ ) the  $\lambda$  parameter must become at least equal to:

$$\lambda_{Y_{\text{lim}}}(i) = \frac{Y - \rho}{\cos \alpha \cos \beta} \Big|_i \quad (13.6)$$

where care must be taken for not dividing by zero. With the replacement of the limiting values with the relevant coordinates  $\{X_{\#\#}, Y_{\#\#}\}$  (equation (13.2)), the  $\lambda$ -limits for the outer machine borders can easily be obtained.

### 13.3 Numerical bounds determination

For the feed eye translation boundary near the wound body contour, the determination of the limiting  $\lambda$ -values is generally not achievable through analytical ways. The  $C_{col}$  function (equation (13.3)) is derived as a vector that is based on interpolating polynomials with the contour length as independent variable. Since these piecewise polynomial approximations might exhibit a rather irregular behaviour for their derivatives (see also chapter 12), application of particular solvers will occasionally fail [ $\mu 2, \mu 14, \mu 15$ ]. However, when applying methods that do not depend on derivatives, e.g. secant method, the solution of  $X_{lim} == X_{col}$  and  $Y_{lim} == Y_{col}$  can easily be obtained. A prerequisite for this is that the guessed initial solution interval must contain the root and that the limiting values of this interval must be sufficient close to that root. As outlined in the previous section, for a particular locus  $i$  we obtain a feed eye tracing curve that is a parametric vector function of  $\lambda$ , namely:  $\Lambda(i, \lambda) = \{X(i, \lambda), Y(i, \lambda), 0\}$ . The feed eye moving space near the body is limited by  $C_{col}(s)$ . To obtain the required initial solution interval we must detect where  $\Lambda(i, \lambda)$  and  $C_{col}(s)$  intersect each other. In the figure below, the depicted straight line segments are crossing each other at the point  $\mathbf{q}$ .

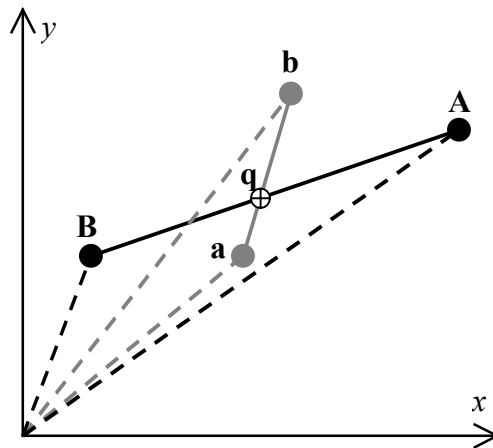


Fig. 13.5: Intersecting line segments in the two-dimensional space

With  $\mathbf{a} = \{a_x, a_y\}$ ,  $\mathbf{b} = \{b_x, b_y\}$ ,  $\mathbf{A} = \{A_x, A_y\}$  and  $\mathbf{B} = \{B_x, B_y\}$  the intersection point  $\mathbf{q}$  can be described as follows:

$$\mathbf{q} = \mathbf{a} + u \begin{Bmatrix} b_x - a_x \\ b_y - a_y \end{Bmatrix} = \mathbf{A} + U \begin{Bmatrix} B_x - A_x \\ B_y - A_y \end{Bmatrix} \quad (13.7)$$

To determine  $u$  and  $U$ , the following system can be constructed:

$$\begin{bmatrix} b_x - a_x & A_x - B_x \\ b_y - a_y & A_y - B_y \end{bmatrix} \cdot \begin{Bmatrix} u \\ U \end{Bmatrix} = \begin{Bmatrix} A_x - a_x \\ B_x - b_x \end{Bmatrix} \quad (13.8)$$

When the lines are parallel, the determinant of the matrix presented in (13.8) becomes equal to zero, so there is no convenient solution for  $u$  and  $U$ . In every other case, the values for  $u$  and  $U$  are given by:

$$\begin{aligned} u &= \frac{(A_y - a_y)B_x + A_x(a_y - B_y) + a_x(B_y - A_y)}{(A_x - B_x)(a_y - B_y) - (a_x - b_x)(A_y - B_y)} \\ U &= \frac{(A_y - a_y)b_x + A_x(a_y - b_y) + a_x(b_y - A_y)}{(A_x - B_x)(a_y - B_y) - (a_x - b_x)(A_y - B_y)} \end{aligned} \quad (13.9)$$

The line segment intersect each other when the following condition is satisfied:

$$0 \leq u \leq 1 \quad \& \quad 0 \leq U \leq 1 \quad (13.10)$$

For a certain locus  $i$ , we define a  $\lambda$ -range  $[0, \lambda_{\max}]$ , sufficiently large to contain all possible intersections. Beginning at  $\lambda = 0$ , we proceed around the border contour  $C_{\text{col}}$  that is divided into sufficiently small line segments and calculate the  $u$  and  $U$  values according to equation (13.9). The obtained values are then subjected to criterion (13.10). When an intersection is detected, the corresponding  $\lambda$ -coordinate is evaluated by solving  $C_{\text{col}}(s) = \Lambda(\lambda)$  with e.g. the secant method for the corresponding  $s$  and  $\lambda$  intervals. The next step is to increase  $\lambda$  with some increment  $\Delta\lambda$  and repeat the same procedure. Although this method could be more sophisticated, it performs sufficiently well in terms of accuracy and computational efforts. It should be noted that this method could alternatively be applied on the complete border  $C_{\text{tot}}(s)$ . However, since the  $\lambda$ -values for the (straight) outer machine boundaries can easily be derived with analytical methods, there is no reason to do so.

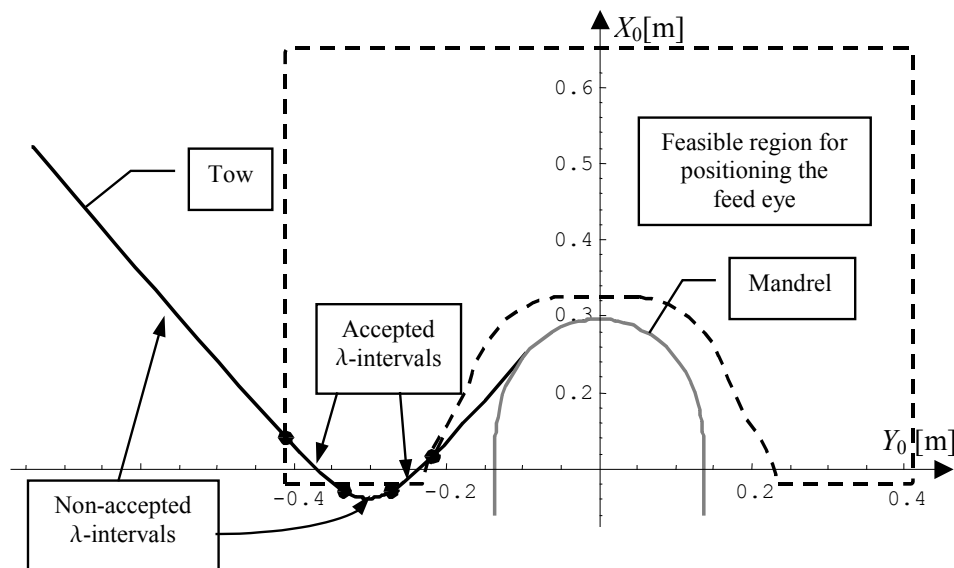


Fig. 13.6: The determination of the allowable  $\lambda$ -intervals (notice that the feed eye positions are not located on a straight line)

## Part C: Production process

For the construction of the search intervals, the choice for the associated  $s$  and  $\lambda$  intervals is rather a matter of trial and error. More specific, the final choice is the result of a trade off between reliability for catching the proper  $\lambda$ -solution and computational efforts [16].

The necessity of a stable and accurate method for determining the suitable  $\lambda$ -ranges is demonstrated in figure 13.7 where it is clearly visible that the upper and lower limits of the obtained intervals do not exhibit smooth behaviour at all. An essential observation is that certain paths through the entire collection of  $\lambda$ -ranges are not possible since they do not provide any continuous  $\lambda$  propagation (as a function of  $i$ ). Moreover, in particular cases that depend on the mandrel shape, the machine limits and the feed eye morphology, winding might not be possible at all.

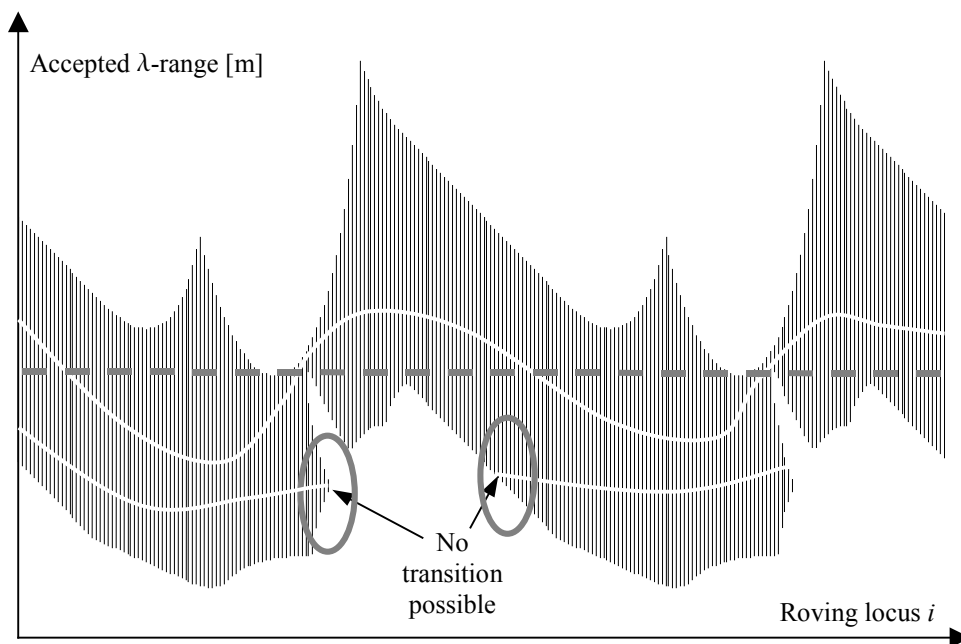


Fig. 13.7: The resulting  $\lambda$ -ranges as a function of the locus  $i$  on the wound fibre path, where at some points, the obtained ranges consist of multiple intervals

The kinematic equations covering filament winding are less in number than the involved unknown parameters [16,19]. In the case of a lathe winder, the additional unknown parameter can be formulated in terms of the cross carriage translation  $X$  or the length of the free hanging fibre  $\lambda$  (as presented in section 11.2).

The usual strategy to eliminate this additional degree of freedom for the feed eye position is to assume that the latter is following a contour similar to the contour of the mandrel, enlarged with some percentage [3,1,2]. As demonstrated in figure 13.3, this assumption might cause collision, especially in the case when the feed eye supporting structure is considerably broader than the feed eye roller itself [16].

The second most popular strategy to determine the cross feed position  $X$  is to assume that the length of the free-hanging fibre is constant throughout the complete winding process  $[\alpha_3, \delta_1, \delta_2]$ . As demonstrated in figure 13.7 with the grey dashed line, this strategy might not be possible at all. Moreover, this impossibility occurs rather often, especially when the mandrel under consideration has a relatively large flat area around the poles. Returning to figure 13.7, winding of the mandrel as presented in figure 13.1 with the depicted machine limits is in this case barely possible.

With the expressions for the associated machine movements  $S(i, \lambda)$ ,  $C(i, \lambda)$ ,  $A(i, \lambda)$ ,  $X(i, \lambda)$  and  $Y(i, \lambda)$  (as given in the figure of the introduction page of chapter 11, and figure 11.1), the proper determination of the allowed  $\lambda$ -ranges and knowledge of the dynamic machine limits, the problem of optimising the production process can now completely be formulated (chapter 14).

## **Part C: Production process**

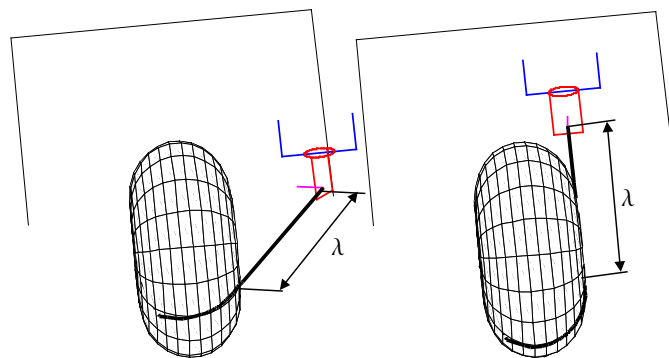
## 14

## Process optimisation

*The tendency of the filament winding technique to become a mass production process inevitably highlights the need for manufacturing costs reduction. Especially the creation and market introduction of lightweight high-performance filament wound pressure vessels and pipes, strongly supports the application of optimisation techniques that are related to their manufacturing process. Up to now, the implementation of several analytical and numerical optimisation techniques has mainly been focussed on maximising the product performance in terms of the best possible strength-to-weight ratio. To ensure the competitiveness of such products with their metallic counterparts, a revisit and evaluation of the associated production process seems to be essential. In contrast to the common techniques applied in optimal control problems (Genetic Algorithms, Neural Networks etc) we propose here the Dynamic Programming method. This method has an extensive field of applications, and applies on cases where the involved control variables have a discrete character.*

*After the problem description in terms of the collision limits and dynamic constraints followed by the formulation of the objective function, we outline the technique for constructing a grid that contains the control variables, and propose a method for reducing the number of the involved nodes (section 14.2). The next section provides the description of the Dynamic Programming method, mainly in the form of a simple example. The chapter concludes (14.4) with the outline of the associated calculation flow diagrams and the presentation of several results.*

*From the results, the conclusion can be drawn that the method presented here works sufficiently well. A major advantage is that it has a straightforward character and that it guarantees the result optimality, however, within the provided grid. Drawbacks are the rather intensive occupation of calculation resources and its considerable sensitivity to the grid properties.*



**The role of  $\lambda$  as a control variable for the resulting machine movements**

## **Part C: Production process**

## 14.1 Problem formulation

We consider here again the filament-winding problem on a lathe winder configuration. Although the theory presented here is certainly not restricted to that configuration, we adapt here the lathe winder to enhance some simplicity and provide a more straightforward character to the calculations.

As seen in the previous chapter, for a particular locus  $t$  belonging to a fibre path that is being placed on some mandrel, the collision boundaries dictate a collection of at least one applicability interval for the free roving length, say  $[\lambda_{\min}(t), \lambda_{\max}(t)]$ . Within that interval, the proper  $\lambda_t$ -value must be selected on such a way that the total production time will obtain a global minimum. Hence, for example, the objective function can be formulated as follows:

$$\min \left[ \sum_{t=1}^n \Delta T(t, \lambda_t) \right] \quad (14.1)$$

This definition is temporary because the time increments for proceeding from locus  $t-1$  to  $t$  do not only depend on the single-valued  $\lambda_t$ .

As outlined in chapter 12, every involved machine movement is subjected to a velocity and acceleration limit. For the lathe configuration, these movements are (as depicted in figures 11.1 and 11.2):

- $S$  = total roving length consumed of the spool [m]
- $C$  = spindle rotational position [rad]
- $A$  = feed eye roller inclination [rad]
- $X$  = cross carriage position [m]
- $Y$  = carriage position [m]

For convenience, the definitions of the machine movements are repeated in figure 14.1. According to equations (11.25) ( $X$  and  $Y$ ), (11.27) ( $C$ ) and (11.28) ( $A$ ), every single position is simultaneously depending on the locus  $t$  and the corresponding free roving length  $\lambda(t)$ , hence,  $C(t, \lambda(t))$ . To reduce repetition we introduce the symbol  $\#(t, \lambda_t)$  replacing the elements of  $\{S(t, \lambda(t)), C(t, \lambda(t)), A(t, \lambda(t)), X(t, \lambda(t)), Y(t, \lambda(t))\}$ . The corresponding velocities and acceleration limits are given in vector form:  $\{\#_{\min}, \#_{\max}\}$  and  $\{\#\prime_{\min}, \#\prime_{\max}\}$ ; an example regarding their quantification is presented in table 12.1. For three consequent loci, the corresponding velocity and acceleration values can be calculated by finite differences, as formulated in equation (12.14):

$$\frac{d\#}{dt} \approx \frac{\#(t) - \#(t-1)}{\Delta T} \quad \frac{d^2\#}{dt^2} \approx \frac{\#(t) - 2\#(t-1) + \#(t-2)}{(\Delta T)^2} \quad (14.2)$$

where, for counters-related reasons the choice has been made for backward differences. Nevertheless, the choice for forward, central or backward differences is not affecting the calculations to be performed.

## Part C: Production process

The majority of the movements presented here is bounded by a positive and a negative velocity or acceleration limit. An important observation is that for every movement from locus  $t-1$  to  $t$ , at least one dynamic constraint will become active. Hence, the idea is to calculate for every involved parameter the minimum time allowed to transit from the  $t-1$  to the  $t$  status. Consequently, every movement will generate two values for  $\Delta T$ : one for the velocity constraint and one for the acceleration. By taking the biggest of the resulting increments  $\Delta T$ , the time needed to transit from  $t-1$  to  $t$  can be determined under the guarantee that every dynamic constraint is respected.

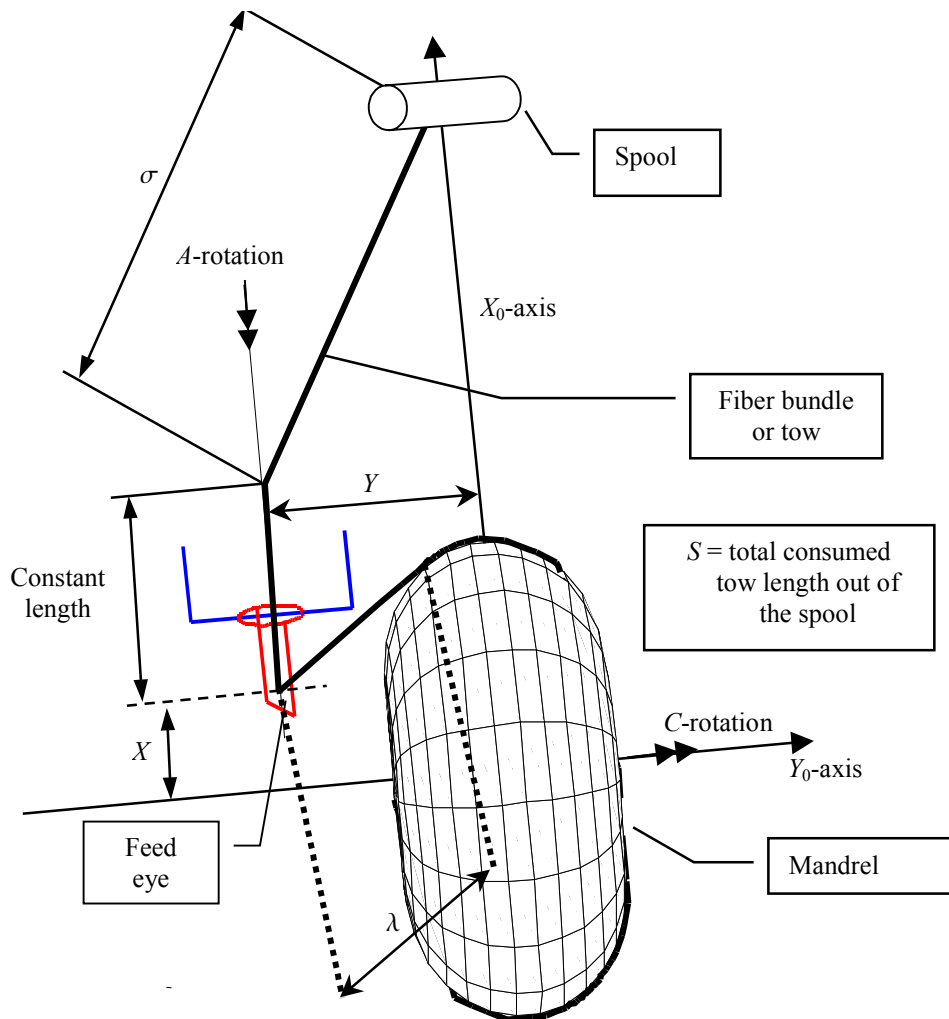


Fig. 14.1: Schematic representation of a lathe-configured winding machine

According to equation (14.2) and by keeping in mind that a movement can be either positive or negative, the corresponding required time increment that is marginally satisfying the velocity constraint is given by:

$$\Delta T_{vel}(\#, t) = \begin{cases} \frac{\#(t, \lambda_t) - \#(t-1, \lambda_{t-1})}{\#'^{\max}}, & 0 < \#(t, \lambda_t) - \#(t-1, \lambda_{t-1}) \\ \frac{\#(t, \lambda_t) - \#(t-1, \lambda_{t-1})}{\#'^{\min}}, & \#(t, \lambda_t) - \#(t-1, \lambda_{t-1}) \leq 0 \end{cases} \quad (14.3)$$

where it is assumed that  $\#'^{\min}$  is negative and  $\#'^{\max}$  positive. On a similar way, the acceleration-related time increments (minimally required values) are given by:

$$\Delta T_{acc}(\#, t) = \begin{cases} \sqrt{\frac{\#(t, \lambda_t) - 2\#(t-1, \lambda_{t-1}) + \#(t-2, \lambda_{t-2})}{\#''^{\max}}}, & \text{for } 0 < \#(t, \lambda_t) - 2\#(t-1, \lambda_{t-1}) + \#(t-2, \lambda_{t-2}) \\ \sqrt{\frac{\#(t, \lambda_t) - 2\#(t-1, \lambda_{t-1}) + \#(t-2, \lambda_{t-2})}{\#''^{\min}}}, & \text{for } \#(t, \lambda_t) - 2\#(t-1, \lambda_{t-1}) + \#(t-2, \lambda_{t-2}) \leq 0 \end{cases} \quad (14.4)$$

The approach presented here is valid for movements that can result in either positive or negative velocity values; these are  $S$ ,  $A$ ,  $X$  and  $Y$ . As previously mentioned, for the determination of the minimum time needed to transit from the  $t-1$  to the  $t$  status, we select the maximum time increment. From the acceleration constraints we obtain:

$$\Delta T_{acc}(t) = \max[\Delta T_{acc}(\#, t)] = \Delta T_{acc}(t, \lambda_{t-2}, \lambda_{t-1}, \lambda_t) \quad (14.5)$$

*with*  $\# = \{S, C, A, X, Y\}$

For monotonic movements however (in this case  $C'$ ) the velocity limits are both either positive or negative. Without any loss of generality we assume here negative values for  $[C'^{\min}, C'^{\max}]$  where  $C'^{\max}$  is very close to zero; for example, according to table 12.1, this interval could be  $[-10\pi/6, -1/20]$ . Since we are dealing here with at least one monotonic movement, the corresponding minimum required time interval must be determined on a slightly modified way. When the resulting velocity for  $C'$  becomes positive, the corresponding time increment is set equal to a very large value (penalty), in our case 1 second:

### Part C: Production process

$$\Delta T_{vel}(t) = \Delta T_{vel}(t, \lambda_{t-1}, \lambda_t) = \begin{cases} \max \left[ \Delta T_{vel}^{pre}(t), \frac{C(t, \lambda_t) - C(t-1, \lambda_{t-1})}{C'_{min}} \right], & \frac{C(t, \lambda_t) - C(t-1, \lambda_{t-1})}{\Delta T_{vel}^{pre}(t)} \leq C'_{max} \\ 1 & \frac{C(t, \lambda_t) - C(t-1, \lambda_{t-1})}{\Delta T_{vel}^{pre}(t)} > C'_{max} \end{cases}$$

where  $\Delta T_{vel}^{pre}(t) = \max[\Delta T_{vel}(\#, t)]$  with  $\# = \{S, A, X, Y\}$

(14.6)

With the aid of equations (14.4) and (14.6) the minimal transition time is given by:

$$\Delta T(t) = \Delta T_t(\lambda_{t-2}, \lambda_{t-1}, \lambda_t) = \max[\Delta T_{vel}(t, \lambda_{t-1}, \lambda_t), \Delta T_{acc}(t, \lambda_{t-2}, \lambda_{t-1}, \lambda_t)] \quad (14.7)$$

The obtained time increments are automatically satisfying the complete set of dynamic constraints. As indicated at the beginning of this section, the free hanging roving length has to be situated in a certain collection of minimally one interval, dictated by the collision avoidance procedure (chapter 13):

$$\lambda_t \in \lambda(t) = \{[\lambda_{min}(t), \lambda_{max}(t)]_1, [\lambda_{min}(t), \lambda_{max}(t)]_2, \dots, [\lambda_{min}(t), \lambda_{max}(t)]_k\} \quad (14.8)$$

Another important aspect of the problem formulated here is that the winding process has a repeating character, hence the involved movements and roving behaviour are periodic (Fig. 14.2). The first locus number of such a period is here denoted by  $b$  and the last one by  $e$ . With this information, the optimisation problem can be finally summarised as follows:

$$\min \left[ \sum_{t=b}^{t=e} \Delta T_t(\lambda_{t-2}, \lambda_{t-1}, \lambda_t) \right] \quad (14.9)$$

with  $\lambda_t \in \lambda(t)$

which is in essence an optimal control problem: for every  $t$  determine  $\lambda_t$  on such a way that the total production time will obtain its global minimum.

## 14.2 Grid construction

### Initial grid definition

As derived in chapter 13, the resulting collection of allowable  $\lambda$ -ranges can possibly exhibit great variations in its upper and lower bounds. In addition, as observed for the machine movements, the resulting  $\lambda$ -ranges are also periodic. Although not necessary, we choose here as an initial locus  $b$  the position of the smallest interval, figure 14.2.

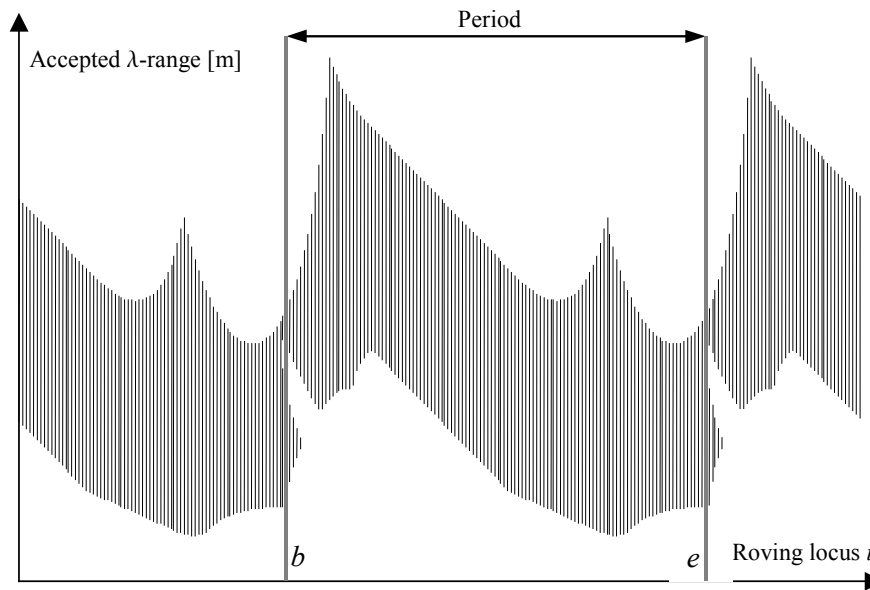


Fig. 14.2: Definition of the initial locus  $b$  and the final position  $e$ , both belonging to the applied roving path

The original determination of the fibre loci is based on a constant length increment  $\Delta L$  (equation (10.8)). On a similar way, for the  $\lambda$ -ranges presented as vertical lines in figure 14.2, we define an increment  $\Delta g_{init}$ . For the evaluation of the optimisation routine however, every range should be divided into an integer number of increments  $\Delta g(t)$  (for simplicity we temporarily do not consider here the fact the a locus  $t$  might correspond to multiple ranges, as formulated in equation (14.8)):

$$\Delta g(t) = \frac{\lambda_{max}(t) - \lambda_{min}(t)}{\text{IP} \left[ \frac{\lambda_{max}(t) - \lambda_{min}(t)}{\Delta g_{init}} \right]} \quad (14.10)$$

A particular  $\lambda(k)$ -value belonging to locus  $t$  will be denoted by  $\lambda_i(k)$ . The choice for  $\Delta g_{init}$  depends mainly on the increment  $\Delta L$ , the accuracy of the machine controllers for the feed eye translations and the trade off between calculation time and desired production time reduction.

## Part C: Production process

An additional aspect to take into consideration is the fact that the smoothness of the resulting machine movements is increasing with a reducing  $\Delta g$ . Obviously the grid should be fine enough to provide sufficiently smooth movements. If not, the production time will dramatically increase since the time increments needed for respecting the velocity and acceleration constraints can become significantly large.

### Grid reduction

Due to the irregular boundaries for the  $\lambda$ -ranges, several transitions are not possible. An example illustrating this impossibility is provided in figure 13.7 where particular  $\lambda$ -intervals are not connectable to neighbouring ones. In addition, when the required step  $\lambda_{t-1}(j) \rightarrow \lambda_t(k)$  demands a considerable difference of  $\lambda$ -magnitudes, the corresponding transition might not be realistic. The reason for this is that the required minimum time increment will almost certainly become very large. Consequently, an acceptance interval  $\Delta a$  must be defined. It can easily be shown that the biggest value a sensible  $\lambda_{t-1}(j) \rightarrow \lambda_t(k)$  transition can obtain is equal to the roving length increment  $\Delta L$ . The reasoning for this is rather simple; only in the case when the feed eye movement is exactly aligned with  $\Delta \mathbf{G}$ , the corresponding translation will be equal to  $\Delta L$ . Including a compensation for fluctuations in  $\Delta g(t)$ , a suitable definition for  $\Delta a$  is:

$$\Delta a = \Delta L + \Delta g_{\text{init}} \quad (14.11)$$

At the same time, the transition  $C[t-1, \lambda_{t-1}(j)] \rightarrow C[t, \lambda_t(k)]$  can violate the requirement for a monotonic rotational speed  $C'$  (or another movement that is required to be monotonic). Hence, the following acceptance criterion for neighbouring  $\lambda$ -values must be constructed:

$$f_t(j, k) = \begin{cases} 1 & \text{for } C[t, \lambda_t(k)] - C[t-1, \lambda_{t-1}(j)] < 0 \text{ \& } \text{abs}[\lambda_t(k) - \lambda_{t-1}(j)] \leq \Delta a \\ 0, & \text{otherwise} \end{cases} \quad (14.12)$$

Evaluation of this criterion for the complete number  $m$  of grid points belonging to the locus  $t-1$  will provide a row vector with  $m$  elements:  $\mathbf{r}_t(j)$ . Assuming that the  $\lambda$ -grid of the  $t$  locus consists of  $n$  points, the matrix containing all possible transitions can be constructed (equation (14.20)). This transition matrix is denoted by  $\mathbf{T}(t)$  and is generally a sparse matrix  $[\mu 10]$ . Especially in the case where the acceptance criterion  $f_t(j, k)$  is exclusively formulated by the interval magnitude-related rule (the second rule in (14.12)), the resulting non-zero elements will be located around the diagonal, where the bandwidth is controlled by  $\Delta a$ . In the case presented here however, the resulting matrix still remains a sparse band matrix, occasionally containing a non-zero element that is not located on the band. Hence, storage and manipulation of the resulting transfer matrices can be performed on a very

effective way in terms of processor capacity and required memory [μ10]. To demonstrate the construction of the transfer matrices and their role in the process of reducing the grid data, we provide here a simple example in figure 14.3.

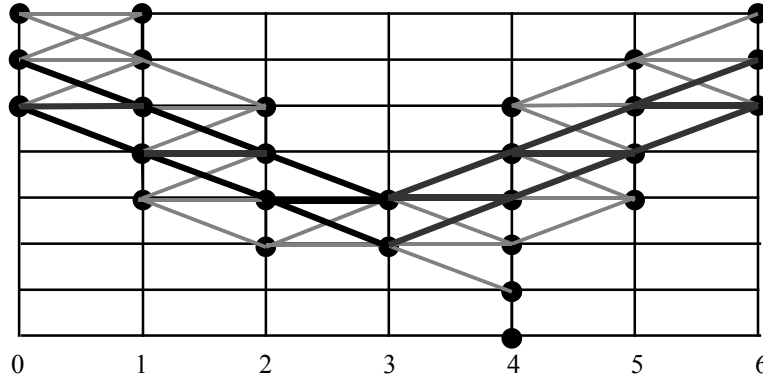


Fig. 14.3: A simple example of transitions through a grid

Every single stage  $t$  in the figure is associated with a collection of grid points  $\lambda_{gr}(t)$ , presented as a column vector. In addition, we depict the complete set of local transitions from stage  $t$  to the next one with grey lines. Depending on the local connection possibilities, several points are useless since they can not be used as an intermediate station for arriving at the final stage. For example, a path beginning at the upper point of stage 0, will not lead to anywhere. The meaningful transitions are depicted with thick black lines. Let us begin at stage 0; to reach the upper point of stage 1 we can either depart on the first or second point of stage 0 (which contains 3 points). The vector indicating the transition possibilities is  $\{1,1,0\}$ . For reaching the second point of stage 1 we obtain the vector  $\{1,1,1\}$  since all points of 0 are leading to this destination. For the third point of 1, the transition possibilities are given by  $\{0,1,1\}$  etc. Stacking of the obtained row vectors will lead to the formulation of the first transition matrix  $\mathbf{T}(1)$ . Repeating the same for the next stages leads to:

$$\begin{aligned}
 \mathbf{T}(1) &= \begin{bmatrix} 1 & 1 & 0 \\ 1 & 1 & 1 \\ 0 & 1 & 1 \\ 0 & 0 & 1 \\ 0 & 0 & 0 \end{bmatrix}, & \mathbf{T}(2) &= \begin{bmatrix} 0 & 1 & 1 & 1 & 0 \\ 0 & 0 & 1 & 1 & 1 \\ 0 & 0 & 0 & 1 & 1 \\ 0 & 0 & 0 & 0 & 1 \end{bmatrix}, & \mathbf{T}(3) &= \begin{bmatrix} 0 & 1 & 1 & 1 \\ 0 & 0 & 1 & 1 \end{bmatrix} \\
 \mathbf{T}(4) &= \begin{bmatrix} 0 & 0 \\ 1 & 0 \\ 1 & 1 \\ 1 & 1 \\ 0 & 1 \\ 0 & 0 \end{bmatrix}, & \mathbf{T}(5) &= \begin{bmatrix} 1 & 0 & 0 & 0 & 0 & 0 \\ 1 & 1 & 0 & 0 & 0 & 0 \\ 1 & 1 & 1 & 0 & 0 & 0 \\ 0 & 1 & 1 & 1 & 0 & 0 \end{bmatrix}, & \mathbf{T}(6) &= \begin{bmatrix} 1 & 0 & 0 & 0 \\ 1 & 1 & 0 & 0 \\ 1 & 1 & 1 & 0 \end{bmatrix}
 \end{aligned} \tag{14.13}$$

## Part C: Production process

Notice the band structure; this is the result of the limitation supporting the creation of figure 14.3: jumps bigger than the vertical distance between two adjacent nodes are not allowed. As usual in real life, the point we are standing now is a result of all decisions made in the past (forward propagation). Moreover, when being located at e.g. stage 1, we are here able to look in the future (backward propagation) and decide that in order to successfully reach the end it is probably better not to go to the upper point of stage 2. Conclusion: the decision whether a point is meaningful or not depends on the entire collection of transfer matrices for the complete set of previous and subsequent stages. We denote now that the first stage by  $b$  (begin) and the last one by  $e$  (end). Furthermore, as depicted in figures 14.2 and 14.3, it is assumed that the first and last stages contain the same number of grid points,  $N$ . Consequently, for the backward propagation we define:

$$\begin{aligned} \mathbf{B}(e) &= \mathbf{I}(N) \\ \mathbf{B}(t) &= \text{sgn}[\mathbf{B}(t+1) \cdot \mathbf{T}(t+1)], \quad b \leq t < e \end{aligned} \quad (14.14)$$

where  $\mathbf{I}(N)$  is a  $N \times N$  identity matrix and the “sgn” function replaces non-zero matrix elements with the number 1. On a similar way, the forward propagation is given by:

$$\begin{aligned} \mathbf{F}(b) &= \mathbf{I}(N) \\ \mathbf{F}(t) &= \text{sgn}[\mathbf{F}(t-1) \cdot \mathbf{T}^T(t)], \quad b < t \leq e \end{aligned} \quad (14.15)$$

We introduce now the symbol  $\otimes$  to denote the following non-additive element by element matrix multiplication (the symbols are just examples):

$$\mathbf{X} \otimes \mathbf{Y} = \mathbf{Z} \quad \text{where } z(i, j) = x(i, j)y(i, j) \quad (14.16)$$

The connectivity matrix  $\mathbf{C}(t)$  selecting the meaningful points that belong to a stage  $t$  can then be constructed according to:

$$\mathbf{C}(t) = \mathbf{F}(t) \otimes \mathbf{B}(t) = \mathbf{B}(t) \otimes \mathbf{F}(t), \quad b \leq t \leq e \quad (14.17)$$

The resulting connectivity matrix consists of a number of columns and a number of rows, equal to the dimension of  $\lambda_{\text{gr}}(t)$  and  $\lambda_{\text{gr}}(t-1)$ , respectively. Depending on the number of feasible connections, the matrix will contain several columns with exclusively zero elements, and some columns with at least one non-zero element. The connectivity matrix is now compressed to a row vector, where the columns containing only zeros are replaced by 0, and otherwise by 1. This compression procedure results in the so-called selector vector  $\mathbf{s}(t)$  that contains ones and zeros and extracts the meaningful points out of  $\lambda_{\text{gr}}(t)$  (recall that  $\lambda_{\text{gr}}(t)$  is a column vector). The result is a reduced grid vector  $\mathbf{g}_t$ :

$$\mathbf{g}_t = \lambda_{\text{gr}}(t) \otimes \mathbf{s}(t) \quad (14.18)$$

Returning to figure 14.3, we present here in table 14.1 the transposed transition matrices (the only reason for transposing them is the layout), the backward and forward propagation matrices, and the resulting connectivity matrices.

$t$	<b>T</b>	<b>B</b>	<b>F</b>	<b>C</b>
0	1 0 0 0 1 0 0 0 1	0 0 0 0 1 1 0 1 1	1 0 0 0 1 0 0 0 1	0 0 0 0 1 0 0 0 1
1	1 1 0 0 0 1 1 1 0 0 0 1 1 1 0	0 0 0 0 0 0 0 1 1 1 0 0 1 1 1	1 1 0 0 0 1 1 1 0 0 0 1 1 1 0	0 0 0 0 0 0 0 1 0 0 0 0 1 1 0
2	0 0 0 0 1 0 0 0 1 1 0 0 1 1 1 0 0 1 1 1	0 0 0 0 0 1 1 1 0 1 1 1	1 0 0 0 1 1 0 0 1 1 1 0	0 0 0 0 0 1 0 0 0 1 1 0
3	0 0 1 0 1 1 1 1	0 0 1 0 1 1	0 0 1 0 1 1	0 0 1 0 1 1
4	0 1 1 1 0 0 0 0 1 1 1 0	1 0 0 0 0 0 1 1 0 0 0 0 1 1 1 0 0 0	0 0 0 0 0 0 0 1 1 1 0 0 0 1 1 1 1 0	0 0 0 0 0 0 0 1 0 0 0 0 0 1 1 0 0 0
5	1 1 1 0 0 1 1 1 0 0 1 1 0 0 0 1 0 0 0 0 0 0 0 0	1 0 0 0 1 1 0 0 1 1 1 0	0 0 0 0 0 1 1 1 0 1 1 1	0 0 0 0 0 1 0 0 0 1 1 0
6	1 1 1 0 1 1 0 0 1 0 0 0	1 0 0 0 1 0 0 0 1	0 0 0 0 1 1 0 1 1	0 0 0 0 1 0 0 0 1

Table 14.1: The resulting transition, propagation and connectivity matrices for the nodes presented in figure 14.4

The associated selector vectors (equation (14.18)) are:

$$\begin{bmatrix} \mathbf{s}(0) \\ \mathbf{s}(1) \\ \mathbf{s}(2) \\ \mathbf{s}(3) \\ \mathbf{s}(4) \\ \mathbf{s}(5) \\ \mathbf{s}(6) \end{bmatrix} = \begin{bmatrix} \{0 \ 1 \ 1\} \\ \{0 \ 0 \ 1 \ 1 \ 0\} \\ \{0 \ 1 \ 1 \ 0\} \\ \{1 \ 1\} \\ \{0 \ 1 \ 1 \ 0 \ 0 \ 0\} \\ \{0 \ 1 \ 1 \ 0\} \\ \{0 \ 1 \ 1\} \end{bmatrix} \tag{14.19}$$

**Part C: Production process**

Notice that while the selector vectors identify the useful grid points, the connectivity matrices additionally contain information about the connection possibilities in the neighbourhood of the point under consideration. Depending on the application purpose, one can choose to either implement  $\mathbf{s}$  or  $\mathbf{C}$  in order to save memory or reduce the calculation time, respectively.

In reality, the intervals we are dealing with are divided into thousands of grid points while the transition matrices can achieve dimensions of the same order. Therefore, it is advisable to store the intermediate results into simple text files for instance.

Returning to figure 14.2 and the acceptance function presented in equation (14.12), the transition matrices are constructed as follows:

$$\mathbf{r}_t(k) \mapsto \underbrace{\begin{bmatrix} \cdot & \cdot & \cdot & \cdot \\ \cdot & f_t(j,k) & \cdot & \cdot \\ \cdot & \cdot & \cdot & \cdot \\ \cdot & \cdot & \cdot & \cdot \end{bmatrix}}_{\mathbf{T}(t)} \quad \left. \vphantom{\begin{bmatrix} \cdot & \cdot & \cdot & \cdot \\ \cdot & f_t(j,k) & \cdot & \cdot \\ \cdot & \cdot & \cdot & \cdot \\ \cdot & \cdot & \cdot & \cdot \end{bmatrix}} \right\} n = \dim[\lambda_{gr}(t)] \quad (14.20)$$

$m = \dim[\lambda_{gr}(t-1)]$

where the symbol “dim” denotes here the length of a vector. After application of the grid reduction procedure, the number of transitions is reduced into the collection of feasible ones, figure 14.4:

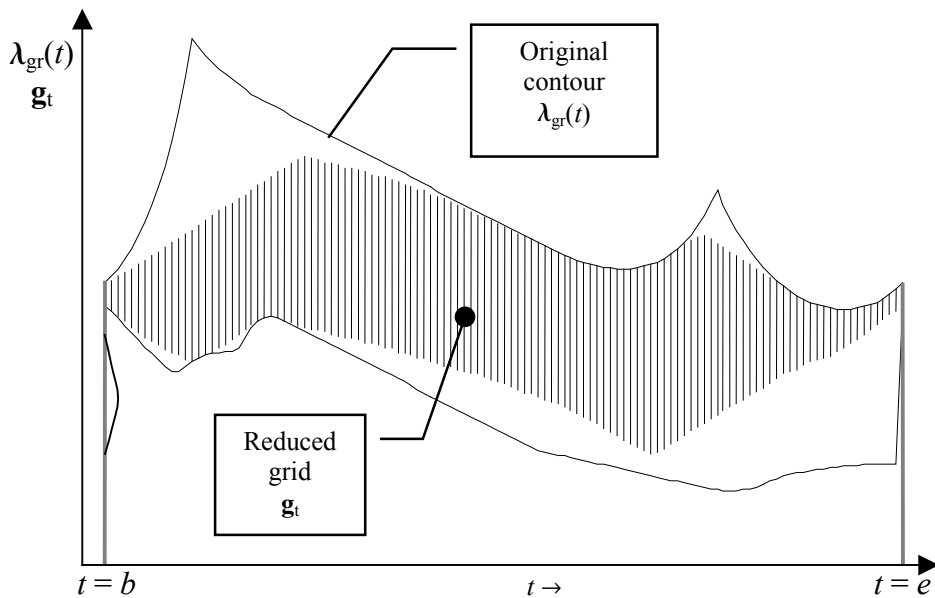


*Fig. 14.4: The initial collection of  $\lambda$ -ranges ( $\lambda_{gr}$ ) that is based on collision avoidance and the reduced grid  $\mathbf{g}$  after dropping the meaningless transitions*

Notice that the grid reduction procedure will automatically cancel the regions indicated with grey ellipses in figure 13.7. Therefore, it can be stated that the reduction method presented here is able to deal with a significantly broad range of grid collections, even if they contain holes or other discontinuities.

### 14.3 Application of dynamic programming

With the reduced grid vectors  $\mathbf{g}_t$  as a departure point, the main issue arising now is how to select for every stage  $t$  a point  $\mathbf{g}_t(k)$  belonging to  $\mathbf{g}_t$  on such a way that the total transition time gets minimised [ $\lambda_1, \lambda_2, \lambda_{12}$ ]. With the term total transition time we mean here the summation of the local time increments  $\Delta T_t$  for the total number of transitions  $t \rightarrow t+1$ .

The local transition time increment  $\Delta T_t$  as defined in equation (14.7) and used in (14.9), depends on three consequent grid points. As outlined in section 14.1, this is caused by involvement of accelerations that are calculated according to finite differences over three neighbouring points. This observation implies that we have to construct triple combinations over the points  $\{i, j, k\}$  that belong to three consequent stages, say  $\{t-2, t-1, t\}$ . To enhance transparency for the calculations while using double, some times even triple counter combinations, we represent here the stage indicator ( $t$ ) as a subscript. In addition, the parameter  $i$  is exclusively used in combination with  $t-2$ ,  $j$  with  $t-1$  and  $k$  with  $t$ . Accordingly, a particular time increment is given by:

$$\Delta T_t(i, j, k) = \Delta T[t, \mathbf{g}_{t-2}(i), \mathbf{g}_{t-1}(j), \mathbf{g}_t(k)] \quad (14.21)$$

#### Reduced transition matrices

In essence, the involved grid combinations require the realisation of two steps back in time. The already derived transition matrices  $\mathbf{T}(t)$  and selector vectors  $\mathbf{s}(t)$  are of great usefulness here. As a matter of fact, since  $\mathbf{T}$  and  $\mathbf{s}$  are used in their complete form (we do not extract particular elements out of them, therefore additional counters are not necessary), we denote for them the parameter  $t$  in its regular appearance, ( $t$ ). Before proceeding to the derivation of the grid combinations, the definition of the  $\otimes$  operation is here extended to cases where a one-to-one multiplication of single elements is not possible. In a fashion similar to the definition provided in equation (14.16), we introduce:

$$\mathbf{X} \circ \mathbf{y} = \mathbf{Z} \quad \text{where} \quad \mathbf{Z}(i) = \mathbf{X}(i) \otimes \mathbf{y} \quad (14.22)$$

where  $i$  denotes a particular row. The operation defined here can be viewed as an inner vector product without addition. The information for the proper grid combinations is actually already stored in the transition matrices  $\mathbf{T}$ . However, for the reduced grid, several rows and columns that are not reflecting on meaningful points anymore, have to be removed. This operation results, after dropping of the zero rows and columns, in the so-called reduced transition matrix  $\mathbf{R}(t)$ :

$$\mathbf{R}(t) = [\mathbf{T}(t) \circ \mathbf{s}(t-1)]^T \circ \mathbf{s}(t) \quad \left| \begin{array}{l} \\ \text{drop zero rows and columns} \end{array} \right. \quad (14.23)$$



## Part C: Production process

There is only one way to reach A with B as a departure point; hence,  $B \rightarrow A = 1$ . On a similar way,  $B \rightarrow a = 3$  and so on. Putting this in matrix form leads to:

$$\begin{array}{c}
 \begin{array}{cc}
 \text{B} & \text{b} \\
 \left[ \begin{array}{cc}
 1 & 0 \\
 3 & 1
 \end{array} \right] & \begin{array}{l} \text{A} \\ \text{a} \end{array}
 \end{array} \\
 \\
 \begin{array}{cc}
 \text{C} & \text{c} \\
 \left[ \begin{array}{cc}
 1 & 3 \\
 0 & 1
 \end{array} \right] & \begin{array}{l} \text{B} \\ \text{b} \end{array}
 \end{array}
 \end{array}
 \Rightarrow
 \begin{array}{c}
 \left[ \begin{array}{cc}
 1 & 0 \\
 3 & 1
 \end{array} \right]
 \cdot
 \left[ \begin{array}{cc}
 1 & 3 \\
 0 & 1
 \end{array} \right]
 =
 \begin{array}{c}
 \begin{array}{cc}
 \text{C} & \text{c} \\
 \left[ \begin{array}{cc}
 1 & 3 \\
 3 & 10
 \end{array} \right] & \begin{array}{l} \text{A} \\ \text{a} \end{array}
 \end{array}
 \end{array}
 \quad (14.27)$$

The total number of possible paths for arriving at the last stage is equal to the summation of the elements contained in  $\mathbf{N}$ , in this case, 17.

### Triple grid combinations

As discussed in section 14.1 and at the beginning of this section, the local transition time depends on a combination of three grid points belonging to three consequent stages (equations (14.9) and (14.20)). This introduces the need for jumping to an artificial grid vector containing the feasible combinations  $\{\mathbf{g}_{t-2}(i), \mathbf{g}_{t-1}(j)\}$  and  $\{\mathbf{g}_{t-1}(j), \mathbf{g}_t(k)\}$ . Next, by constructing the set of vectors that contain the complete set of feasible combinations  $\{\mathbf{g}_{t-2}(i), \mathbf{g}_{t-1}(j), \mathbf{g}_t(k)\}$  the collection of the corresponding time increments can be created. The basic idea is to properly link the combination vectors of subsequent steps to each other and add the corresponding time increments. After this evaluation, the only values that have to be stored are the shortest time paths for achieving a particular  $\{\mathbf{g}_{t-1}(j), \mathbf{g}_t(k)\}$  combination belonging to the last stage. By repeating this process throughout the complete set of stages (running from  $t = b$  to  $t = e$ ) the shortest time paths can easily be obtained. For the periodic  $\lambda$ -field assumed here (figures 14.2 and 14.4), the final combination vector  $\{\mathbf{g}_{e-1}(j), \mathbf{g}_e(k)\}$  is identical to  $\{\mathbf{g}_{e-1}(j), \mathbf{g}_b(k)\}$  because  $\mathbf{R}(b-1) = \mathbf{R}(e)$ .

Referring to figure 14.5, an additional step before stage 0 is here assumed; this additional stage is indicated by (-1) and is equal to stage 5. Hence  $\mathbf{R}(-1) = \mathbf{R}(6)$  which means that the process for the transition  $-1 \rightarrow 0$  is the same as  $5 \rightarrow 6$ , figure 14.6. For every stage we indicate here the upper grid point by the index 1. The corresponding reduced transition matrices provide the information needed to construct the  $\{\mathbf{g}_{t-1}(j), \mathbf{g}_t(k)\}$  vectors that we denote here by  $\mathbf{V}_t$ ; these vectors contain a number of rows that is equal to the number of double combinations.

The positions of non-zero elements in the  $\mathbf{R}$ -matrices immediately provide the combinations for  $\mathbf{V}_t$ ; for example, the  $\mathbf{R}(1)$  matrix contains non-zero elements in the positions  $\{\{1,1\}, \{2,1\}, \{2,2\}\}$ , and so on. The resulting  $\mathbf{V}$  matrices are given in figure 14.6.

It should additionally be noted that since the **R**-matrices will probably be stored as sparse matrices, the position of non-zero elements is immediately available [ $\mu 10$ ].

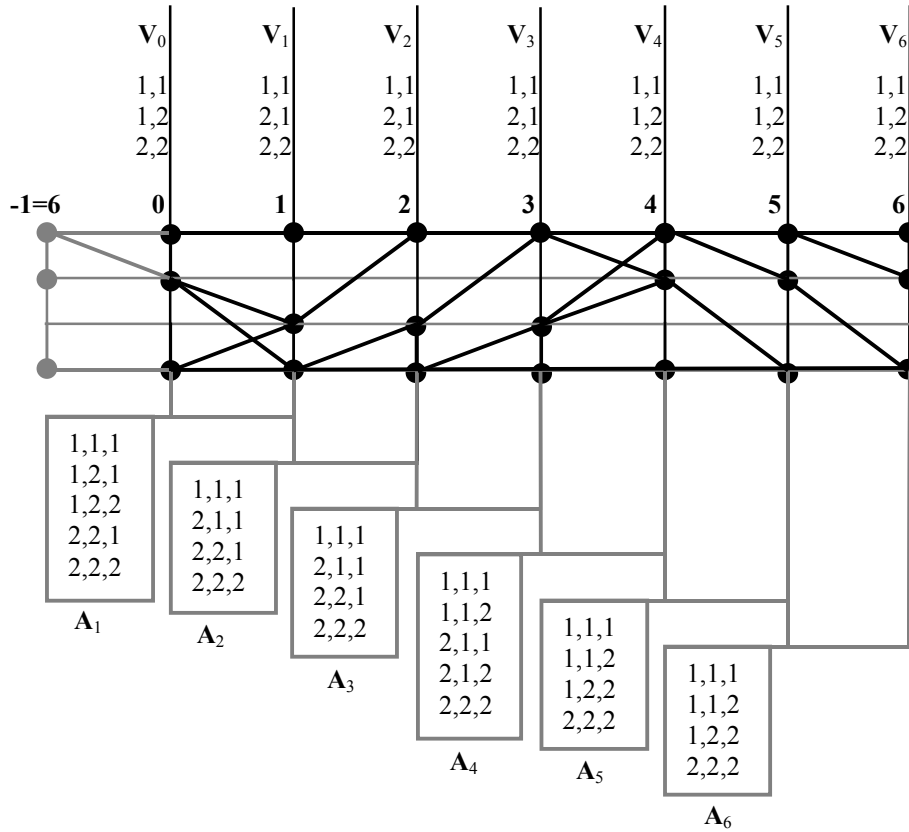


Fig. 14.6: Construction of the triple grid combination vectors  $\mathbf{A}_\#$  out of  $\mathbf{V}_\#$

With the  $\mathbf{V}$  vectors as a basis, the triple combination vectors  $\mathbf{A}$  can be constructed (figure 14.6). This combinatorial procedure can be described as follows: as an example, the first element of the first row in  $\mathbf{V}_1$  is 1. We select in  $\mathbf{V}_0$  the rows having 1 as the last element (in this case, the row that contains the number 11) and combine them with the first row of  $\mathbf{V}_1$  (which contains the number 11); the result is  $\{1,1\} \& \{1,1\} \rightarrow \{1,1,1\}$ . The second row of  $\mathbf{V}_1$  is  $\{2,1\} \Rightarrow$  connection number=2. The rows in  $\mathbf{V}_0$  ending on 2 are  $\{\{1,2\}, \{2,2\}\}$ . Hence:  $\{\{1,2\}, \{2,2\}\} \& \{2,1\} \rightarrow \{\{1,2,1\}, \{2,2,1\}\}$ . Similarly, the third row of  $\mathbf{V}_1$  results in  $(\{1,2,2\}, \{2,2,2\})$ . The obtained combinations lead to a vector  $\mathbf{A}_1$ , as depicted in figure 14.6. This combination procedure is very accessible for programming. This operation is denoted by:

$$\mathbf{A}_t = \mathbf{V}_{t-1}[\rightarrow 1] \& \mathbf{V}_t[1 \leftarrow] \quad (14.28)$$

where “&” stands for combining, “ $\rightarrow 1$ ” first element on the right side and “ $1 \leftarrow$ ” first element on the left side.

## Part C: Production process

### Best path construction

Every single row of  $\mathbf{A}_t$  contains the indices  $\{i, j, k\}$  referring to the  $i^{\text{th}}$  element of the  $\mathbf{g}_{t-2}$  vector, the  $j^{\text{th}}$  element of the  $\mathbf{g}_{t-1}$  vector, and the  $k^{\text{th}}$  element of the  $\mathbf{g}_t$  vector, respectively. With this information and equation (14.21) the corresponding time increments can be determined. The combination of these results with the corresponding  $\mathbf{A}_\#$  vectors leads to a new set of vectors  $\mathbf{U}_\#$  (equation (14.29)), where the hereby provided time increments are random and serve only the purpose of creating an example. These vectors contain two columns: the first one is referred to as indicator. The second column, denoted as  $\Delta\mathbf{T}_\#$ , contains the corresponding local time increments.

$$\begin{array}{c}
 \mathbf{U}_1 \\
 \left[ \begin{array}{l} \{1,1,1\}, 5 \\ \{1,2,1\}, 7 \\ \{1,2,2\}, 6 \\ \{2,2,1\}, 8 \\ \{2,2,2\}, 3 \end{array} \right] \\
 \mathbf{A}_1, \Delta\mathbf{T}
 \end{array}
 \quad
 \begin{array}{c}
 \mathbf{U}_2 \\
 \left[ \begin{array}{l} \{1,1,1\}, 7 \\ \{2,1,1\}, 6 \\ \{2,2,1\}, 3 \\ \{2,2,2\}, 8 \end{array} \right]
 \end{array}
 \quad
 \begin{array}{c}
 \mathbf{U}_3 \\
 \left[ \begin{array}{l} \{1,1,1\}, 5 \\ \{2,1,1\}, 7 \\ \{2,2,1\}, 8 \\ \{2,2,2\}, 2 \end{array} \right]
 \end{array}
 \quad
 \begin{array}{c}
 \mathbf{U}_4 \\
 \left[ \begin{array}{l} \{1,1,1\}, 3 \\ \{1,1,2\}, 8 \\ \{2,1,1\}, 6 \\ \{2,1,2\}, 5 \\ \{2,2,2\}, 5 \end{array} \right]
 \end{array}
 \quad
 \begin{array}{c}
 \mathbf{U}_5 \\
 \left[ \begin{array}{l} \{1,1,1\}, 3 \\ \{1,1,2\}, 2 \\ \{1,2,2\}, 2 \\ \{2,2,2\}, 9 \end{array} \right]
 \end{array}
 \quad
 \begin{array}{c}
 \mathbf{U}_6 \\
 \left[ \begin{array}{l} \{1,1,1\}, 9 \\ \{1,1,2\}, 1 \\ \{1,2,2\}, 8 \\ \{2,2,2\}, 5 \end{array} \right]
 \end{array}
 \tag{14.29}$$

On a way similar to the construction procedure for the  $\mathbf{A}$  matrices we connect  $\mathbf{U}_{t-1}$  and  $\mathbf{U}_t$  to each other and add the corresponding transition times. For example, the second row of the indicator of  $\mathbf{U}_2$  is  $\{2,1,1\}$ . The first two elements of this indicator row should match the two last elements of the rows contained in the indicator of  $\mathbf{U}_1$ ; these are the second  $\{1,2,1\}$  and 4<sup>th</sup> row  $\{2,2,1\}$ . Hence, we obtain:  $\{\{1,2,1\}, 7\} \& \{\{2,1,1\}, 6\} \rightarrow \{\{1,2,1,1\}, 7+6\} = \{\{1,2,1,1\}, 13\}$  (combination of  $\mathbf{U}_1(2) \& \mathbf{U}_2(2)$ ) and  $\{\{2,2,1\}, 8\} \& \{\{2,1,1\}, 6\} \rightarrow \{\{2,2,1,1\}, 14\}$  (combination of  $\mathbf{U}_1(4) \& \mathbf{U}_2(2)$ ). Repetition of this procedure for the remaining rows of  $\mathbf{U}_2$  leads to:

$$\mathbf{U}_1[\rightarrow 2] \& \mathbf{U}_2[2 \leftarrow] = \left[ \begin{array}{l} \{1,1,1,1\}, 12 \\ \{1,2,1,1\}, 13 \\ \{2,2,1,1\}, 14 \\ \{1,2,2,1\}, 9 \\ \{2,2,2,1\}, 6 \\ \{2,2,2,2\}, 11 \end{array} \right] \tag{14.30}$$

where, as introduced in equation (14.28), the indicated operation is matching the last two elements  $[\rightarrow 2]$  of every single indicator row of  $\mathbf{U}_1$  with the first two  $[2 \leftarrow]$  elements of every single indicator row that belongs to  $\mathbf{U}_2$ , and combine them into a new indicator vector. The second column contains the summations of the corresponding local time increments. With this operation, the complete set of possible combinations for reaching the double

combinations in  $V_2$  is determined. However, some elements of  $V_2$  appear in (14.30) more than once. It is evident to chose here for the most profitable combinations, providing minimal transition time values:

$$\mathbf{E}_2 = \min[(\mathbf{U}_1[\rightarrow 2] \& \mathbf{U}_2[2 \leftarrow]) \& \mathbf{V}_2] = \begin{bmatrix} \{1,1,1,1\}, & 12 \\ \{2,2,2,1\}, & 6 \\ \{2,2,2,2\}, & 11 \end{bmatrix} \quad (14.31)$$

The obtained matrix  $\mathbf{E}_2$  suggests the most economical way to reach  $V_2$  and is the only result that has to be stored, as least, temporary  $[\lambda 2]$ . The combinations for the next step are given by:

$$\mathbf{E}_2[\rightarrow 2] \& \mathbf{U}_3[2 \leftarrow] = \begin{bmatrix} \{1,1,1,1,1\}, & 12+5 \\ \{2,2,2,1,1\}, & 6+7 \\ \{2,2,2,2,1\}, & 11+8 \\ \{2,2,2,2,2\}, & 11+2 \end{bmatrix} \Rightarrow \mathbf{E}_3 = \begin{bmatrix} \{2,2,2,1,1\}, & 13 \\ \{2,2,2,2,1\}, & 19 \\ \{2,2,2,2,2\}, & 13 \end{bmatrix} \quad (14.32)$$

Once  $\mathbf{E}_3$  is known, the matrix  $\mathbf{E}_2$  is not needed anymore, therefore it can be deleted. Repetition of the same procedure for the next points will finally result in the best path identification for achieving every single combination that is contained in the last  $\mathbf{V}$  vector:

$$\mathbf{E}_t = \begin{cases} \mathbf{U}_{b+1} & t = b+1 \\ \min[(\mathbf{E}_{t-1}[\rightarrow 2] \& \mathbf{U}_t[2 \leftarrow]) \& \mathbf{V}_t] & b+1 < t \leq e \end{cases} \quad (14.33)$$

Notice that it makes no sense to define  $\mathbf{E}_b$ . The final result will consist of  $(e-b)-1$  indicator columns and 1 time increment column, hence,  $e-b$  columns. The number of rows is equal to the number of rows contained in  $\mathbf{V}_e$ .

## 14.4 Results & discussion

### Constraints

The results presented here are based on the mandrel that is defined in section 11.4, figure 11.4, being attached on a lathe winder (figure 14.1). Some frames of the simulations performed here are given in appendix B. The moving space for the feed eye is determined in chapter 13 and depicted in figure 13.6. Demanding a winding process with constant pay out ratio, the constraints for this particular case are given below:

Lathe winder	#' min [#s]	#' max [#s]	#'' min [#s <sup>2</sup> ]	#'' max [#s <sup>2</sup> ]
$S$ [m]	0.28	0.32	-0.15	0.15
$C$ [rad]	$-10\pi/6$	-0.05	$-4\pi$	$4\pi$
$A$ [rad]	$-20\pi/6$	$20\pi/6$	$-20\pi$	$20\pi$
$X$ [m]	-0.5	0.5	-3.5	3.5
$Y$ [m]	-1	1	-5	5

Table 14.2: Dynamic constraints for the lathe winder, as assumed in this example

The resulting grid after dropping the meaningless transitions is depicted in figure 14.4 and repeated in figure 14.7 including the optimal  $\lambda$ -trajectory.

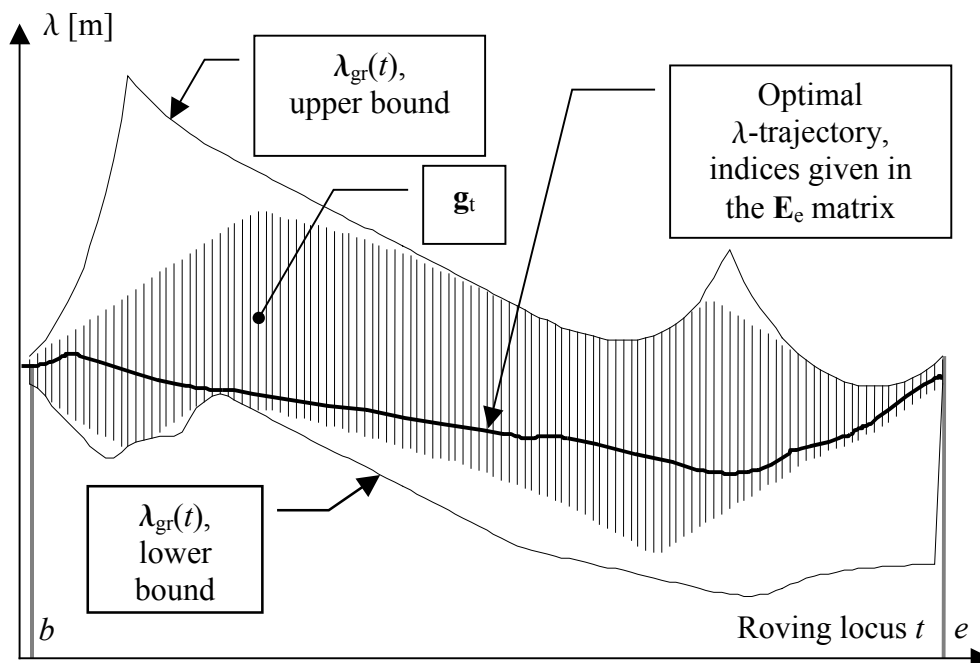


Fig. 14.7: The initial  $\lambda$ -gridlines  $\lambda_{gr}(t)$ , the reduced grid collection  $g_t$  and the optimal  $\lambda$ -trajectory

Calculation flow diagram

With the given values for  $\Delta L$ ,  $\Delta g_{init}$  and the grid vectors  $\lambda(t)$ , we first determine the grid increments  $\Delta g(t)$  and the acceptance tolerance  $\Delta a$ . With the increments known, we construct the discretised grid. The tolerance interval is used for the definition of the selection function  $f_i(j,k)$  that identifies the feasible transitions. An additional demand in the selection function is that the transition from one grid point to the other must guarantee a monotonic  $C$  propagation. With the obtained  $\mathbf{T}$  matrices, the reduced grid can finally be constructed.

Other derivatives of the  $\mathbf{T}$  matrices are the  $\mathbf{V}$  matrices which, in combination with the time increments  $\Delta T$  that reflect on a consequence of three connectable grid points, result in the  $\mathbf{U}$  matrices. These matrices contain all possible paths to reach a particular triple combination of grid points. By selecting the most economical among them, the matrix containing the optimal path indicators can finally be obtained.

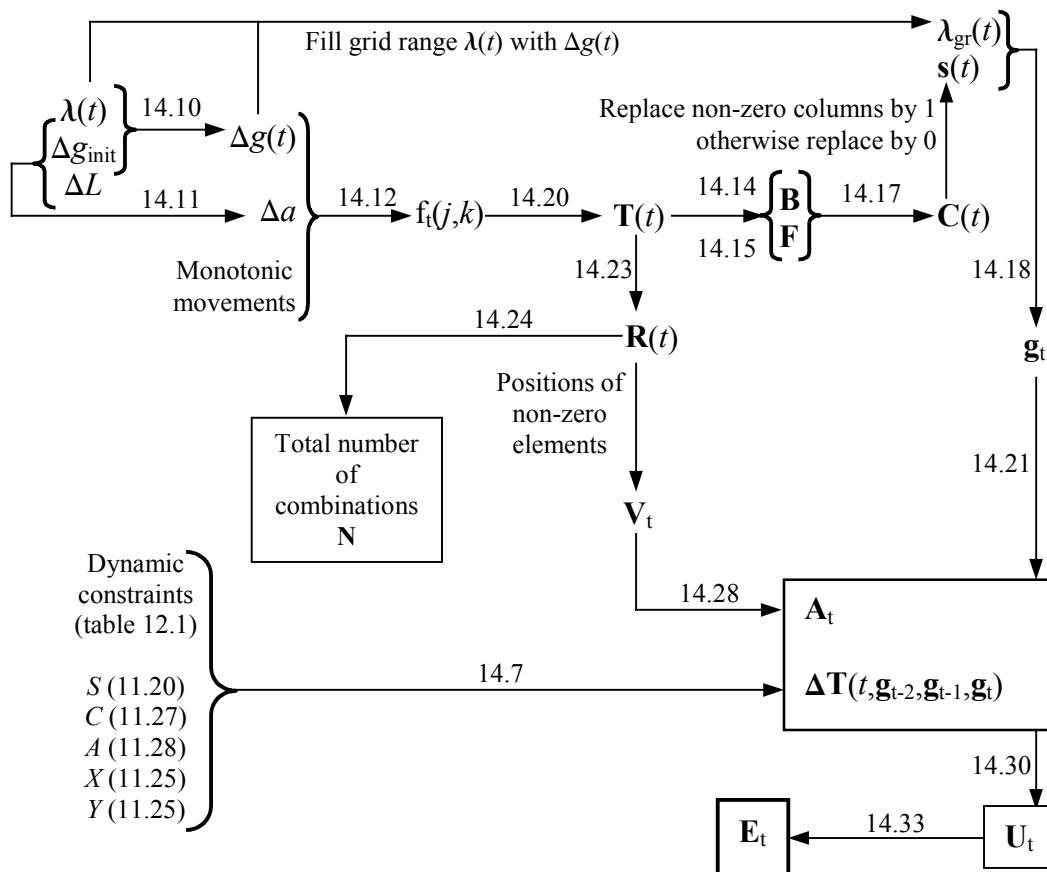


Fig. 14.8: Calculation flow diagram for the grid reduction and the determination of the optimal trajectory matrices  $\mathbf{E}_t$

## Part C: Production process

### Resulting machine movements

In the next figures we provide the feed eye trace  $\{X, Y\}$ ,  $C'$ ,  $S'$ , and the accelerations of the spindle ( $C''$ ) and the consumed roving ( $S''$ ) as functions of time.

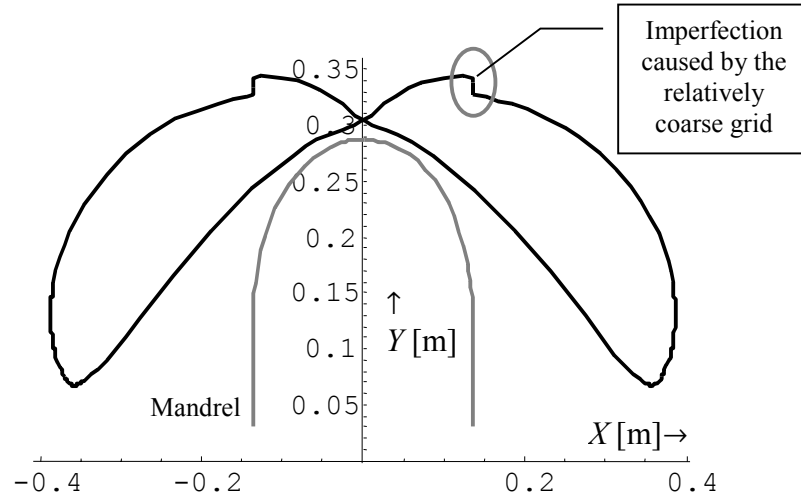


Fig. 14.9: Top view of the feed eye movement, including the mandrel profile

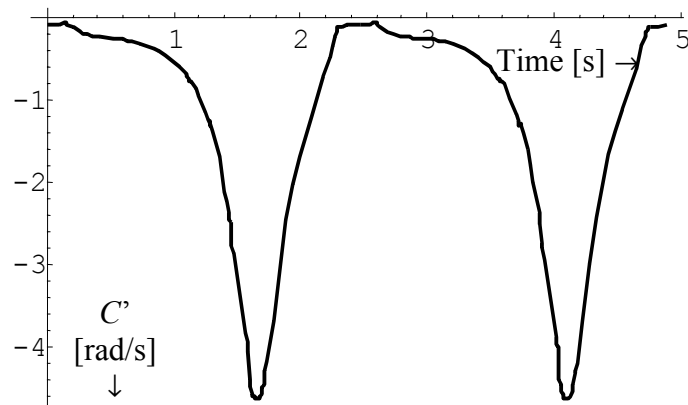


Fig. 14.10: The resulting rotational speed of the spindle for constant  $S'$

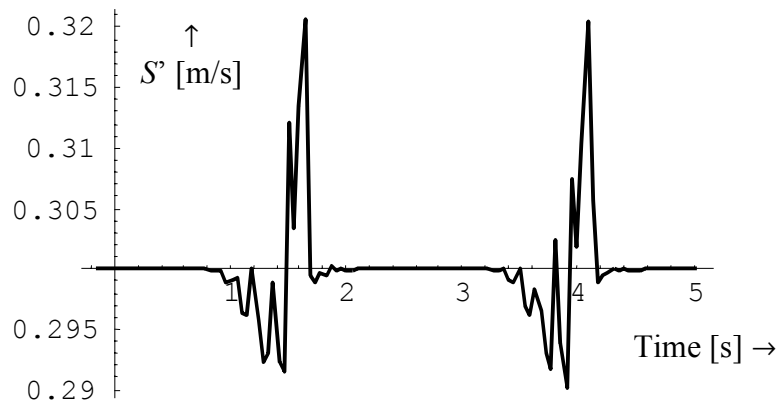


Fig. 14.11: The resulting consumed fibre speed  $S'$  (required to approximately remain constant)

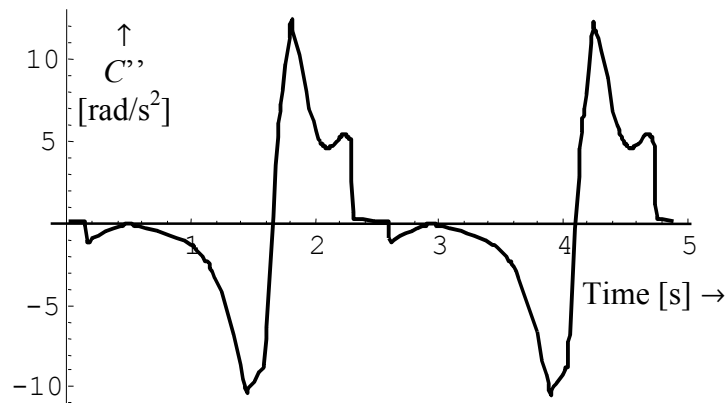


Fig. 14.12: The resulting rotational acceleration of the spindle

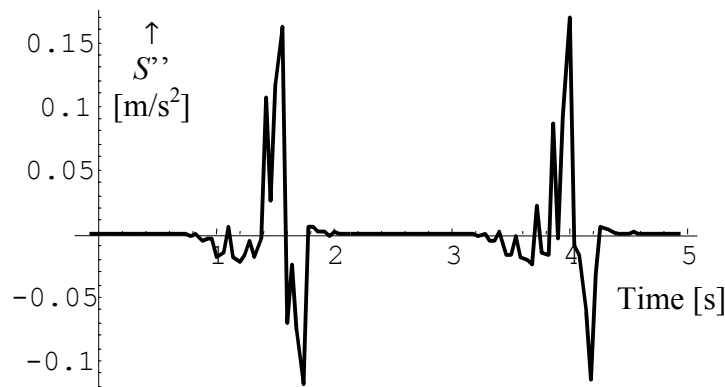


Fig. 14.13: Consumed roving accelerations

The most important constraint, a constant consumed fibre speed is here respected (figure 14.11). Notice however the presence of some instability for the obtained  $S''$  values (figure 14.13). The rotational velocity of the spindle is obviously not constant (14.10) and, at some points, the accelerations needed are quite large (figure 14.12). The reason for this is that when the applied roving is passing the polar area of the mandrel, the associated speed can theoretically drop to zero. Nevertheless, the production time reduction obtained here is 40% when compared to winding with a constant  $\lambda$ -value that is equal to 41 [mm] (as depicted in figure 13.7 with the dashed grey line).

### Mesh refinement vs. calculation time and obtained results

The basic  $\lambda$ -period for defining the grid for a complete wound circuit contains 120 stages; the initial grid increment is 1 [mm]; the biggest  $\lambda$ -vector contains 574 points. The average number of points contained in the  $\mathbf{g}_t$  vectors is approximately 300. The acceptance interval  $\Delta a$  is set equal to 6 [mm], therefore, the average length of  $\mathbf{U}_t$  is  $6^3 \times 300 = 64.8 \times 10^3$ . This means that the determination of the optimal grid requires  $8 \times 10^6$  time increment evaluations.

## Part C: Production process

Although this number is not exceptionally large, the determination of the optimal grid is generally time-consuming. This is the reason for limiting the calculations to a rather coarse grid. Nevertheless, when compared to winding with a constant  $\lambda$ -value (in this case equal to 41 [mm]), the production time drops with 40%. It is expected that a finer grid will result to a larger reduction due to smoother machine movements. However, in the example presented here, the most prominent factor inhibiting the production time to drop is the feed eye roller inclination  $A$ ; when passing the polar areas, the roller has to rapidly jump from the  $-\pi/2$  orientation to  $\pi/2$  and vice versa (see also appendix B). This sudden angle modification is forcing the winding machine to substantially decelerate.

Due to the selected  $\Delta g_{init}$ -value of 1 [mm], at a particular region of the feed eye movement, the best solution obtained here corresponds with a constant  $X$  position while the  $Y$  movement is still active (figure 14.9, region within the grey ellipse). This movement combination reflects on roving placement on the flat polar areas of the mandrel, as depicted in figure 14.1. For the corresponding range of  $t$ -values, the roving path on the mandrel is exactly parallel to the  $Y$ -axis and the collision limits are generously respected, hence, there is no reason for the observed  $Y$ -movement. The cause of this inconvenient movement is that within the grid provided here, the optimiser is choosing for the least unsatisfying solution. In other words, the obtained movements can not be smoother than the grid forces them to go through. Consequently, the grid should actually be chosen with a smaller  $\Delta g_{init}$ -value. On the other hand, with a very small  $\Delta g_{init}$  and an unchanged acceptance tolerance  $\Delta a$ , the required number of combinations will rapidly obtain astronomical values. For example, with  $\Delta g_{init} = 0.1$  [mm] and  $\Delta a = 6$  [mm], the required number of evaluations becomes  $60^3 \times 300 \times 120 = 8 \times 10^9$ .

Suppose that a single circuit has a length  $L_c$  and is divided according to a  $\Delta L$  increment while the average  $\lambda$ -value (defining the range where the feed eye is allowed to move in) is given. The required number of time increment evaluations is then given by:

$$\left( \frac{\Delta a}{\Delta g_{init}} \right)^3 \left( \frac{\lambda_{average}}{\Delta g_{init}} \right) \left( \frac{L_c}{\Delta L} \right) \quad (14.34)$$

From this result it becomes evident that the number of grid points fitting in the tolerance interval ( $\Delta a$ ) should be limited. Just to provide an idea, when a positioning accuracy of 0.1 [mm] is desired for the feed eye translations, one can assume:  $\Delta g_{init} = 0.1$  [mm],  $\Delta a = 0.3$  [mm],  $\Delta L = 0.2$  [mm]. The required number of evaluations becomes equal to  $1350 \times (\lambda_{average} [\text{mm}] \times L_c [\text{mm}])$ . It should be noted here that the idea of initially calculating with a coarse grid followed by a refinement will generally not lead us to improved solutions due to the considerable grid sensitivity of the optimiser. An initial study with  $\Delta g_{init} = 3$  [mm], has resulted in a substantially different optimal  $\lambda$ -curve when compared with the results given in figure 14.7.

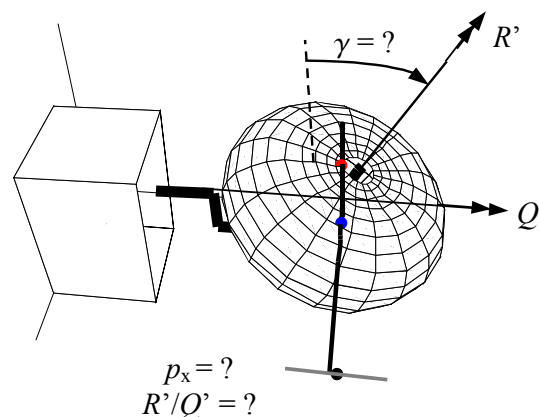
## 15

## Pressure vessels revisited (2)

*Our second visit to the class containing the general  $qrs$  pressure vessel is now focussed on the associated production process (in chapter 9 we judged the optimality of an isotensoidal vessel in terms of patterns and fibre stacking)*

*With a particular vessel given, one has to select the best winding machine configuration and, at the same time, determine the most suitable process parameters. For example, when deciding for the tumble winder, the optimal cross carriage position has to be determined and the angle between the main rotations has to be set. On the other hand, for a lathe winder, the optimal cross carriage motion is of significant importance (chapters 11 and 14).*

*Although it is not possible to formulate conclusions with general applicability, the observation of some trends and the derivation of simple approximating rules as a function of the initial shape parameters, is probably justified. In the first section, we outline the assumptions made here, and we provide some definitions for the relevant geometric shape coefficients. In addition, the similarity between spheroids and isotensoids is here demonstrated. Next, in order to predict the feed eye translation amplitude and its behaviour in time, some simple criteria are derived; these are verified in section 15.2. In the last section we highlight and demonstrate the influences of the  $q$ ,  $r$  and  $s$  parameters on the windability of the resulting vessel. In addition, this section contains some proposals related to novel machine configurations for the production of both donut-shaped and cylindrical vessels, including the creation of transitional circuits and the simultaneous placement of hoop and polar windings.*



**Winding of a donut-shaped vessel on a tumble winder: with a proper choice of the indicated parameters, a significant production time reduction can be realised. Is this also the best configuration for a cylindrical vessel?**

## **Part C: Production process**

## 15.1 Winding of quasi-ellipsoidal shapes

### Assumptions and definitions

This choice for a particular winding machine configuration depends mainly on the physiology of the roving path that has to be created. Assuming geodesic winding, the geometry of the resulting towpaths is entirely defined by the meridian profile generating the supporting shell under consideration.

More specific, when considering composite pressure vessels, the resulting meridian profile is strongly elliptical, hence suitable for approximation by an ellipse. For a vessel designed according to the netting theory, the aspect ratio of such an ellipse approaches the value 0.6 with an increasing shape parameter ( $q$ ), figure 15.1:

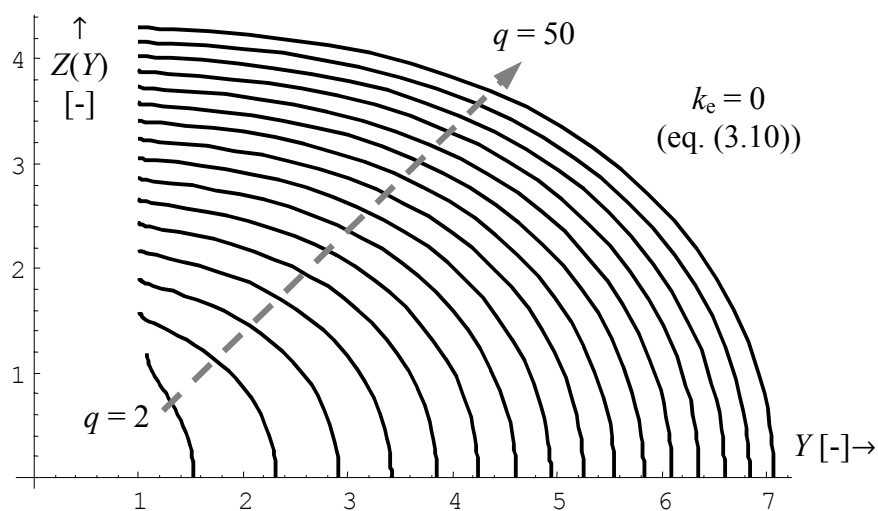


Fig. 15.1: Various optimal meridian profiles for increasing  $q$  by  $k_e = 0$  (netting theory)

Throughout this dissertation, we adapted the netting theory that is ignoring the matrix properties of the involved laminate. When these properties are taken into consideration, the parameter  $k_e$  will remain below 1 since the stiffness in the transverse direction of the fibre bundle (including matrix) will always remain lower than the stiffness in longitudinal direction. Therefore, according to equation (3.10), we obtain  $k_e < 1$ . However, Vasiliev et al. [ζ34,ζ35] introduced the idea of winding with in-situ fabricated orthotropic tapes providing a greater range for the  $k_e$  values. When the latter is bigger than 1, the resulting shape becomes very similar to a prolate spheroid. For  $k_e = 1$  we obtain almost a sphere and for  $k_e < 1$  the result will be comparable to an oblate spheroid. In addition, the resulting shape depends mainly on the stress ratio as formulated in equation (3.9) and derived in chapters 3 and 4.

Returning to the production process, the idea is now to approximate this range of pressure vessels by a generic ellipsoidal shell of revolution that will serve the aim of deriving the most suitable machine configuration.

## Part C: Production process

As described in chapter 10 and elaborated in chapter 11, we adapt here the generic winding machine configuration. In addition, it is temporarily assumed that the feed eye can only perform a one-dimensional movement in the  $\mathbf{j}_0$  direction, and that the angle  $\gamma$  can freely be adjusted before carrying out the manufacturing process, but has to remain unchanged during running of the machine. Furthermore,  $p_x = \text{constant}$  and  $p_z = 0$ . The elaborated machine configuration is depicted again in the figure below:

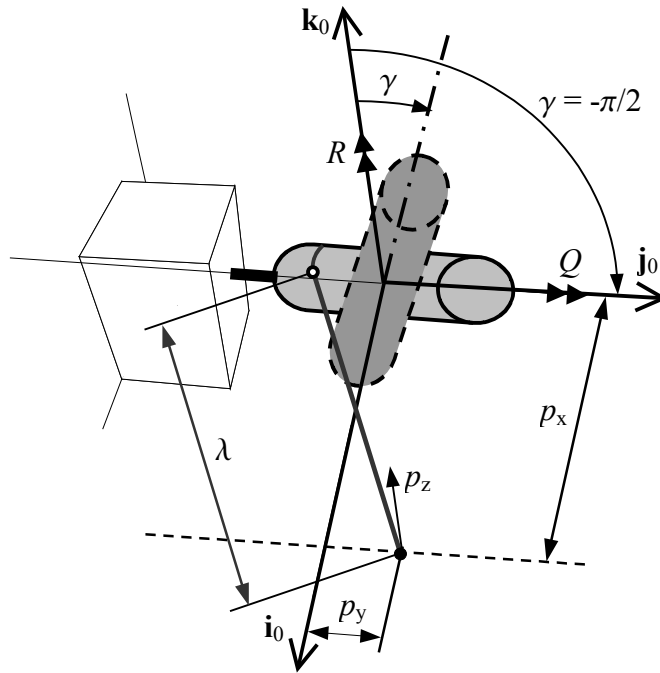


Fig. 15.2: Winding machine configuration with a one-dimensional feed eye movement and an  $[-\pi/2, 0]$  adjustment space for  $\gamma$

As presented in equations (10.4) and (10.6), the winding equations are:

$$\begin{bmatrix} cQcR + sQs\gamma sR & -cQsR + sQs\gamma cRsQc\gamma \\ c\gamma sR & c\gamma cR & -s\gamma \\ -sQcR + cQs\gamma sR & sQsR + cQs\gamma cR & cQc\gamma \end{bmatrix} \begin{Bmatrix} S_x \\ S_y \\ S_z \end{Bmatrix} = \begin{Bmatrix} p_x \\ p_y \\ p_z \end{Bmatrix} \quad (15.1)$$

with:

$$\begin{Bmatrix} S_x \\ S_y \\ S_z \end{Bmatrix} = \begin{Bmatrix} G_x \\ G_y \\ G_z \end{Bmatrix} + \lambda \begin{Bmatrix} \Delta G_x \\ \Delta G_y \\ \Delta G_z \end{Bmatrix} \quad (15.2)$$

where  $\lambda$  stands for the length of the free hanging fibre (figure 15.2). The value for this parameter is given by equation (11.18):

$$\lambda = -h + \sqrt{(p_x^2 + p_y^2 + p_z^2) - \|\mathbf{G}\|^2 + h^2} \quad (15.3)$$

where  $h$  is a function related to the angle (in three-dimensional space) enclosed by the position vector  $\mathbf{G}$  and the orientation vector  $\Delta\mathbf{G}$  (equation (11.17)).

The most important assumption is that the main rotations  $Q$  and  $R$  are coupled to each other with a constant gearing ratio (for reasons of mass inertia and facilitated machine control), as expressed in equation (11.37). The challenge is now to maximally reduce the feed eye amplitude by a proper selection of  $\gamma$  while  $p_x = \text{constant}$ ,  $p_z = 0$  and  $R$  is constantly coupled to  $Q$ . From the second row of equation (15.1) and  $\gamma \neq 0$ , we obtain:

$$S_y \cos(R) + S_x \sqrt{1 - \cos^2 R} - S_z \tan \gamma = p_y \quad (15.4)$$

Setting the feed eye amplitude equal to zero and solving for  $R$  leads to (equation (11.35)):

$$\cos R_{ideal} = \frac{S_y S_z \tan \gamma \pm S_x \sqrt{S_x^2 + S_y^2 - S_z^2 \tan^2 \gamma}}{S_x^2 + S_y^2} \quad (15.5)$$

Similarly, we obtain for  $\gamma$ :

$$\gamma_{ideal} = \arctan\left(\frac{S_y \cos R + S_x \sin R}{S_z}\right) \quad (15.6)$$

The meridian shape of the vessel dominates the development of  $Q$  as a function of the applied roving locus. Since the secondary rotation  $R$  is coupled to  $Q$ , satisfaction of (15.4) will hardly be possible (chapter 11); the absolute value of the right side in equation (15.5) must always be smaller than 1. At the same time, a particular setting of  $\gamma$  can not guarantee zero amplitude for the feed eye during the entire winding process. Hence, a compromise has to be found that leads to acceptable feed eye amplitudes and favourable dynamic behaviour. The latter reflects on the creation of a smooth feed eye motion. To globally describe the influences of the meridian shape and the roving path on the feed eye amplitude we introduce here several dimensionless quantities [18].

Let a shell be defined in a polar coordinate system  $\{\rho \cos \phi, \rho \sin \phi, z\}$  (figure 15.3). With  $\rho_g$  and  $z_g$  as the meridian coordinates at the upper pole (figure 10.5) and  $\rho_{eq}$  as the equatorial radius, we define [18]:

## Part C: Production process

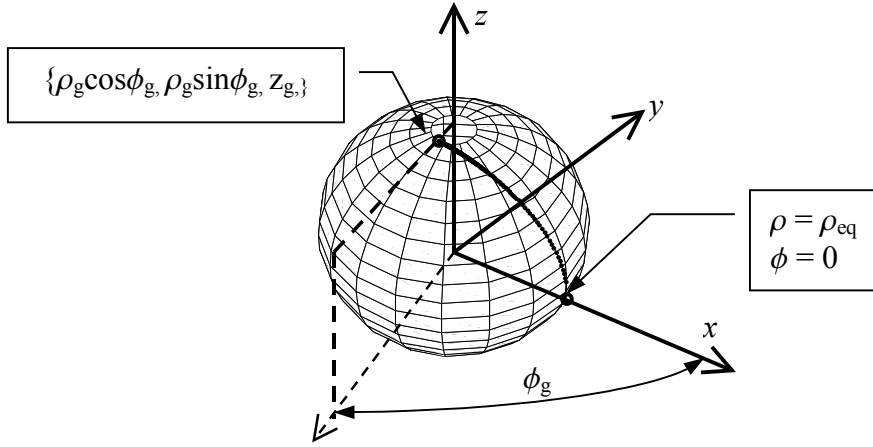


Fig. 15.3: Geodesic roving path on a shell of revolution that is defined in polar coordinates

$$\begin{aligned}
 k &= \frac{p_x}{\rho_{eq}}, \quad k > \max[1, \mu] \\
 \zeta &= \frac{\rho_g}{\rho_{eq}}, \quad 0 < \zeta < 1 \\
 \mu &= \frac{z_g}{\rho_{eq}}, \quad \mu > 0
 \end{aligned} \tag{15.7}$$

where  $\rho_{eq}$  denotes the equatorial radius. The value of the parallel angle  $\phi$  at the upper polar opening is denoted by  $\phi_g$  (negative value). The winding angle  $\alpha$  is defined as positive, hence  $\phi$  is proceeding from  $\phi_g$  to 0 at the equator (figure 15.3). Furthermore, the winding angle is equal to  $\pi/2$  and  $\arcsin(\zeta)$  at respectively the pole and equator.

### Feed eye amplitude prediction

To estimate the feed eye amplitude, we examine here two conditions for the angle  $\gamma$ : zero amplitude at the pole and zero amplitude at the equator, respectively. For the pole condition we obtain:

$$\left. \begin{aligned}
 \rho &= \rho_g \\
 z &= z_g \\
 h &= 0 \\
 \alpha &= \pi/2 \\
 \beta &= -\pi/2 \\
 \phi &= \phi_g
 \end{aligned} \right\} \Rightarrow \begin{Bmatrix} S_x \\ S_y \\ S_z \end{Bmatrix} = \begin{Bmatrix} \zeta \cos \phi_g - \sqrt{k^2 - \zeta^2 - \mu^2} \sin \phi_g \\ \zeta \sin \phi_g + \sqrt{k^2 - \zeta^2 - \mu^2} \cos \phi_g \\ \mu \end{Bmatrix} \tag{15.8}$$

Substituting equation (15.8) in equation (15.6) leads to:

$$\gamma_{ideal}^{pole} = \arctan\left(\frac{\sqrt{\kappa^2 - \zeta^2 - \mu^2} \cos(R + \phi_g) + \zeta \sin(R + \phi_g)}{\mu}\right) \quad (15.9)$$

The only acceptable solution combination becomes (see also section 11.3 where the initial  $R$ -value is derived, right after equation (11.39)):

$$\gamma_{ideal}^{pole} = -\arctan\left(\frac{\zeta}{\mu}\right) \quad \text{for} \quad R = -\frac{\pi}{2} - \phi_g \quad (15.10)$$

Note that the obtained  $\gamma$ -solution is equal to  $\arctan(\rho_g/z_g)$ , figure 15.3. The components of  $\mathbf{S}$  (equation (11.33)) at the equator are given by:

$$\left. \begin{array}{l} \rho = \rho_{eq} \\ z = 0 \\ h = 0 \\ \alpha = \arcsin(\zeta) \\ \beta = -\pi \\ \phi = 0 \end{array} \right\} \Rightarrow \left\{ \begin{array}{l} S_x \\ S_y \\ S_z \end{array} \right\} = \left\{ \begin{array}{l} 1 \\ \zeta \sqrt{k^2 - 1} \\ -\sqrt{1 - \zeta^2} \sqrt{k^2 - 1} \end{array} \right\} \quad (15.11)$$

Substitution of equation (15.11) in equation (15.6) leads to:

$$\gamma_{ideal}^{equator} = -\arctan\left(\frac{\zeta \cos R + \frac{\sin R}{\sqrt{\kappa^2 - 1}}}{\sqrt{1 - \zeta^2}}\right) \quad (15.12)$$

With the initial value given in (15.10), the  $R$ -angle corresponding to the equator locus gets equal to zero (equations (11.37) and (11.43)); hence, the only acceptable solution becomes:

$$\gamma_{ideal}^{equator} = -\arctan\left(\frac{\zeta}{\sqrt{1 - \zeta^2}}\right) = -\arcsin(\zeta) \quad \text{for} \quad R = 0 \quad (15.13)$$

The obtained  $\gamma$ -angle is equal to the opposite-signed winding angle at the equator. Substitution of the latter in equation (15.5) confirms the derived  $R$ -value (= 0) that corresponds with the equator of the shell.

To facilitate understanding of the prediction method for the expected amplitudes, we provide here an example in the form of a quasi-ellipsoidal pressure vessel with:  $\kappa = 2$ ,  $\zeta = 0.1588$ ,  $\mu = 0.463$  and  $\phi_g = -1.4709$  [rad].

### Part C: Production process

In figure 15.4, the grey inclined line represents the solution for  $\gamma$ , satisfying the condition of zero delivery eye translation when passing the equator of the wound shell (equation (15.12)). The black inclined line represents  $\gamma$ -values providing zero feed eye translation for the pole of the shell (equation (15.9))

The horizontal dashed line satisfies simultaneously the conditions:  $R$  propagation  $\equiv (R_{\text{equator}} - R_{\text{pole}})$  and zero delivery eye translation at both the pole and the equator. The intersection of that line with the  $\gamma$ -axis represents the corresponding  $\gamma$  inclination angle, while the intersection of the vertical dashed line with the  $R$ -axis determines the initial value for the secondary rotation  $R$ . Consequently, the obtained  $\gamma$ - and  $R$ -values provide the optimal solution due to feed eye zero translation at both the equator and pole passage, while the  $R$ -propagation is still equal to the winding pattern-determined one (equations (11.37) and (11.43)).

It should be noted that except for a sphere, the pole and equator conditions do not coincide. However, the slopes of respectively the continuous grey line and dashed black line provide a convenient tool for the a-priori judgement of the feasibility to wind a particular shape (best case: line slopes = 0). Additionally, with the vertical distance between the “ $\gamma$  equator condition” and the “ $\gamma$  pole condition” the feed eye amplitude can be estimated (best case:  $\zeta/\mu = 1$ ).

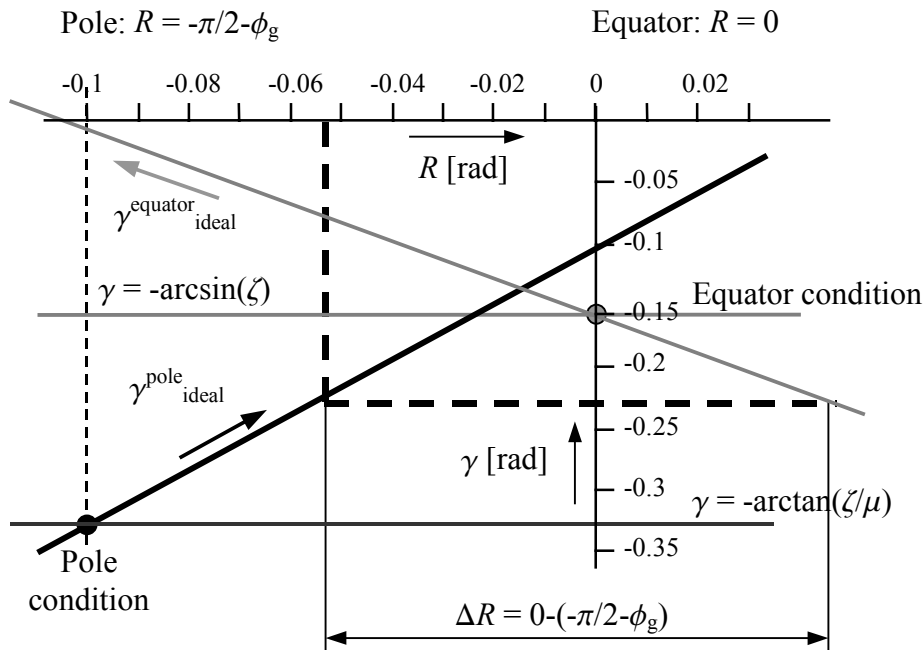


Fig. 15.4: Comparison of the pole and equator conditions that provide zero feed eye amplitudes

Satisfaction of the pole condition corresponds with the  $\gamma$ - and  $R$ -value given in equation (15.10). When passing the equator (virtually returning backwards to the begin point), the  $R$ -value becomes equal to zero (equation (15.13)). Plugging these conditions in equation (15.4) leads, after substitution of equation (15.11), to:

$$p_{y \text{ for } \gamma = -\arctan(\zeta / \mu) \text{ and } R=0}^{\text{equator}} = \frac{\zeta \sqrt{\kappa^2 - 1} (\mu - \sqrt{1 - \zeta^2})}{\mu \sqrt{1 + \frac{\zeta^2}{\mu^2}}} \quad (15.14)$$

When passing the pole, the  $R$  value becomes equal to  $-\pi/2 - \phi_g$ . Substituting this condition, together with equation (15.8) in (15.4) gives:

$$p_{y \text{ for } \gamma = -\arcsin(\zeta), \text{ and } R = -\pi/2 - \phi_g}^{\text{pole}} = \zeta (\mu - \sqrt{1 - \zeta^2}) \quad (15.15)$$

It should be noted that equations (15.14) and (15.15) provide only an initial indication reflecting on the pole and equator passages. There is no guaranty that other roving placement positions between pole and equator will provide smaller feed eye translations. Furthermore, another important restriction is associated with the fact that the  $R$ -propagation between pole and equator is equal to  $0 - (-\pi/2 - \phi_g)$ . Since  $R$  is constantly coupled to  $Q$ , the difference between  $Q_{\text{equator}}$  and  $Q_{\text{pole}}$  is here exactly equal to  $\pi/2$ ; this is generally not valid, except for shapes having  $\mu$ - and  $h$ -values sufficiently close to 1 and 0, respectively. Nevertheless, for common filament winding-related shapes (reasonable values for  $\{k, \zeta, \mu\}$ ), the deviations in the  $R$  propagation can be neglected in an initial consideration.

## 15.2 Results & discussion

With the kinematic equations presented in chapter 11 and the theory outlined in the previous section, several filament winding cases have been studied for both testing the amplitude prediction method, as well as to evaluate the smoothness of the resulting feed eye movement.

### Feed eye amplitudes

Several ellipsoidal shells have been tested with different aspect ratios. The applied fibre bundle width is 1 [mm]. With the term aspect ratio we denote here the main axes ratio of the generic ellipse that provides the shells under consideration. Due to the slope of the meridian profile at the vicinity of the polar opening, the corresponding  $\mu$ -values are slightly smaller.

Aspect ratio	0.2	0.6	1	1.2	1.8	2.4
$\kappa$	2	2	2	2	2	3
$\zeta$	0.1005	0.1005	0.100503	0.100504	0.100508	0.100514
$\mu$	0.198987	0.596962	0.994937	1.19392	1.79089	2.38785
$\phi_g$	-1.4772	-1.51466	-1.57079	-1.60386	-1.71807	-1.84969
$R/Q$ ratio	-0.05959	-0.03574	0	0.021049	0.093757	0.177549
<b>Pole condition</b>						
$R$	-0.0936	-0.05614	0	0.03306	0.147277	0.278897
$\gamma$	-0.46769	-0.16679	-0.10067	-0.08398	-0.05606	-0.04207
$p_{y \text{ equator}}$	0.621514	0.114438	0	0.028911	0.07725	0.165694
$p_y$ (simulation)	*0.74114	0.123587	0	0.026421	*0.0297	*0.0867
Abs. error	0.119624	0.009149	0	-0.00249	-0.04755	-0.07899
Rel. error %	16.14058	7.402882	0	-9.42319	-160.1	-91.1119
<b>Eq. condition</b>						
$R$	-0.0936	-0.05614	0	0.03306	0.147277	0.278897
$\gamma$	-0.10067	-0.05614	-0.10067	-0.10067	-0.10068	-0.10068
$p_{y \text{ pole}}$	0.079993	0.039997	0	0.02	0.08	0.140008
$p_y$ (simulation)	*0.08746	0.041295	0	0.02	*0.08	*0.14736
Abs. error	0.00747	0.001298	0	1E-08	1E-07	0.007361
Rel. error %	8.541173	3.142784	0	5E-05	0.000125	4.994945

Table 15.1: Results for the delivery eye amplitude applying on ellipsoidal shells of revolution

Note that the values indicated with (\*) do not apply at either the pole or the equator of the treated wound shape. As previously stated, the in some cases considerable errors occur by the large deviation of the  $\mu$  and  $h$ -values when compared to the values 1 and 0, respectively.

The results obtained with the equator condition (which means: adjust  $\gamma$  on such a way that the feed eye displacement is equal to zero when the roving passes the equator) are generally more reliable. However, for aspect ratios around 0.6, both methods (polar and equator) perform satisfactory.

**Feed eye movement morphology**

In section 11.4 we have provided some results reflecting on filament winding of an ellipsoidal shell of revolution with flat polar areas. The conclusion for that particular shape is that the optimal value for the  $\gamma$ -angle is equal to approximately 0.1 [rad] (chapter 11 and appendix A). Ideally, from a dynamics-related point of view, the feed eye movement (as a function of time) should be very similar to e.g. a sinus function.

For the calculation of the feed eye motion, an extension of the results is here realised, containing both oblate and prolate spheroids. The main emphasis is here given to the shape of the curve describing the feed eye movement as a function of  $Q$ . By assuming that  $Q'$  is constant, the resulting curves can be interpreted as providing  $p_y$  as a function of time. Notice that the in the tables presented symbol  $A$  denotes the maximally required feed eye roller inclination (figure 11.2).

The examined group consists of the following  $\mu$  ratios (equation (15.7)): {0.2, 0.4, 0.6, 0.8}. Especially the range [0.6, 0.7] is of great interest since it corresponds with the typical aspect ratios of isotensoid domes for a reasonable  $q$ -factor (figure 15.7). It should be noted here that the cases corresponding with  $\mu = 0.2$  and  $\mu = 0.4$  represent rather extreme objects, at least when compared to common mandrel shapes.

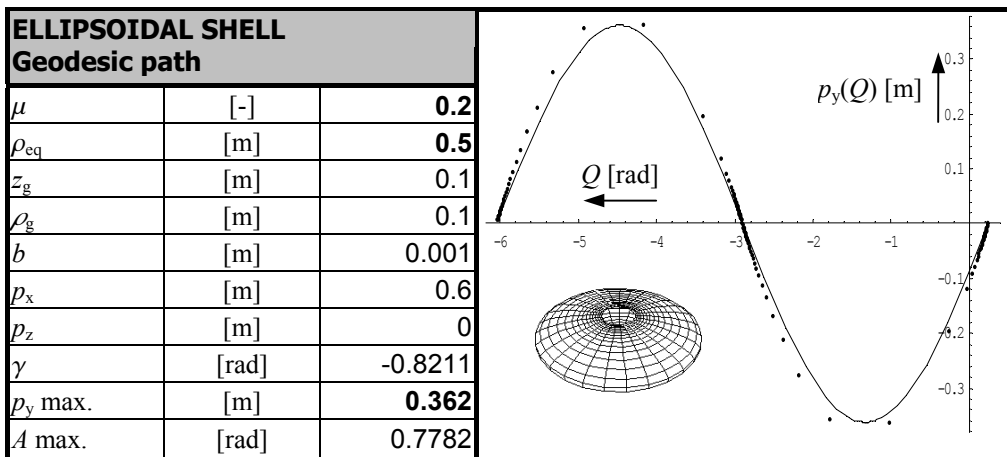


Table 15.2: Feed eye motion for an oblate spheroid with  $\mu = 0.2$

## Part C: Production process

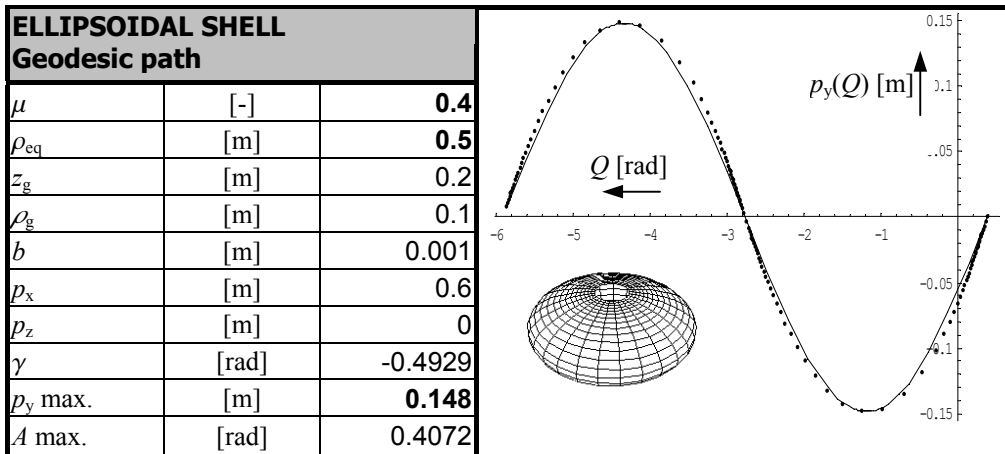


Table 15.3: Feed eye motion for an oblate spheroid with  $\mu = 0.4$

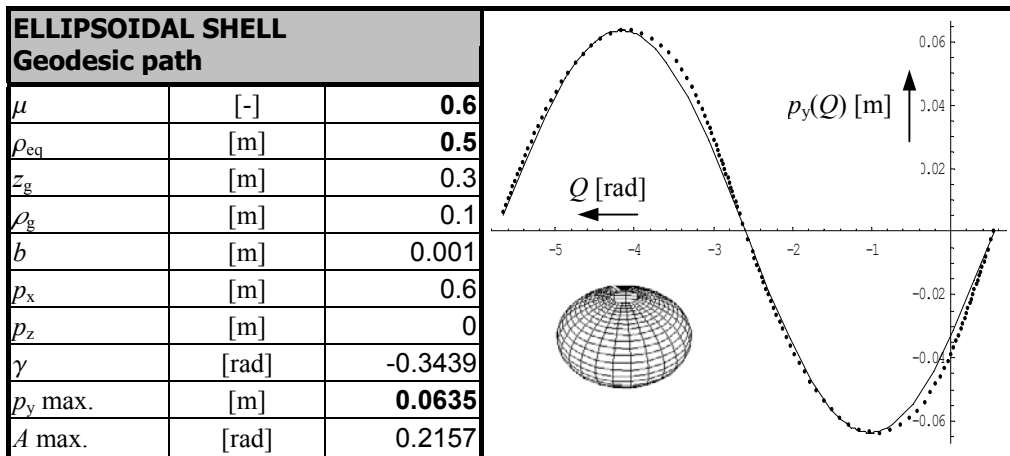


Table 15.4: Feed eye motion for an oblate spheroid with  $\mu = 0.6$

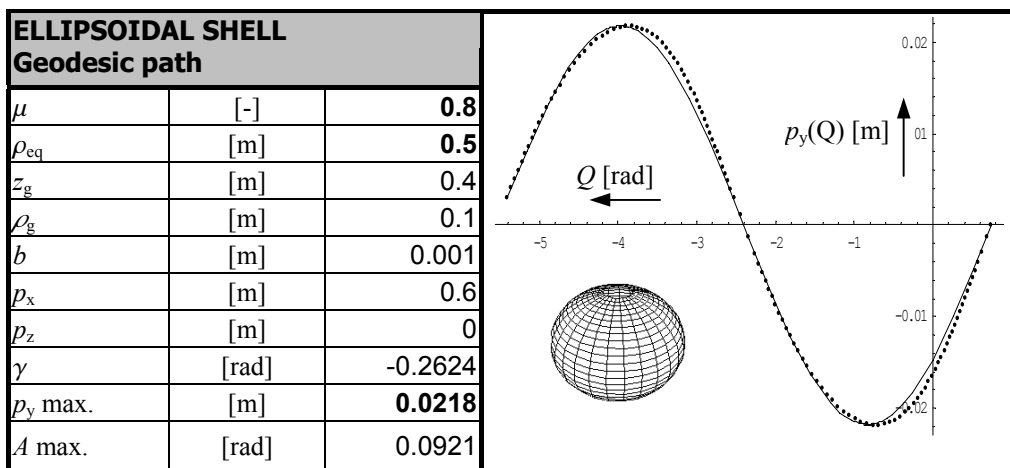
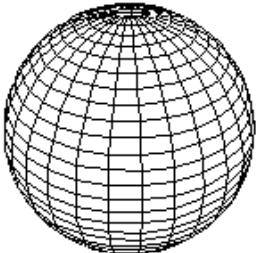


Table 15.5: Feed eye motion for an oblate spheroid with  $\mu = 0.8$

SPHERE Geodesic path		
$\mu$	[-]	<b>1</b>
$\rho_{eq}$	[m]	<b>0.5</b>
$z_g$	[m]	0.5
$\rho_g$	[m]	0.1
$b$	[m]	0.001
$p_x$	[m]	0.6
$p_z$	[m]	0
$\gamma$	[rad]	-0.2118
$p_y$ max.	[m]	<b>5.41E-07</b>
$A$ max.	[rad]	0



$|\max[p_y]| \leq 5.41 \cdot 10^{-7}$

Table 15.6: Feed eye motion for a spheroid ( $\mu = 1$ )

In regard to oblate spheroids, the resulting feed eye movement is almost sinusoidal. Recalling the kinematic assumptions, it can easily be concluded that the best equipment for producing donut-shaped pressure vessels is the simplified tumble winder configuration with constantly coupled rotations. According to [a23], the production time can, depending on the application of impregnated or dry fibre bundles, be reduced by a factor 10 to 20, respectively.

Proceeding towards prolate objects, it should be noted that the sphere is an ideal test case. It can be shown that the feed eye movement must here be equal to zero since a geodesic path on a circle is actually a ring (chapter 5). More specific, when the inclination of the plane that contains the ring matches  $\gamma$ , the amplitude of the delivery eye movement becomes equal to zero, table 15.6.

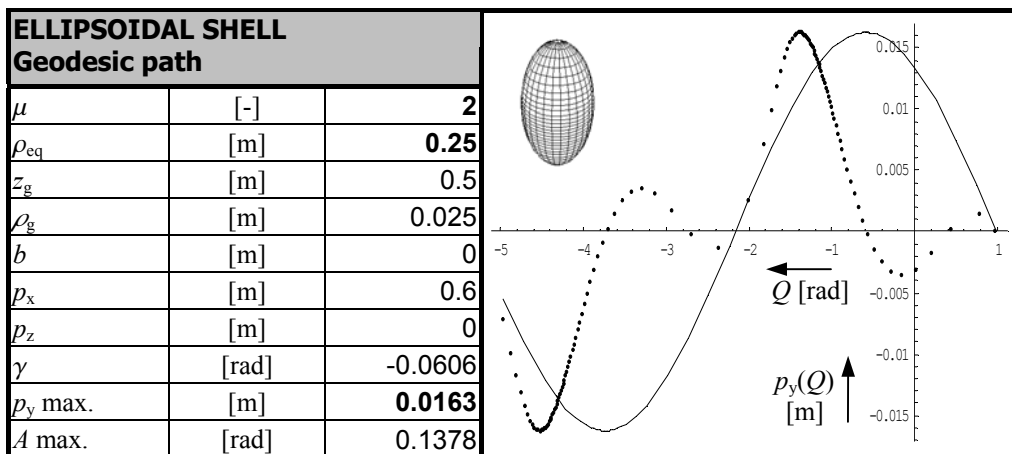


Table 15.7: Results applying on a cigar-shaped shell of revolution with  $\mu = 2$

## Part C: Production process

The prolate spheroid can generally be characterised by excessive turn around ( $\phi$ -propagation) of the roving near the poles due to the dramatic reduction of the corresponding radii in this region as proceeding upwards. For example, consider a prolate spheroid with  $\mu = 5$ ,  $\rho(\pi/2) = 1$  [m],  $\rho_{\text{equator}} = 0.1$  [m] and a fibre bundle bandwidth of 0.001 [m]. When departing from the equator and arriving at the pole using a geodesic path, the total turn-around angle ( $\phi$ -propagation) becomes equal to 2.53 [rad]. As a comparison, the combination “cylinder with isotenoid domes” of similar dimensions has a total turn-around angle of app. 1.5 [rad].

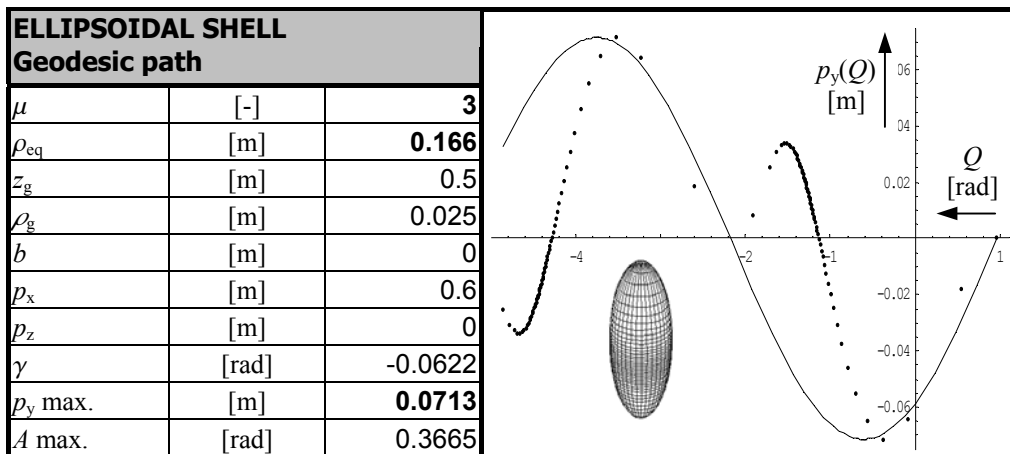


Table 15.8: Results applying on a cigar-shaped shell of revolution with  $\mu = 3$

From tables 15.7 and 15.8 it becomes clear that despite the reasonable delivery eye amplitude, the assumed sinusoidal movement (continuous line) is not able to satisfy the required feed eye motion, represented by the black dots. Nevertheless, the resulting movement can easily be decomposed into a simple combination of basic trigonometric functions. Hence, for the mechanical control of the delivery eye movement, a camshaft mechanism can be used here [α23,α24,α41,α42]. Such a machine is relatively easy and economical to build, and will not require expensive software and controllers. As demonstrated in [α23], the production time reduction achieved with dedicated machines, is certainly noticeable.

### 15.3 Winding a qrs vessel

#### Shape proportions

Without claiming that the ratio of the biggest dimensions of a qrs-vessel can completely determine the winding machine configuration and the adjustment of the process parameters, there is a certain influence of the  $\{q, r, s\}$  parameters on the, say, windability of the resulting structure. With windability we mean here the suitability of that product for being manufactured by the filament winding technique.

As derived in chapter 4, the  $\{q, r, s\}$ -parameter set is able to completely determine the meridian shape of the vessel. For a given value  $q$ , the aspect ratio of the resulting meridian profile will strongly depend on the  $r$ -value. According to equation (4.15), the  $r$ -parameter must be bigger than a certain value, while, for  $r < -1/q$  the maximum height of the resulting meridian is not located at the pole anymore, but somewhere between  $Y_{\min}$  and  $Y_{\text{eq}}$ . At that point, the slope of the meridian is obviously equal to zero. With equations (4.3) and (4.10), the  $Y$ -value where this maximum height is achieved ( $Y_m$ ), can be calculated as follows [27]:

$$k_a Y + Y^3 = 0 \Rightarrow Y^2 - k_a = 0 \Rightarrow Y_m(q, r) = \sqrt{-r} Y_{\text{eq}}(q, r) \\ -\frac{1+q}{2q} \leq r < -\frac{1}{q} \quad (15.16)$$

The coordinate  $Y$  is given as a parametric function of  $\theta$  (equation (4.12)). The  $\theta$ -value ( $\theta_m$ ) generating  $Y_m$  is:

$$Y_m(q, r) = Y(q, r, \theta) \Rightarrow \theta_m = \arccos\left(\sqrt{\frac{1+qr}{1-q}}\right) \quad (15.17)$$

The corresponding meridian profile height at that point is then given by:

$$Z_m(q, r) = Z(q, r, \theta_m) \quad (15.18)$$

where the expression for  $Z_m$  is provided by equation (4.20). Setting  $Z$  equal to zero will result in the value of  $r$  that is required for transforming the vessel into a closed donut. We denote this value by  $r_0$ :

$$Z(q, r, \pi/2) = 0 \rightarrow r_0(q) \quad (15.19)$$

The influence of  $r$  on the meridian shape is depicted in figure 15.5. We recall here that the axial force at the polar region can additionally obtain positive values, ( $r > 0$ ).

**Part C: Production process**

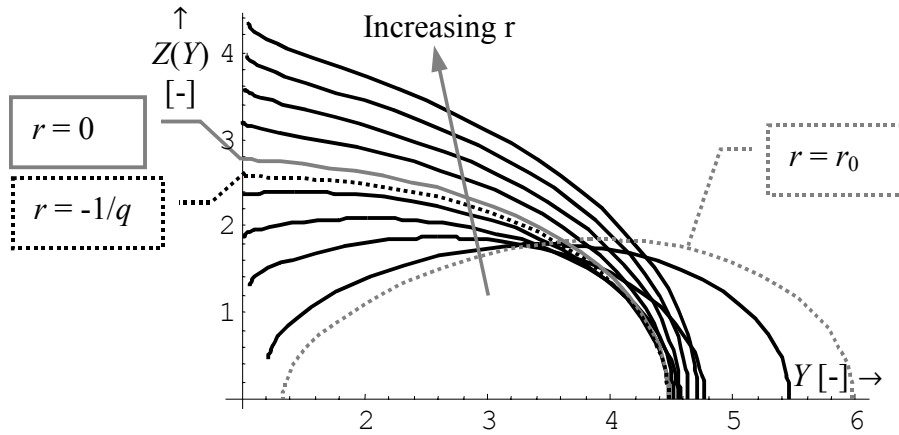


*Fig. 15.5: Influence of the  $r$  factor on the resulting meridian profile*

While positive  $r$ -values are always resulting in vessels that can immediately be wound, for a sufficiently large compressive axial force ( $r$  becomes increasingly negative) this might not be the case. More specific, when passing the polar region the roving will inevitably undergo bridging, since it can not follow concave surfaces. Hence, for the generation of manufacturing process-related input data, the polar area has to be modelled as a disk (figure 15.6). Nevertheless, despite the fact that the roving trajectories are not the aimed ones anymore, the resulting fibre bed can be pushed onto the surface by the polar end caps, therefore it will be forced to follow (more or less) the optimal geometry. In practice, this solution seems to perform sufficiently well [α24]. However, as a preference, the designer should try to keep the  $r$  parameter within the range  $[-1/q, 0]$ .

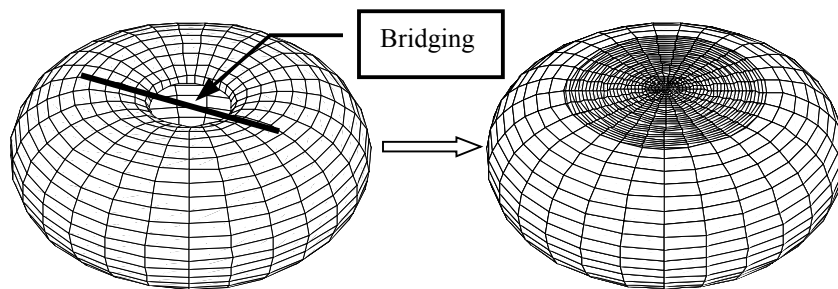


*Fig. 15.6: Concave vessel area (left) and its geometry as modelled in filament winding software (right)*

Another parameter that influences the resulting shape and especially the aspect ratio, is the  $q$  parameter. As outlined in section 15.2, the aspect ratio is asymptotically approaching the value 0.6 with an increasing  $q$ -parameter

(figure 15.7). It should be noted however, that the usual range for  $q$  reflecting on the design of common pressure vessels is  $q \in [5, 20]$ .

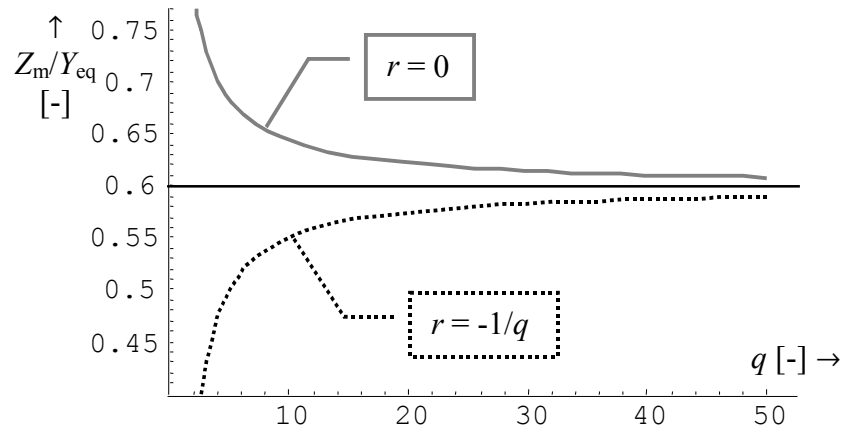


Fig. 15.7: Aspect ratio of an isotensoid meridian profile as a function of  $q$  for  $r \in [-1/q, 0]$

For vessels containing a cylindrical part, the aspect ratio is accordingly given by (see definitions in chapter 4):

$$\frac{\text{max. length}}{\text{max. diameter}} = \frac{Z_m(q, r) + H_{\max}}{Y_{eq}(q, r)} = \frac{Z_m(q, r)}{Y_{eq}(q, r)} + s \quad (15.20)$$

where  $s$  is the dimensionless length of half the cylindrical part (equation (4.11)).

### Curvature distribution

For the solution of the kinematic equations, a property greatly facilitating the numerical evaluation procedure is knowledge of the curvature distribution that characterises the roving path (equations (11.48) and (11.49)). For geodesic roving paths, the normal curvature is the same as the total curvature (equation (2.16)). The dimensionless normal curvature for an isotensoid can be derived from equation (3.29):

$$R_v(q, r, \theta) = \frac{a(q, r)}{2Y^2(q, r, \theta) \cos \alpha(q, r, \theta)} \quad (15.21)$$

where  $\alpha$ ,  $a$  and  $Y$  are given in (4.2), (4.14) and (4.12), respectively. At the equator, where the isotensoid meets the cylindrical part, the curvature is:

$$R_v|_{eq} = \frac{1 + q + 2qr + q^2(1+r)^2}{2q^2(1+r)} \quad (15.22)$$

## Part C: Production process

The cylindrical part has a zero meridional curvature, while the dimensionless parallel curvature is equal to  $1/Y_{eq}(q,r)$ . With the aid of equation (2.15), we obtain:

$$R_v|_{cyl} = \frac{\sin^2 \alpha_{eq}}{Y_{eq}^2} = \frac{[1+q+2qr+q^2(1+r)^2]^{3/2}}{(1+q+2qr)^{3/2}} = R_v|_{eq} \times \left( \frac{2q^2(1+r)}{1+q+2qr} \right)^{3/2} \quad (15.23)$$

The equatorial and cylindrical curvatures will never match, unless the following conditions are satisfied:

$$r = -\frac{1+q}{2q} - \frac{1}{2}, \quad \text{or} \quad q = 1 \quad (15.24)$$

The first condition is impossible since  $r$  is smaller than the lower bound given in (15.16), while the second condition provides an entirely cylindrical vessel without end domes (in this case, for  $r = 0$  the radius will become equal to  $(3/2)^{1/2}$  [ $\zeta 2, \zeta 14, \zeta 15$ ]). When solving the kinematic equations, one has to be aware of this curvature jump. This is the reason for slightly modifying the predictors  $u$  and  $d$  in equation (11.48). In conclusion, the cylinder is not optimal in both structural and production process related issues.

## Winding process evaluation

For results regarding the winding process of donut-shaped vessels we refer here to the previous section. For the evaluation of vessels containing a cylindrical part, we examined here two cylindrical pressure vessels that share the same isotensoid end dome with  $\rho_{eq} = 70$  [mm] and  $z_{pole} = 43$  [mm]. The cylindrical part of the first vessel has a length of 60 [mm], while the second one shows a length of 400 [mm]. The results are given in table 15.9. The winding process is based on a tumble winder where:

- $p_x = \text{constant}$
- $p_z = 0$
- $\gamma = \text{constant}$
- $R^2/Q = \text{constant}$ , according to equation (11.37)

From a comparison between the presented values for  $p_y$  (simulation) and the predicted amplitude it becomes rather evident that the prediction method outlined in section 15.1 is not applicable to qrs-vessels with a cylindrical part. However, when  $\zeta$  is close to  $1/\mu$ , the required feed eye amplitude becomes considerably small. Hence, adaptation of these ratios to each other is certainly worth taking into consideration.

In regard to the implemented winding machine configuration, it can be stated that the lathe winder is performing better for cylindrical objects where the difference between  $\zeta$  and  $1/\mu$  is relatively large. For small differences, the tumble winder is apparently a better option.

qrs vessel	Short	Long
$\kappa$	1.42857	4.28571
$\zeta$	0.221293	0.214186
$\mu$	1.04619	3.47515
$\phi_g$	-1.5475	-2.07826
$R/Q$ ratio	-0.01483	0.323061
<b>Pole condition</b>		
$R$	-0.0233	0.50746
$\gamma$	-0.20845	-0.06156
$p_{y \text{ equator}}$	0.014987	0.640495
$p_y$ (simulation)	0.0028	1.24
Abs. error	-0.01219	0.599505
Rel. error %	-435.239	48.34718
<b>Eq. condition</b>		
$R$	-0.0233	0.50746
$\gamma$	-0.22314	-0.21586
$p_{y \text{ pole}}$	0.015709	0.535114
$p_y$ (simulation)	0.00319	1.46906
Abs. error	-0.01252	0.933943
Rel. error %	-392.429	63.57432

Table 15.9: Feed eye amplitude results applying on respectively a short and a long qrs-vessel

For the selection of the proper machine configuration, we have also to consider the fact that the vessel has to additionally be covered by hoop windings (see figure at the introductory page of chapter 4). Returning to figure 15.2, we propose here the idea of a hybrid winding machine. For the creation of the polar windings, the inclination angle  $\gamma$  ( $= \gamma_{\text{polar}}$ ) should be adjusted according to a value belonging to the interval  $[\alpha_{\text{eq}}, \arctan[1/(\text{aspect ratio})]]$ . This value can be determined with a procedure similar to the method outlined in figure 15.4. Alternatively, one can perform the simulation of the winding process for a series of  $\gamma$  angles and select the value providing the best results in terms of both the feed eye movement amplitude and the associated feed eye movements morphology (section 11.4). For the creation of hoop windings, the inclination angle  $\gamma$  ( $= \gamma_{\text{hoop}}$ ) must be set equal to  $-\pi/2$ . For the transitional circuits one has to gradually change the  $\gamma$ -value from  $\gamma_{\text{hoop}}$  to  $\gamma_{\text{polar}}$  and vice versa.

Consequently, the best configuration for winding with an uninterrupted roving is probably the hybrid winder. However, the process optimisation should preferably include both the inclination angle  $\gamma$  and the cross carriage

## Part C: Production process

translation  $p_x$ . From a dynamics-related point of view, the requirement of a constant  $Q'/R'$  coupling should remain unaffected, while the feed eye elevation  $p_z$  must remain equal to zero. Nevertheless, when machine dynamics are not an issue, one can also include  $p_z$  in the optimisation process as a control variable for reducing the velocity fluctuations in the consumed roving. In this case, the complete set of degrees of freedom (3 translations and 3 rotations, chapter 10) is into the game.

For the production of cylindrical pressure vessels, another machine configuration that can significantly reduce the manufacturing time is depicted in figure 15.8. The key issue of the proposed configuration is the simultaneous placement of polar and hoop circuits coming out of separate spools. With a constant rotational speed  $Q'$ , and the rotation  $R$  coupled to  $Q$ , the speed of the spool providing the roving for the hoop windings will remain constant, hence a fibre tensioner is here not necessary. However, the polar circuits-related roving will still require such a device. Moreover, with a constant  $Q'$ , its speed will considerably fluctuate.

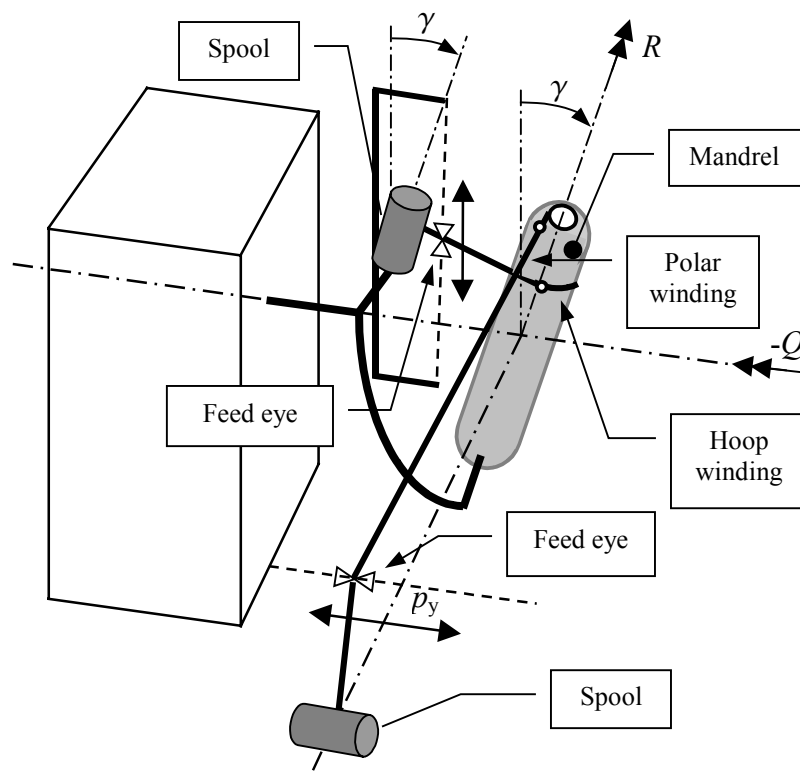


Fig. 15.8: Schematic view of the proposed winding machine configuration for the simultaneous placement of hoop and polar circuits

An important property here is that the number of  $Q$  revolutions must be sufficient for completely covering the cylindrical part with hoop windings. The problem can also be reversed: for a given pattern and a fixed cylindrical length, the applied hoop fibre bundle must at least have the following width:

$$b = \frac{h_{\max}}{kd} \Rightarrow B = \frac{H_{\max}}{kd} = \frac{sY_{eq}(q, r)}{kd} \quad (15.25)$$

where  $h_{\max}$  is the length of the half cylindrical part (section 4.1, figure 4.2),  $\{k, d\}$  are pattern-related integer numbers (section 8.1, equation (8.12)), and  $s$  is the dimensionless length of the half cylinder, related to the dimensionless equatorial radius  $Y_{eq}$  (equation (4.11)). It should be noted that, depending on the vessel dimensions and the resulting pattern, the required hoop roving width might become relatively large. In this case, one has to seek for an alternative pattern, increase the layer number  $d$  (obviously with a decreasing polar roving width as the total number of fibres is usually fixed), or continue the process without polar circuits. In this case however, the resulting reinforcing layer will not be symmetric anymore with respect to the equator of the vessel. Furthermore, in case of simultaneously completing the required number of polar and hoop circuits, the degree of interweaving is rather high. This property might negatively affect the performance of the vessel [η10].

## **Part C: Production process**

# D

## Design issues

*Inspired by the simplicity and elegance of the equilibrium equations for shells of revolution, we describe in chapter 16 a novel configuration that includes isotensoids as basic shells, axially stacked on each other. In addition, particular issues are provided, like a brief structural analysis of the proposed configuration and the evaluation of several applications for these structures. Perhaps the most interesting facet of the structures considered here, is their ability to translate significant axial loads while remaining sufficiently stable.*

*With the same equilibrium equations that are presented in chapters 3 and 4 as point of departure, chapter 17 contains a brief description of non-geodesically overwound pressure vessels, and outlines the analysis of the effects the application of radial loads on geodesically overwound isotensoids can have. In addition, we propose some novel configurations like an alternative for cylindrical pressure vessels, and we describe the class of hyperbolic shells of revolution. Furthermore, a novel configuration combining isotensoids with toroids is here introduced. Another issue presented in this chapter reflects on a proposal for curvature-based surface discretisation of continuous surfaces in general, providing  $C^2$  continuity. As a last item, we briefly discuss the application of membranes with optimal roving orientation as pressure-resisting elements in aircraft fuselages.*

### Keywords per chapter

- 16: **Articulated Pressurisable Structures (APS), Coefficient of friction, Roving twist, Stability**
- 17: **Non-geodesic trajectories, Radial forces, Toroid, Hyperboloid, Combivessel, Membrane element**

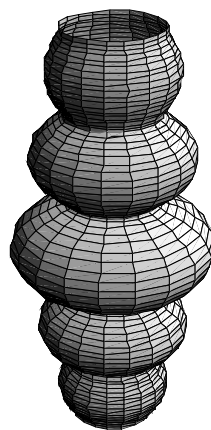
## **Part D: Design issues**

# 16

## Articulated pressurisable structures

*The axial load carrying capability of isotensoidal pressure vessels is mainly the result of the internal pressure that transforms compressive roving stresses in to tensional ones. Hence, when loaded, a qrs-vessel will almost certainly provide sufficient stability. The combination of this property with an extended degree of flexibility (inflatable version) introduces a new range of applications where rather large forces can be translated over certain distances. These distances however, are not unlimited, since the dimensions of such a vessel are finite. The solution for this problem is a configuration of vessels being stacked on top of each other, and overwound in an integral fashion. These mainly geodesically overwound isotensoidal structures are here referred to as APS: Articulated Pressurisable Structures. In this chapter we provide their shape description, investigate their structural properties and propose several application fields.*

*Beginning with the outline of the basic APS geometry, we point out several geometrical restrictions in terms of production methodology, and identify limitations generated by the restriction that the participating cells have to be stacked on each other. In section 16.2, the structural properties are briefly discussed, while the next section provides a short description of several possible applications. An additional application is provided in the last section (16.4) where we evaluate the APS as vertical supporting structure in a prescribed space (buildings, where the storey height is usually fixed).*



**Example of an APS configuration where the differing cells are created by partially non-geodesic winding**

## **Part D: Design issues**

## 16.1 Geometry

### Meridian profiles

As outlined in chapters 3 and 4, the slope of an isotensoid meridian profile at  $Y = Y_{\min}$  and  $Y = Y_{\text{eq}}$  is vertical (figure 16.1). The verticality of the profile at the aforementioned points creates the ability for interconnecting several pressure vessels without roving interruption and, more important, without deviating from the optimal geodesic path; this is the basic idea for this novel class of structures. The result of this concept is a sequence of alternating convex and concave regions, figure 16.2.

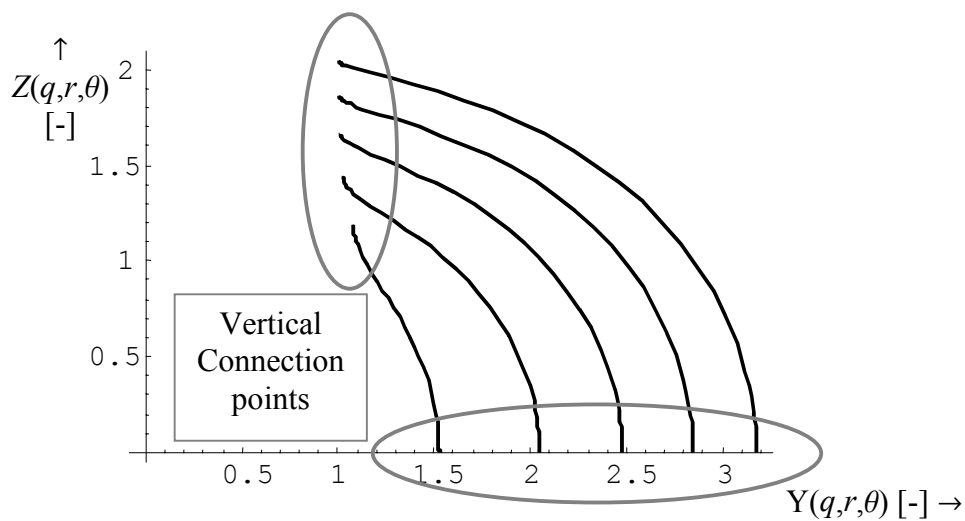


Fig. 16.1: Isotensoid profiles having vertical slopes at their end regions

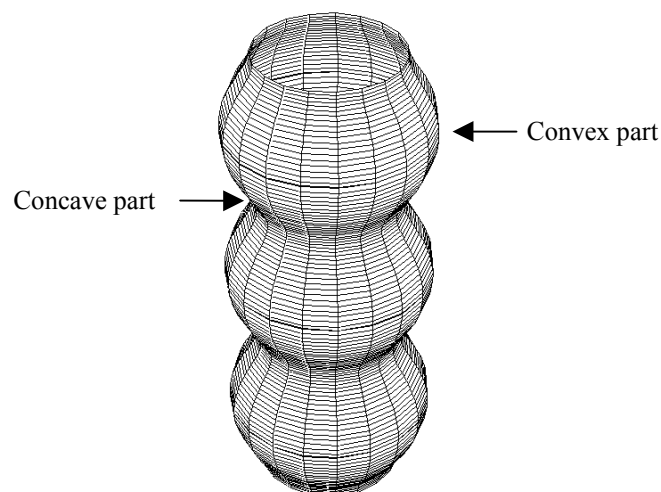
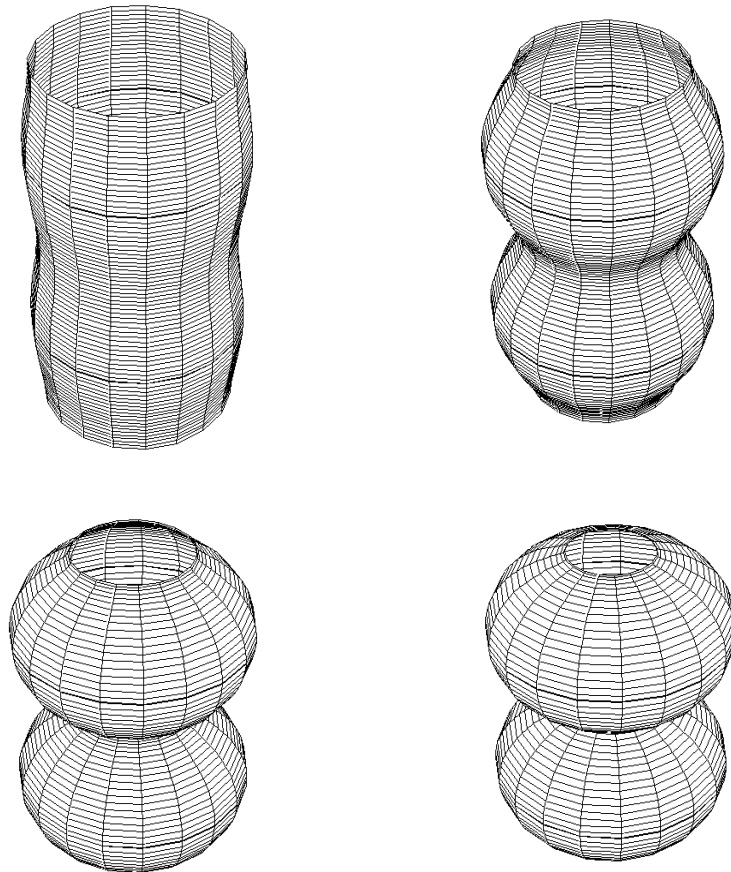


Fig. 16.2: Convex and concave regions on an Articulated **P**ressurisable **S**tructure (APS)

## Part D: Design issues

It should be noted that the roving stress is in principle constant. At the polar regions however, this is in general not entirely possible (equation (4.3), where the denominator nullifies before  $Y$  can reduce to 1). However, this inability is independent of the roving orientation after passing the smallest radius (the orientation angle  $\beta$  in equation (3.21) becomes equal to  $\pi$  anyway). A basic cell belonging to the APS is entirely optimal only in the case where  $r = -1/q$  (section 4.2).

At the same time, for this  $r$ -value, the maximum height of the profile is equal to the height it achieves at the polar opening. With a further  $r$ -reduction, the  $Z$ -value at the pole is not the maximal one anymore (figure 15.5). Hence, the resulting cells can in this case not be stacked on each other. From an external loads-related point of view, the maximum performance is achieved for  $r = -1/q$ . In addition, the second parameter,  $q$ , is significantly influencing the resulting structure, figure 16.3.



*Fig. 16.3: Several APS with different  $q$ -ratios*

Returning to the equilibrium of forces, the inability of the polar regions to satisfy equation (3.21) will require some additional reinforcements, for instance in the form of radial rings covering the bottlenecks. However, since normal pressure vessels do usually not exhibit problems at these areas, the same is expected for the APS.

### Roving trajectories

The combination of the  $q$  and  $r$ -parameters is in addition strongly affecting the windability of the resulting structure. Depending on the concavity at the polar areas and the available space between two adjacent cells, one can basically follow two different winding strategies [α22,α33]:

- $r$  close to zero and  $q$  relatively small: since the winding angle at the pole (smallest radius) is exactly equal to  $\pi/2$  and the concavity is generally small (radius of normal curvature at the bottleneck is large), the fibre bundle is able to contact the concave surface at every point with the same side while performing a total twist of maximally equal to  $\pi$  (figure 16.4, left side).
- $r$  close to the limiting case  $r = -1/q$ , and/or  $q$  rather large: the winding angle at the pole remains approximately equal to  $\pi/2$  while the concavity is generally very large (the upper surface of the lower vessel almost contacts the lower surface of the upper vessel). The applied fibre bundle should alternate its contact side, see figure 16.4, right side:

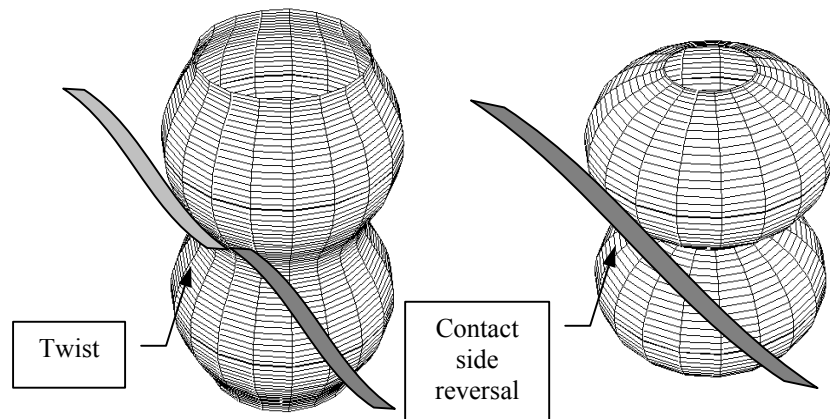


Fig. 16.4: Roving transition strategies for passing the bottlenecks

As previously mentioned, the strategy for the roving passage at the pole is not only depending on the meridian profile, but also on the applied fibre bundle dimensions. For example, a broad rigid tape is likely to face difficulties for performing the required twist, while a narrow roving will generally have increased thickness (to comply with the required level of reinforcement) and will not get sufficient space for being placed into the concave area (recall that for  $r = -1/q$ , the cells are contacting each other). Consequently, it is rather difficult to exactly formulate a criterion for the selection of the roving passage strategy. According to [α22] and [α33] however, an initial criterion can be extracted from figure 16.5, where we distinguish various areas reflecting on

## Part D: Design issues

different strategies. Notice however, that for particular  $\{q, r\}$  combinations, overlapping of these areas is inevitable.

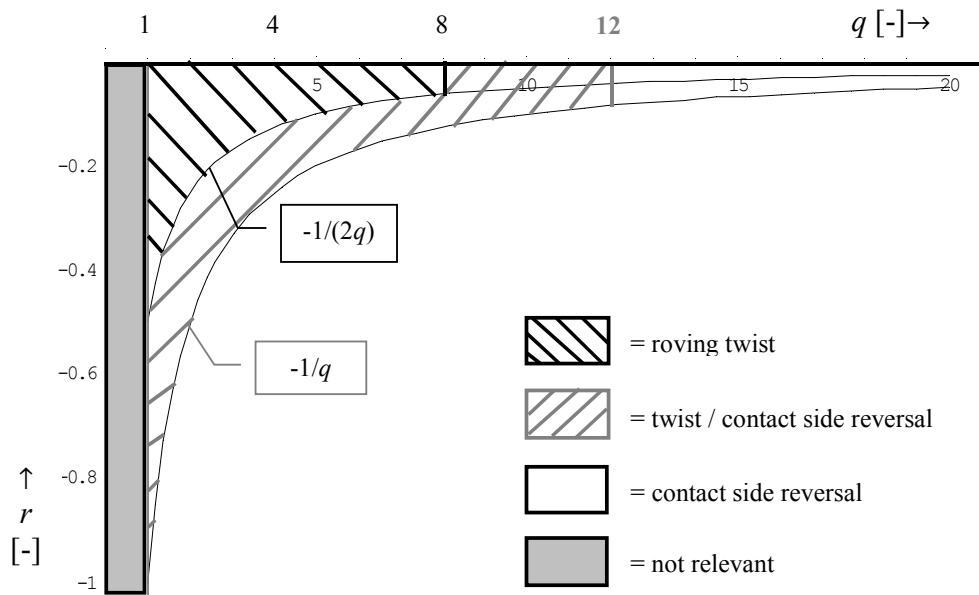


Fig. 16.5: Initial selection for the roving passage strategy at the polar areas

An additional parameter for the characterisation of the roving trajectories placement is the choice between geodesic and non-geodesic trajectories. A geodesic fibre path does not require any friction between the roving and the supporting surface, while the opposite case is applying on a non-geodesic path (chapters 5 and 6). The impact of this selection on the ability to manufacture several APS is:

- Geodesic winding: assuming zero friction ( $\mu = 0$ ), there is no possibility to create linked cells that correspond to unequal  $q$  ratios. This property results in the re-use of the same profile for every cell contained in the APS. Additionally, when applying rather small  $q$  values, a considerable radius for the pole opening is the result.
- Non-geodesic winding: depending on the magnitude of  $\mu$  and the design constraints  $\{q, r\}$ , the possibility appears for modifying the  $q$ -value when passing from one cell to the other. Consequently, the ability for decreasing the pole-opening radius becomes here a fact. This polar radius reduction depends mainly on the dimensionless equator radius  $Y_{eq}$  and the available friction  $\mu$ , see figures 16.6 and 16.7.

For a particular  $\mu$ -value, the pole-opening radius can even become equal to zero. The corresponding dimensionless critical equatorial radii are given in figure 16.7.

Figures 16.6 and 16.7 are based on an isotensoidal shape according to the application of non-geodesic winding. It should be noted that the resulting meridian profile is very similar to the geodesic-isotensoidal one; hence the original geodesic meridian profile can be maintained.

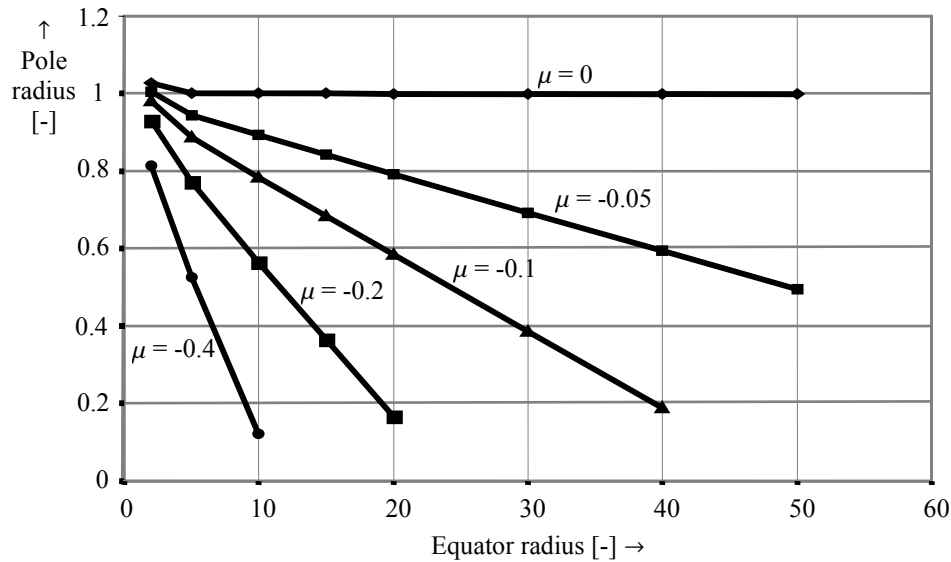


Fig. 16.6: Influence of the friction on the ability to reduce the polar opening radius

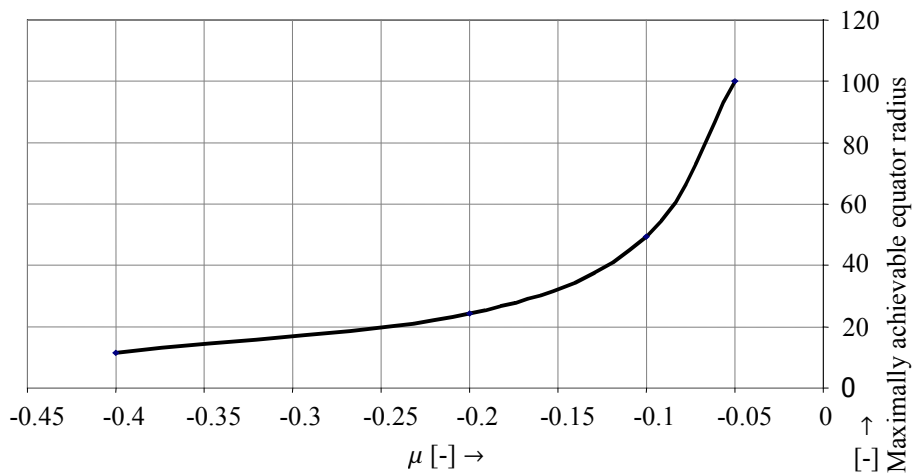


Fig. 16.7: Maximum equatorial radius that can be achieved when the polar opening is equal to zero, by maximum utilisation of the available friction

## Part D: Design issues

Summarising, the shape-related key properties of the APS can be formulated as follows:

- Continuous and rotationally symmetrical objects created by filament winding and / or braiding, based on meridian profiles that alternate between convex and concave ones.
- Uninterrupted fibre-bundle application while passing every concave area (bottleneck). This passage is based on two methods: profound roving twist or contact side reversal.
- Theoretically infinite length of the created object.
- Possible variation of the pole opening radius as a result of friction between the roving and the surface of application.
- Variation of the concavity and convexity for the participating cells as a result of the design parameters  $\{q, r, \mu\}$ .

## 16.2 Structural properties

The proposed configuration can be designed as a rigid or an inflatable structure. Irrespective of this distinction, the associated shape determination procedure is entirely comparable to the design methodology for pressure vessels (chapters 3 and 4). Therefore, we are focussing here on the load displacement characteristics of the APS and their lateral stability.

### Pressure-Displacement curves

The initial geometry considered here is a linkage of isotensoidal pressure vessels that are based on a certain  $\{q, r\}$ -combination, and are subjected to internal pressure. For the deflation, the pressure reduction is described by the parameter  $\xi$  ( $= P_{\text{deflation}} / P_{\text{initial}}$ ). The dimensionless displacement (height decreasing) of the highest meridian point depends entirely on the pressure reduction and the initial  $q$  and  $r$ -values.

Assuming that the polar opening radius and the external axial force remain unaffected during deflation, we obtain (recall equations (3.17) and (4.10)):

$$F_{\text{init}} = r_{\text{init}} \pi P (Y_{\text{eq.init}} \rho_{\text{pole}})^2 = F_{\text{defl}} = r_{\text{defl}} \pi \xi P_r (Y_{\text{eq.defl}} \rho_{\text{pole}})^2$$

$$\Rightarrow r_{\text{defl}} = \frac{r_{\text{init}}}{\xi} \left( \frac{Y_{\text{eq.init}}}{Y_{\text{eq.defl}}} \right)^2 \quad \text{where } Y_{\text{eq.defl}} = Y_{\text{eq.defl}}(q_{\text{defl}}, r_{\text{defl}}) \quad (16.1)$$

The deflated shape geometry is both depending on  $r_{\text{defl}}$  and  $q_{\text{defl}}$ , so a second condition is here required. By neglecting the roving strain modification, one can assume that the total roving length will remain the same (equation (4.24) where, at  $Y = Y_{\text{min}}$ , the independent coordinate  $\theta$  is equal to  $\pi/2$ ):

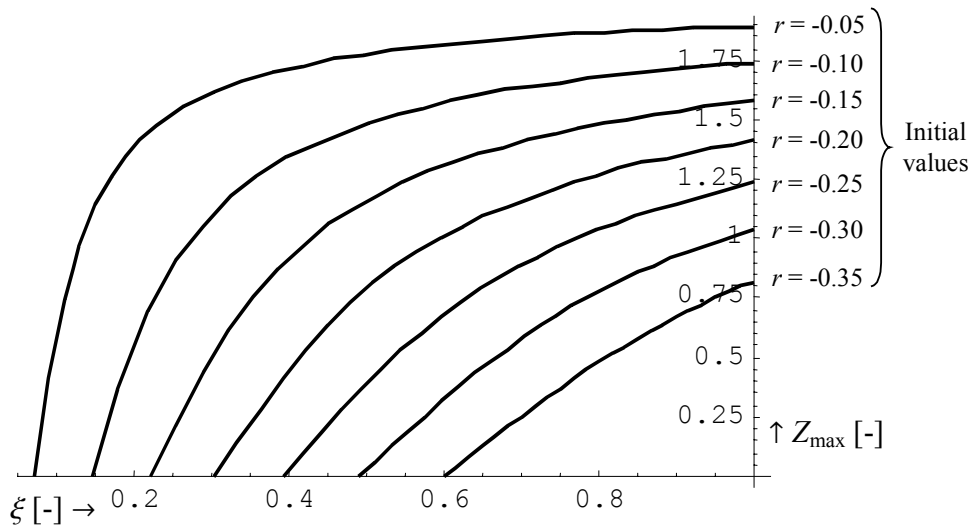


Fig. 16.8: Deflation behaviour of the APS under constant axial load

**Part D: Design issues**

$$L(q_{init}, r_{init}, \pi / 2) == L(q_{def}, r_{def}, \pi / 2) \quad (16.2)$$

With these two equations, the reduction of the cell height can be derived as a function of the relative deflation  $\xi$ , figure 16.8. As the vessel deflates, the axial forces will relatively increase (when compared to the total axial force generated by the internal pressure). Consequently, the  $r$ -coefficient will become more negative, figure 16.9.

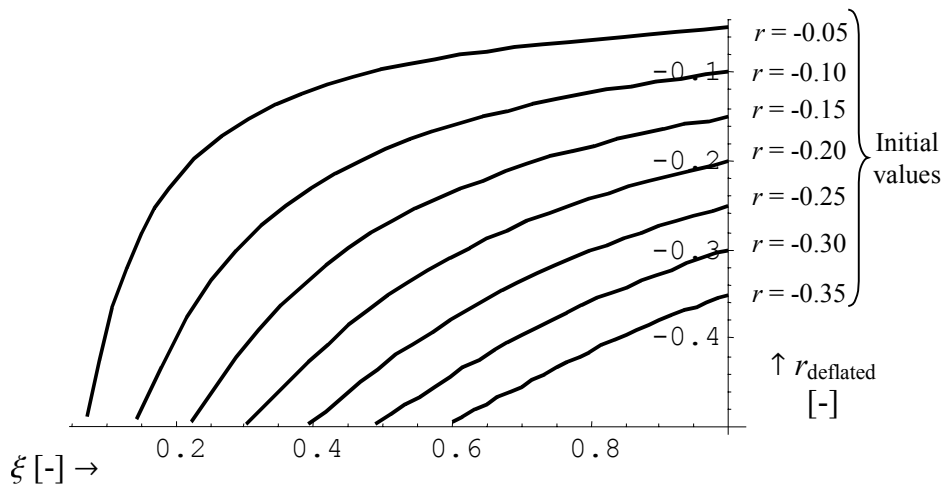


Fig. 16.9: The resulting  $r$ -values after partial deflation of the APS by a constant axial force

The minimum  $\xi$ -value is associated with the threshold pressure for neutralising the external axial force on top of the APS configuration. The most important property of the APS is its ability to adapt the pressure-displacement characteristic by changing the  $q$  and / or  $r$ -values, eventually in combination with a modification of the number of parallel arranged APS or in series linked vessels. Profiles based on non-geodesic winding create also an additional pressure-displacement curve adaptation possibility.

Except vertical movements, the proposed configuration is able to perform rotations with respect to an axis vertical to the axis of rotational symmetry. This can be achieved by an asymmetrical roving length distribution around the periphery of the cells. Furthermore, with the same mechanism, when designing an asymmetrical vessel row (with respect to the axis of rotational symmetry), a rotation with respect to the radial direction can be performed.

We recall here that as the APS deflates, the effective parameter  $r$  becomes increasingly negative. When becoming smaller than  $-1/q$ , the vessel will behave slightly stiffer than the predicted pressure-displacement curve indicates, because of extensive contact with the above and under positioned neighbouring cells. However, for sufficiently small displacements, the deformation behaviour of the APS can be assumed as linear.

### Lateral stability

For the simplified analysis presented here, we assume that the APS is subjected to a forced angular deformation that is applied on the upper polar region, figure 16.10:

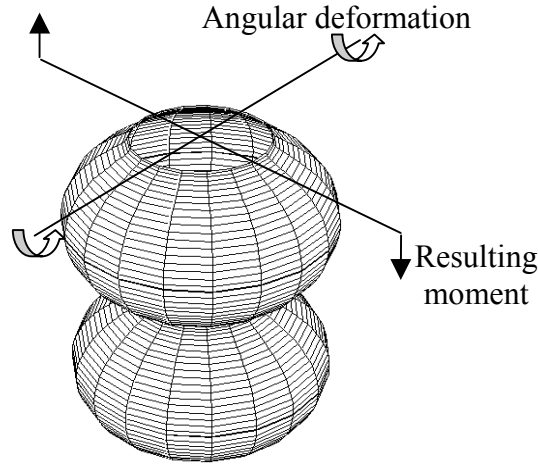


Fig. 16.10: Assumed APS deformation (forced displacement condition)

The forced displacement at the upper pole results in a modified height distribution around the polar circumference:

$$Z_{def}(\varphi) = Z(q_{init}, r_{init}, \pi/2) - Y_{min}(q_{init}, r_{init})\Delta Z \cos \varphi \quad (16.3)$$

where  $\Delta Z$  is the maximum displacement value that is distributed around the pole with the aid of the  $\cos \varphi$  term. For the determination of the resulting APS shape, the following system of equations must be solved:

$$\begin{Bmatrix} q_{def}(\varphi) \\ r_{def}(\varphi) \end{Bmatrix} = \text{solution of } \begin{Bmatrix} Z(q_{def}, r_{def}, \pi/2) == Z(\varphi) \\ L(q_{def}, r_{def}, \pi/2) == L(q_{init}, r_{init}, \pi/2) \end{Bmatrix} \quad (16.4)$$

where we use again the principle of unmodified roving length. Obviously, the resulting form is not rotationally symmetric anymore; for every  $\varphi$  we obtain a new set of  $\{q_{def}, r_{def}\}$ , hence a new meridian profile is created. The total dimensionless axial force generated by the deformed APS should be equal to the initial one:

$$k_{a,total} = \int_{\varphi=0}^{\varphi=2\pi} r_{def}(\varphi) Y_{eq}^2 [q_{def}(\varphi), r_{def}(\varphi)] d\varphi = k_{a,init} \quad (16.5)$$

At the same time, the resulting moment is given by:

**Part D: Design issues**

$$M(\varphi) = \int_{t=0}^{t=\varphi} r_{def}(t) Y_{eq}^2 [q_{def}(t), r_{def}(t)] Y_{min} [q_{def}(t), r_{def}(t)] \cos t dt \quad (16.6)$$

To obtain the real dimensioned version of the resulting moment, one has to multiply the result of (16.6) by  $\pi P_r \rho_0$ . The dimensionless moment as a function of the displacement amplitude  $\Delta Z$  is depicted below:

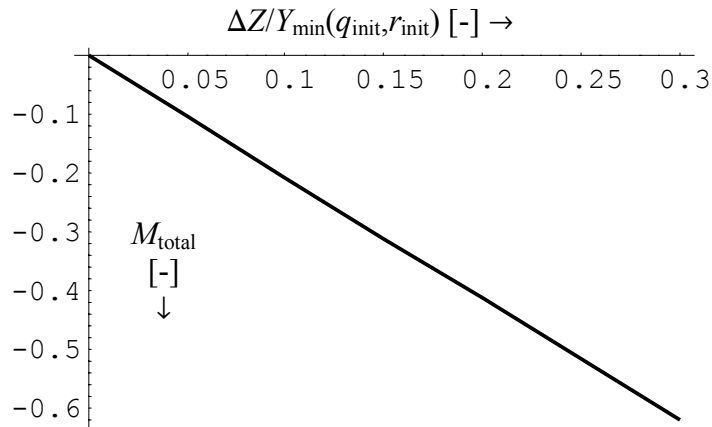


*Fig. 16.11: The resulting displacement-opposing moment*

The deformed shape is given in figure 16.12:

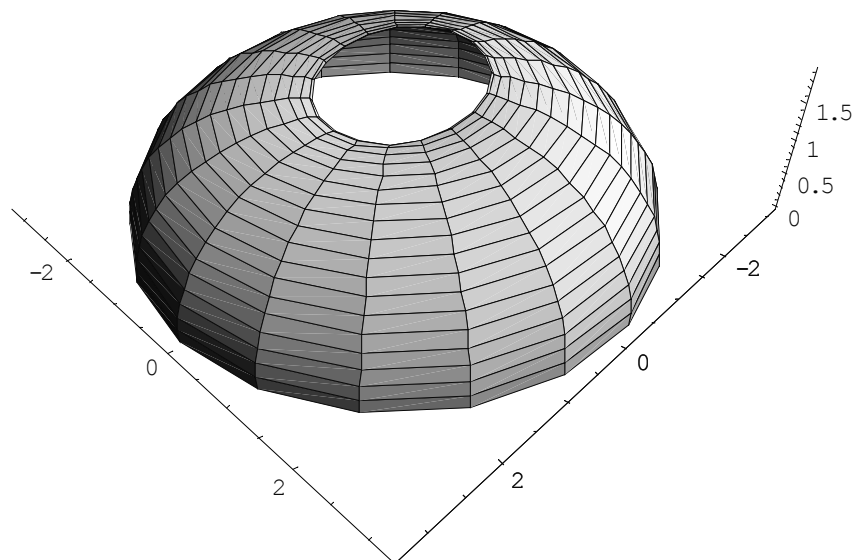


*Fig. 16.12: The resulting deformed APS structure, after a forced polar area inclination. Although not visible here, the equatorial periphery is not exactly circular anymore*

### Maximum deformation and stresses

The initial situation corresponds to a particular row of vessels having distinguished  $\{q, r\}$  combinations for each stage. When reducing the height, the worst case scenario is described by pressing the vessel row until it becomes a stacking of disks having the same pole radius as the original construction. In order to maintain the roving length of a particular circuit unchanged, the equatorial radius should increase. Consequently, the matrix should be able to withstand the generated stresses and strains.

The simplified analysis performed here is based on the assumption of having a plane stress situation. Furthermore, the fibres are considered as infinite stiff (zero strain). Without proceeding to the complete analysis, we provide here the resulting stresses, based on a typical rubber material as matrix.

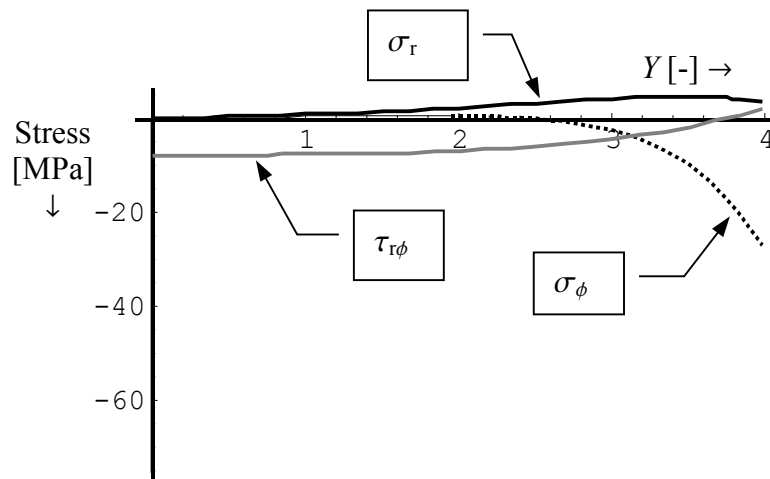


Fig. 16.13: The stresses in the rubber matrix as a result of forcing the APS to become entirely flat

When applying a typical rubber material as matrix (e.g. Polyurethane rubber), the maximum equivalent Hubert-Hencky stresses remain below the critical value.

### Applied pressure level

Although depending on the applied roving properties and the number of wound circuits, the internal pressure level is theoretically unlimited. However, in practice, even with the strongest fibres in use, the degree of laminate stacking around the poles will limit the number of circuits that can be placed on the mandrel. This limit sets a restriction on the design pressure. Nevertheless, it is believed that pressure levels of e.g. 300 [bar] are achievable. This forms the main difference between a typical non-reinforced inflatable structure and the proposed APS configuration.

## Part D: Design issues

### Impact performance

Compared to their steel counterparts, it is easily defensible that flexible composite structures show improved impact performance [27]. However, the impact performance is decreasing at higher pressures, since the effective structural stiffness becomes higher.

### Structural key properties

Considering the structural properties of the APS, the following items can be summarised:

- APS as rigid or inflatable.
- Virtually unlimited displacements in the direction of the axis of rotational symmetry.
- Various combinations of desired displacements and rotations are possible.
- Possibility for tailoring the pressure-displacement and or pressure-rotational displacement characteristics by varying the  $q$  and  $r$ -values, the coefficient of friction, and the number of in series or parallel linked vessels or entire APS configurations.
- Stability, since every lateral deflection creates an opposing moment.
- Increased deformation tolerance, convenient for inflation and / or deflation.
- Considerably higher pressure levels when compared to the existing non-reinforced inflatable structures.
- High axial load bearing capacity, being mainly directed along the axis of rotational symmetry.

## 16.3 Applications

### Pressure vessels / containers

A given installation space can be filled with various combinations of APS arrangements that are operating at considerably high pressures. Three-dimensional stacking can further increase the available space utilisation. An additional advantage of implementing APS configurations is that when a failure occurs, the remaining vessels will still contain fuel or gas for keeping the corresponding energy converter in a running situation. This fail-safe property is extremely important for e.g. the aerospace industry.

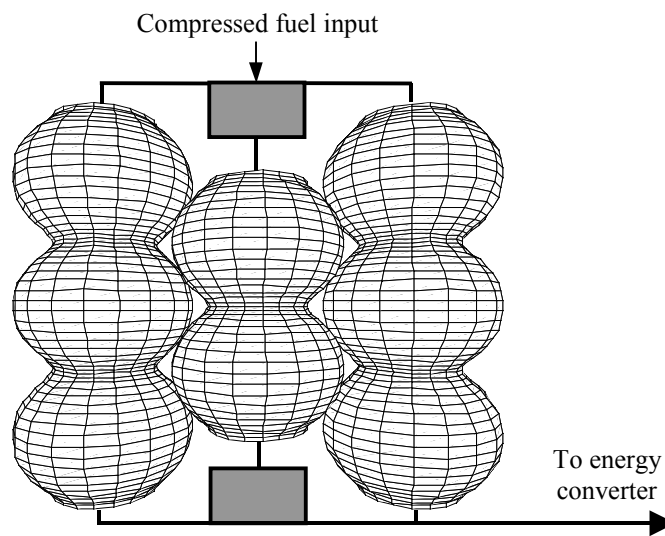


Fig. 16.14: An example of an APS arrangement

### Adjustable springs

A particular number of linked vessels (series or parallel) are able to create a spring element with certain load-displacement characteristics. Other influencing elements on these characteristics are  $\{q, r\}$  and the coefficient of friction ( $\mu$ ) that determines the roving trajectories in combination with the created meridian profile(s).

Depending on the applied external loads, the variation of the internal pressure provides a tool for adjusting the behaviour of that spring element. This principle has successfully been applied by particular car manufacturers and has proven its success. The innovation corresponding with the introduction of the APS is that the spring stiffness is adjusted by the pressure itself, and not by a reacting hydraulic load (as occasionally done). Additionally, since we apply considerably high pressures, the implemented spring element dimensions can dramatically be reduced (when the magnitude of the reacting load is the most important criterion). Furthermore, the total possible length of such a spring element is virtually unlimited.

## Part D: Design issues

### Actuators

Several industrial applications involve hydraulic cylinders, especially in mechanisms subjected to considerable external loads. These cylinders can be replaced by the APS, a modification leading to the solution of the problem of leaks. An additional advantage can be found in the elimination of various moving mechanical elements (wear). Since the pressure-displacement curve of the APS is easily adjustable, a large spectrum of application fields appears: elevators (figure 16.15 left), excavators (figure 16.15 centre) and heavy industrial robots (figure 16.15 right).

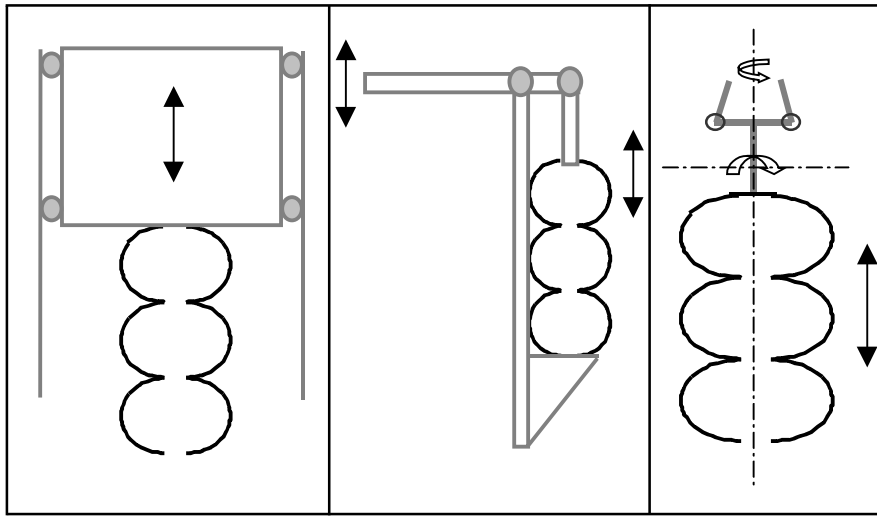


*Fig. 16.15: Applications of the APS as actuating element*

Focussing on the performance of multiple movements combined with considerable external loads, the APS is believed to represent a usable solution. As mentioned in section 16.2, several combinations of various well-controlled translational and rotational motions become feasible. Additionally, when considering a combination of parallel linked cells attached at different loci in space, a well-controlled stable movement can be achieved.

### Flexible pipelines

The combination of high pressure, translational and rotational flexibility in addition to the theoretically infinite length of the proposed cell configurations creates the ability for constructing continuous and flexible pipelines. Depending on the required flexibility, the concavity and convexity can be adjusted. Furthermore, the pipelines can be constructed in situ, or be transported in their folded state. The latter results in a considerable volume reduction, and applies also on the case of transporting goods in pressurised vessels and containers in general.

## 16.4 Strut elements

### Definitions

In this section we examine the hypothetical application of the APS as a strut element for supporting storeys in large buildings. The main difficulty in this case is the constant height  $h$  of every storey in combination with the obvious fact that the number of elements forming a strut must be an integer one.

Let us denote the floor load per surface unit by  $\sigma_f$  and the axial force in the strut by  $F_a$ . Furthermore, the APS has an internal pressure  $P_r$ , and the span of e.g. a square supported by four struts is  $L$ , figure 16.16:

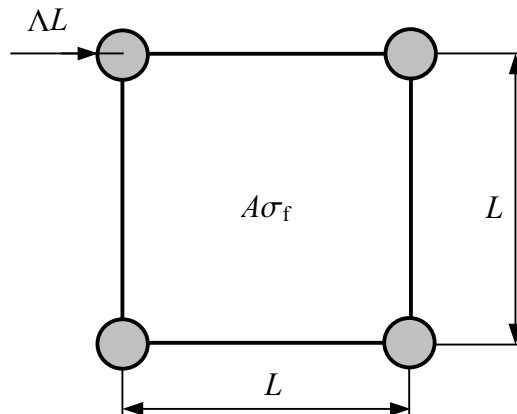


Fig. 16.16: Schematic view of a floor supported by four APS configurations

Every floor, numbered by  $m$ , contains  $i(m)$  identical cells in a single strut with a maximum radius  $\Lambda(m) \times L$ . The total number of floors is  $n$ , where the top level is assigned to number 1. Furthermore, to keep the  $r$ -value in the workable range  $[-1/q, 0]$  we assume here that the aspect ratio of the cells is approximately equal to  $3/5$ , as derived in section 15.3 and showed in figure 15.7. Hence:

$$Z_{\max}(m) = \frac{3}{5} Y_{eq}(m) \quad (16.7)$$

With the polar opening radius denoted by  $\rho_0$ , the axial force equilibrium is given by:

$$F_a(m, P_r) = \sigma_f A = r(m, P_r) \pi P_r [\rho_0 Y_{eq}(m, P_r)]^2 \quad (16.8)$$

The demand for an integer number of cells per floor in combination with the assumed aspect ratio of a single cell, results in:

**Part D: Design issues**

$$\left. \begin{aligned} 2i(m)Z_{\max}(m, P_r)\rho_0 &= h \\ Z_{\max}(m, P_r) &\approx \frac{3}{5}Y_{eq}(m, P_r) \end{aligned} \right\} \Rightarrow (\rho_0 Y_{eq}(m, P_r)) = \frac{6}{5} \frac{h}{i(m)} \quad (16.9)$$

Substitution of the last expression into equation (16.8) gives:

$$r(m, P_r) = \left( \frac{36}{25} \right) \left( \frac{m}{\pi} \right) \left( \frac{\sigma(m)}{P_r} \right) \left( \frac{A}{h^2} \right) i^2(m) \quad (16.10)$$

The only unknown parameter here is  $i(m)$ . However, since the external load is linearly proportional to the floor number while the load-carrying capability of the cells is increasing in a quadratic fashion with  $Y_{eq}$ , we obtain:

$$ni^2(n) = mi^2(m) \quad (16.11)$$

With this expression, the required number of cells (belonging to a single strut) per floor can be approximated by:

$$i(m) \approx \text{round} \left( \sqrt{\frac{ni^2(n)}{m}} \right) \quad (16.12)$$

Furthermore, with  $\Gamma = h/L$  and equation (16.9), the maximum relative radius  $\Lambda$  of a cell is given by:

$$\Lambda(m) = \frac{5}{6} \frac{\Gamma}{i(m)} \quad (16.13)$$

For a certain  $Y_{eq}(m, P_r)$ -value, the corresponding required pole radius  $c(m, P_r)$  can be obtained as follows:

$$c(m, P_r)Y_{eq}(m, P_r) = \Lambda(m)L \Rightarrow c(m, P_r) = \frac{\Lambda(m)L}{Y_{eq}(m, P_r)} \quad (16.14)$$

With the total number of floors  $n$ , the individual floor number  $m$  and the assumed value for  $i(n)$  as input parameters, the corresponding  $r(m, P_r)$  can be calculated with equation (16.10), after selection of the internal pressure level  $P_r$ . With  $r(m, P_r)$  and (16.7), the proper  $Y_{eq}(m)$  and  $q(m)$ -values can be obtained. As a final step, equation (16.14) provides the value for the polar opening radius that adjusts the APS structure to the required height  $h$ .

### Cell selection strategies

Once the initial number of cells belonging to a ground level-related strut are selected, the APS configurations supporting the remaining storeys can be dimensioned according to three strategies:

- Constant internal pressure, and a constant number  $i(m)$  that results in a reducing absolute value for  $r(m)$ , while the equatorial radius is showing a slight reduction as the indicative floor number  $m$  decreases (upward direction of the building); there is a slight uniformity of the struts per level, but the load carrying capacities of the cells are not fully utilised.
- $\{r(m), i(m)\} = \text{constant}$  will result in a pressure distribution function  $P_r(m)$  dropping with approximately a constant gradient with decreasing  $m$ .
- $P_r$  approximately constant and  $r$  as close as possible to  $-1/q$ : the strut elements will generally obtain the smallest possible value for  $Y_{\text{eq}}(m)$  or, in other words,  $\Lambda(m)$ . However, depending on the floor loads and floor number, equation (16.11) will provide cells that are too strong for a particular level; for example, equation (16.11) will decide that several floors must have the same number of cells per strut, while the loads are clearly dropping with increasing floor number.

Summarising, as faced by the construction of winding patterns, the main problem here is that we are trying to obtain integer answers from real-valued functions. Depending on the importance of the maximum load capacity, utilisation of the cells ( $r$  as close as possible to  $-1/q$ ), available space ( $A$  as small as possible), maximum pressure ( $P_r$  as low as possible) and the willingness to accept some fluctuations in the height of the storeys ( $h$ ), the final decision will probably be a matter of economics or aesthetics.

### Example

We consider here a simple structure where the floor shape is a square  $L \times L$  and every corner is supported by an APS configuration (figure 16.16). Hence, the surface corresponding to every APS is  $25 \text{ [m}^2\text{]}$ . The complete set of initial design parameters is given below:

$$\begin{aligned}
 n &= 10 && \text{integer} \\
 h &= 3 && \text{[m]} \\
 L &= 10 && \text{[m]} \\
 A &= 25 && \text{[m}^2\text{]} \\
 \sigma_f &= 300 && \text{[Kg/m}^2\text{]} \\
 \Lambda(n) &= 1/8 && \text{[-]} \\
 P_r &= 50 && \text{[bar]}
 \end{aligned}$$

## Part D: Design issues

The strategy followed here is based on the application of a constant pressure level  $P_r$  for every floor  $m$ . The tolerance for deviating from the prescribed height is set equal to zero. Due to the assumed aspect ratio, the  $r(m)$ -values are automatically kept in the range  $[-1/q, 0]$ , where obviously the optimal case is achieved for  $r(m)$  values as close as possible to the lower limit of that range. However, due to the demand for constant pressure, this requirement can not always be satisfied. The result is depicted in figure 16.17 (due to the available space for printing, the aspect ratio of the graph is strongly modified here):

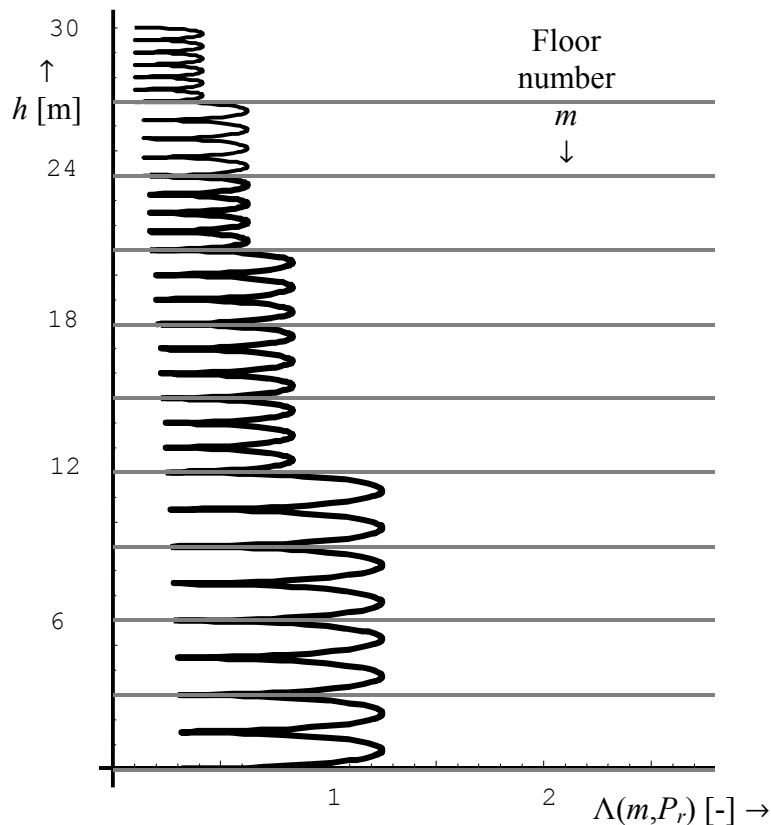


Fig. 16.17: The resulting building-supporting structure, based on APS struts

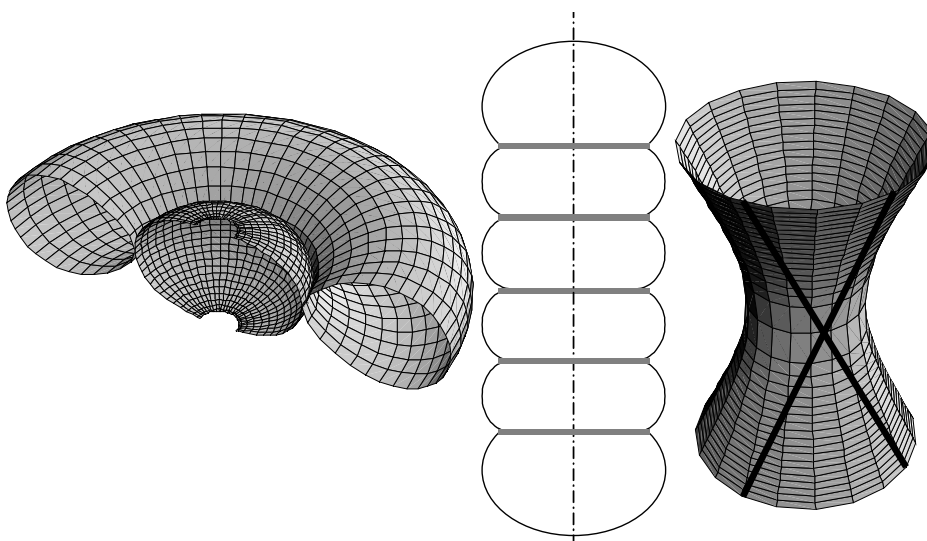
The remarkable property of the APS is their capability for supporting rather high axial loads while inflated with moderate pressures. However, for structures containing a significantly large number of storeys, the required internal pressure level can reach several hundreds of atmospheres. Furthermore, we did not bring here any safety factor into account and did not evaluate the dynamic behaviour of the resulting structure. Nevertheless, it is believed that the flexibility of the APS in combination with its load-carrying capacity, make it an extremely useful tool for constructing entire buildings by completing the floors on ground level and lifting them up to the required height.

## 17

## Pressure vessels revisited (3)

*Our last visit to the pressure vessel family can be viewed as an attempt to look further than the single, occasionally cylindrical, geodesically overwound shell of revolution. Dictated by the elegant equilibrium equations as presented in chapter 3, (in particular equation (3.21)), we end up with a collection of basic geometrical surfaces that belong to the same class: the isotenoid.*

*In the first section, an analysis is provided regarding non-geodesically overwound isotenoids. The resulting shapes are similar to the geodesically overwound vessels. The ability of these new shapes to reduce or enlarge the polar radius proves very useful, especially for connecting dissimilar articulated pressurisable structures (APS) to each other. Next, in section (17.2) we elaborate the idea of applying radial forces to the qrs vessels and we accordingly put them together. The result of this idea is a worm-shaped tank that can be adjusted to any desired aspect ratio, as long as it is bigger than 0.6. Additional proposals are the hyperboloid as a strut (also a solution of (3.21)) and the isotenoid-toroidal shell (again a solution of (3.21)). With the combination of the isotenoid and the obtained toroid attached to each other, a configuration is here generated that is believed to provide certain advantages, especially for automotive applications. The proposed configuration can adapt any desired aspect ratio, as long as it is smaller than 0.6. Hence, with the worm vessels, the complete range of aspect ratios can be covered. The last section briefly discusses the application of fibre-reinforced membrane elements as pressure resistors in aircraft fuselages, and highlights several expected benefits.*



**The depicted shapes are all related to the same equilibrium equation**

## **Part D: Design issues**

## 17.1 Extended netting theory

### Optimal shape determination for non-geodesic roving trajectories

The main constraint for the creation of isotensoidal pressure vessels is the application of geodesic roving trajectories. As experienced with the minimally achievable parameter ( $Y_{\min}$ ) that can usually not reach the dimensionless value of the polar opening radius, the exclusive involvement of such trajectories sets several design limitations. A possible solution for enlarging the design space of an optimal composite vessel can be found in the implementation of non-geodesic trajectories. To facilitate the derivations presented here, we consider instead of  $\{q, r\}$  the set  $\{Y_{\text{eq}}, r\}$  as input parameters.

With  $K = k_a \rho_0^2$  ( $= r Y_{\text{eq}}^2 \rho_0^2$ ) and  $S = a \rho_0^2$  (equations (3.17) and (3.22), respectively) we present here the basic axial equilibrium condition opposing the internal pressure and external axial load with the fibre forces (based on equation (3.24)). The winding angle is here temporarily undefined:

$$z'(\rho) = \frac{K + \rho^2}{\sqrt{(K + \rho^2)^2 - S^2 \cos^2 \alpha(\rho)}} \quad (17.1)$$

The shape equation (17.1) provides real values if condition (4.1) is satisfied:

$$\alpha(\rho) \geq \arccos\left(\frac{K + \rho^2}{S}\right) \quad (17.2)$$

Furthermore, the coefficients of the first fundamental form and the meridional and parallel curvatures of the vessel are given by equations (6.22) and (6.23), respectively. The differential equation for the winding angle (6.25) can be simplified to the form:

$$\frac{d\alpha}{d\rho} = -\frac{\tan \alpha(\rho)}{\rho} \pm \mu \left( \frac{\sin \alpha(\rho) \tan \alpha(\rho) z'(\rho)}{\rho} + \cos \alpha(\rho) \frac{z''(\rho)}{1 + z'^2(\rho)} \right) \quad (17.3)$$

The axial equilibrium of forces at the equator leads to (similar to equation (4.9)):

$$S = \frac{K + \rho_{\text{eq}}^2}{\sqrt{1 - \left(\frac{\rho_0}{\rho_{\text{eq}}}\right)^2}} \quad (17.4)$$

where  $\rho_{\text{eq}}$  and  $\rho_0$  are the equatorial and polar radius, respectively. For the satisfaction of this condition and the creation of  $C^1$  continuity of the roving path when passing the equator, the derivative presented in (17.3) must have

## Part D: Design issues

the same value as the derivative of a geodesic path (derivative of  $\arcsin(1/\rho)$ ) at exactly the equator. Therefore, the friction at that point should be equal to zero. For this reason we introduce the following friction distribution:

$$\mu(\rho) = m \frac{\rho_{eq} - \rho}{\rho_{eq} - \lambda \rho_0} \quad (17.5)$$

where  $m$  is the maximally available coefficient of friction and  $\lambda$  a constant influencing the slope of the linear friction distribution.

Furthermore, by eliminating  $q$  in equation (4.13), the minimum dimensionless radius  $Y_{\min}$  can be related to  $Y_{eq}$  according to:

$$Y_{\min}(Y_{eq}, r) = \frac{1}{\sqrt{2}} \sqrt{\frac{-Y_{eq}(Y_{eq}^2 - 1)(1 + 2r) + Y_{eq}^2 \sqrt{(Y_{eq}^2 - 1)[3 + 4r + Y_{eq}^2(1 + 2r)]}}{Y_{eq}^2 - 1}} \quad (17.6)$$

where  $r$  is given in equation (4.10). With  $z = Z\rho_0$  and  $\rho = Y\rho_0$ , and the substitution of (17.1) and (17.5) into (17.3), we obtain:

$$\frac{d\alpha}{dY}(Y_{eq}, r, \lambda, m, Y) = -\frac{C_1 + (C_2 + C_3) \tan \alpha(Y)}{Y(C_2 + C_3)} \quad (17.7)$$

where:

$$\begin{aligned} C_1 &= \frac{m(Y_{eq} - Y)(Y^2 + 2Y_{eq}^2) \cos \alpha(Y)}{Y_{eq} - \lambda} \\ C_2 &= \sqrt{\frac{-(Y^2 + rY_{eq}^2)^2 + \frac{Y_{eq}^4(1+r)^2 \cos^2 \alpha(Y)}{1 - \frac{1}{Y_{eq}^2}}}{1 - \frac{1}{Y_{eq}^2}}} \\ C_3 &= \frac{m(Y_{eq} - Y)(Y^2 + 2Y_{eq}^2) \sin \alpha(Y)}{Y_{eq} - \lambda} \end{aligned} \quad (17.8)$$

At the same time, the minimum allowable value for the winding angle (17.4) becomes:

$$\alpha_{\min}(Y, r) = \arccos \left( \frac{Y^2 + rY_{eq}^2}{Y_{eq}^3(1+r)^2} \sqrt{Y_{eq}^2 - 1} \right) \quad (17.9)$$

With a given maximum coefficient of friction  $m$  and the friction distribution gradient parameter ( $\lambda$ ), the winding angle  $\alpha(Y)$  is given by the numerical solution of (17.7). The associated evaluation procedure for non-geodesic trajectories is discussed in section 6.3.

**Examples**

To demonstrate the effect of non-geodesic trajectories on the resulting winding angle distribution and meridian profile, we examined here two cases corresponding with  $m = -0.2$  and  $m = 0.2$ . Furthermore, we assumed that  $Y_{eq} = 10$ ,  $r = 0$  and  $\lambda = 1$ .

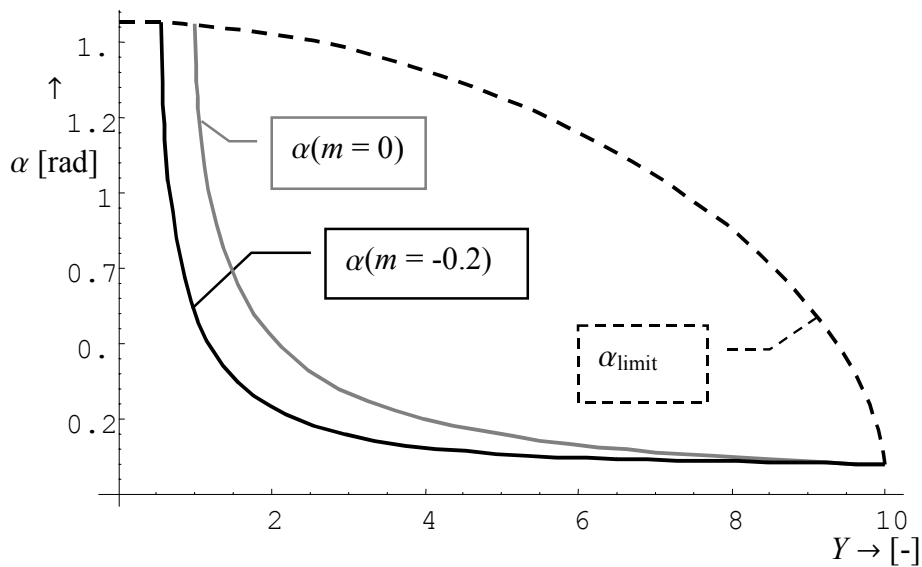


Fig. 17.1: Roving path deviation for an optimal pressure vessel dictated by a negative coefficient of friction

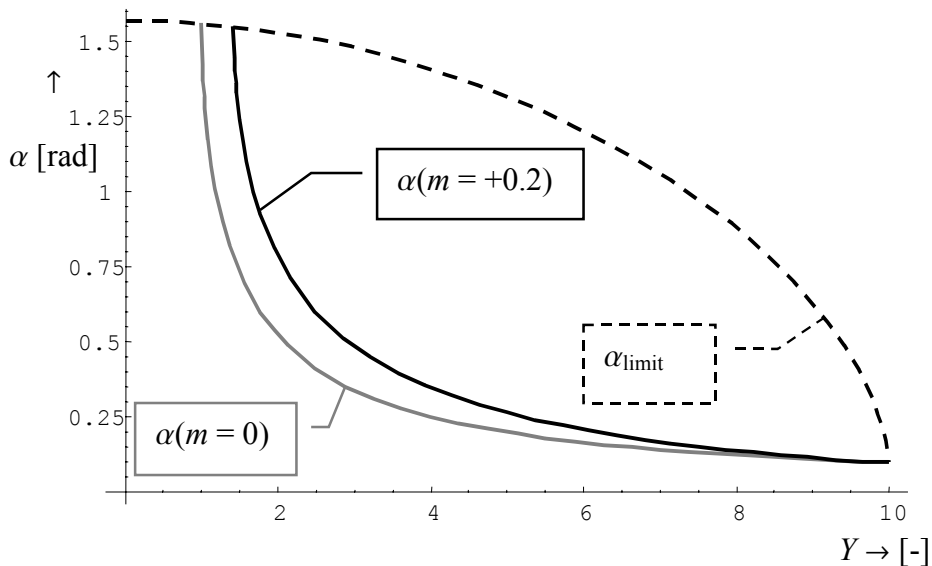


Fig. 17.2: Roving path deviation for an optimal pressure vessel dictated by a positive coefficient of friction

## Part D: Design issues

As expected, the sign of the friction applied on the roving is accordingly influencing the winding angle distribution (figures 17.1 and 17.2). Notice that the sign of the applied coefficient of friction is additionally influencing the polar opening radius, which can be increased or reduced. This principle sets the ability for controlling the polar opening radius; this is of significant importance for the connectability of dissimilar cells belonging to the same articulated pressurisable structure (APS) (picture on the introductory page of chapter 16).

In order to fully utilise the space provided for the winding angle deviation, one has to apply considerable friction levels, which are usually not achievable in practice. Therefore, the resulting meridian profiles will hardly show any difference with the original, geodesically covered isotenoids. For the realisation of substantial winding angle deviations, the technique of fibre placement seems to be a more convenient solution. An important conclusion however, is that the winding angle distribution does not have to be very accurate. Therefore, contrary to [ζ13], inclusion of the winding angle deviation for the structural analysis of the real laminate covering the vessel is here probably not necessary. An additional key feature is that the undetermined winding angle distribution provides the ability for reverse design. For example, when assuming that the meridian profile is an ellipse, one can calculate the required winding angle distribution. With this information, the corresponding distribution of coefficients of friction can be derived with equation (17.3).

## 17.2 Isotensoid-related shapes

### qrs vessel with external radial forces

The forces in a fibre bundle that is placed on a shell of revolution, can be decomposed into a radial, a circumferential (tangential) and an axial direction, figure 17.3:

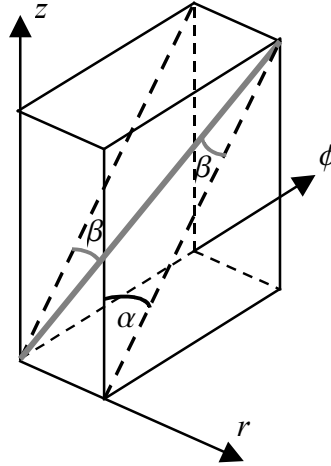


Fig. 17.3: Decomposition of a fibre force into three directions, perpendicular to each other

The force resultants are given by:

$$\begin{Bmatrix} F_r \\ F_\phi \\ F_z \end{Bmatrix} = F \cdot \begin{Bmatrix} \sin \beta \\ \sin \alpha \cos \beta \\ \cos \alpha \cos \beta \end{Bmatrix} \quad (17.10)$$

Considering a geodesically overwound shell of revolution with a meridian profile given by  $z(\rho)$ , the corresponding angles are (chapter 2):

$$\sin \alpha = \frac{c}{\rho}, \quad \cos \alpha = \sqrt{1 - \left(\frac{c}{\rho}\right)^2}, \quad \sin \beta = \frac{1}{\sqrt{1 + z'^2(\rho)}}, \quad \cos \beta = \frac{z'(\rho)}{\sqrt{1 + z'^2(\rho)}} \quad (17.12)$$

where  $c$  is the smallest radius of the shell. For an isotensoid without external axial forces, the radial force is given by:

$$F_r = a \sin \beta \quad (17.12)$$

**Part D: Design issues**

where  $a$  is the dimensionless fibre force, as defined in equation (3.22). The radial component of the internal pressure is given by:

$$dP_r(\rho) = P_r ds \cos \beta = P_r \sqrt{1 + z'^2(\rho)} d\rho \frac{z'(\rho)}{\sqrt{1 + z'^2(\rho)}} = P_r z'(\rho) d\rho \quad (17.13)$$

Hence:

$$P_r(\rho) = \int_{t=c}^{\rho} dP_r(t) dt \quad (17.14)$$

For the definition of the metric  $ds$  along the meridian we refer here to figures 2.5 and 3.3 and equation (2.6).

We consider now the total radial force generated by the internal pressure at a particular  $\rho$ -value, figure 17.4:

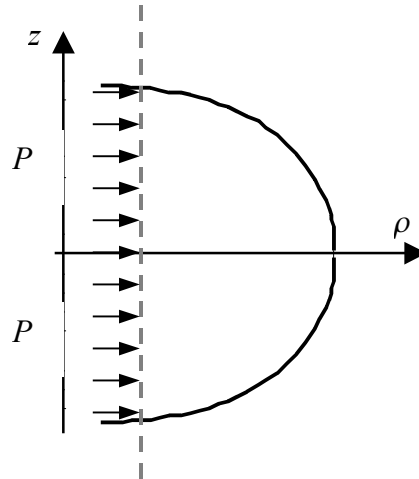


*Fig 17.4: Radial cut-out (dashed line) of a pressure vessel*

For  $\rho = c$ , the total pressure-induced force is equal to  $a$ . By increasing  $\rho$ , the total generated radial force will finally reduce to zero when approaching the equator (the vertical dashed line in figure 17.4 moves towards bigger  $\rho$ -values). An additional item to take into consideration is that the radial force is simultaneously generated by the upper and by the lower half of the vessel. With the dimensionless coordinates  $Z = z/c$  and  $Y = \rho/c$ , we obtain:

$$F_r(Y) = a + 2 \int_{t=Y \min}^Y t Z'(t) dt \quad (17.15)$$

Notice that  $Z'(t)$  is negative, therefore the pressure will reduce as  $Y$  is approaching the equator. For the determination of the minimum dimensionless

radius  $Y_{\min}$  we refer here to chapter 4. Obviously, the graphs of equations (17.14) and (17.15) must be identical.

The presence of radial forces will virtually not influence the shape of the qrs vessel; the axial equilibrium of forces is automatically satisfied by the roving geometry over the isotenoidal meridian profile, while the radial and tangential forces are automatically in equilibrium due to the rotational symmetry. Application of a radial force in the form of a reinforcing ring will result in the junction of two uncompleted qrs-vessels, axially connected to each other (multiple combinations are also possible). Depending on the  $Y$ -value where this connection takes place ( $Y_r$ ), the required radial force and resulting shape can easily be determined. For an impression of the resulting shapes, one can take figure 17.5 into consideration:

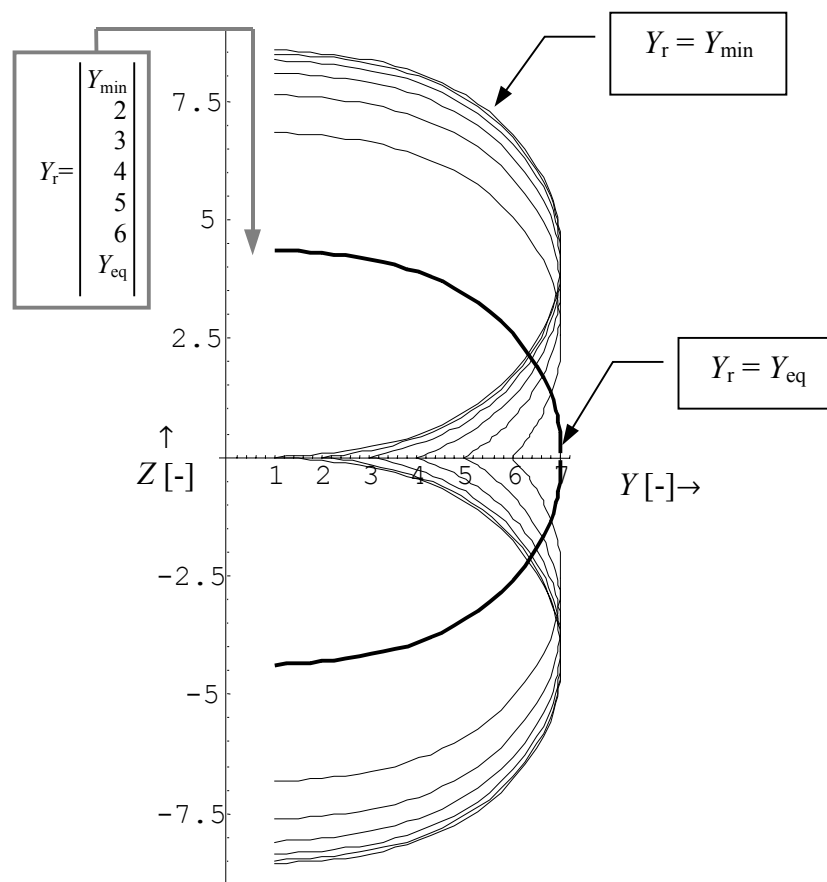


Fig. 17.5: The resulting meridian profiles for several  $Y$ -values ( $=Y_r$ ) where the external radial ring force is applied

From figure 17.6 it becomes evident that the required radial force will rapidly increase with  $(Y_{\text{eq}}-Y_r)$ . For example, for  $Y_{\text{eq}} = 7$  and  $Y_r = 6.5$ , the dimensionless axial force becomes equal to  $a/2$  ( $a =$  dimensionless roving force). Suppose that  $a$  corresponds to 200 circuits of a carbon roving with a width of 4 [mm] and a thickness of 0.3 [mm] (typical values for medium sized pressure vessels with, say, an internal pressure of 50 [bar]). In this case, the axial ring must have a cross section of at least 120 [mm<sup>2</sup>].

## Part D: Design issues

This cross section area corresponds to a carbon-equivalent square of  $11 \times 11$  [mm], still being an item of reasonable dimensions.

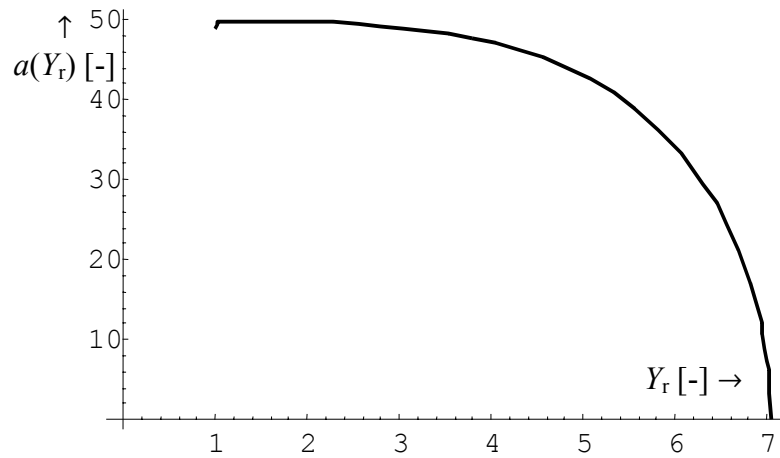


Fig. 17.6: The required dimensionless radial force in the ring surrounding the vessel at  $Y = Y_r$

With the repeated application of axial rings, one can construct a suitable alternative for the well-known cylindrical pressure vessel, figure 17.7:

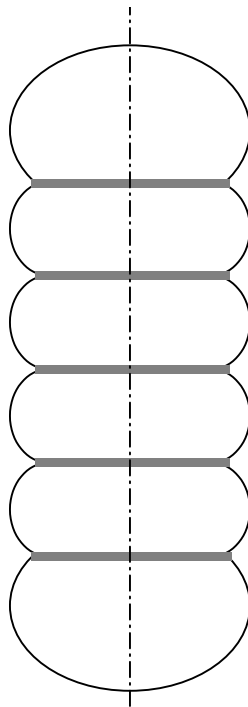


Fig. 17.7: Schematic representation of a series junction of uncompleted qrs-vessels, enhanced by the presence of radial reinforcing elements (grey lines)

With a sufficiently flexible liner, the proposed configuration obtains a fail-safe character; by failure of one ring, the internal volume will automatically increase and reduce the resulting pressure, since the configuration will jump to a new isotensoid with less rings (we assume here that the rovings are embedded in a substantially flexible matrix material, and that an eventual ring failure is already incorporated in the pressure vessel design). Another advantage is that the rings can be integrated with fuel tank supporting structures, for instance brackets surrounding the fuel tanks in trucks. In this case, the well-known problem of introducing undesired radial stresses into cylindrical tanks by the supporting structure [176] can be transformed into a great benefit.

### Hyperboloids

We consider here the axial equilibrium of a shell of revolution, subjected to external axial forces and no pressure (equation (3.21)):

$$-FN_f \cos \alpha \cos \beta = 0 + A \quad (17.16)$$

The winding angle is assumed as geodesic; to enhance this, we introduce:

$$\alpha(Y) = \arcsin\left(\frac{1}{Y}\right) \quad (17.17)$$

where  $Y$  is the dimensionless radius of the shell. In addition, the (virtual) minimum dimensionless radius of the shell is denoted by  $Y_0$  ( $>1$ ), and the dimensionless height by  $Z(Y)$ . Furthermore, we define:

$$a_h = \frac{A}{FN_f} \quad (17.18)$$

At the equator, the hyperboloid obtains its minimum radius  $Y_0$  and the angular quantity  $\beta$  becomes equal to  $\pi$  (vertical meridian slope). Hence, from equation (17.16) we obtain:

$$a_h = \cos \alpha(Y_0) = \sqrt{1 - \frac{1}{Y_0^2}} \quad (17.19)$$

Substitution of equation (17.12) and equation (17.19) into (17.16) followed by integration of  $Z'(Y)$  with respect to  $Y$ , leads to:

$$Z(Y_0, Y) = \sqrt{Y_0^2 - 1} \sqrt{Y^2 - Y_0^2}, \quad Y_0 \leq Y \leq Y_{\max} \quad (17.20)$$

where  $Y_{\max}$  is the maximum dimensionless radius of the hyperboloid. This maximum radius is not subjected to any restrictions.

**Part D: Design issues**

With the obtained function, the principal curvatures can be derived with equation (3.25). Plugging this result and equation (17.17) into (2.15) leads to the dimensionless normal curvature  $K_n(Y)$ :

$$K_n(Y) = \frac{-Z'(Y_0, Y)[1 + Z'^2(Y_0, Y)] + YZ''(Y_0, Y)[1 - Y^2]}{[Y^3(1 + Z'^2(Y_0, Y))]^{2/3}} = 0 \quad (17.21)$$

which is an expectable result (no internal pressure  $\rightarrow$  no curvature, see figure 17.8).

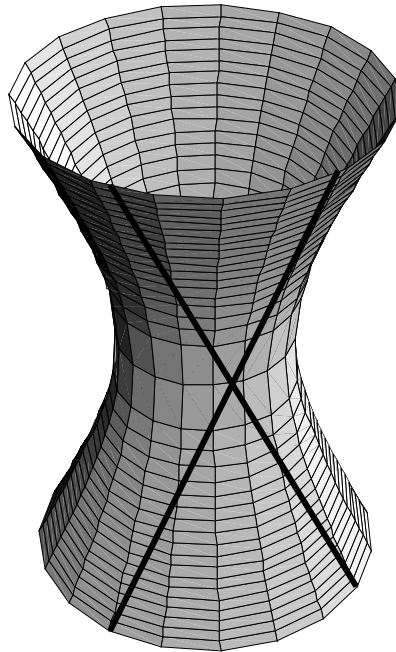


*Fig. 17.8: Hyperboloid, where a geodesic trajectory placed on it has no curvature at all*

Irrespective the fact that the rovings are subjected to a constant force, the shell will certainly need a matrix or additional hoop windings for creating the required equilibrium of forces in the radial and circumferential directions. With equations (17.11), (17.17) and (17.20), the shell forces are given by:

$$\begin{Bmatrix} F_r \\ F_\phi \\ F_z \end{Bmatrix} = FN_f \begin{Bmatrix} \frac{1}{Y_0} \sqrt{\frac{Y_0^2 - 1}{Y^2 - 1}} \\ \frac{1}{Y_0} \sqrt{\frac{Y^2 - Y_0^2}{Y^2 - 1}} \\ \sqrt{1 - \frac{1}{Y_0^2}} \end{Bmatrix} \quad (17.22)$$

where one can immediately observe the axial force is constant, and the quadratic summation of the radial and tangential forces is equal to  $FN_f$ .

Depending on the constant  $Y_0$ , various hyperboloids with particular degrees of slenderness can be created. Their suitability as strutting elements however, should certainly be further investigated. Nevertheless, it is believed that hyperboloids can provide better stability than cones or cylinders, despite the fact that cylinders are more effective in terms of fibre strength utilisation.

### Isotensoidal toroids

Another example provided by the shape family that is induced by equation (3.21), is the case where the axial force is sufficiently large for forcing the resulting meridian profile to become closed. Referring to figure 15.5 for a particular  $r$ -value ( $= r_0$ ), a toroidal vessel is here obtained, figure 17.9:

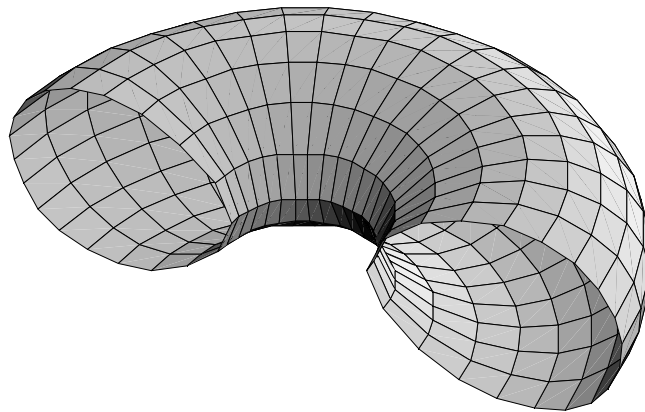


*Fig. 17.9: Mandrel shape for an optimal toroidal pressure vessel*

By neglecting several practical problems like the connection of devices for filling it, the isotoroid is an interesting alternative for spaces having limited height, for example pressure vessels in the spare wheel position of cars. After all, the aspect ratio of isotensoids can never be low enough, at least for reasonable axial forces. Note that the tensional forces of the rovings that proceed from the polar area towards the equator replace here the theoretically required external axial force, which is applied on the polar cap.

An additional proposal leading to a better space utilisation can be found in the combination of a toroid and an isotensoid that are overwound on an integral way, figures 17.10 and 17.11.

## Part D: Design issues

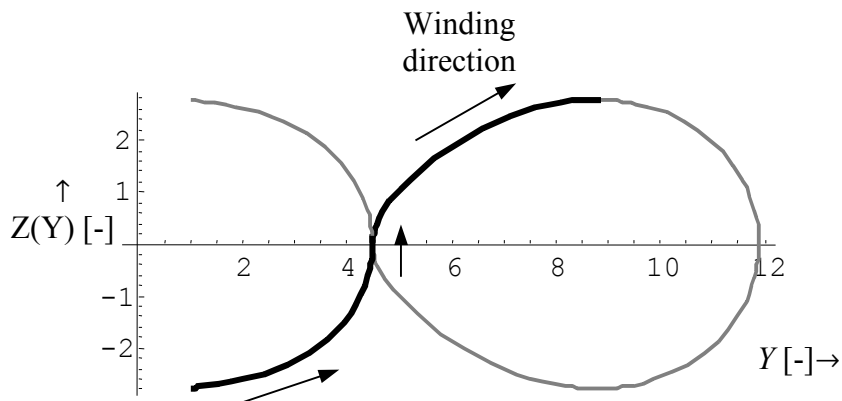


*Fig. 17.10: Integral winding of the isotensoid-toroid combination*

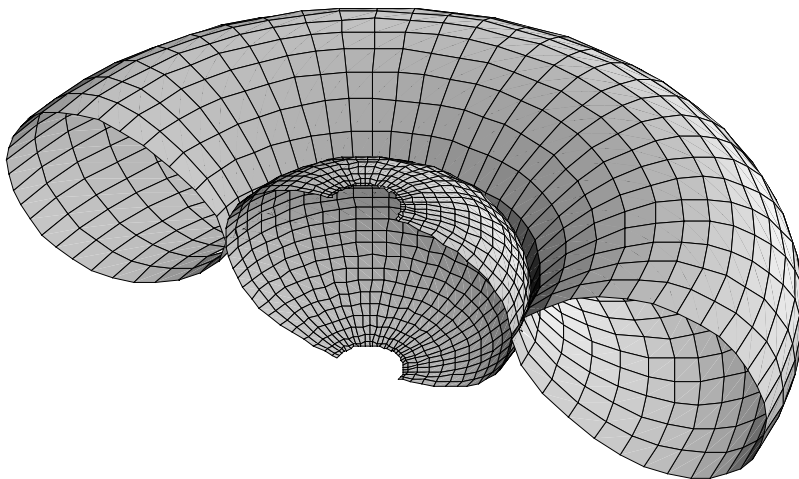


*Fig. 17.11: Three-dimensional impression of the proposed isotensoid - toroid combination*

With the introduced isotensoid-toroid configuration, the aspect ratio is reduced from 0.62 to 0.23. This value is comparable with the aspect ratio of a typical spare wheel. At the same time, the space utilisation is far better than by a single qrs-vessel. However, several drawbacks can be found in the windability of such a combination. Nevertheless, with a dedicated machine configuration similar to [δ1], manufacturing of such a structure can probably become feasible.

### 17.3 Aerospace applications: Fuselage element

To eliminate fatigue damage in pressurisable aircraft fuselages, we propose here the idea of applying fibre-reinforced membranes as pressure resisting elements (figure 17.13). As derived in chapter 3, the structural analysis of such elements can easily be performed and does not require massive computational efforts. However, since the shapes under consideration are not rotationally symmetric, one can expect that the principal curvatures will generally not be perpendicular to each other; hence the relation between membrane stresses and forces becomes here more complicated.

For the analysis of such structures, a curvature-based approximation is probably better. We propose here a square element where, for every node, two curvature directions are defined. These directions are preferably orthogonal to each other, as depicted in figure 17.12. The curvature distribution along the edges of the depicted element is assumed as linear. With a bilinear interpolation, the curvatures at every point of that element can be evaluated. A roving having a particular orientation  $\alpha$  with respect to an axis belonging to  $\{E(i)\}$ , has a normal curvature that can be calculated with an equation similar to (2.15). Notice that we neglect here the fact that the surface might be characterised by  $F = 0$ , where  $F$  is the second coefficient of the first fundamental form (equation 2.5); in the most general case, the main shell directions are not perpendicular to each other.

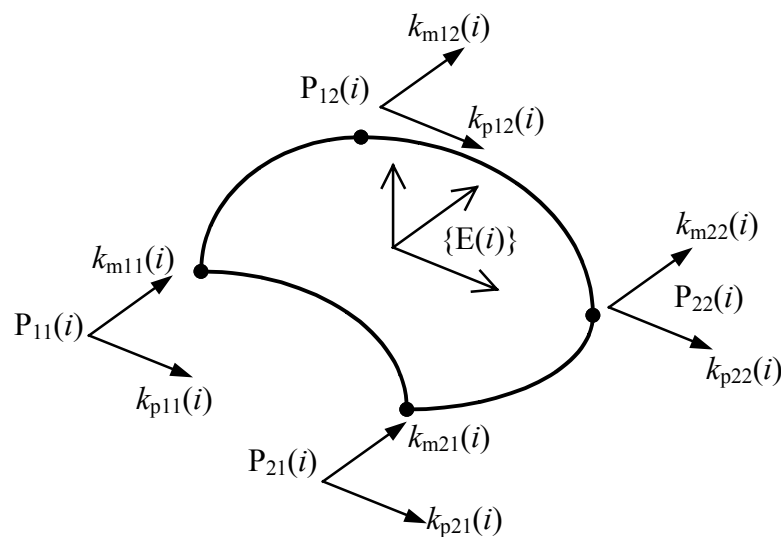
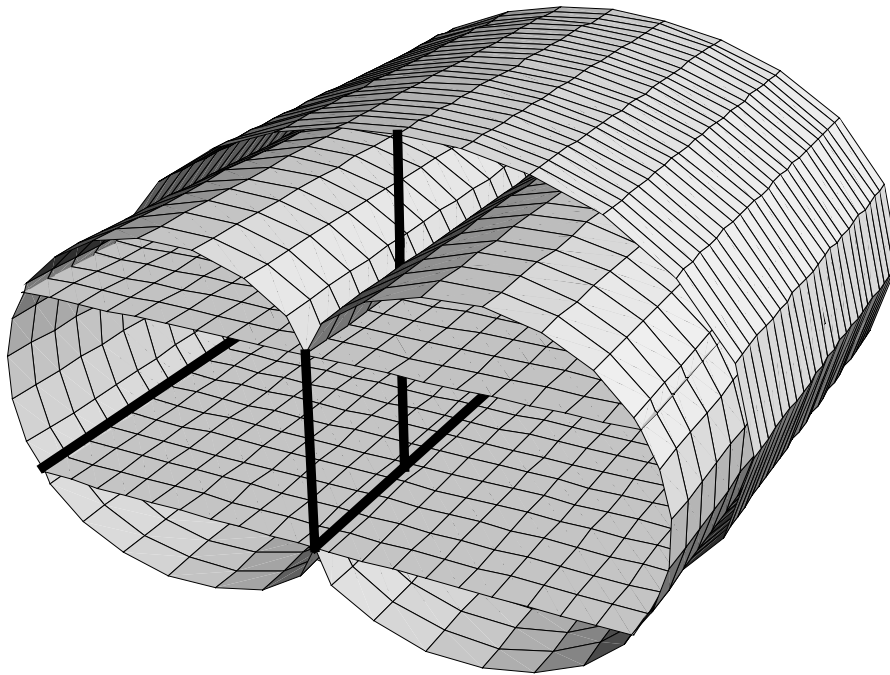


Fig. 17.12: Proposal for a square membrane element with a bilinear curvature distribution



*Fig. 17.13: Schematic representation of an elliptical fuselage containing two merged quasi-cylindrical pressure resistors that are fibre reinforced according to geodesic and non-geodesic trajectories*

Returning to the fuselage proposal, the principal idea here is segregation of the functions. Since the internal fibre-reinforced membrane structure is completely resisting the cabin pressure, the outer shape of the fuselage does not need to be cylindrical anymore; this property can greatly enlarge the design space for aircraft. According to [α7], the benefits in terms of weight and maintenance costs reduction (no fatigue) are certainly not negligible, especially when applied in Blended Wing Bodies.

Notice that since the profile of the membranes remains unchanged throughout the fuselage length, the structural analysis of the pressure resistor as depicted in figure 17.13 is not particularly complicated. The struts in the central part are acting on the same way as the axial load for single qrs vessels, and are exclusively subjected to tensional forces. In addition, by a convenient connection of the pressure resistors with the cabin floor, one can partly reduce the bending stresses occurring at the floor-supporting structure. Furthermore, with the application of transparent glass fibres and matrix materials at several loci, the creation of windows will not introduce any additional stresses [κ8]. As a final remark, we point out that the calculation of the bias angle along the tubes and the determination of the number of eventual hoop circuits for the membrane elements can be done by means of simple force equilibrium analyses, in combination with the classical lamination theory [α49,η17].

# 18

## Conclusions

*In this chapter we provide, after a brief recapitulation of the issues considered in this thesis (section 18.1), an overview of the contributions the author believes are achieved here (18.2). In a separate section (18.3), we discuss and try to qualitatively assess the degree in which the integral design principle announced in the introduction chapter (1) is satisfied or not. As usual, the research conducted here can not be considered as complete. Hence, we additionally provide several directions for future research (section 18.4).*

*For a more comprehensive outline of the contents of this thesis we refer here to the introductory chapter, section 1.3. For an overview of the thesis per included part (A, B, C, D), one can additionally consult the first page of that part. The same principle applies on chapter level.*

### 18.1 Extended summary

#### General

In this dissertation we have presented an overview and performed a comprehensive elaboration of the majority of facets associated with filament winding. Beginning with the outline of several fundamental issues related to differential geometry and the theory of thin anisotropic shells of revolution (part **A**), we have proceeded to the derivation of several types of roving trajectories, mainly placed on shells of revolution (part **B**). Subsequently, a methodology for the construction of winding patterns has been outlined. The obtained results have been demonstrated on the class of isotensoid pressure vessels that occasionally contain a cylindrical part. Next, in part **C**, an extensive treatment of the production process has been provided, including some collision control and optimisation routines. The methods derived here have been applied on the same class of filament wound pressure vessels, as we have done for part B. In the last part (**D**) we have introduced several novel design issues whereby various applications have been proposed. The mathematical origin of these shapes can be found in the equilibrium equations for optimal filamentary pressure vessels.

#### Part A

The first part provides an overview of several basic concepts and parameters from differential geometry like fundamental forms, curvatures and

## Conclusions

the Frenet frame, and specifically outlines the derivation of these quantities for shells of revolution (chapter 2). In chapter 3, the basic theory for the structural analysis of thin anisotropic shells of revolution is presented and coupled to the concepts of the previous chapter. The parameterisation of the class of optimal pressure vessels is elaborated in chapter 4, where we completely defined these objects by three parameters:  $q$  (shape factor),  $r$  (axial load factor) and  $s$  (dimensionless cylindrical length). In addition, with the filament-winding engineer in mind, several directly applicable results have been created. The class of vessels described here is used as a platform for the evaluation and verification of several results obtained throughout the thesis.

## Part B

The second part is mainly associated with the mathematical description of roving trajectories, both geodesic and non-geodesic. The majority of the derivations provided here are limited to shells of revolution. With the description of geodesic trajectories (chapter 5), the switch to non-geodesic paths has been realised in chapter 6 where we have presented geodesic trajectories as a special solution of the general path-description equation. Issues reflecting on the experimental determination of the available coefficient of friction have been outlined in chapter 7, where a bullet-shaped design is introduced for that purpose. Next, the creation and automatic determination of winding patterns is given in chapter 8 where the geometrical and mechanical properties of the applied fibre bundle form the entire set of control variables for achieving a suitable pattern. The complete set of methods and results obtained in chapters 5-8 is applied on a donut-shaped pressure vessel, in chapter 9. Here, the concept of optimal design has been extended to the inclusion of suitable patterns that match the requirements dictated by the structural analysis of the vessel.

## Part C

The third part provides a comprehensive treatment of production process-related issues. With the description of the basic geometry and the outline of procedures for the computer-friendly creation of the input parameters (position and orientation vectors, curvatures and torsion), chapter 10, the kinematic equations are formulated and solved in chapter 11. In addition, an analytical solution for the lathe winder configuration has been created. The involved machine movements are described as a function of the placed roving length (in discrete form) and co-depend on the metric distance between the roving contact locus on the mandrel and the feed eye reference point. Some considerations in regard to the determination of the associated velocities and accelerations are given in chapter 12. An additional item, collision control, is the main issue of chapter 13 where we have formulated the allowable moving space for the delivery eye as a function of the same parameters that provide the machine movements. With the obtained formulations, the production

process has been subjected to production time minimisation in chapter 14. The technique implemented here is dynamic programming, applied on a reduced grid of feasible combinations. The machine movements are subjected to both collision avoidance-related and dynamic constraints. The dynamic constraints are formulated in terms of velocity and acceleration limits, including the dynamic limitations of the roving itself. In the same spirit as part B, the obtained methodologies and results have been applied on a donut shaped pressure vessel. In the last chapter of this part, 15, we have formulated several rules of thumb to facilitate the selection of a proper machine configuration and enhance the determination of its adjustments. In addition, we have proposed several additional machine configurations.

### Part D

Part D is related to the design of novel shapes intended to be manufactured by filament winding techniques. In chapter 16, the layout of a new configuration that is formed by axial stacking of isotensoids has been described. In addition, we have proposed several application fields, mainly associated with the displacement of considerable axial loads. In addition, we evaluated the suitability of the proposed structures to serve as columns in civil constructions. With the governing equations of optimal anisotropic shells as a basis, we derived in chapter 17 some additional shapes, essentially dedicated to serve as unpressurised struts or pressurised containers, and we placed some remarks on the usage of anisotropic membrane elements as pressure resistors in aircraft fuselages.

## Conclusions

### 18.2 Contributions overview

For the presented topics we refer here to figure 18.1, which is similar to figure 1.1. The latter is mainly intended to explain the interactions between the facets involved in filament winding, while figure 18.1 is highlighting the place in the flow diagram where the contributions or improvements should be addressed to.

#### $\alpha$ Application of differential geometry

- Demonstration of the role this elegant branch of mathematics can play in filament winding and fibre placement process modelling in general.

#### $\beta$ Pressure vessels

- Derivation of the stress-curvatures relationship for shells of revolution that include axial forces (equation (3.18)).
- With the shape factor  $q$  and the axial load factor  $r$  given, introduction of a third parameters  $s$  for the dimensionless cylindrical length.
- Overview of the complete set of equations for the design procedure of isotenoid pressure vessels.

#### $\gamma$ Roving trajectories

- Comprehensive treatment of the theory for (non-) geodesic trajectories.
- Overview of several results, reflecting on both geodesic and non-geodesic winding.
- Proposal for defining the friction distribution function along the roving on such a way, that the differential equation providing the winding angle can be solved analytically.
- Introduction of a bullet-shaped mandrel that enhances the experimental determination of the coefficient of friction on lathe-configured filament winding machines by means of a linear relationship between the obtained measurements and the carriage translation.

#### $\delta$ Winding patterns

- Formulation of the turn-around angle and the resulting winding pattern as functions that additionally depend on the applied roving dimensions.
- Algorithm for the determination of suitable winding patterns omitting the solution of the first order Diophantine equation.

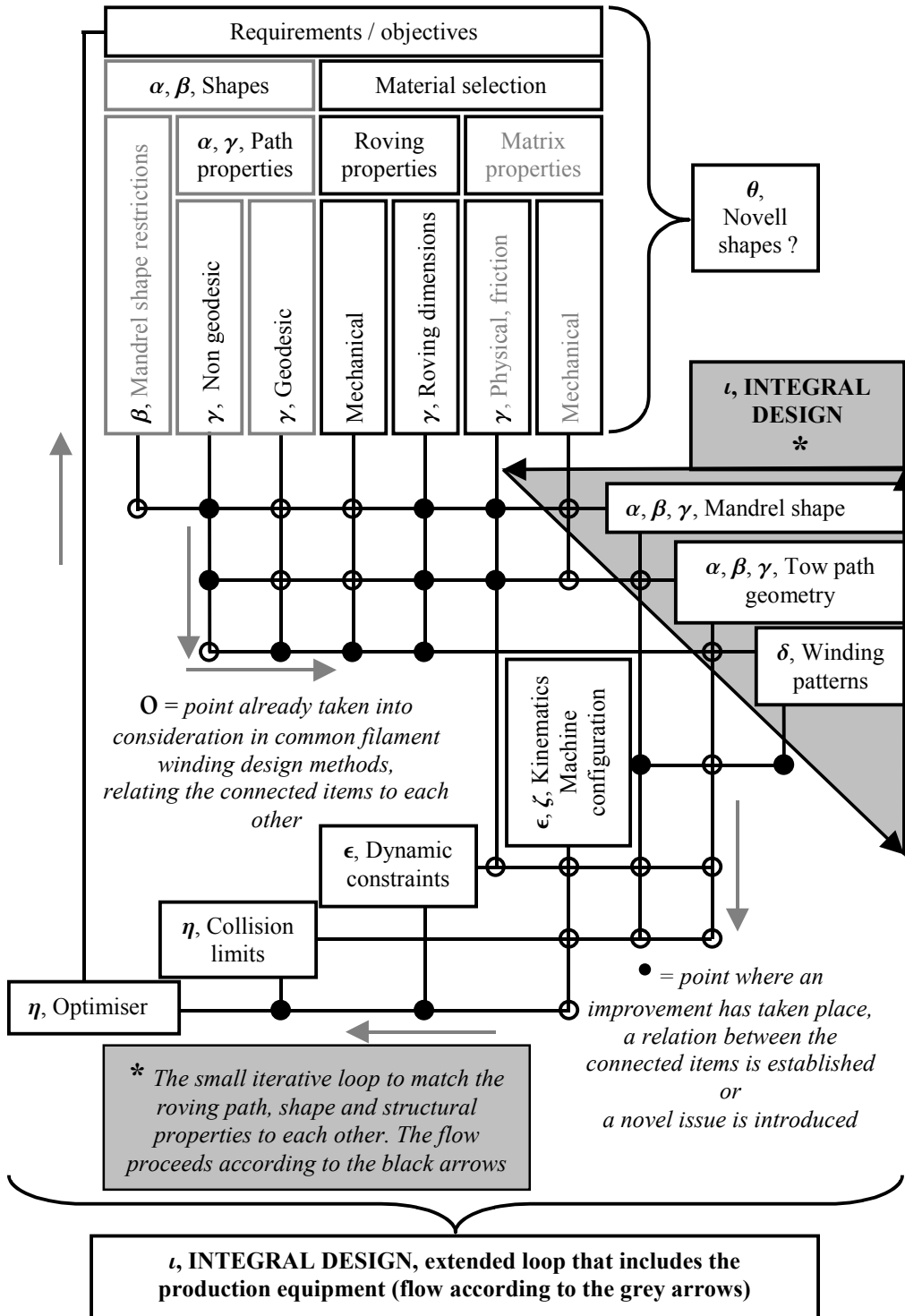


Fig. 18.1: The design and production process for filament wound items and the facets for where it is believed that improvements have taken place

## Conclusions

- Formulation and derivation of optimal winding patterns in terms of minimal number of rovings, adaptation of the resulting pattern into the required number of layers (dictated by the structural analysis of the vessel) and maximal reduction of undesired fibre bundle overlap.
- Procedure for automatically matching the required number of rovings (dictated by the structural analysis of the vessel) to the integer numbers governed by the associated winding pattern. The result is an entirely optimal pressure vessel, both in the sense of mechanical performance and perfect coverage by using a minimum number of windings.

### € Kinematics of filament winding

- Comprehensive treatment of the kinematic equations by means of a generic model. Solution through the determinant of the reduced set of equations.
- Analytical solution for the entire set of movements for a lathe winder.
- Comparison of various methods for the estimation of the velocities and accelerations that occur during the winding process.

### ζ Machine configurations

- Reintroduction of the tumble winder with constantly coupled rotations and a one-dimensional feed eye movement.
- Introduction of novel configurations: for the uninterrupted creation of polar, hoop and transitional windings: lathe-tumble hybrid. For the simultaneous placement of hoop and polar windings: combi-winder.

### η Collision control & process optimisation

- Derivation of a simplified quasi-numerical procedure for the determination of the feed eye collision boundaries.
- Introduction of an easily accessible reduction technique for the transition through a two-dimensional grid that approaches the field containing the control variables. These variables govern the entire set of machine part movements and determine the roving behaviour during filament winding. With simple matrix manipulations, the number of grid nodes is dramatically reduced by dropping the complete set of points that can not take part into a transition from the very beginning of the process to its ending.

- Straightforward minimisation of the production time by application of dynamic programming. The objective function is formulated as a summation of individual time increments, and the constraints consist of the dynamic machine limits, the restrictions on the consumed roving velocity profile, and the collision avoidance–dictated boundaries for the feed eye motion.
- Creation of rules of thumb for the selection and adjustment of the machine configuration to significantly reduce the production time.

### $\theta$ New shapes

- Proposal for articulated pressurisable structures comprising several isotenoidal cells, stacked on each other in the axial direction of the resulting structure. Introduction of several application fields that are mainly characterised by the displacement of significant axial forces over an extensive range of distances.
- Proposal for non-geodesically overwound isotenoidal pressure vessels, providing more design possibilities.
- Introduction end evaluation of isotenoids with external radial forces.
- Derivation of the combination isotenoid & toroid, and introduction of the hyperboloid as a special case of the isotenoid.
- Proposal for a double-curved membrane element that provides  $C^2$  continuity by means of a bilinear curvature distribution along its edges.

### $\iota$ Integral design

- Demonstration of the close and complicated interaction between the entire set of facets associated with the design and manufacturing of filament wound products: shape, materials and production process. Where possible, this interaction has been demonstrated by means of involving the same characteristic parameters and by evaluating the same concepts. This has been done in the extend this complicated interaction allows us to catch it in simple logical reasoning and calculation flow diagrams.

## Conclusions

### 18.3 Main issues: Integral design & insight

As outlined in section 1.2, last paragraph, the principle of integral design is slightly opposed by the immediate usage of simulation software. On the other hand, if we neglect the purchase and maintenance costs, such software is indeed providing great benefits. However, the main issue arising here is the case where an evaluated design does not comply with its requirements: which modifications have to be realised? Is an entirely alternative design perhaps better? What about the application of e.g. stronger fibre bundles? Will a proper pattern still be obtainable?

#### Integral design

In this dissertation by (sometimes briefly) covering several aspects involved in filament winding and by interrelating them to each other, an attempt has been made to provide insight and to enhance understanding of the complete design game (at least up to a certain level). This game comprises the interaction between shape determination, materials selection and production process configuration.

The design game is divided into two loops. The minor loop (grey triangle in figure 18.1, black arrows) depicts the iterative process for matching the structural properties, used materials, roving path characteristics and winding patterns to each other. This iterative procedure is in its majority outlined in chapter 9. As demonstrated, the creation of an optimal filament wound product satisfying this matching procedure is rather straightforward, at least in simple cases where the mandrel under consideration is rotationally symmetric and the applied roving paths are geodesic ones. For more complicated cases, one has to perform several iterations, as depicted in figure 18.1 with the black arrows.

The situation becomes more complicated with the additional involvement of the winding machine selection and the optimisation of its motions for obtaining minimal production time (major loop in figure 18.1, given by grey arrows). As outlined in chapter 11, the choice for a particular winding pattern will directly affect the coupling between the primary and the secondary rotation, at least in the case of using a tumble winder. In a more general perspective, even the physiology of the involved mandrel and the characteristics of the applied roving paths (geodesic versus non-geodesic) will force us to probably modify the original vessel design at several points. For example, in order to automatically obtain a perfect winding pattern (for instance according to entirely geodesic roving trajectories), the length of the cylindrical part contained in a pressure vessel has to slightly be modified. The resulting pattern will immediately influence the resulting machine movements and the associated design space for minimising the production time. The aspect ratio of the resulting product is directly influencing the choice for a particular machine configuration (chapter 15). However, when the arc tangent of this aspect ratio does not properly match the winding angle distribution along the path, a tumble winder might be useless. Hence, an alternative

machine configuration must be found, for instance, the lathe winder. The associated production time however, will probably increase. Hence, the designer must choose between entirely modifying the original design or accepting a less favourable production time.

### Insight

An additional target we tried to fulfil here, is the creation of a textbook that is of use for the filament winding engineer in practice. However, since we have almost exclusively treated shells of revolution, the contents can not be considered as fully covering the filament winding topic. The original set-up has probably suffered from the (almost universal) principle of mathematical modelling; the more generic, the more numeric. Nevertheless, it is believed that the overview of mathematical expressions, calculation flow diagrams and proposals provided here are able to enhance the insight forming process, and perhaps lead to some improvements.

For the creation of (quasi-) analytical formulations and solutions that are outlined in this thesis, the limitation to shells of revolution was rather necessary. Unless a simple parametric description of the shape under consideration is available, the construction of a (quasi-) analytical approach will require several (sophisticated) approximation techniques. An alternative method is the implementation of simple discretisation techniques. With both methods however, the connection between shape properties, roving trajectories and production process is not transparent anymore. Hence, taking the aims of providing insight and enhancing the performance of integral design into consideration, the choice has been made for an analytical treatment of rotationally symmetric objects.

## Conclusions

### 18.4 Future directions

#### Pressure vessels

With the parameterisation, roving trajectory description method, pattern determination module, kinematic solver and optimiser provided here, a dedicated software tool for the complete design and production procedure of a generic pressure vessel should be created. The only required input parameters are the internal pressure, desired volume, length of the cylindrical part (zero is also possible), axial force, and the roving strength and dimensions of its cross section.

#### Design

Further elaboration and experimental verification of the proposed pressure vessel variants is here recommended: non-geodesic isotenoids (fig. 17.1 and 17.2), isotenoids with radial forces (fig. 17.7), toroidal isotenoids (fig. 17.9) and the combination isotenoid-toroid (fig. 17.11). Moreover, in regard to the producibility of the isotenoid with radial forces, several solutions have to be created for the fibre placement at the concave areas, in the vicinity of the reinforcing rings. Note that this is not a problem for the articulated pressurisable structures outlined in chapter 16, since the winding angle is strongly approaching  $\pi/2$  at the concave areas. However, the manufacturing process of the isotenoid-toroid combination will almost certainly generate specific difficulties.

In regard to the hyperbolic shells of revolution, their stability and ability to withstand axial loads should be compared with existing structures, like conical and cylindrical composite struts. In addition, the structural properties, functionality and producibility of the articulated pressurisable structures should be further investigated and experimentally verified.

More general, in regard to the design procedure of filament wound structures, the evaluation of thick shells according to the continuum theory should also be incorporated. An extension towards non-rotationally symmetric shells is also worth recommending. However, these subjects are rather complicated.

#### Roving trajectories & broad tape deformations

In order to be able to cover every continuous surface in filament winding models, one should certainly try to evaluate a large variety of discretisation techniques. Some solutions to this problem can be found in approximations by bi-cubic splines or curvature-determining functions for a single surface element. An example of the latter can be found in figure 17.12, where a square element with double curvature is approximated by linear curvature distributions along its edges. With a simple bilinear interpolation, the

curvature at every point belonging to that surface can easily be found. Consequently, the (non-) geodesic trajectories can be calculated per element by relatively simple geodesic curvature equations or static roving force equilibrium in both normal and lateral directions. Moreover, the associated normal curvature distributions can directly be coupled to the structural analysis of the body under consideration (evaluation of force equilibrium in the normal and tangential direction).

For filament winding with broad tapes, the shearing and twisting of the tape that is placed on the mandrel should additionally be taken into account since it can have a profound influence on the product quality. Hence, several methodologies already applied in draping simulations should be integrated into filament winding-related software. With this principle, the gap between draping and winding gets closed, and a universal tool for roving & tape placement becomes reality.

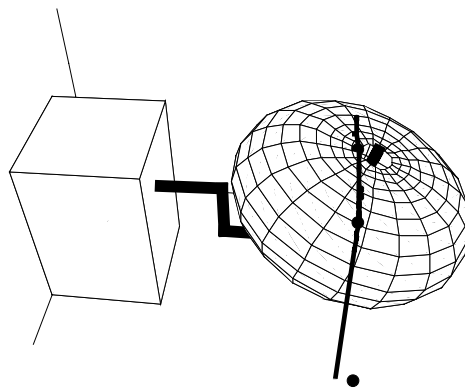
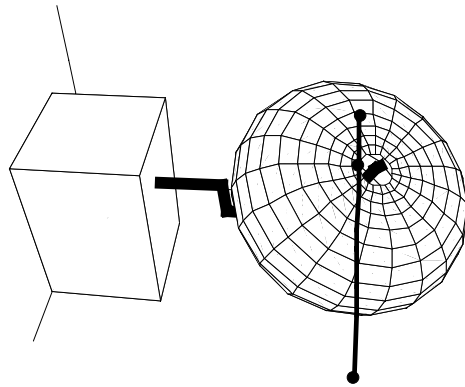
### Production process

An extension of the kinematic model towards fibre placement will certainly increase the usability of filament winding software. It is strongly recommended to create a kinematic model additionally incorporating the complete set of the movements the feed eye itself can perform. With this extension, the same model can be used for evaluating filament winding and fibre placement at the same time. In addition, improved optimisation strategies and a more convenient derivation of the resulting velocities and accelerations (reflecting on the machine parts and the placed tape) will further increase the usefulness of such software. Furthermore, the proposed configurations, lathe-tumble hybrid (fig. 15.2) and combi-winder (fig. 15.9) should be further developed and experimentally evaluated.

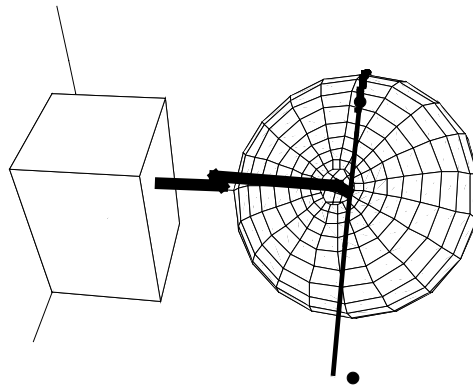
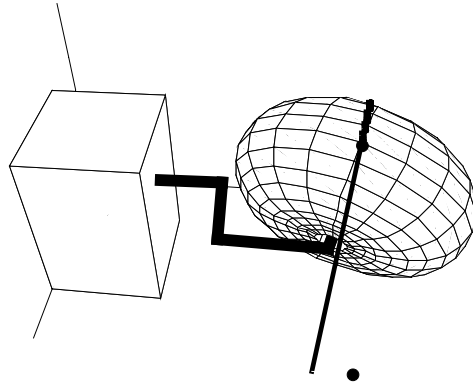
## Conclusions

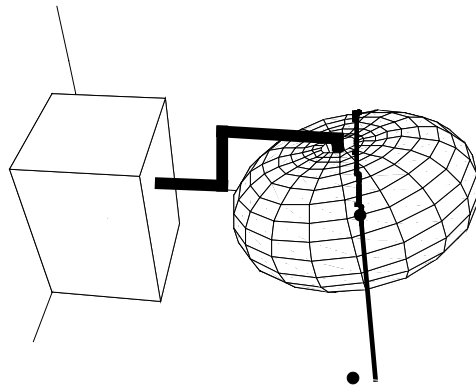
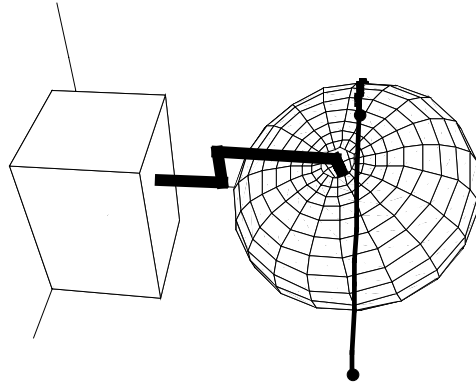
# A

## Production process simulation on a tumble winder

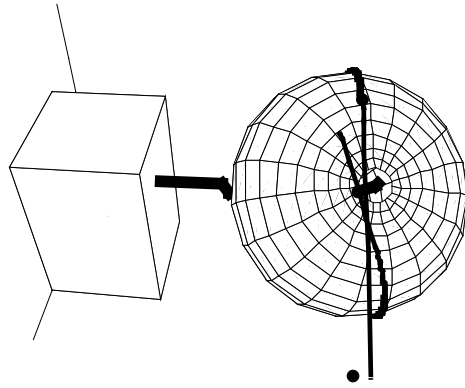
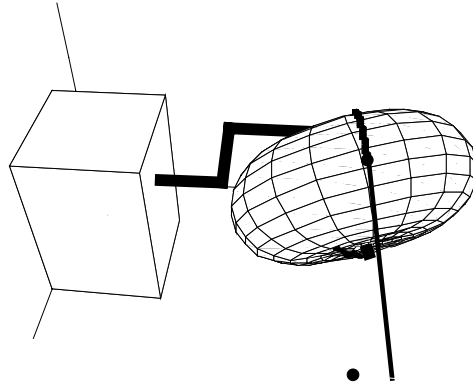


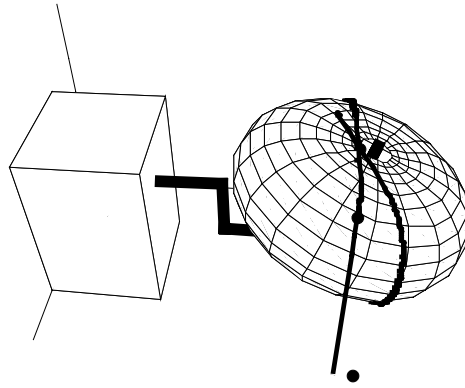
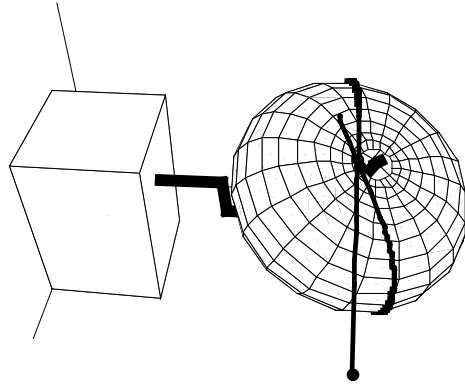
Appendix A



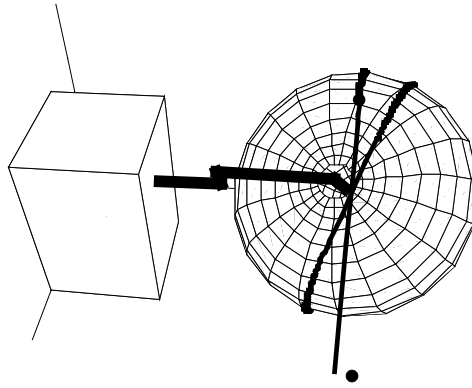
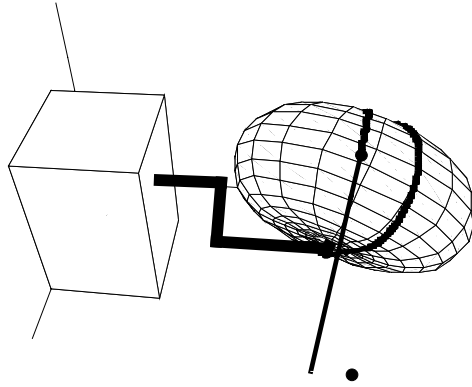


**Appendix A**



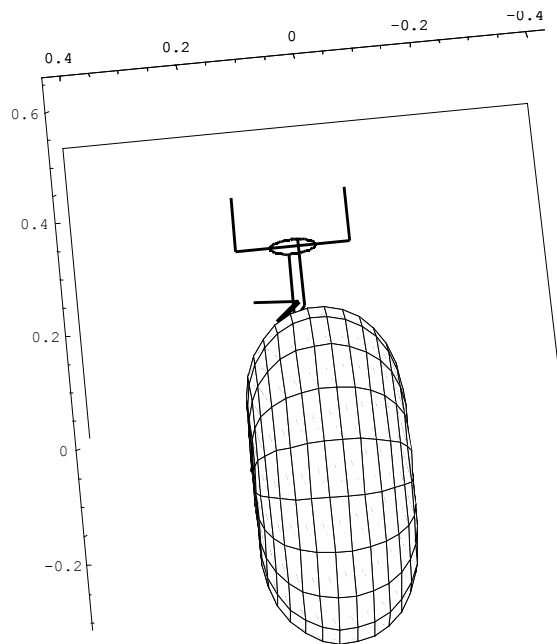
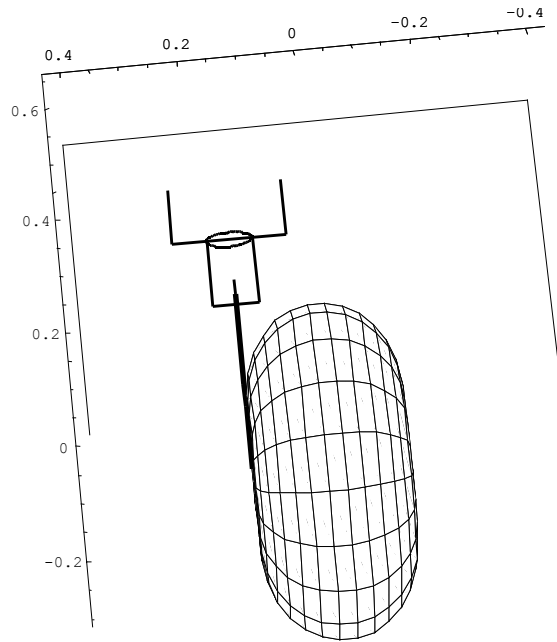


**Appendix A**

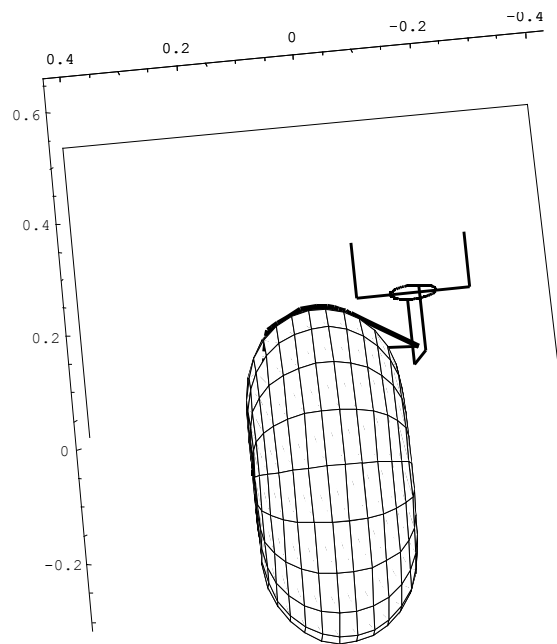
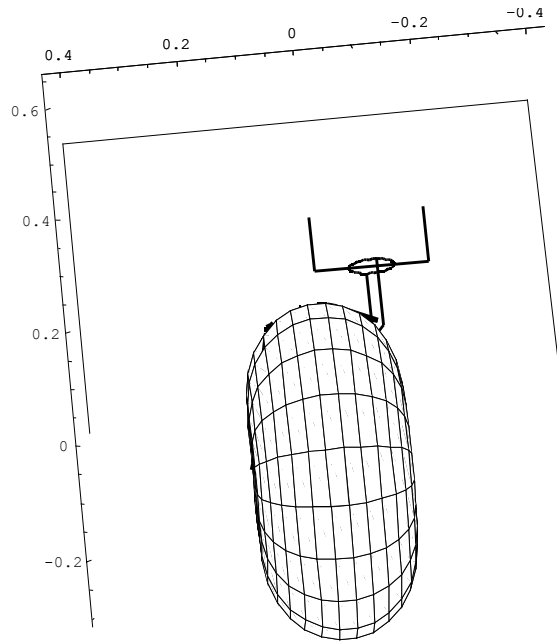


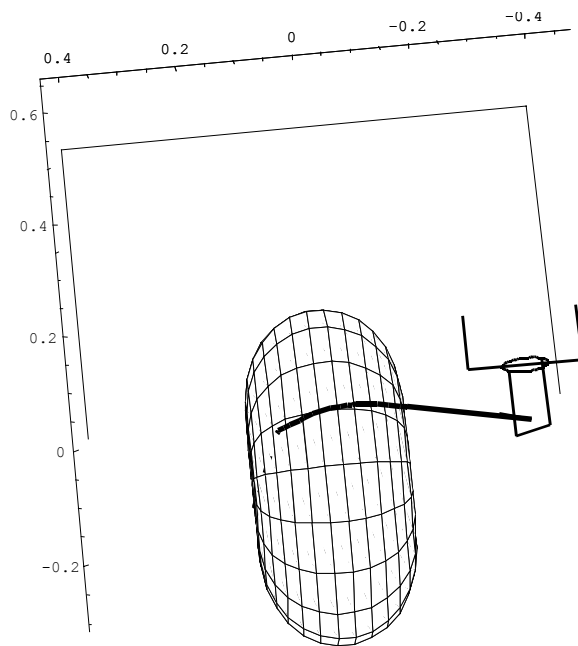
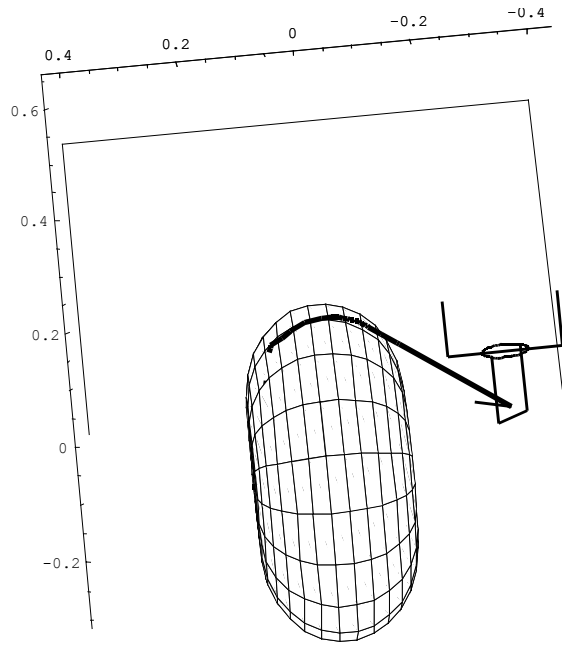
# B

## Production process simulation on a lathe winder

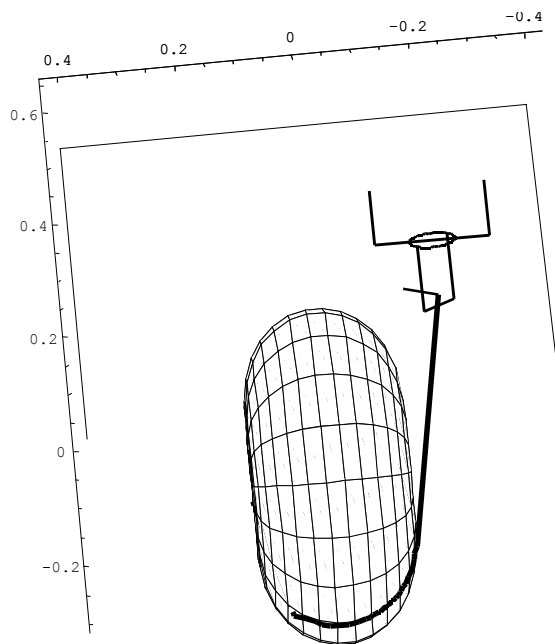
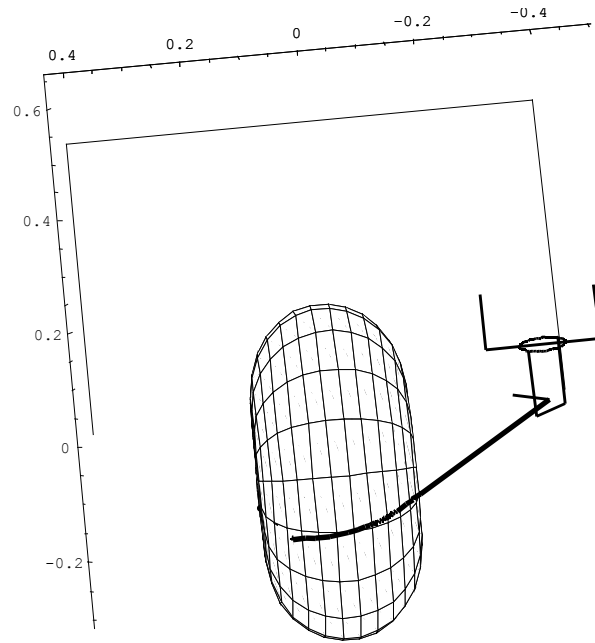


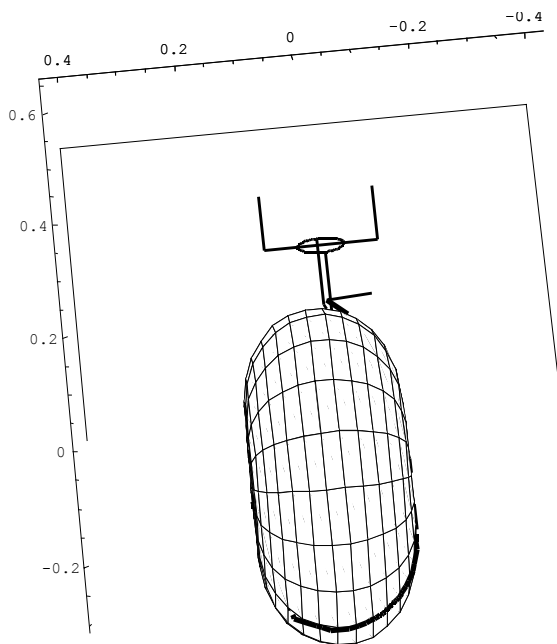
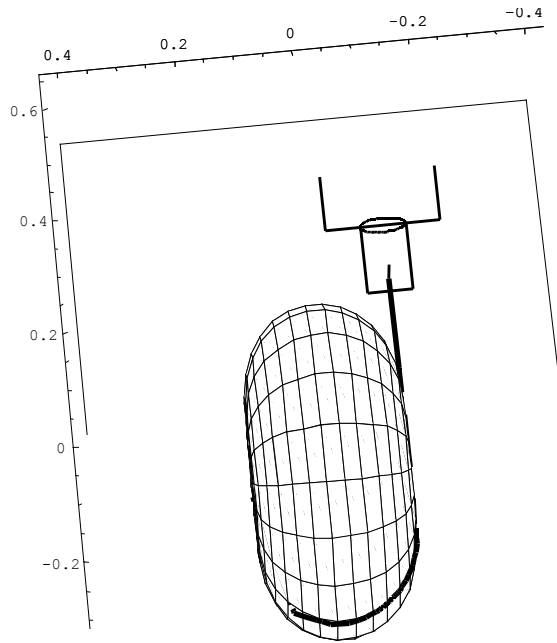
## Appendix B



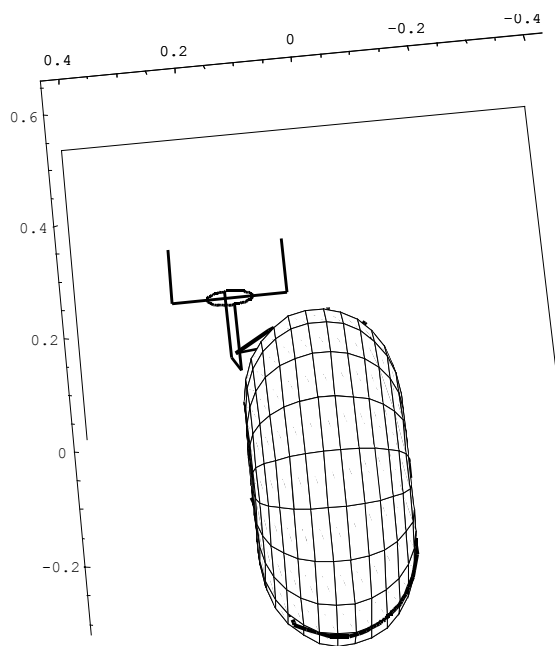
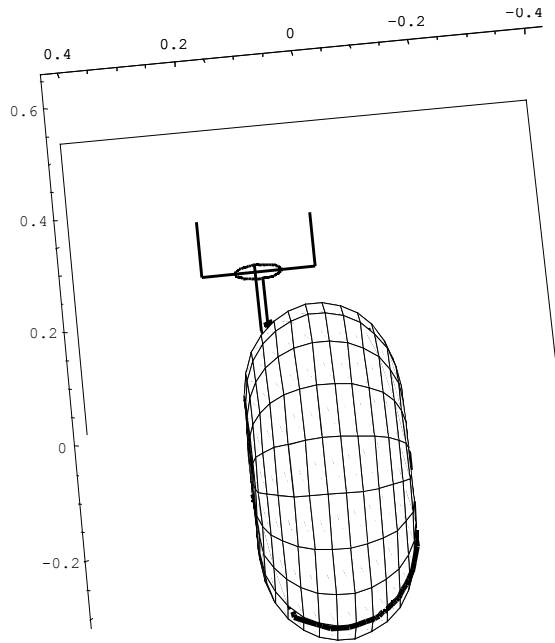


## Appendix B





## Appendix B



# Samenvatting

## Wikkeltechnologie: een generieke benadering

door Sotiris Koussios

Het ontwerpen en produceren van vezelversterkte constructies vereist een integrale aanpak bestaande uit materiaalselectie, vormbepaling en productieproces configuratie. Een van de vele voorbeelden onderhevig aan dit principe, is het zogenaamde wikkelp proces.

Oorspronkelijk bedoeld als productiemethode voor raketmotoren, het wikkelp proces beleeft nu een wedergeboorte, geïnduceerd door het verbreden van het toepassingsgebied der gewikkelde constructies. Een gevolg daarvan is dat het kostenaspect een in relevantie toenemende rol is gaan spelen. Het beheersen en eventueel reduceren van de totale productiekosten vereist in eerste instantie een heroverweging van het proces zelf. Door een recapitulatie van alle wikkelp proces aspecten, zoveel mogelijk gerelateerd aan dezelfde wiskundige basis, het interactief spel van ontwerp, materiaalselectie en productieproces krijgt hier een bewerkbare vorm. Het beoogde resultaat is een optimaal ontwerp, met de term “optimaal” in haar meest brede zin.

Dit proefschrift is georganiseerd in vier delen. Het eerste deel omvat geselecteerde onderwerpen uit de differentiaalgeometrie en beschrijft het gesimplificeerde sterkte berekeningsproces van rotatiesymmetrische membraanelementen, versterkt door continue vezels. Het deel sluit af met een voorbeeld van drukvatenontwerp, volledig bepaald door drie parameters. Een variabele van cruciale betekenis hier, is het vereiste aantal vezelbundels voor het behalen van een zekere statische sterkte.

Het tweede deel is gerelateerd aan de formulering en uitwerking van de wiskundige beschrijving van vezelbanen, zowel geodetisch als niet geodetisch. Voor de experimentele bepaling van de beschikbare wrijving tussen vezels en ondersteunend oppervlak, een speciale mal is hier ontworpen. Daarnaast, de creatie van geschikte wikkelpatronen is hier gepresenteerd als een proces dat mede afhankelijk is van de geometrische en mechanische eigenschappen van de gebruikte vezelbundels. Het resulterende wikkelpatroon vereist een bepaald aantal vezelbundels dat in overeenstemming moet zijn met het aantal bundels dat gedictieerd is door de statische berekeningen. Er moet bovendien rekening worden gehouden met de hier bondig onschreven sterktereductie van de resulterende constructie, veroorzaakt door vezelophoping in bepaalde gebieden.

Het derde deel omvat een uitgebreide beschrijving van de kinematische vergelijkingen die ter grondslag liggen aan de uitwerking van het wikkelp proces zelf. Met een algemene formulering als uitgangspunt, verscheidene oplossingen voor specifieke machine configuraties worden hier aangeboden. Na een korte behandeling van de aan wikkelen gerelateerde dynamische eigenschappen, de formulering van de beschikbare

bewegingsruimte voor het vezeloog komt hier aan de orde. Met de dynamische limieten voor de wikkelmachine componenten en de beschrijving van de bewegingsruimte voor het vezeloog als beperkende factoren, de optimalisatie van het wikkelp proces is hier opgezet en uitgewerkt. Het daarbij beoogde resultaat was het minimaliseren van de productietijd. Als basis voor de optimalisatieroutine, de “Dynamic Programming” methode heeft hier een belangrijke rol gespeeld. Het derde deel sluit af met specifieke voorstellen voor nieuwe wikkelmachine configuraties, het doel dienende van productietijd reductie en, als gevolg daarvan, de beperking van de aan het productieproces gerelateerde kosten.

In het vierde en tevens laatste deel, het ontwerpproces voor rotatiesymmetrische drukvaten wordt nader bekeken. Een uitgebreide beschrijving van een integraal gewikkelde serieschakeling van isotensoïde elementen wordt hier gegeven, waarbij zowel de vorm, constructieve eigenschappen en potentiële toepassingsgebieden aan bod komen. Voor de serieschakeling van niet-identieke elementen, het creëren van niet geodetisch gewikkelde isotensoïdes is hier behandeld. Daarnaast, met dezelfde basisvergelijkingen voor het krachterevenwicht van rotatiesymmetrische objecten als basis, verscheidene vormen zijn hier voorgesteld zoals de gesloten isotensoïde (toroïde), de quasi-cilindrische druktank met externe radiale krachten, de hyperboloïde en de combinatie toroïde-isotensoïde. Het vierde deel sluit af met een voorstel voor het schematiseren van oppervlakken op basis van bilineaire krommingsdistributies, en een korte verhandeling over de geschiktheid van dunne, niet rotatiesymmetrische vezelversterkte membranen in vliegtuigrompen voor het opvangen van de cabinedruk.

Als rode draad door dit schrijven, de behandelde onderwerpen zijn toegepast op isotensoïde drukvaten en geëvalueerd door middel van experimenten en computersimulaties. Het op sterkte testen van de voorgestelde configuraties is hier achterwege gelaten en zal desalniettemin tot de aanbevelingen moeten behoren.

## Curriculum Vitae

Sotiris Koussios was born on the 10<sup>th</sup> of January 1971 in Hilversum, The Netherlands. After finishing his secondary education at the “Polykladiko Lykeio Verias”, Veria, Greece, he studied Classic Piano at the “Hoge Kunst Academie” and Mechanical Engineering at the “Hogeschool Gelderland”, both in Arnhem, The Netherlands. He graduated in both studies in 1994, with “cum laude” for his B.Sc. in Mechanical Engineering. In the same year, he attended the Faculty of Aerospace Engineering, Delft University of Technology, where he obtained his M.Sc. in 2000, on the development of a high-speed tumble winder. In 2000 he started his Ph.D. studies at the group of Design and Production of Composite Structures, headed by Prof. A. Beukers. The research he conducted in this group has resulted in approximately 20 international publications. He is currently appointed as an assistant professor, teaching courses in structural analysis of composites and the production technology of filament wound structures. His interests are structural analysis, simulation of production processes, composites design, classic music, and the reconditioning of old cars.



# List of publications

*In ascending chronological order*

## Journal papers

1. Koussios S, Bergsma OK, Beukers A. Filament Winding Part 1: Determination of the Wound Body Related Parameters. *Composites Part A: Applied Science and Manufacturing* 2004; 35: 181-195.
2. Koussios S, Bergsma OK, Beukers A. Filament Winding Part 2: Generic Kinematic Model and its Solutions. *Composites Part A: Applied Science and Manufacturing* 2004; 35: 197-212.
3. Koussios S, Bergsma OK, Mitchell G. Non-geodesic Filament Winding on Generic Shells of Revolution. *Journal of Materials Part L: Design & Applications*. Submission date: May, 2003. Acceptance date: July 2004.
4. Koussios S, Bergsma OK. Friction Experiments for Filament Winding Applications. *Journal of Thermoplastic Composite Materials*. Submission date: November, 2003. Acceptance date: July 2004.

## Conference papers

1. Koussios S, Bergsma OK. Development of a tumble winder for dedicated products. In: *Proceedings of the 15<sup>th</sup> annual conference of the American Society for Composites*. College Station, TX, 2000.
2. Koussios S, Bergsma OK. Influence of the fibre bundle bandwidth on the determination of a winding pattern. In: *Proceedings of the ESA European conference on Spacecraft Structures, Materials and mechanical Testing*. Noordwijk, November, 2000. P. 375-381.
3. Koussios S, Bergsma OK. On the calculation of geodesic tracks on generic shells of revolution. In: *Proceeding of the 13<sup>th</sup> International Conference on Composite Materials*. Beijing, June, 2001.
4. Koussios S, Bergsma OK. Kinematics of winding: a quasi-analytical approach using four degrees of freedom, applied on the class of ellipsoidal shells of revolution. In: *Proceedings of 13<sup>th</sup> International Conference on Composite Materials*. Beijing, June, 2001.
5. Koussios S, Bergsma OK. Filament winding of generic shells of revolution using a simplified low-budget tumble winder configuration: selection of the process parameters and determination of the possibilities. In: *Proceedings of the 16<sup>th</sup> annual conference of the American Society for Composites*. Blacksburg, VA, 2001.
6. Koussios S, Bergsma OK, Mitchell G. Non-geodesic filament winding on generic shells of revolution. In: *Proceedings of the 10<sup>th</sup> European Conference on Composite Materials*. Brugge, June, 2002.
7. Koussios S, Bergsma OK. Uninterrupted hoop- and polar fibre paths on cylindrical pressure vessels using non-geodesic trajectories. In: *Proceedings of the 17<sup>th</sup> annual conference of the American Society for Composites*. West Lafayette, IN, 2002.
8. Koussios S, Bergsma OK. Winding Pattern Determination for Pressure Vessels Comprising Fibre Bundles of Finite Dimensions. In: *Proceedings of the 14<sup>th</sup> International Conference on Composite Materials*. San Diego, CA, July 2002.
9. Koussios S, Bergsma OK. Analysis of Filament Wound Pressure Vessels Considering the Laminate Thickness Variation through the Meridional Direction. In: *Proceedings of the 14<sup>th</sup> International Conference on Composite Materials*. San Diego, CA, July 2002.
10. Koussios S, Bergsma OK. Automatic Optimal Pattern Generation for Filament Winding Applications. In: *Proceedings of the 18<sup>th</sup> annual conference of the American Society for Composites*. Gainesville, FL, October, 2003.

11. Koussios S, Bergsma OK. Dynamics of Filament Winding: a Comparison between Various Methods for the Estimation of the Induced Fibre and Machine Parts Velocities and Accelerations. In: Proceedings of the 18<sup>th</sup> annual conference of the American Society for Composites. Gainesville, FL, October, 2003.
12. Koussios S, Bergsma OK, Beukers A. Filament Winding: Analytical Kinematic Solutions and Collision Control. In: Proceedings of the 19<sup>th</sup> annual conference of the American Society for Composites. Atlanta, GA, October, 2004.
13. Koussios S, Bergsma OK, Beukers A. Filament Winding: Process Optimisation through Application of Dynamic Programming. In: Proceedings of the 19<sup>th</sup> annual conference of the American Society for Composites. Atlanta, GA, October, 2004.

## **Patents**

Koussios S, Bergsma OK, Beukers A. Pressurizable Structures Comprising Different Surface Sections. Patent Application PCT/NL02/00534. International Filing Date: August 8, 2002. Publication Date: February 19, 2004.

## **Reports**

Koussios S. Preliminary design of a high-speed tumble winder. M.Sc. thesis report. Structures and materials laboratory, Faculty of Aerospace Engineering, Delft University of Technology. Delft, March, 2000.

## **Submitted for Publication**

1. Koussios S, Bergsma OK. Filament winding: Kinematics, Collision Control and Optimisation through Application of Dynamic Programming. Composites Part A: Applied Science and Manufacturing. Submission date: November, 2004.
2. Koussios S, Bergsma OK. Isotensoid Pressure Vessels Based on Non-Geodesic Trajectories. Submitted to: 15<sup>th</sup> International Conference on Composite Materials. Durban, South Africa, June-July, 2005.
3. Koussios S, Bergsma OK. Filament Winding: Analytical Kinematic Solutions for Lathe Configured Winding Machines. Submitted to: 15<sup>th</sup> International Conference on Composite Materials. Durban, South Africa, June-July, 2005.

## Bibliography

■ = *Cited reference*

$\alpha$	General: filament winding & composites design_____	351
$\beta$	Winding patterns_____	354
$\gamma$	Roving trajectories_____	355
$\delta$	Dissertations on filament winding_____	357
$\epsilon$	Shell theory_____	358
$\zeta$	Composite pressure vessels: general design_____	359
$\eta$	Cylindrical parts of composite pressure vessels / Drive shafts_____	361
$\theta$	Filament wound anisogrid composite lattice structures_____	362
$\iota$	Kinematics & dynamics_____	363
$\kappa$	Mechanics of (an) isotropic materials_____	365
$\lambda$	Optimisation_____	366
$\mu$	General and numerical mathematics / Differential geometry_____	367
$\nu$	Fibre tensioners_____	368

## **Bibliography**

**$\alpha$  General: filament winding & composites design**

1. Anglani A, Nucci F, Spagnolo A. Filament winding: an integrated simulation environment for automated cell programming. <http://tsl.unile.it>
2. Automation sets filament winding on the right path. Reinforced plastics, September, 1998: 48-50.
3. ■Baer filament winding machine instruction manual. Josef Baer Maschinenfabrik D-7987 Weingarten/Württ, 1988.
4. ■Bannister M. Challenges for composites into the next millennium – a reinforcement perspective. Composites Part A: Applied science and manufacturing 2001: 32: 901-910.
5. ■Beckwith SW. Filament Winding – The string and the Glue. [http://lanceressex.netfirms.com/webdocs/filament\\_winding.htm](http://lanceressex.netfirms.com/webdocs/filament_winding.htm)
6. ■Bergsma OK. Three Dimensional Simulation of Fabric draping. PhD. thesis report. Structures and materials laboratory, Faculty of Aerospace Engineering, Delft University of Technology. Delft, November 1995.
7. ■Beukers A (in Dutch). “Lichtheid als Gedachtegoed”. Inaugural speech, Delft, The Netherlands: March, 2003.
8. ■Beukers A, Hinte E van. Lightness: The inevitable renaissance of minimum energy structures. Amsterdam: 010 Publishers, 1998.
9. ■Beukers A. A new approach to low cost manufacturing of advanced structures. In: Proceedings of the 7<sup>th</sup> International Conference on Composite Materials. Guangzhou, China: November, 1989.
10. Borgschulte K, Burkhardt G, Effing M, Kirberg K, Mahlke M, Rosenbaum U. Faserwickeln mit Prepregs und GMT-Verarbeitung. Plastverbeiter, May, 1998: 39(5): 48-65.
11. Chen FC. A filament wound structure technology overview. Materials Chemistry and Physics 1995: 96-100.
12. Coffey AB, Brazier A, Tierney M, Gately AG, O’Bradaigh CM. Development of thin-walled fibre-reinforced structures for medical applications. Composites Part A: Applied science and manufacturing 2003: 34: 535-542.
13. DuVall FW. Cost comparisons of wet filament winding versus prepreg filament winding for type ii and type iv CNG cylinders. SAMPE journal, January/February, 2001: 37(1): 38-42.
14. ■Elliman DG, Young K, Edwards KL, Middleton V, Owen MJ. Computer aided design and manufacture of filament wound components. In: Proceedings of the International conference on computer-aided production engineering 1986: 357-361.
15. ■Frate del R, Rae R. Production of conical structures using continuous fibre composites. In: Proceedings of the 40<sup>th</sup> International SAMPE technical conference, May, 1995: 903-913.
16. ■Gemerden J van. “Technische Informatie voor werktuigbouwkundigen”. Culemborg: Educaboek BV, 1989.
17. Giacometto HL. The art of filament winding. Reinforced Plastics, October 2002: 30-31.
18. Green JE. Overview of filament winding. SAMPE journal, January/February 2001: 37(1): 7-11.
19. ■Guillermin O. Advanced CAD integrated software for the cost-effective design and manufacturing of composite structures. In: Proceedings of the 14<sup>th</sup> International Conference on Composite Materials. San Diego, CA, July 2002.
20. ■Jacob A. Automation sets filament winding on the right path. Reinforced Plastics, September 1998.

## Bibliography $\alpha$ (21–45)

21. ■Kooij T, Jagt O van der, Beukers A. A full composite LOX tank for a hybrid rocket. . In: Proceedings of the ESA European conference on Spacecraft Structures, Materials and mechanical Testing. Noordwijk, November, 2000: 187-192.
22. ■Koussios S, Bergsma OK, Beukers A. Pressurizable Structures Comprising Different Surface Sections. Patent Application PCT/NL02/00534. International Filing Date: August 8, 2002. Publication Date: February 19, 2004.
23. ■Koussios S, Bergsma OK. Development of a tumble winder for dedicated products. In: Proceedings of the 15<sup>th</sup> annual conference of the American Society for Composites. College Station, TX, 2000.
24. ■Koussios S. Preliminary design of a high-speed tumble winder. M.Sc. thesis report. Structures and materials laboratory, Faculty of Aerospace Engineering, Delft University of Technology. Delft, March, 2000.
25. ■Mazumdar SK. Composites Manufacturing: Materials, Product, and Process Engineering. Boca Raton, FL: CRC Press, 2002.
26. ■McClean Anderson company. Retrofits expand filament-winding capabilities. Reinforced plastics, November, 2001: 38-39.
27. ■Medney J, Lowrie McLarty J, Kurz CB. Designing with filament winding. In: Proceedings of filament winding conference. Pasadena CA, March 28-30, 1961.
28. ■Middleton V, Young KW, Elliman DG, Owen MJ. Software for filament winding. Automated Composites. The plastics & rubber institute 1986: 9.1-9.6.
29. ■Mobasher B, Pivacek A. A filament winding technique for manufacturing cement based cross-ply laminates. Cement and Concrete Composites 1998: 20: 405-415.
30. ■Munro M. Review of manufacturing of fibre composite components by filament winding. Polymer Composites 1988: 9(6): 352.
31. ■Muttana Suresh Babu, Gudavalli Srikanth, Soumitra Biswas. Composite Fabrication by Filament Winding – An Insight. <http://www.tifac.org.in/acfil.htm>.
32. ■Newling DO. Filament winding: a critical survey of materials, processes and applications, AWRE report no. 081/68. United Kingdom Atomic Energy Authority, 1968.
33. ■Nouwen G. Filament Winding Strategies for Articulated Shells of Revolution. Preliminary thesis report. Structures and Materials Laboratory, Faculty of Aerospace Engineering, Delft University of Technology. Delft, November, 2002.
34. ■Owen MJ, Elliman DG, Middleton V, Young K, Weatherby N. Advanced manufacturing technology for filament winding. Polymer processing. Automation. The plastics & rubber institute 1986: 22.1-22.13.
35. ■Peters ST, Donald Humphrey WD. Filament winding. In: Dostal CA, editor. Engineered materials handbook, Volume 1: Composites. Ohio, 1987.
36. ■Peters ST, Donald Humphrey WD. Filament winding. In: Dostal CA, editor. Engineered materials handbook, Volume 2: Engineering Plastics. Ohio, 1987.
37. ■Peters ST, Humphrey WD, Foral RF. Filament Winding Composite Structure Fabrication. Covina CA: SAMPE International Business Office, 1999.
38. Poggiali B, Busch JV. Micro-computer based cost estimation of filament winding. Automated Composites. The plastics & rubber institute 1986: 7.1-7.8.
39. ■Rijn LPVM van. Design & Composites. Lecture Notes LR27 c. Faculty of Aerospace Engineering, Delft University of Technology. Delft, July, 1994.
40. ■Rijswijk K van, Koussios S, Bergsma OK. Filament wound container made of natural fibres and –rubber. In: Proceedings of the 10<sup>th</sup> European Conference on Composite Materials, Brugge, 2002.
41. ■Rijswijk K van. Feasibility study on a natural fibre wound vessel for the Vietnamese market. M.Sc. thesis report. Structures and materials laboratory, Faculty of Aerospace Engineering, Delft University of Technology. Delft, July, 2001.
42. ■Rijswijk K van. The design of a tumble winder prototype. Preliminary thesis report. Structures and materials laboratory, Faculty of Aerospace Engineering, Delft University of Technology. Delft, February, 2001.
43. ■Rosato DV, Grove CS. Filament winding: its development, manufacture, applications, and design. Polymer engineering and technology. New York: Interscience, 1964.
44. Rosenbaum JU. Flechten (in German). Köln: Verlag TÜV Rheinland GmbH, 1991.
45. Rowan JHC. Advanced filament winding: evolution and revolution. Metals and materials 1998: 280-284.

46. Russel DK, Farrington PA, Messimer SL, Swain JJ. Incorporating environmental issues in a filament winding composite manufacturing system simulation. In: Medeiros DJ, Watson EF, Carson JS, Manivannan MS, editors. Proceedings of the 1998 Winter Simulation Conference: 1023-1028.
47. Shen FC. A filament wound structure technology overview. *Materials chemistry and physics* 1995; 42: 96-100.
48. ■Tooren MJL van, Sinke J, Bersee HEN. Composites: materials, structures and manufacturing processes. Lecture notes AE4-632. Structures and materials laboratory, Faculty of Aerospace Engineering, Delft University of Technology. Delft, 1993.
49. ■Veldman, S.L., Vermeeren, C.A.J.R., "Inflatable structures in aerospace engineering - An overview" Presented at the European conference on spacecraft structures, materials and mechanical testing, Noordwijk, the Netherlands, 29 November - 1 December 2000, (ESA SP-468, March 2001), 2001.
50. ■Wells GM, Eckold GC. Computer aided design and manufacture of filament wound composite structures. *The Plastics & Rubber Institute* 1986: 6.1-6.16.

### $\beta$ Winding patterns

1. ■Johansen BS, Lystrup A. CADPATH: a complete program for the CAD-, CAE- and CAM-winding of advanced fibre composites. *Journal of Materials Processing Technology* 1998; 77: 194-200.
2. ■Koussios S, Bergsma OK. Automatic Optimal Pattern Generation for Filament Winding Applications. In: Proceedings of the 18<sup>th</sup> annual conference of the American Society for Composites. Gainesville, FL, October, 2003.
3. ■Koussios S, Bergsma OK. Winding Pattern Determination for Pressure Vessels Comprising Fibre Bundles of Finite Dimensions. In: Proceedings of the 14<sup>th</sup> International Conference on Composite Materials. San Diego, CA, July 2002.
4. ■Koussios S. Influence of the fibre bundle bandwidth on the determination of a winding pattern. In: Proceedings of the ESA European conference on Spacecraft Structures, Materials and mechanical Testing. Noordwijk, November, 2000: 375-381.
5. ■Liang YD. A simple filament winding pattern generation algorithm. In: Proceedings of the 28<sup>th</sup> International SAMPE technical conference, 1996: 1027-1039.
6. ■Rijswijk K van, Koussios S, Bergsma OK. Fibre thickness distribution of a filament wound rotational symmetric pressure vessel. In: Proceedings of the third European conference on launcher technology. Strasbourg, December, 2001.

$\gamma$  Roving trajectories

1. ■Carvalho JD, Lossie M, Vandepitte D, Van Brussel, H. Optimization of Filament-wound Parts Based on Non-geodesic Winding. *Composites Manufacturing*, 1995: 79-84.
2. ■Di Vita G, Grimaldi M, Marchetti M, Moroni P. The filament winding manufacturing technique: studies on the determination of the friction coefficient and on the optimisation of feed-eye motion. In: *Proceedings of the 22<sup>nd</sup> International SAMPE technical conference*, 1990: 972-979.
3. ■Di Vita G, Marchetti M, Perugini P. Designing complex shape filament-wound structures. *Composites manufacturing* 1992: 3(1): 53-58.
4. Elhage-Hussein A, Keulen F van, Boer H de. Numerical simulation of filament winding process using an asymptotic technique. Pre-print submitted to Elsevier Preprint, September, 1999.
5. ■Hongtao Su. Modelling stable filament winding on general curved surface. In: *Proceedings of the 31<sup>st</sup> SAMPE technical conference*, October, 1999.
6. ■Koussios S, Bergsma OK, Beukers A. Filament Winding Part 1: Determination of the Wound Body Related Parameters. *Composites Part A: Applied Science and Manufacturing* 2004: 35: 181-195.
7. ■Koussios S, Bergsma OK, Mitchell G. Non-geodesic filament winding on generic shells of revolution. In: *Proceedings of the 10<sup>th</sup> European Conference on Composite Materials*. Brugge, June, 2002.
8. ■Koussios S, Bergsma OK, Mitchell G. Non-geodesic Filament Winding on Generic Shells of Revolution. *Journal of Materials Part L: Design & Applications*. Submission date: May, 2003. Acceptance date: July 2004.
9. ■Koussios S, Bergsma OK. Friction Experiments for Filament Winding Applications *Journal of Thermoplastic Composite Materials*. Submission date: November, 2003. Acceptance date: July 2004.
10. ■Koussios S, Bergsma OK. On the calculation of geodesic tracks on generic shells of revolution. In: *Proceeding of the 13<sup>th</sup> International Conference on Composite Materials*. Beijing, June, 2001.
11. ■Koussios S, Bergsma OK. Uninterrupted hoop- and polar fibre paths on cylindrical pressure vessels using non-geodesic trajectories. In: *Proceedings of the 17<sup>th</sup> annual conference of the American Society for Composites*. West Lafayette, IN, 2002.
12. Liang YD, Zou ZQ, Luo G. Non-axisymmetric filament winding for elbows based on the quasi geodesics. In: *Proceeding of the 29<sup>th</sup> International SAMPE technical conference*, 1997: 366-375.
13. ■Liang YD, Zou ZQ, Zhang ZF. Quasi-geodesics- a new class of simple and non-slip trajectories on revolutionary surfaces. In: *Proceedings of the 28<sup>th</sup> International SAMPE technical conference*, 1996: 1071-1079.
14. ■Marchetti M, Cutolo D, Di Vita G. Filament winding of composite structures: validation of the manufacturing process. In: *Proceedings of the 7<sup>th</sup> International Conference on Composite Materials*, 1989; 7: 135-140.
15. ■Mitchell, G. Non-geodesic filament winding equation and solution for surfaces of revolution. Internship report. Structures and materials laboratory, Faculty of Aerospace Engineering, Delft University of Technology. Delft, July, 2001.
16. ■Perugini P, Ferraro F, Di Vita G. Optimisation of mandrel coverage for complex shape structures made by filament winding technology. In: Miravete A, editor. *Proceedings of the 9<sup>th</sup> International Conference on Composite Materials*. Madrid, Spain, 1993; Vol 3: 455-461.
17. ■Renggli M. Friction tests for Filament Winding. Internship report. Structures and Materials Laboratory, Faculty of Aerospace Engineering, Delft University of Technology. Delft, June, 2003.
18. ■Scholliers J, Brussel H van. Computer-integrated filament winding: computer-integrated design, robotic filament winding and robotic filament winding and robotic quality control. *Composites manufacturing*, 1994: 5(1): 1103-1112.

## **Bibliography $\gamma$ (19-21)**

19. ■Simoes JAO, Wu ST, Loseries F. Visual Simulation of the Geodesic and Non-geodesic Trajectories of the Filament Winding. *Graphics Modelling and Visualization in Science and Technology*, 1993: 199-215.
20. ■Wells GM, McAnulty KF. Computer aided filament winding using non-geodesic trajectories. In: *Proceedings of the second European Conference on Composite Materials (ICCM/ECCM)*. London, 1987; 1.161-1.173.
21. ■Xian-li Li, Dao-hai Lin. Non-geodesic winding equations on a general surface of revolution. In: *Proceedings of the second European and 6<sup>th</sup> International Conference on Composite Materials (ICCM/ECCM)*. London, 1987; 1.152-1.160.

**$\delta$  Dissertations on filament winding**

1. ■Kirberg KW. Concept of process-simulation in filament winding technology. PhD. Thesis. Faculty of Mechanical Engineering, RWTH Aachen. Aachen, December, 1988.
2. ■Scholliers J. Robotic filament winding of asymmetric composite parts. PhD. Thesis. Faculty of applied sciences. Department of Mechanical Engineering. Leuven University. Leuven, December, 1992.

## **Bibliography €**

### **€ Shell theory**

1. ■ Baker EH, Kovalevsky L, Rish FL. Structural analysis of shells. New York: McGraw Hill Book Company, 1972.
2. ■ Flügge W. Stresses in Shells. Berlin / Heidelberg / New York: Springer Verlag, 1966.

## ζ Composite pressure vessels: general design

1. ■Bell JE. The effect of glass fibre geometry on composite material strength. In: SAMPE Filament winding conference. Pasadena, CA, March 1961.
2. ■Cho-Chung Liang, Heng-Wen Chen, Cheng-Huan Wang. Optimum design of dome contour for filament winding composite pressure vessels based on a shape factor. *Composite Structures* 2002; 58: 469-482.
3. Cohen D, Mantell SC, Zhao L. The effect of fibre volume fraction on filament wound composite pressure vessels strength. *Composites Part B: Engineering* 2001; 32: 413-429.
4. Cohen D. Influence of filament winding parameters on composite vessel quality and strength. *Composites Part A: Applied science and manufacturing* 1997; 28A: 1035-1047.
5. ■Davis R Jr. Stress analysis of filament wound motor cases. In: SAMPE Filament winding conference. Pasadena, CA, March 1961.
6. Denos JP. Design of filament wound rocket cases. Head of programs for filament wound structures, Aerospatiale, St-Médard-en-Jalles, 33165, France.
7. ■Design of Filament Wound Pressure Vessels. European Space Agency, February 1994. *Structural Materials Handbook: Vol. 1: Polymer Composites: Section VI: Design of Structures*, chapter 29.
8. Engels H, Becker W. Elliptical reinforcement of a circular hole in a laminate under inplane load or bending. In: *Proceedings of the 16<sup>th</sup> Conference of the American Society for Composites*. Blacksburg, VA, 2001.
9. ■Gerard G, Lakshmikantham C. Optimum thin-wall pressure vessels of anisotropic materials. *Journal of Applied Mechanics, Transactions of the ASME*, 1966: 623-828.
10. ■Grammol K. Stress analysis of filament wound open-ended composite shells. <http://eml.ou.edu/Grammol/Research/>, University of Oklahoma, 1997.
11. ■Hofeditz JT. Structural design considerations for fibrous glass pressure vessels. *Modern Plastics*, April, 1964: 127-145.
12. Hoffman O. Stresses and deformations in filament-reinforced structures. IAS paper No. 62-26, 1962.
13. ■Jae-Sung Park, Chang-Sun Hong, Chun-Gon Kim, Cheol-Ung Kim. Analysis of filament wound structures considering the change of winding angles through the thickness direction. *Composite Structures* 2002; 55: 63-71.
14. ■Jong de Th (in Dutch). “Het wikkelen van drukvaten volgens de netting theorie”. Report VTH-166. Structures and materials laboratory, Faculty of Aerospace Engineering, Delft University of Technology. Delft, April, 1971.
15. ■Jong de Th. A theory of filament wound pressure vessels. Report LR-379. Structures and materials laboratory, Faculty of Aerospace Engineering, Delft University of Technology. Delft, April, 1983.
16. ■Kabir MZ. Finite element analysis of composite pressure vessels with a load sharing metallic liner. *Composite structures* 2000; 49: 247-255.
17. Khalid AA, Sahari BB, Khalid YA. Performance of composite cones under axial compression loading. *Composites science and technology*, 2002; 62: 17-27.
18. Kim BS, Kim BH, Kim JB, Joe CR. Study on the development of composite CNG pressure vessels. *Cryogenics* 1998; 38: 131-134.
19. ■Kooij T. Development of a liquid oxygen compatible composite pressure vessel. M.Sc. thesis report. Structures and materials laboratory, Faculty of Aerospace Engineering, Delft University of Technology. Delft, March, 2001.

## Bibliography $\zeta$ (20-37)

20. ■Kooij T. Towards a full composite LOX container. Preliminary thesis report. Structures and materials laboratory, Faculty of Aerospace Engineering, Delft University of Technology. Delft, March, 2001.
21. ■Koussios S, Bergsma OK. Analysis of Filament Wound Pressure Vessels Considering the Laminate Thickness Variation through the Meridional Direction. In: Proceedings of the 14<sup>th</sup> International Conference on Composite Materials. San Diego, CA, July 2002.
22. Lifshitz JM, Dayan H. Filament wound pressure vessel with thick metal liner. *Composite Structures* 1995; 32: 313-323.
23. Linde LF van der. Design and production of a LOX pressure vessel. . M.Sc. thesis report. Structures and materials laboratory, Faculty of Aerospace Engineering, Delft University of Technology. Delft, November, 1999.
24. ■Lossie M, Brussel H van. Design principles in filament winding. *Composites manufacturing*, 1994; 5(1): 5-13.
25. ■Marchetti M, Cutolo D, Di Vita G. Design of domes by use of the filament winding technique. In: Developments in the science and technology of composite materials. European association for composite materials, Bordeaux, March, 1989: 401-408.
26. Morozov EV. Application of the boundary-layer theory to the analysis of composite shells of revolution. *Composite Structures*, 2001; 54: 261-265.
27. ■Nieuwenhuizen E. Composite LPG fuel containers for motor vehicles. M.Sc. thesis report. Structures and materials laboratory, Faculty of Aerospace Engineering, Delft University of Technology. Delft, August, 1995.
28. ■Parnas L, Katirci N. Design of fibre-reinforced composite pressure vessels under various loading conditions. *Composite structures*, 2002; 58: 83-95.
29. Schuerch HU, Burggraf OR. Analytical design for optimum filamentary pressure vessels. *AIAA Journal*, May, 1964; 5: 809-820.
30. Tae-Kyung Hwang, Chang-Sun Hong, Chun-Gon Kim. Probabilistic deformation and strength prediction for a filament wound pressure vessel. *Composites Part B: Engineering* 2003; 34: 481-497.
31. Takayuki Shimoda, Jianmei He, Yoshihiro Mizutami, Yoshiki Morino. Test of filament wound CFRP prototype for cryogenic propellant tank of space plane. In: Proceedings of the 11<sup>th</sup> AIAA/AAAF conference on space planes and hypersonic systems technology, Orleans, France, Sept./Oct. 2002.
32. ■Tarnopols'skii Y. Problems of the mechanics of winding thick-walled composite structures. In: Miravete A, editor. Proceedings of the 9<sup>th</sup> International Conference on Composite Materials. Madrid, Spain, 1993; Vol. 3: 417-422.
33. Tsuyoshi Hayashi. Some structural problems in filament wound pressure vessels having embedded liner. In: Proceedings of the 4<sup>th</sup> Japan-US Conference on Composite Materials. June, 1988.
34. ■Vasiliev VV, Krikanov AA. New generation of filament-wound composite pressure vessels for commercial applications. In: Proceedings of the fourth international conference on composite science and technology, ICCST 4, Durban, South Africa, January, 2003:10-29.
35. ■Vasiliev VV, Krikanov AA. New generation of filament-wound composite pressure vessels for commercial applications. *Composite Structures* 2003; 62: 449-459.
36. ■Zickel J. Filament Wound Pressure Vessel. Patent Specification Nr. 1,064,590. Application Nr. 4912/64; Publication date: April, 1967.
37. Zoller P. "Das Glasfaserwickelverfahren". *Technische Rundschau* 1964: 25.

$\eta$  Cylindrical parts of composite pressure vessels / Drive shafts

1. Bèakou A, Mohamed A. Influence of variable scattering on the optimum winding angle of cylindrical laminated composites. *Composite structures*, 2001: 53: 287-293.
2. ■Calius EP, Springer GS. A model of filament-wound thin cylinders. *Int. Journal of Solids and Structures*, 1990: 26(3): 271-297.
3. ■Dreumel WHM van (in Dutch). "Onderzoek naar de optimale wikkelhoek voor g.v.k. cylinders onder inwendige hydrostatische overdruk volgens de continuum theorie". Structures and materials laboratory, Faculty of Aerospace Engineering, Delft University of Technology. Delft, January, 1974.
4. Gibson AG, Hicks PNH, Wriqth H, Fahrer A. Development of glass fibre reinforced polyethylene pipes for pressure applications. *Plastics, Rubber and Composites*, 200: 29(10): 509-519.
5. Jensen DW, Suresh PP. Theoretical sensitivity of composite cylinders in compression to filament winding pattern. In: Miravete A, editor. *Proceedings of the 9<sup>th</sup> International Conference on Composite Materials*. Madrid, Spain, 1993; Vol. 3: 447-454.
6. ■Jones IA. Approximate solutions to the orthotropic pinched cylinder problem. *Composite structures*, 1998: 42: 73-91.
7. Lee DG, Kim HS, Kim JW, Kim JK. Design and manufacture of an automotive hybrid aluminum/composite drive shaft. *Composite Structures* 2004: 63: 87-99.
8. Lee SY, Springer GS. Filament winding cylinders: I process model. *Journal of composite materials*, 1990: 24: 1270-1298.
9. Mertiny P, Ellyin F, Hothan A. An experimental investigation on the effect of multi-angle filament winding on the strength of tubular composite structures. *Composites science and technology* 2004: 64: 1-9.
10. ■Rousseau J, Perreux D. Verdière N. The influence of winding patterns on the damage behaviour of filament-wound pipes. *Composites science and technology* 1999: 59: 1439-1449.
11. Sakaguchi M, Nakai A, Hamada H, Takeda N. The mechanical properties of unidirectional thermoplastic composites manufactured by a micro-braiding technique. *Composites science and technology*, 200: 60: 717-722.
12. Tizzi S. Free frequencies and modal shapes of cylindrical vibrating composite structures. *Computers and structures*, 199: 73: 629-653.
13. ■Wild PM, Vickers GW. Analysis of filament wound cylindrical shells under combined centrifugal, pressure and axial loading. *Composites Part A: Applied science and manufacturing* 1997: 28A: 47-55.
14. Xia M, Kemmochi K, Takayanagi H. Analysis of filament-wound fibre-reinforced sandwich pipe under combined internal pressure and thermomechanical loading. *Composite structures*, 2001: 51: 273-283.
15. ■Yousefpour A, Ghasemi Nejhad MN. Effects of Geometric Optimization of Plug-supported End-caps on the Performance of Thick Thermoplastic Composite Pressure Vessels under External Hydrostatic Pressure. *Journal of Thermoplastic Composite Materials* 2002: 15: 402-428.
16. Yuan FG, Yang W, Kim H. Analysis of axisymmetrically-loaded filament wound composite cylindrical shells. *Composite structures*, 200: 20: 115-130.
17. ■Veldman, S.L., Bergsma, O.K., Beukers, A. Drechsler, K. Load deflection behaviour of inflated beams made of various foil materials. Presented at the 45th AIAA Structures, Structural Dynamics, and Materials Conference, 19- 22 Apr 2003 Palm Springs, California AIAA-2004-1504

## **Bibliography $\theta$**

### **$\theta$ Filament wound anisogrid composite lattice structures**

1. Vasiliev VV, Barynin VA, Rasin AF. Anisogrid lattice structures – survey of development and application. *Composite Structures* 2001; 54: 361-370.
2. Vasiliev VV, Rasin AF. Optimal design of filament wound anisogrid composite lattice structures. In: *Proceedings of the 16<sup>th</sup> annual conference of the American Society for Composites*. Blacksburg, VA, 2001.

**$\iota$  Kinematics & dynamics**

1. ■Anglani A, Nucci F, Spagnolo A. Filament winding: simulation for robotic cell design. <http://tsl.unile.it>
2. Atangana Ateba J, Aivazzadeh S, Verchery G. Simulation and control of a filament winding machine with heating for thermoplastic prepregs. In: Miravete A, editor. Composites modelling and processing science. Proceedings of the ninth international conference on composite materials. Madrid, July, 1993.
3. Banerjee A, Sun L, Mantell SC, Cohen D. Model and experimental study of fibre motion in wet filament winding. *Composites part A*, 1998; 29A: 251-263.
4. ■Belle B van. Simulation of filament winding. M.Sc. thesis report. Structures and materials laboratory, Faculty of Aerospace Engineering, Delft University of Technology. Delft, 1994.
5. ■Calius EP, Springer GS. Filament winding process simulation. In: The manufacturing science of composites. Proceedings of manufacturing international, 1988.
6. ■Carrino L, Polini W, Sorrentino L. A New Robotized Filament Winding Cell to Manufacture Complex Shapes. In: Proceedings of the 14<sup>th</sup> International Conference on Composite Materials. San Diego, CA, July 2002.
7. ■Carrino L, Polini W, Sorrentino L. Modular structure of a new-deposition head for a robotized filament winding cell. *Composites Science and Technology* 2003; 63: 2255-2263.
8. ■Chan S, Munro M, Fahim A. Accuracy-speed relationships of a robotic filament winding cell. *Robotics & Computer Integrated Manufacturing* 1996; 12(1), 3-13.
9. ■Di Vita G, Farioli M, Marchetti M. Process simulation in filament winding of composite structures. *Composite materials: design and analysis*, 1990: 19-37.
10. ■Di Vita G, Perugini P. Process simulation models for filament winding technology. In: Miravete A, editor. Composites modelling and processing science. Proceedings of the ninth international conference on composite materials. Madrid, July, 1993.
11. ■Gamarra-Rosado VO, Yuhara EAO. Dynamic modelling and simulation of a flexible robotic manipulator. *Robotica* 1999; 17: 523-528.
12. ■Ginsberg JH. *Advanced Engineering Dynamics*. Cambridge: Cambridge University Press, 1995.
13. ■Holten Th van (in Dutch). "Mechanica III". Lecture notes LR 3-14. Faculty of Aerospace Engineering, Delft University of Technology. Delft, September, 1998.
14. Ikononopoulos G, Marchetti M. Theoretical approach and numerical simulation of the winding and curing cycles in filament winding manufacturing. *Techn. Chron. Sci.*, 1998; IV(1): 67-77.
15. ■Koussios S, Bergsma OK, Beukers A. Filament Winding Part 2: Generic Kinematic Model and its Solutions. *Composites Part A: Applied Science and Manufacturing* 2004; 35: 197-212.
16. ■Koussios S, Bergsma OK, Beukers A. Filament Winding: Analytical Kinematic Solutions and Collision Control. In: Proceedings of the 19<sup>th</sup> annual conference of the American Society for Composites. Atlanta, GA, October, 2004.
17. ■Koussios S, Bergsma OK. Dynamics of Filament Winding: a Comparison between Various Methods for the Estimation of the Induced Fibre and Machine Parts Velocities and Accelerations. In: Proceedings of the 18<sup>th</sup> annual conference of the American Society for Composites. Gainesville, FL, October, 2003.
18. ■Koussios S, Bergsma OK. Filament winding of generic shells of revolution using a simplified low-budget tumble winder configuration: selection of the process parameters and determination of the possibilities. In: Proceedings of the 16<sup>th</sup> annual conference of the American Society for Composites. Blacksburg, VA, 2001.
19. ■Koussios S, Bergsma OK. Kinematics of winding: a quasi-analytical approach using four degrees of freedom, applied on the class of ellipsoidal shells of revolution. In: Proceedings of 13<sup>th</sup> International Conference on Composite Materials. Beijing, June, 2001.

## Bibliography $\iota$ (20-29)

20. ■Lye SW, Boey FYC. Development of a low-cost filament winding system for composite components. *Journal of Materials Processing Technology* 1995; 52: 570-584.
21. ■Machetti M, Cutolo D, Di Vita G. Filament winding of composite structures: validation of the manufacturing process. In: *Proceedings of the 7<sup>th</sup> ICCM conference*. Guangzhou, China, November, 1989.
22. Markov L, Cheng RMH. Conceptual design of robotic filament winding complexes. *Mechatronics* 1996; 6(8), 881-896.
23. ■Mazumdar SK, Hoa SV. Analytical models for low cost manufacturing of composite components by filament winding, Part I: Direct kinematics. *Journal of Composite Materials* 1995; 29(11), 1515-1541.
24. ■Mazumdar SK, Hoa SV. Analytical models for low cost manufacturing of composite components by filament winding, Part II: Inverse kinematics. *Journal of Composite Materials* 1995; 29(13), 1762-1789.
25. Michaeli W, Goedel M. Process simulation in filament winding: new insights show the way to cost effective component development. In: D. Hui, Kozik TJ, editors: *Composite materials for PVP applications*. The American society of mechanical engineers, 1990: 35-40.
26. ■Moree AC. Geodesic winding of rotational symmetric bodies. M.Sc. thesis report. Faculty of Aerospace Engineering, Delft University of Technology. Delft, December 1986.
27. ■Scholliers J, Brussel H van. Design and off-line programming of a robotic tape winding cell. *Robotics & Computer Integrated Manufacturing* 1996;12(1), 93-98.
28. ■Steltenpool MH. A new approach to filament winding simulation. M.Sc. thesis report. Structural Optimisation and Computational Mechanics group, Faculty of Mechanical Engineering, Delft University of Technology. Delft, August 2000.
29. Zhao L, Mantell S, Cohen D. McPeak R. Finite element modelling of the filament winding process. *Composite structures*, 2001: 52: 499-510.

**K Mechanics of (an) isotropic materials**

1. ■ Jones RM. *Mechanics of Composite Materials*. New York: Hemisphere Publishing Corporation, 1975.
2. Ludolph GL, Potma AP, Legger RJ (in Dutch). “Leerboek der mechanica 2: sterkteleer”. Groningen: Wolters-Noordhoff, 1976.
3. Miroslioubov I et al. “Problèmes de résistance des matériaux”. Moscow: Editions MIR, 1973.
4. ■ Nijhof AHJ (in Dutch). “Vezelversterkte Kunststoffen”. Delft University Press, Delft, 2004
5. ■ Spies GJ (in Dutch). “Versterkte materialen in de vliegtuigbouw”. Lecture notes AE4-684. Structures and materials laboratory, Faculty of Aerospace Engineering, Delft University of Technology. Delft, 1989.
6. Timoshenko SP, Goodier JN. *Theory of Elasticity*. New York: McGraw-Hill Publishing Company, 1987 (Reissued).
7. ■ Tooren MJL van, Stijn IPM van, Beukers A. Curvature effects on the stress distribution in sandwich cylinders with a circular cut-out. *Composites Part A: Applied science and manufacturing* 2002; 33: 1557-1572.
8. ■ Tooren MJL van. Sandwich fuselage design. PhD. thesis report. Structures and materials laboratory, Faculty of Aerospace Engineering, Delft University of Technology. Delft, December, 1998.
9. ■ Tsai SW, Thomas Hahn H. *Introduction to Composite Materials*. . Lancaster-Basel: Technomic Publishing Company, Inc., 1980.
10. ■ Vasiliev VV, Gürdal Z. *Optimal Design*. Lancaster: Technomic Publishing Company, 1999.
11. ■ Whitney JM. *Structural Analysis of Laminated Anisotropic Plates*. Lancaster-Basel: Technomic Publishing Company, Inc., 1987.

### $\lambda$ Optimisation

1. ■Becerra VM. Optimal Control (Unit 3/CY/E0). Lecture Notes. Department of Cybernetics, the University of Reading, 2003. <http://www.rdg.ac.uk/~shs99vmb/notes>
2. ■Bertsekas DP. Dynamic Programming. Lecture Slides for MIT course 6.231, Massachusetts Institute of Technology, Cambridge, Mass. Fall 2003.
3. ■Chin Pei Tang. Time-Optimal Control of Planar Robotic Manipulators. Final Project Report. MAE 672: Optimal Control Systems. Department of Mechanical and Aerospace Engineering, State University of New York at Buffalo.
4. Griesse R, Walther A. Parametric sensitivities for optimal control problems using automatic differentiation. Optimal Control Applications and Methods 2003; 24: 297-314.
5. <http://www.documents.wolfram.com>
6. ■Koussios S, Bergsma OK, Beukers A. Filament Winding: Process Optimisation through Application of Dynamic Programming. In: Proceedings of the 19<sup>th</sup> annual conference of the American Society for Composites. Atlanta, GA, October, 2004.
7. Luus R. Iterative Dynamic Programming. Boca Raton, FL, Chapman & Hall/CRC, 2000.
8. Saramago SFP, Steffen V JR. Optimization of the Trajectory Planning of Robot Manipulators Taking into Account the Dynamics of the System. Mech. Mach. Theory 1998; 33: 883-894.
9. Simon D. Globally Optimal Periodic Robot Joint Trajectories. J. Franklin Inst. 1996; 333B: 5: 659-668.
10. ■Takanori Shibata. Motion Planning by Genetic Algorithm for a redundant Manipulator Using a Model of Criteria of Skilled Operators. Information Sciences 1997; 102: 171-186.
11. ■Wei-Min Yun, YU-Geng Xi. Optimum motion planning in joint space for robots using genetic algorithms. Robotics and Autonomous Systems 1996; 18: 373-393.
12. ■Wen JT. Optimal Control. Lecture Notes ECSE 6440. Electrical, Computer and Systems Engineering Department, Rensselaer Polytechnic Institute, 2004. <http://www.cat.rpi.edu/~wen/ECSE644S04/lectures.htm>
13. ■Wilson E, Karr C, Messimer S. Genetic Algorithm Optimization of a Filament Winding Process Modelled in WITNESS. Materials and Manufacturing Processes 2003; 3: 509-521.
14. Xuan F. Zha. Optimal pose trajectory planning for robot manipulators. Mechanism and Machine Theory 2002; 12: 1063-1086.

$\mu$  General and numerical mathematics / Differential geometry

1. ■Abramowitz M. Handbook of Mathematical Functions. New York: Dover 1970.
2. ■Almering JHJ et all (in Dutch). "Analyse". Delft: Delftse uitgevers maatschappij, 1993.
3. ■Blachman N, Geurts L (in Dutch). Mathematica. Hemel Hempstead: Prentice-Hall, 1992 & Schoonhoven: Uitgeverij Academic Service, 1993.
4. ■Boyce WE, DiPrima RC. Elementary Differential Equations and Boundary Value Problems. New York: John Wiley & Sons, Inc. 1986.
5. ■Goldman R. Lagrange Interpolation and Neville's Algorithm. Lecture Slides. Department of Computer Science, Rice University.
6. ■Gray A. Modern Differential Geometry of Curves and Surfaces. CRC press, 1993.
7. ■Kan J van (in Dutch). "Numerieke wiskunde voor technici. Delft: Delftse uitgevers maatschappij, 1993.
8. ■Kreyszig E. Advanced Engineering Mathematics. New York: John Wiley & Sons, Inc. 1999.
9. ■Kreyszig E. Mathematical Expositions Nr. 11: Differential Geometry. Toronto: University of Toronto Press, 1959.
10. ■Stathis PT. Sparse Matrix Vector Processing Formats. PhD. thesis report. Department of Computer Engineering, Faculty of Electrical Engineering, Mathematics and Computer Science, Delft University of Technology. Delft, November 2004.
11. ■Teller O (in Dutch). "Vademecum van de wiskunde". Utrecht: Uitgeverij Het spectrum BV, 1988.
12. ■Various Authors (in Dutch). Sesam: Atlas van de Wiskunde (in Dutch). Baarn, The Netherlands, Bosch & Keuning NV, 1980.
13. ■Vidovic D. Superlinear Unstructured Staggered Schemes for Compressible and Incompressible Flows. To appear in 2005. Department of Numerical Analysis, Faculty of Electrical Engineering, Mathematics and Computer Science. PhD thesis report. Delft University of Technology. Delft, 2005.
14. ■Wolfram S. Mathematica: A System for Doing Mathematics by Computer. Champaign IL: Wolfram Research, Inc. 1991.
15. ■[www.mathworld.wolfram.com](http://www.mathworld.wolfram.com)

## **Bibliography v**

### **v Fibre tensioners**

1. ■Kahriman A. Introduction to the preliminary design and development of a low budget fibre tensioner. Internship report. Structures and materials laboratory, Faculty of Aerospace Engineering, Delft University of Technology. Delft, June, 2001.